INVESTIGATING THE EFFECTS OF MICROSTRUCTURE AND MAGNETIC SUSCEPTIBILITY IN MRI

Matthew John Cronin, BSc.

Sir Peter Mansfield Imaging Centre

School of Physics and Astronomy

Thesis submitted to the University of Nottingham for the degree of Doctor of Philosophy

December 2015

"I think this would be a good time for a beer."

Franklin Delano Roosevelt, March 22nd 1933

ABSTRACT

Over the last decade, phase measurements derived from gradient echo MRI have increasingly been used as a source of quantitative information, allowing tissue composition and microstructure to be probed *in vivo* and opening up many new avenues of research. However, the non-local nature of phase contrast and the complexity of the underlying sources of phase variation mean that care must be taken in the interpretation and exploitation of phase information. The work described in this thesis explores the application of phase-based quantitative susceptibility measurements *in vivo*, and uses theory, experiment, and simulation to investigate the contribution of local structural effects to measurements of MRI signal phase.

In initial work, the use of phase imaging and quantitative susceptibility mapping (QSM) is compared in the analysis of white matter lesions in multiple sclerosis, demonstrating *in vivo* the dipolar distortions inherent in phase images, and the correction of such artefacts through the application of QSM, based on a thresholded k-space division method . Visual analysis of the lesions with a focus on the presence of the peripheral rings that occur in some white matter lesions allows comparison of our data with previous studies.

A theoretical description of effects of magnetic susceptibility anisotropy using a susceptibility tensor model is then presented, and its predictions tested using macroscopic phantoms composed of pyrolytic graphite sheet, a highly anisotropic and diamagnetic material. The results of these experiments confirm that the full tensor model must be used to predict the effects of structures composed of such materials on the magnetic field.

Finally, Monte Carlo simulation is used to demonstrate the effects of perturber shape and diffusion on the MRI signal phase measured from a volume containing oriented, NMR-invisible, spheroidal perturbers with constant bulk magnetic susceptibility. The rate of phase accumulation over time is shown to be highly dependent on perturber shape and diffusion, and the possible implication of these results on real MRI measurements are discussed.

ACKNOWLEDGEMENTS

I would like to thank my supervisors Prof. Richard Bowtell and Prof. Penny Gowland for their teaching, support and guidance both during my time as an undergraduate and throughout my PhD; Dr Samuel Wharton, whose insight and patient mentoring helped to build a solid foundation for the work presented here; and all the staff at the Sir Peter Mansfield Imaging Centre and the School of Physics and Astronomy who have provided endless help and support throughout my time in Nottingham.

I would like to thank my parents for their unwavering support and encouragement throughout my life, without which I would not be where I am today.

Finally I would like to thank all of my friends who have touched my life over the past 8 years. We have shared happy times, we have shared sad times, we have sung, we have danced; we have celebrated successes and drowned sorrows. I couldn't have made it through without you. Particular thanks go to Dr Laurence Day, BSc. Ph.D., who has been there for me with irreverence, sarcasm, questionable wit, and loyal friendship from the very beginning, and Benjamin Tendler, MPhys (and soon to be Ph.D.), my protégé (ha.), my friend, my infinitely cheerful counsellor, and the kind person who will deliver this thesis to its final destination. Thank you all, I owe you a beer.

CONTENTS

1 INTRODUCTION

1.1 Introduction

Magnetic resonance imaging (MRI) is a non-invasive medical imaging technique based on the manipulation of nuclear magnetization produced by high magnetic fields. Imaging sequences can be varied to reflect or measure various tissue properties depending on the aims of the investigation, making MRI a versatile tool in both clinical and research settings. Most conventional MRI techniques are based on the measurement of a weighted signal magnitude to probe various properties, such as signal relaxation times, target nucleus concentration, blood oxygenation, or diffusion [1, 2] , researchers have increasingly been turning to imaging techniques based on MRI signal phase in order to extract more quantitative information about the underlying structure and composition of tissue. Such techniques include phase imaging, susceptibility-weighted imaging (SWI) [3], quantitative susceptibility mapping (QSM) [4-14] as well as a number of novel techniques exploiting the orientation [15-21] and time [15] dependent rate of accumulation of local signal phase to probe the sub-voxel level structure of the brain. The work presented in this thesis begins with an investigation into the application of phase imaging and QSM *in vivo* in the imaging of white matter lesions in multiple sclerosis, before going on to consider in greater detail the effects of magnetic susceptibility anisotropy on the local MRI frequency, and the effects of oriented mesoscopic susceptibility inclusions on measured MRI signal phase.

1.2 Thesis Overview

Chapter 2 describes the background theory of the phenomenon of nuclear magnetic resonance (NMR), the foundation of magnetic resonance imaging. It discusses the magnetisation of a population of nuclear spins in an applied magnetic field, as well as excitation, relaxation, and detection of the NMR signal.

Chapter 3 contains theory relating to the formation of magnetic resonance images from the NMR signal, including the theory of slice selection and signal encoding, as well as accelerated imaging and the formation and control of contrast in images.

In Chapter 4, the theory of quantitative susceptibility mapping is introduced, including the processing of MRI phase data to remove wraps and the effects of externally produced field variations, the calculation of magnetic field maps from known susceptibility distributions, and a number of methods of conditioning the ill-posed inversion of this calculation to generate susceptibility maps from phase data.

Chapter 5 presents an investigation comparing the imaging of white matter lesions in multiple sclerosis (MS) using phase imaging and quantitative susceptibility mapping. The non-local nature of phase contrast is demonstrated *in vivo* in MS lesions, and QSM is shown to provide local contrast more consistent with the structure shown in T_2^*-weighted magnitude images. The prevalence and representation of peripheral rings observed around a subset of white matter lesions in MS is also compared between phase images and quantitative susceptibility maps.

The magnetic susceptibility measured using QSM has been shown to be dependent on the orientation of structures with respect to the applied magnetic field, B_0, in some regions of the brain. This effect has been attributed to the anisotropy of the magnetic susceptibility of the myelin sheath. In Chapter 6, the effects of magnetic susceptibility anisotropy are modelled using phantoms constructed using pyrolytic graphite sheet, a highly diamagnetic, anisotropic material. Novel field perturbations are demonstrated in macroscopic models of long cylinders and spherical shells, as well as from point-like sources. These results are used to validate a full, tensor-based model of susceptibility anisotropy, while also showing that a simplified model fails to accurately predict the measured field perturbation.

In Chapter 7, Monte Carlo simulations are used to simulate the evolution of the MRI signal phase and frequency from an ensemble of precessing particles in a volume

containing NMR-invisible oriented spheroidal perturbers. The effects of varying the diffusion of the particles, and the shape and volume fraction of the perturbers are considered.

The findings and implications of the work presented in this thesis are summarised and discussed in Chapter 8. Possible future work is also suggested.

1.3 References

1. Bernstein, M.A., X.J. Zhou, and K.F. King, *Handbook of MRI pulse sequences*. 2004, Amsterdam ; Boston: Academic Press. xxii, 1017
2. Brown, R.W., et al., *Magnetic resonance imaging: physical principles and sequence design*. 2014: John Wiley & Sons.
3. Haacke, E.M., et al., *Susceptibility weighted imaging (SWI).* Magnetic resonance in medicine : official journal of the Society of Magnetic Resonance in Medicine / Society of Magnetic Resonance in Medicine, 2004. **52**: p. 612-8.
4. Marques, J.P. and R. Bowtell, *Application of a Fourier-based method for rapid calculation of field inhomogeneity due to spatial variation of magnetic susceptibility.* Concepts in Magnetic Resonance Part B: Magnetic Resonance Engineering, 2005. **25B**: p. 65-78.
5. Liu, T., et al., *Calculation of susceptibility through multiple orientation sampling (COSMOS): a method for conditioning the inverse problem from measured magnetic field map to susceptibility source image in MRI.* Magnetic resonance in medicine : official journal of the Society of Magnetic Resonance in Medicine / Society of Magnetic Resonance in Medicine, 2009. **61**: p. 196-204.
6. Shmueli, K., et al., *Magnetic susceptibility mapping of brain tissue in vivo using MRI phase data.* Magnetic resonance in medicine : official journal of the Society of Magnetic Resonance in Medicine / Society of Magnetic Resonance in Medicine, 2009. **62**: p. 1510-22.
7. de Rochefort, L., et al., *Quantitative susceptibility map reconstruction from MR phase data using bayesian regularization: validation and application to brain imaging.* Magnetic resonance in medicine : official journal of the Society of Magnetic Resonance in Medicine / Society of Magnetic Resonance in Medicine, 2010. **63**: p. 194-206.
8. Wharton, S., A. Schäfer, and R. Bowtell, *Susceptibility mapping in the human brain using threshold-based k-space division.* Magnetic resonance in medicine : official journal of the Society of Magnetic Resonance in Medicine / Society of Magnetic Resonance in Medicine, 2010. **63**: p. 1292-304.
9. Wharton, S. and R. Bowtell, *Whole-brain susceptibility mapping at high field: a comparison of multiple-and single-orientation methods.* NeuroImage, 2010. **53**(2): p. 515-525.

10. Wharton, S., *Susceptibility Mapping in High Field MRI*. 2011. p. 190.

11. Liu, J., et al., *Morphology enabled dipole inversion for quantitative susceptibility mapping using structural consistency between the magnitude image and the susceptibility map.* NeuroImage, 2012. **59**(3): p. 2560-2568.

12. Schweser, F., et al., *Toward online reconstruction of quantitative susceptibility maps: Superfast dipole inversion.* Magnetic Resonance in Medicine, 2013. **69**(6): p. 1581-1593.

13. Liu, C., et al., *Susceptibility-weighted imaging and quantitative susceptibility mapping in the brain.* Journal of Magnetic Resonance Imaging, 2014. DOI: 10.1002/jmri.24768

14. Haacke, E.M., et al., *Quantitative susceptibility mapping: current status and future directions.* Magnetic Resonance Imaging, 2015. **33**(1): p. 1-25.

15. Wharton, S. and R. Bowtell, *Gradient echo based fiber orientation mapping using R2* and frequency difference measurements.* NeuroImage, 2013. **83**: p. 1011-1023.

2 NUCLEAR MAGNETIC RESONANCE THEORY

Nuclear magnetic resonance (NMR) is a phenomenon in which certain atomic nuclei, when placed in a magnetic field, can be excited and caused to resonate at a characteristic frequency, leading to the emission of electromagnetic (EM) radiation. NMR is observed in atoms whose nuclei have intrinsic spin angular momentum, such as ^{1}H, ^{13}C, and ^{31}P. In medical imaging, hydrogen nuclei (with spin $\frac{1}{2}$) are typically, although not exclusively, the nuclei of interest, due to their high concentration in the body.

The resonant frequency of a particular nucleus is related to the strength of the applied magnetic field by the gyromagnetic ratio, the ratio of its magnetic dipole moment to its angular momentum, which is characteristic of the nuclei:

$$\omega_0 = \gamma B_0 \quad .$$

Eq. 2.1

Here, ω_0 is the resonant angular frequency, γ is the gyromagnetic ratio ($267.5 \times 10^6\ rad\ s^{-1}T^{-1}$ for a proton [1]), and B_0 is the strength of the applied magnetic field.

2.1 Magnetization

If we consider an ensemble of N protons in a volume, V, at room temperature and in the absence of a magnetic field, the spin angular momentum of the protons will be randomly oriented, leading to no net magnetization. If a magnetic field is applied, the spins can exist with two quantised energy levels; in the low energy $\left(\text{spin} = +\frac{1}{2}\right)$ spin-up state with a net magnetization parallel to B_0, and the high energy $\left(\text{spin} = -\frac{1}{2}\right)$ spin-down state with a net magnetization anti-parallel to B_0. The energy difference between these levels is proportional to the gyromagnetic ratio and B_0, as shown in Figure 2-1. In Cartesian coordinates, B_0 is conventionally considered to be applied in the z-direction.

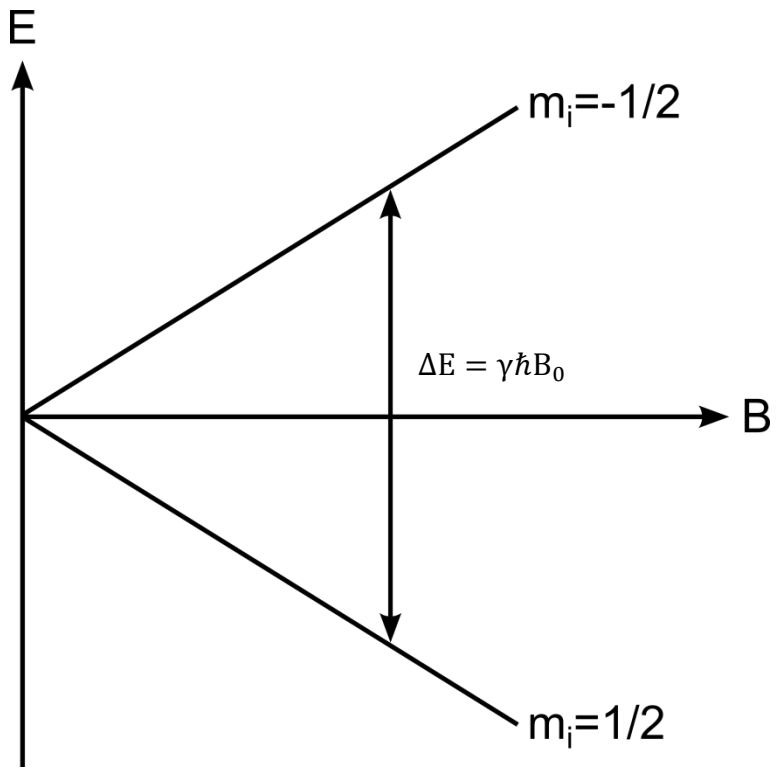

Figure 2-1 – Quantised proton energy levels in an applied magnetic field

The population of spins will exhibit a net magnetization in the direction of the magnetic field, proportional to the population difference, n, between the spin up and spin down energy levels. This population difference is related to B_0 by

$$n = \frac{N\hbar\gamma B_0}{2k_B T} \quad ,$$

Eq. 2.2

where N is the total number of nuclei, γ is the gyromagnetic ratio, B_0 the applied magnetic field strength, k_B the Boltzmann constant, $\hbar$ the reduced Planck constant, and T the temperature. The net magnetization, M_0, is usually referred to as the bulk magnetisation, and NMR and MRI can be considered classically in terms of the evolution of this magnetisation, which at equilibrium is given by

$$M_0 = \frac{NV(\hbar\gamma)^2 B_0}{4k_B T} \quad .$$

Eq. 2.3

2.2 Excitation

At equilibrium, the bulk magnetization is oriented along the z-direction in the laboratory frame, parallel to the applied field, as shown in Figure 2-2.

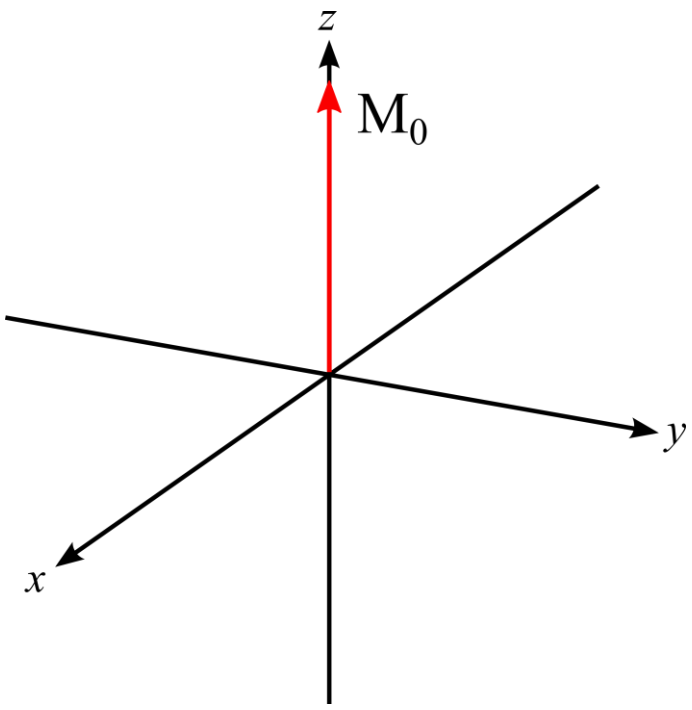

Figure 2-2 – Bulk magnetization at equilibrium

When radiofrequency (RF) energy is applied to the sample at the Larmor frequency, ω_0, with an amplitude B_1, for a time, τ, it causes a rotation of the magnetization by an angle α about an axis in the transverse plane, such that

$$\alpha = \gamma B_1 \tau \quad .$$

Eq. 2.4

RF pulses in NMR and MRI are often referred to by the angle through which they rotate the magnetization, for example a 90˚ pulse rotates the bulk magnetisation completely into the transverse plane, and a 180˚ pulse completely inverts the bulk magnetisation so that it is directed along the –z direction.

In a simple NMR experiment, a sample may be excited by a 90˚ RF pulse of electromagnetic radiation at the resonant frequency of the target nuclei. This has the effect of rotating the bulk magnetisation from the z-direction into the x-y plane, as shown in Figure 2-3

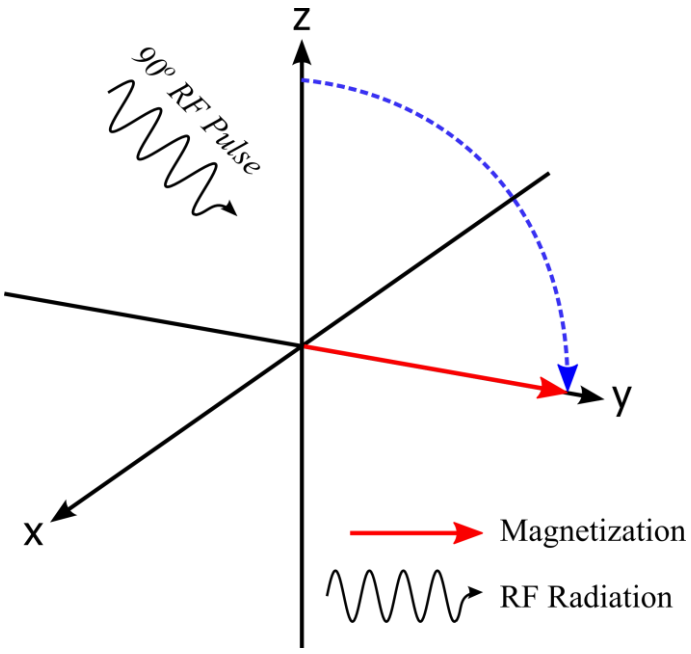

Figure 2-3 – Excitation of the bulk magnetization with a 90˚ RF pulse

Once in the x-y plane, the transverse component of the magnetisation precesses about the z-axis at the Larmor frequency, defined in Eq. 2.1, generating an NMR signal, as shown in Figure 2-4.

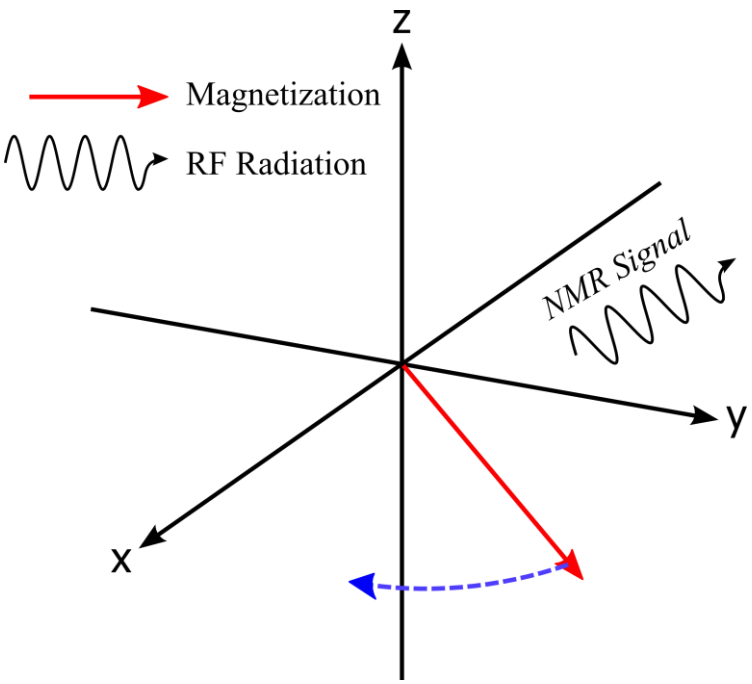

Figure 2-4 – Precession of the transverse magnetization in the laboratory frame, generating an NMR signal.

The transverse magnetisation is often considered in a rotating frame of reference, rotating at the reference frequency of the scanner (typically the Larmor frequency for a proton), with axes x', y' and z. If the spins precess at the Larmor frequency, the transverse magnetization remains stationary along the y'-axis.

2.2.1 Specific Absorption Rate

When RF energy is applied to a sample, energy is deposited, which can cause heating. When scanning heat-sensitive samples, especially humans or animals, this heating must be carefully limited in order to avoid damage or harm. The deposition of energy in tissue can be measured as a specific absorption rate (SAR), and is defined as power absorbed per unit mass of tissue, in units of watts per kilogram (WKg^{-1}). It may be measured over the whole body or by exposed body part. SAR levels are strictly regulated, and especially important in poorly perfused areas such as the eye, where heat dissipation is slow. SAR is increased in ultra high field scanners, such as the 7T scanner used for *in vivo* imaging of MS patients in Chapter 5, and accurate modelling of SAR is necessary to fully exploit the power of these scanners [2].

2.3 Relaxation

Relaxation of the signal in NMR reflects a combination of longitudinal recovery of the bulk magnetisation in the z-direction (and consequent decrease in the magnitude of transverse magnetisation in the x-y plane), and the loss of phase coherence between the precession of individual spins, causing further attenuation of the measured signal amplitude.

Longitudinal recovery is also known as T_1 relaxation and the recovery of the longitudinal magnetization M_z is described by

$$\frac{dM_z}{dt} = \frac{M_0 - M_z}{T_1} \quad ,$$

Eq. 2.5

where M_0 is the equilibrium longitudinal magnetisation, and T_1 is the longitudinal relaxation time constant. T_1 relaxation is caused by the return of the excited spin population to thermal equilibrium via exchange of energy between the spins and the lattice. Figure 2-5 shows the recovery of the longitudinal magnetization after inversion with a 180° RF pulse. T_1 varies between tissues in the body, and forms the basis of contrast in widely used anatomical imaging sequences, as discussed in section 3.4.1.

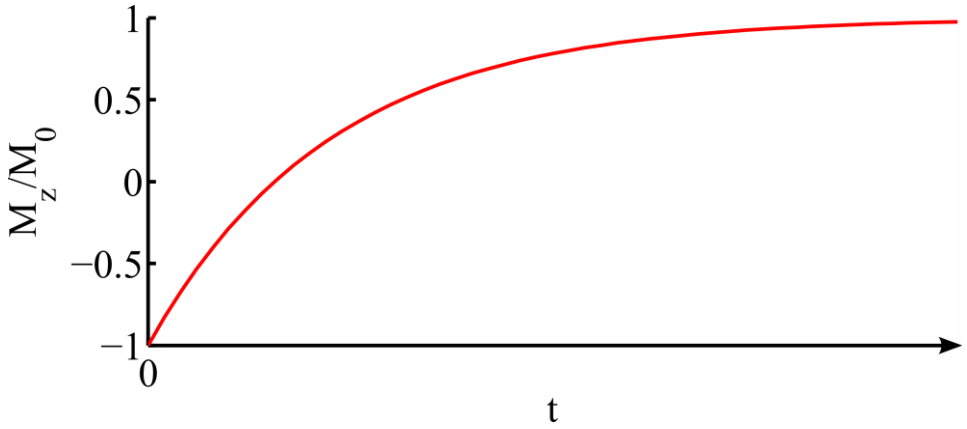

Figure 2-5 – Recovery of the longitudinal magnetization

Decay of the magnetization in the x-y plane is known as transverse relaxation, shown schematically in Figure 2-6. It is caused by small variations in the local magnetic field experienced by individual spins at different locations in the volume. These variations are divided into those resulting from time-varying processes, such as molecular motion, and those caused by static processes, such as the variation in the

magnetic field due to spatial variations of the magnetic susceptibility in the sample. Signal loss due to time-varying processes is described by the time constant T_2. In protons, the dominant source of T_2 relaxation is dipole-dipole interactions occurring between protons and other protons or protons and electrons. Signal loss due to static processes is described by T_2', accounting for dephasing due to poorly shimmed magnetic fields and the field perturbations caused by heterogeneous magnetic susceptibility. The combined transverse decay constant T_2^* is defined as

$$\frac{1}{T_2^*} = \frac{1}{T_2} + \frac{1}{T_2'} \quad .$$

Eq. 2.6

Transverse relaxation is then described by

$$\frac{dM_{x,y}}{dt} = \frac{-M_{x,y}}{T_2^*} \quad .$$

Eq. 2.7

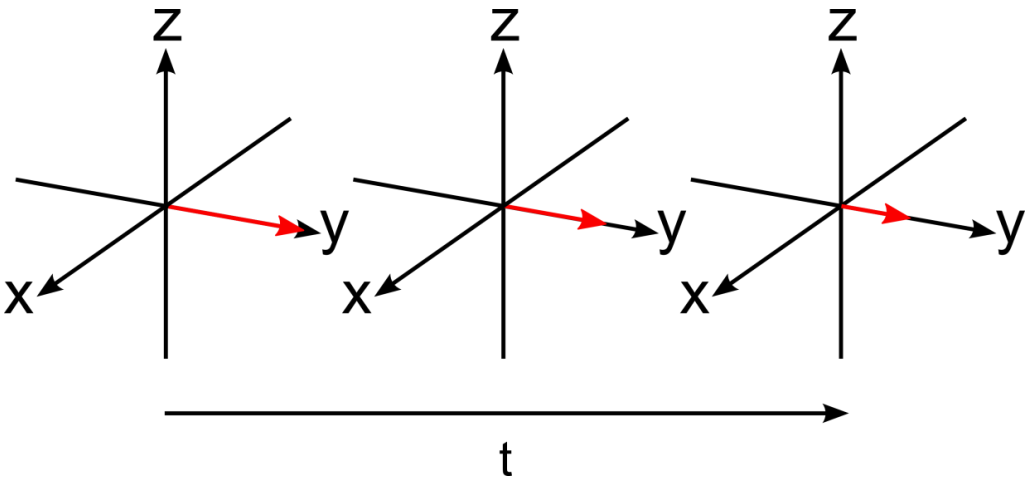

Figure 2-6 - Decay of the transverse magnetization in the rotating frame of reference

2.4 The Bloch Equation

The general expression for the evolution of the magnetization **M** due to nuclei with a gyromagnetic ratio γ in the presence of an applied magnetic field $\mathbf{B}_{ext}$ i is the Bloch equation [3]

$$\frac{d\mathbf{M}}{dt} = \gamma \mathbf{M} \times \mathbf{B}_{ext} + \frac{1}{T_1}(M_0 - M_z)\hat{\mathbf{z}} - \frac{1}{T_2} M_{xy} \quad ,$$

Eq. 2.8

where $M_0$is the equilibrium magnetization, M_z is the longitudinal magnetization, M_{xy} is the transverse magnetization, and T_1 and T_2 are the spin-lattice and spin-spin relaxation times. Solving the Bloch equation for $\mathbf{B}_{ext} = B_0\hat{\mathbf{z}}$ yields the rate of change of the magnetization components $M_x, M_y,$ and M_z as

$$\begin{aligned} \frac{dM_z}{dt} &= \frac{M_0 - M_z}{T_1} \\ \frac{dM_x}{dt} &= \omega_0 M_y - \frac{M_x}{T_2} \\ \frac{dM_y}{dt} &= \omega_0 M_x - \frac{M_y}{T_2} \end{aligned} \quad ,$$

Eq. 2.9

where $\omega_0 = \gamma B_0$.

Integration of these equations gives the magnetization components M_x, M_y and M_z at a time t, such that

$$\begin{aligned} M_x(t) &= \big(M_x(0)\cos\omega_0 t + M_y(0)\sin\omega_0 t\big)e^{-t/T_2} \\ M_y(t) &= \big(M_y(0)\cos\omega_0 t - M_x(0)\sin\omega_0 t\big)e^{-t/T_2} \\ M_z(t) &= M_z(0)e^{-t/T_1} + M_0(1 - e^{-t/T_1}) \end{aligned} \quad .$$

Eq.2.10

The transverse magnetization $M_{xy}(t)$ can be represented as a complex quantity $M_+(t)$, a complex combination of the individual transverse components, $M_x(t)$ and $M_y(t)$ so that

$$M_+(t) = M_x(t) + iM_y(t) \quad ,$$

and

$$M_+(t) = |M_+(t)|e^{i\phi(t)} = M_{xy}(t)e^{i\phi(t)} \quad ,$$

giving

$$M_+(t) = M_+(0)e^{-i\omega_0 t}e^{-t/T_2} \quad .$$

Eq. 2.11

Here, $\phi(t)$ is the signal phase, describing the orientation of M_{xy} in the transverse plane. In the laboratory frame of reference is it given by

$$\phi(t) = \phi(0) - \omega_0 t \quad ,$$

Eq. 2.12

where $\phi(0)$ is the phase when $t = 0$. In the rotating frame of reference, $\phi = \phi(0)$ assuming that there is no perturbation to the applied magnetic field.

2.5 The Free Induction decay

The measurement of the free induction decay is the simplest NMR experiment, and forms the basis of many MRI pulse sequences. A 90˚ pulse is applied to the sample, rotating the magnetisation into the x-y plane. The magnetisation then precesses about the field, generating a signal, known as a free induction decay (FID), shown in Figure 2-7.

The signal relaxes exponentially such that the signal magnitude S at a time t is

$$S = S_0 e^{-t/T_2^*}$$

Eq. 2.13

where S_0 is the signal amplitude when $t = 0$, and T_2^* is the transverse relaxation constant. The signal decays to zero in a time of approximately $5T_2^*$.

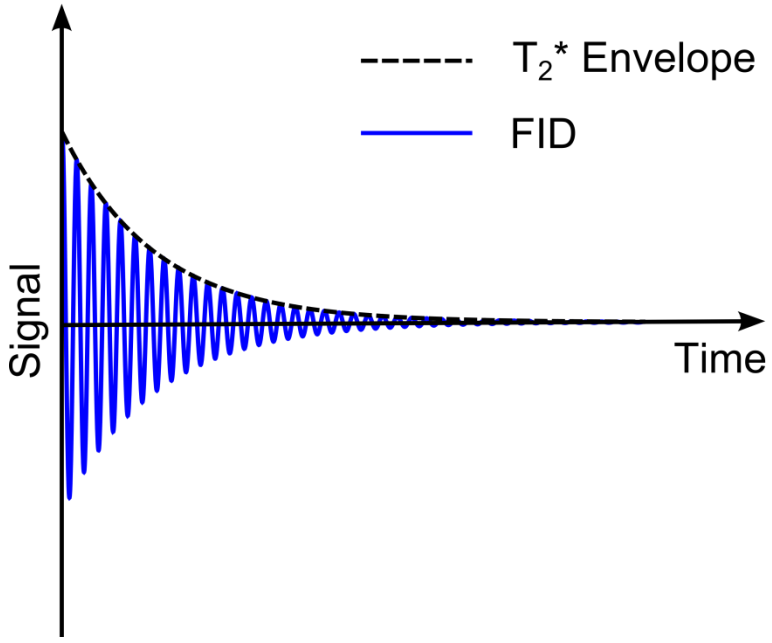

Figure 2-7 – The Free Induction Decay

2.6 Detection

The NMR signal is recorded by one or more RF receiver coils. A voltage is induced in the coil by the time-varying magnetic field generated by the precessing spins, and discretely sampled by the scanner. The high frequency of the NMR signal (~300 MHz for protons at 7 T) makes direct discrete sampling of the signal impractical due to the Nyquist limit. To overcome this, the detected signal is demodulated with a reference signal, typically close to ω_0. This signal is then passed through a phase sensitive detector (PSD), separating it into real and imaginary components (in and out of phase with the reference signal, respectively), before being digitised by an analog to digital converter (ADC) and recorded as a function of time.

The magnitude of the signal, S, may then be calculated by combining the real (Re) and imaginary (Im) signals in quadrature so that

$$Magnitude = \sqrt{Re^2 + Im^2}$$

Eq. 2.14

The phase, ϕ, of the signal relative to the reference frequency of the scanner may be calculated by taking the 4-quadrant arctangent of the ratio of the real and imaginary signals so that

$$\phi = arctan_{4q}\left(\frac{Im}{Re}\right)$$

Eq. 2.15

The calculated phase is always mapped into the range $+\pi$ to $-\pi$, leading to "phase wrapping" when the true phase of the signal goes beyond these limits, as discussed in section 4.3.1.

2.7 References

1. Shifrin, V.Y., et al., *A new low-field determination of the proton gyromagnetic ratio in water.* Instrumentation and Measurement, IEEE Transactions on, 1998. **47**(3): p. 638-643.
2. Wolf, S., et al., *SAR simulations for high-field MRI: How much detail, effort, and accuracy is needed?* Magnetic Resonance in Medicine, 2013. **69**(4): p. 1157-1168.
3. Brown, R.W., et al., *Magnetic resonance imaging: physical principles and sequence design*. 2014: John Wiley & Sons.

3 MAGNETIC RESONANCE IMAGING THEORY

Magnetic resonance imaging (MRI) uses the principles of NMR to form an image of the inside of a body or sample of interest in a non-invasive manner. The NMR signal is spatially encoded using magnetic field gradients, which allow images to be calculated from the measured signal. Contrast in MRI images can be based on various properties of the sample, including the concentration of hydrogen nuclei, the different relaxation times described in Section 2.3, local signal phase, or other physical properties such as local magnetic susceptibility.

Here we will consider MRI signal encoding using a basic gradient echo imaging sequence in both 2D and 3D. This is followed by a discussion of the fast low-angle shot (FLASH), and the magnetisation prepared rapid gradient echo (MPRAGE) sequence.

3.1 Slice Selection

Almost all MRI sequences start with selective excitation of a slice or volume to be imaged. A magnetic field gradient is first applied along the slice direction, for example a gradient G_z. The spins in the volume of interest now have a spatially varying resonant frequency given by

$$\omega = \gamma(B_0 + G_z z)$$

Eq. 3.1

While this gradient is applied, a 90° RF pulse can be applied at the resonant frequencies within the volume of interest, selectively exciting the spins in that slice.

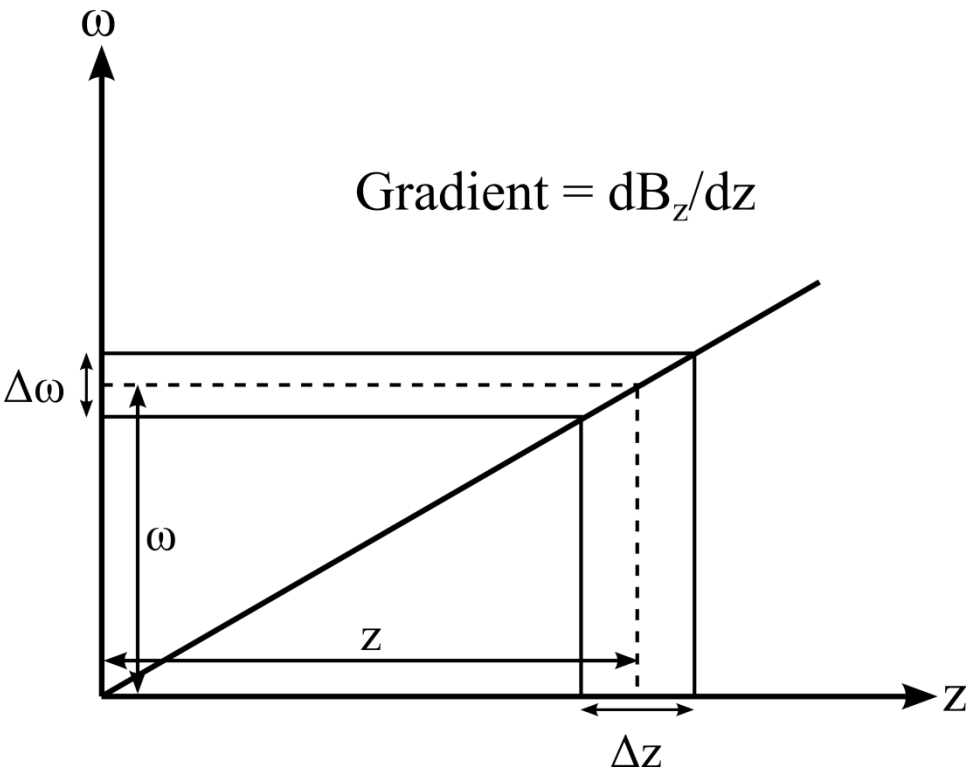

Figure 3-1 – Spatial encoding in the slice direction

The bandwidth, $\Delta\omega$, and centre frequency, ω, of the RF pulse can be altered to change the thickness, $\Delta z = \Delta\omega/\gamma G_z$ and position of the slice, $z = \omega/\gamma G_z$, as can be seen in Figure 3-1.

3.2 The Gradient Echo

As well as RF pulses, magnetic field gradients can be applied spatially across a sample volume to manipulate the behaviour of the spins. An example of this is the 1D gradient echo sequence [1] shown in Figure 3-2.

In the gradient echo sequence, a 90˚ RF pulse is first applied to the sample, tipping the magnetization into the transverse plane. The magnetisation then precesses at the Larmor frequency, as described by Eq. 2.1.

A dephasing magnetic field gradient $-G_z$ is then applied across the sample in the z-direction, starting at time t_1 and ending at time t_2. The spins' precession frequency now varies spatially, and is given by

$$\omega(z) = \gamma(B_0 - G_z z)$$

Eq. 3.2

and at a time t, the position-dependent phase of the spins in the rotating frame is given by

$$\phi_G(z,t) = -\gamma G_z z(t - t_1) \qquad (t_1 < t < t_2)$$

Eq. 3.3

This defocussing causes a loss of phase coherence of the signal generated by the precession of the spins across the sample, attenuating the combined signal recorded by the scanner.

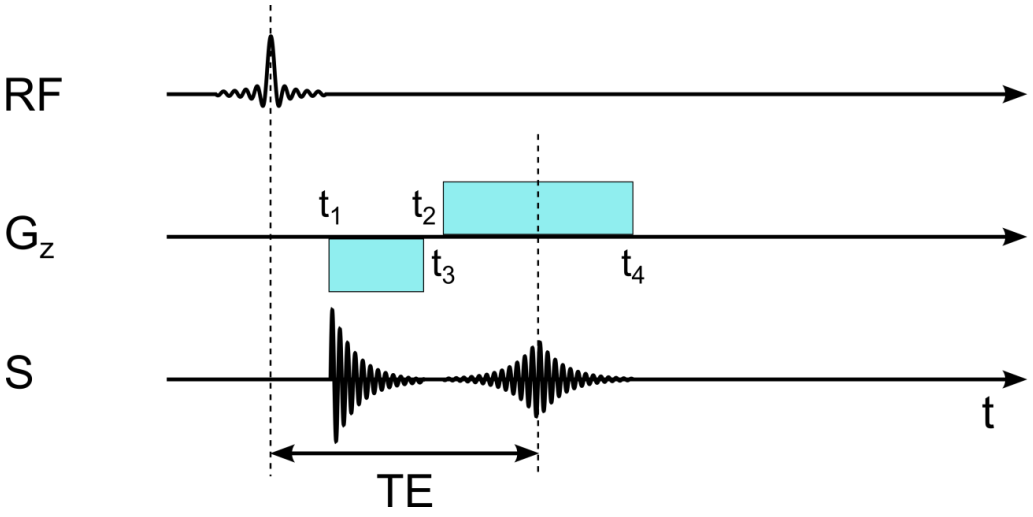

Figure 3-2 – A simple 1D gradient echo sequence

A refocussing gradient $+G_z$ is then applied across the sample between times t_3 and t_4, and the phase now evolves as

$$\phi_G(z,t) = \gamma G_z z(t - t_3) - \gamma G_z z(t_2 - t_1) \qquad (t_3 < t < t_4)$$

Eq. 3.4

This refocussing causes an echo of the original FID, which peaks at a time TE, referred to as the echo time, and given by

$$TE = t_3 + t_2 - t_1$$

Eq. 3.5

with an amplitude S, given by

$$S = S_0 e^{-TE/T_2^*}$$

Eq. 3.6

where S_0 is the amplitude of the initial FID. The T_2^* of a sample can be measured simply by repeating a simple gradient echo sequence while varying TE, and fitting an exponential function to the amplitude of the gradient echo vs echo time.

3.3 Simple Gradient Echo Imaging

3.3.1 Frequency Encoding

In a gradient echo sequence, the signal is encoded in the frequency dimension by applying a magnetic field gradient to de-phase the FID, and then reversing the polarity of the gradient to induce a gradient echo. The application of a gradient G_x causes the frequency of the signal to vary spatially as

$$\omega = \gamma(B_0 + G_x x)$$

Eq. 3.7

As a consequence of this frequency variation, the spins will acquire a phase offset, $\phi_G(x,t)$, relative to the reference frequency of the scanner, given by

$$\phi_G(x,t) = \int_0^t \gamma G_x x dt = \gamma G_x x t$$

Eq. 3.8

Ignoring relaxation terms, the complex signal generated by precession of the spins will then be described by

$$S = \int \rho(x) exp\big(-i\phi_G(x,t)\big) dx = \int \rho(x) exp(-i\gamma G_x x t) dx$$

Eq. 3.9

where $\rho(x)$ is the spin density.

Data given as a function of spatial position can be expressed as a function of spatial frequency by use of a Fourier transform. The 1D Fourier transform is given by

$$F(k) = FT(f(x)) = \int_{-\infty}^{\infty} f(x)\, exp(-ikx)\, dx$$

Eq. 3.10

where $f(x)$ is a function of real-space coordinate x, and $F(k)$ is a function of frequency-space coordinate k. Frequency-space is commonly referred to as k-space. If we define the spatial frequency coordinate

$$k(G,t) = \gamma G t \quad m^{-1}$$

Eq. 3.11

then the time-dependent signal $S(t)$ can be expressed as a function of k as

$$S(k) = \int \rho(x) \exp(-ikx)\, dx$$

Eq. 3.12

Using Eq. 3.12, the spin density $\rho(x)$ can be recovered from the signal via an inverse Fourier transform, giving

$$\rho(x) = FT^{-1}\big(S(k)\big) = \frac{1}{2\pi}\int S(k) \exp(ikx)\, dk$$

Eq. 3.13

To perform this calculation, the signal from the excited slice must be recorded as a function of k.

Figure 3-3 shows a simple gradient echo imaging sequence. The signal is collected along a line in k-space in the frequency encoding direction between the value $\pm k_{max}$. The signal is first defocussed with a gradient $-G_x$ applied for a time t_1, after which

$$k = \gamma(-G_x)t_1 = -k_{max}$$

Eq. 3.14

The negative gradient is then switched off and a positive gradient G_x applied for a time $2t_2$, where $t_2 = t_1$. The signal refocuses as a gradient echo, peaking after a time t_2, at which point $k = 0$, and reaches $+k_{max}$ after $2t_2$. The time between the RF excitation pulse and the peak of the gradient echo is the echo time, TE.

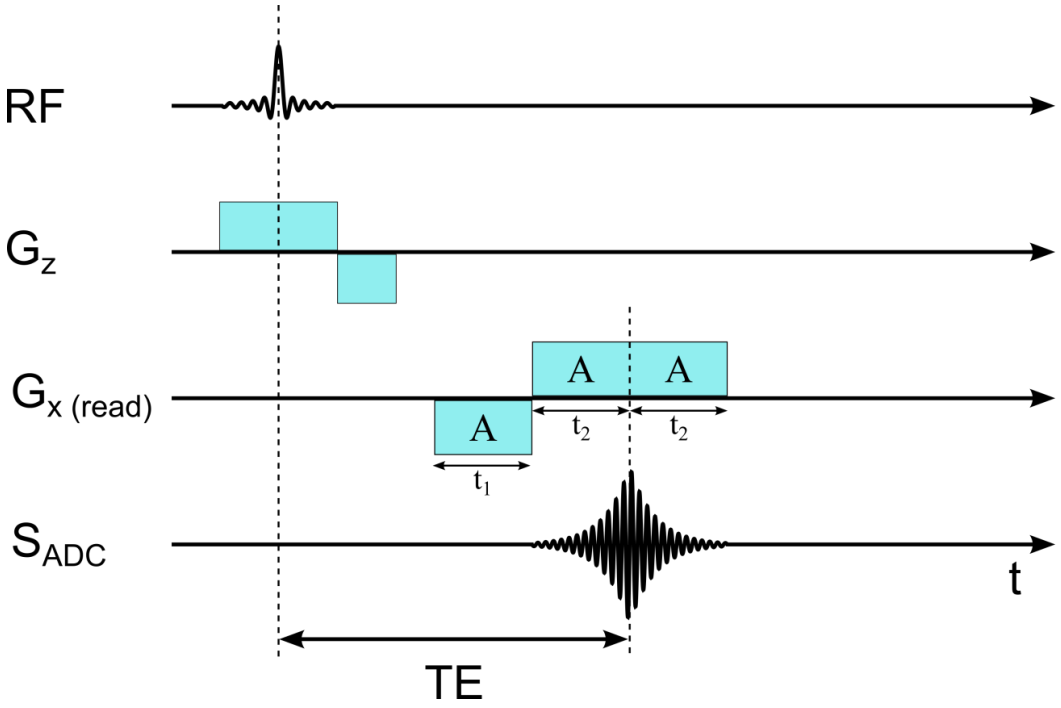

Figure 3-3 - A simple 1D gradient echo with frequency encoding in the x-direction

As can be seen in Figure 3-3, the gradient echo peaks when the area underneath the positive gradient is equal to the area underneath the negative gradient. In real MRI sequences, t_1 and t_2 are not necessarily equal in length and the amplitudes of the positive and negative gradients may differ, however the integral of the applied gradient over time will determine TE.

The signal is received by RF coils and transmitted to an analog-to-digital converter (ADC), which samples the signal at discrete time intervals of length Δt as it traverses k-space during the application of the positive gradient, as shown in Figure 3-4. The resolution of the sampling in k-space is related to the time between samples by

$$\Delta k = \gamma G_x \Delta t$$

Eq. 3.15

The separation of points sampled in k-space is, in turn, related to the field of view (FOV) in real space by

$$FOV_x = \frac{2\pi}{\Delta k_x} = \frac{2\pi}{\gamma G_x \Delta t}$$

Eq. 3.16

The resolution in real space is inversely proportional to the field of view in k-space. If $FOV_k = 2k_{max}$,

$$\Delta x = \frac{\pi}{k_{xmax}} = \frac{2\pi}{\gamma G_x T}$$

Eq. 3.17

where $T = 2t_2$ is the total time over which the signal is sampled by the ADC. Following sampling of the required amount of k-space, the recorded signal $S(k)$ can be used to calculate the spin density $\rho(x)$ using a discrete Fourier transform Eq. 3.13.

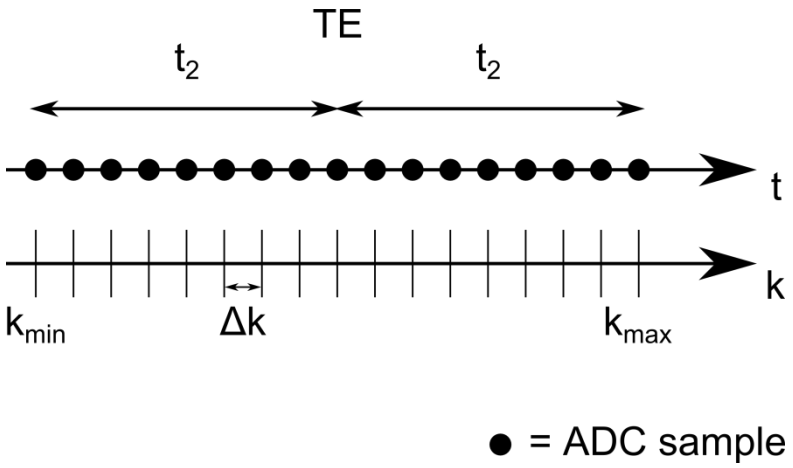

Figure 3-4 – Signal read-out trajectory in k-space for the sequence shown in Figure 3-3

3.3.2 Phase Encoding

To create a 2D image, rather than a 1D profile of spin density across the excited slice, the signal must also be encoded in a second spatial dimension. This is the phase encoding dimension, considered here to be in the y-direction of the laboratory frame.

When 2D encoding is applied, a grid of points is sampled in k-space, instead of a single line in the frequency encoding direction. To achieve this, a second defocussing gradient G_y is applied at the same time as G_x. This adds a second dimension to k, which may now be considered to consist of two k-space coordinates giving $\mathbf{k} = (k_x, k_y)$, and so the signal becomes a function $S(\mathbf{k}) = S(k_x, k_y)$. The phase encoding gradient is only applied for a time T during the dephasing of the

signal in the read direction, and is not then reversed, leaving a fixed displacement of the k-space coordinate k_y. The signal is then sampled between $(\pm k_x, k_y)$, as shown in Figure 3-5. The process is repeated *N* times to sample the desired range of k-space, with the amplitude of G_y changed by ΔG_y between for each acquisition, with a repetition time TR separating the n^{th} and $(n+1)^{th}$ acquisition sequences. In this example we assume that TR $\gg T_1$, allowing full recovery of the longitudinal magnetisation and full loss of transverse magnetisation between excitations. The FOV and spatial resolution in the phase encoding direction are then related to the FOV and resolution of k-space by

$$FOV_y = \frac{2\pi}{\Delta k_y} = \frac{2\pi}{\gamma G_y T}$$

Eq. 3.18

and

$$\Delta y = \frac{\pi}{k_{ymax}} = \frac{2\pi}{\gamma G_{y_{max}} T} \quad ,$$

Eq. 3.19

where $G_{y_{max}}$ is the largest positive value of the phase encode gradient.

A 2D Fourier transform can then be applied to the 2D k-space representation of the signal to generate a 2D MRI image. A simple 2D gradient echo sequence is shown in Figure 3-6.

3.3.3 3D Image Encoding

In most real-world applications of MRI it is typical to want to acquire a number of 2D images covering a 3D volume of interest. One way to achieve this is to repeat a two dimensional imaging sequences while using selective excitation with varying frequency offsets to image different individual slices.

Alternatively, the entire volume may be excited and k-space sampled in 3D by the addition of a second phase encoding gradient in the slice direction. K-space is then sampled line-by-line in the frequency encoding direction, with phase encoding gradients G_y and/or G_z being varied between each repetition of the acquisition sequence. A simple 3D gradient echo sequence is shown in Figure 3-7.

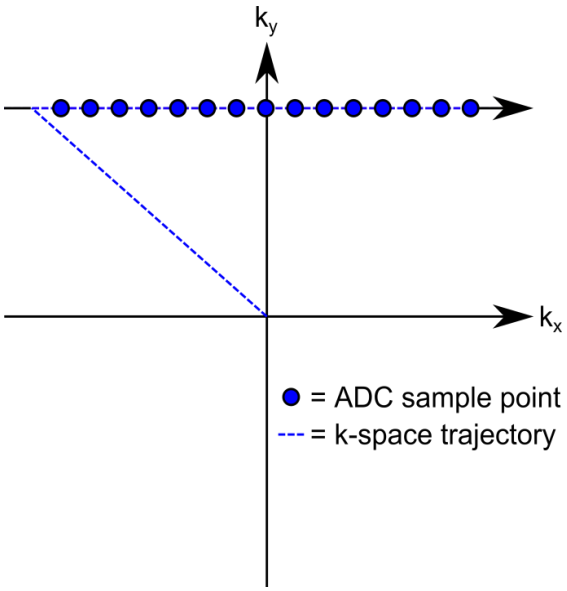

Figure 3-5 – Signal trajectory in k-space for one TR period of the sequence shown in Figure 3-6

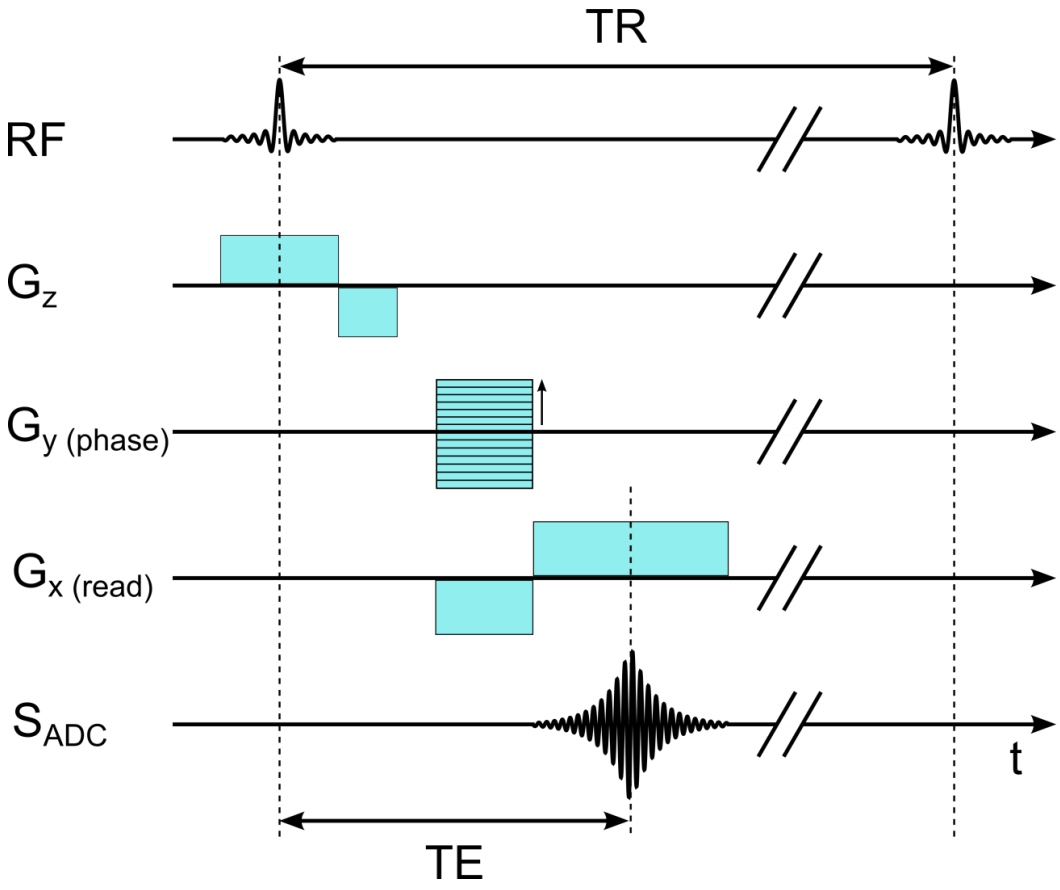

Figure 3-6 - A simple 2D gradient echo sequence with frequency encoding in the x-direction and phase encoding in the y-direction

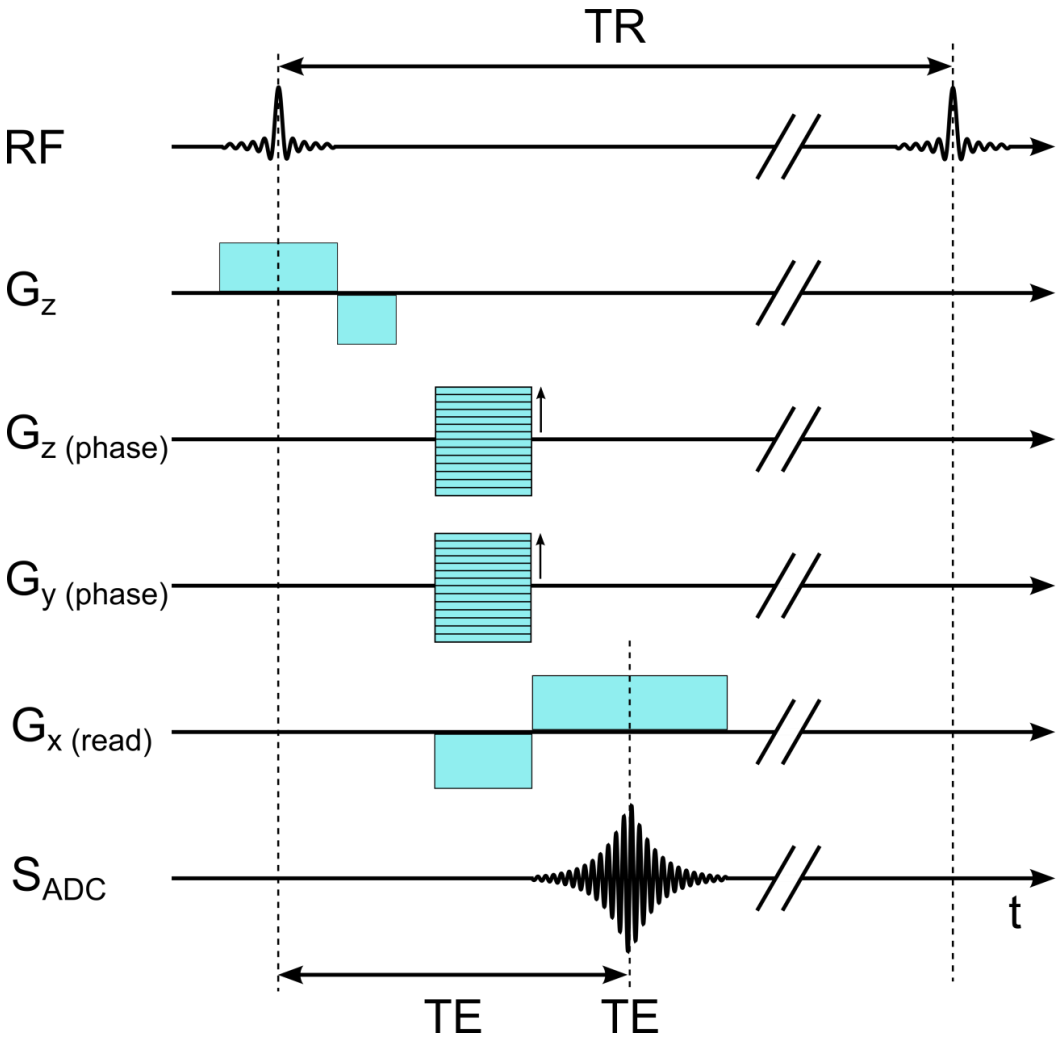

Figure 3-7 – A simple 3D gradient echo sequence with frequency encoding in the x-direction and phase encoding in the y-direction and z-direction

3.4 Controlling Contrast and Accelerating Imaging

In Sections 3.1 and 3.2 a method was described for the formation of an MR image using a simple gradient echo sequence. In practice, MRI pulse sequences are more complex, accounting for signal relaxation (and how this can be exploited to change the contrast in the image), and the need for time-efficient image acquisition.

3.4.1 Contrast in MRI images

The utility of MRI as a medical imaging technique arises in part from the variety of mechanisms through which contrast in images may be manipulated, allowing the probing of many different tissue properties and the investigation of a wide range of disease pathologies. In addition to measurement of the local proton density of tissue,

MR images may be weighted by, or used to measure quantitatively, the signal relaxation parameters T_1, T_2, and T_2^*. These parameters are affected by tissue properties such as iron content, myelination, uptake of contrast agents, and vary strongly between tissue types and between healthy and diseased or damaged tissue. The relaxation parameters for grey and white matter in the brain, measured at 7 T (the field strength at which *in vivo* data were acquired for the work presented in Chapter 5), are shown in Table 1. Other factors affecting contrast include flow, magnetization transfer, and diffusion [1].

	$\boldsymbol{T_1}$ (ms)**[2]**	$\boldsymbol{T_2}$ (ms)**[3]**	$\boldsymbol{T_2^*}$ (ms)**[4]**
Grey matter	1940 ± 150	$\sim 45 \pm \sim 10$	33 ± 1
White matter	1130 ± 100	$\sim 45 \pm \sim 10$	27 ± 1

Table 1 – Relaxation times in the brain at 7 Tesla [2-4]

In a simple 90° flip angle gradient echo imaging sequence, the contrast between two tissue types (A and B) is given by [1]

$$\begin{aligned} C_{AB} &= S_A(TE) - S_B(TE) \\ &= \rho_{0_A}\left(1 - e^{-TR/T_{1_A}}\right)e^{-TE/T_{2_A}^*} - \rho_{0_B}\left(1 - e^{-TR/T_{1_B}}\right)e^{-TE/T_{2_B}^*} \quad , \end{aligned}$$

Eq. 3.20

where S_A is the signal from tissue A, S_B is the signal from tissue B, and ρ_{0_A} and $\rho_{0_B}$are their respective proton densities. Appropriate values of TR and TE can then be selected to maximise or minimise the influence of the T_1 and T_2^* decay terms as desired. Noting that when $x \ll 1$, $e^{-x} \approx (1 - x)$, and when $x \gg 1$, $e^{-x} \approx 0$, it can be seen from Eq. 3.20 that to maximise proton density, T_1, or T_2^*-based contrast, TR and TE values should be chosen as shown in Table 2.

Type of contrast	**TR**	**TE**
Spin density	As long as possible	As short as possible
$T_1 - weighted$	Of the order of the T_1 values	As short as possible
$T_2 - weighted$	As long as possible	Of the order of the T_2 values
$T_2^* - weighted$	As long as possible	Of the order of the T_2^* values

Table 2 – Guidelines for generating tissue contrast [1]

In addition to the appropriate selection of TR and TE values, T_1 contrast may be further enhanced by the inclusion of magnetization preparation steps prior to the excitation and image acquisition. Such techniques are discussed in Section 3.4.6. If T_2-weighting is desired, a simple spin echo sequence may be used in place of the gradient echo sequence described here. In a simple spin echo sequence, the refocusing gradient in the read direction in the gradient echo sequence is replaced by an RF pulse rotating the magnetization by 180° in the transverse plane, causing refoucussing of the signal component lost to T_2' effects. TR and TE chosen as shown in Table 2 [1].

3.4.2 Accelerated Imaging

In both clinical and research settings, minimising the duration of imaging sequences is essential to ensure both the comfort and compliance of the subject, and to make efficient use of available scanner time which may be in considerable demand. While the example of the simple gradient echo provides a convenient illustration of the important principles of MR image acquisition and contrast, such a sequence would be prohibitively long in duration in practice. For example, to acquire a 3D T_2^*-weighted image using a simple gradient echo with a 90° flip angle, $200 \times 200 \times 100$ mm field of view, and 0.5 mm isotropic resolution, a TR of 10 s (~$5T_1$) [2] might be chosen to maximise the recovery of the longitudinal magnetisation. Using Eq. 3.18 and Eq. 3.19 we find that such a scan would require the acquisition of 20 000 lines in k-space, giving a total scan time of over 273 hours.

To overcome such excessive acquisition times, various adjustments can be made to the acquisition sequence to significantly reduce the time required. For example, a technique called echo planar imaging (EPI) [5, 6, 27, 28] allows the rapid acquisition

of entire planes of k-space. In the work presented in this thesis, T_2^*-weighted images were acquired using an accelerated gradient echo sequence known as a spoiled fast field echo (FFE) or fast low-angle shot (FLASH) [7].

3.4.3 Echo Planar Imaging

In echo planar imaging, all lines of k-space are acquired in a single TR period. [5, 8, 27, 30]In the same manner as the simple 2D gradient echo described above, an EPI sequence begins with a selective excitation of a slice of the object under examination. Read and phase encoding gradient echoes de-phase the FID, and the read gradient is reversed and ADC activated to sample a line of k-space. In EPI, however, the readout is followed by the application of a short pulse or 'blip' of a gradient in the phase encode direction, which moves the k-space coordinate by Δk_y. This is followed by a reversal of the read gradient. The latter causes a formation of a subsequent echo, which allows a read-out of the following line of k-space. This step is then repeated until the whole of k-space has been sampled, as shown in Figure 3-8, greatly reducing the time required to acquire an image. The echo time is defined by the time where the centre of k-space is sampled. A schematic representation of an EPI sequence is shown in Figure 3-9. While EPI offers significant time savings, this is achieved at the cost of reduced SNR, and increased distortions due to susceptibility artefacts [9], as well signal dropout in regions surrounding strong susceptibility sources such as the sinuses, where the rapidly varying magnetic field causes rapid T_2^* decay.

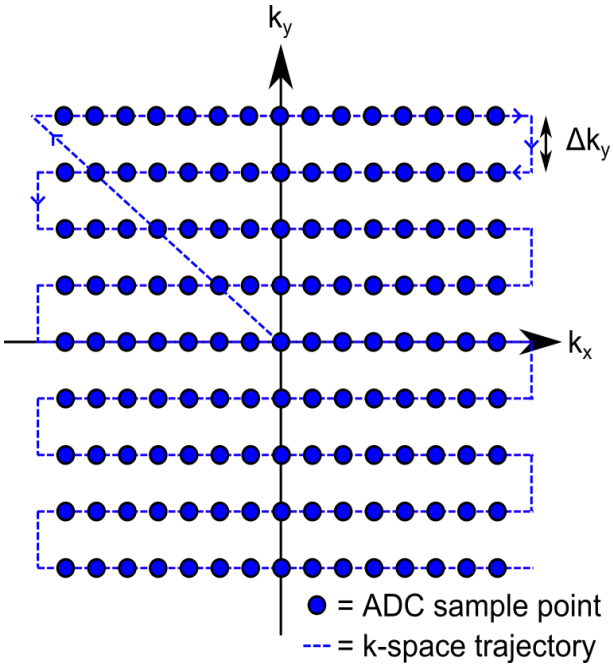

Figure 3-8 – Signal trajectory in k-space for an EPI sequence, as shown in Figure 3-9

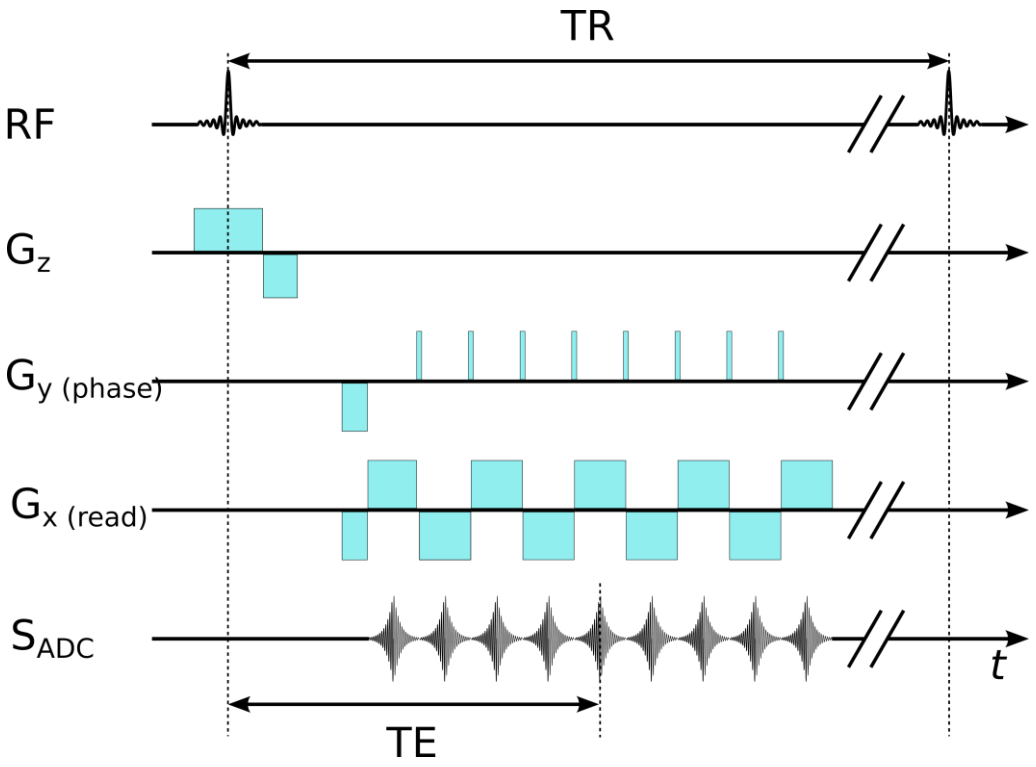

Figure 3-9 – A simple EPI pulse sequence

3.4.4 FLASH – Reducing Flip Angle and TR

The major time constraint of the simple gradient echo sequence is the length of time, TR, required for the longitudinal magnetisation to recover fully following a 90° excitation pulse. The FLASH sequence [7] utilises B_1 pulses with a flip angle that is significantly less than 90°, and a TR significantly shorter than T_1, meaning that subsequent excitation pulses are applied before the longitudinal magnetisation has fully recovered.

As with the simple gradient echo, the signal strength in the FLASH sequence is proportional to the transverse magnetisation. If the longitudinal magnetisation before the n^{th} RF pulse is $M_z(TR)_{n-1}$, the transverse magnetisation at a time t following the n^{th} RF pulse, $M_{xy}(TR)_n$ is

$$M_{xy}(t)_n = M_z(TR)_{n-1} \sin(\theta)\ exp\left(-\frac{t}{T_2^*}\right) \quad , \qquad \text{Eq. 3.21}$$

where θ is the flip angle. The evolution of the longitudinal magnetisation $M_z(t)_n$ during the same time period is given by the solution to the Bloch equation

$$M_z(t)_n = M_0\left(1 - exp\left(-\frac{t}{T_1}\right)\right) + M_z(TR)_{n-1}\cos(\theta)\, exp\left(-\frac{t}{T_1}\right) \quad .$$

Eq. 3.22

After a number of TRs, the longitudinal and transverse magnetisations reach a dynamic steady state, where the signal is the same at corresponding time points in each TR period so that the longitudinal magnetisation at the beginning and end of TR_n is equal to that at the beginning and end of TR_{n-1}. In the steady state, $M_z(TR)_n = M_z(TR)_{n-1} = M_{z_e}$, and Eq. 3.22 becomes

$$M_{z_e} = M_0\left(1 - exp\left(-\frac{TR}{T_1}\right)\right) + M_{z_e}\cos(\theta)\, exp\left(-\frac{TR}{T_1}\right) \quad .$$

Eq. 3.23

Using Eq. 3.23, the steady-state longitudinal magnetisation can be expressed as

$$M_{z_e} = \frac{M_0\left(1 - exp\left(-\frac{TR}{T_1}\right)\right)}{\left(1 - \cos(\theta)\, exp\left(-\frac{TR}{T_1}\right)\right)} \quad .$$

Eq. 3.24

The signal strength, which depends on the amount of transverse magnetization for a spoiled 3D FLASH sequence, with echo time TE, can therefore be expressed as

$$S \propto \rho_0 \sin(\theta) \frac{\left(1 - exp\left(-\frac{TR}{T_1}\right)\right)}{\left(1 - \cos(\theta)\, exp\left(-\frac{TR}{T_1}\right)\right)} exp\left(-\frac{TE}{T_2^*}\right) \quad ,$$

Eq. 3.25

showing that the signal strength is governed by the ratios TR/T_1 and TE/T_2^*, and the flip angle θ. The flip angle at which the peak signal is achieved is known as the Ernst angle, as shown in Figure 3-10. The Ernst angle is related to the TR and T_1 by $\cos\theta = exp(-TR/T_1)$. As can be seen in Figure 3-10, maximum signal is achieved with lower flip angles as TR/T_1 reduces, however the maximum absolute signal possible increases as TR/T_1 increases.

During a steady-state gradient echo acquisition with $TR \leq T_2$, additional steps must also be taken to reduce as far as possible the remaining transverse magnetisation at the end of each TR period, and to avoid constructive addition of transverse magnetisation from the $(n-1)^{th}$ excitation to that generated by the n^{th} excitation. Failure to do so can lead to imaging artefacts due to stimulated echoes. Such steps are known as 'spoiling mechanisms', and can be divided into gradient spoiling and RF spoiling mechanisms.

In the FLASH sequence, both gradient and RF spoiling are generally applied. The gradient spoiling involves the application of 'crushing' gradients in the read and slice directions after signal read-out. This is designed to dephase any remaining transverse magnetisation after readout. In addition, RF spoiling is applied, whereby the phase of the n^{th} excitation pulse is incremented by $117°$ relative to that of the $(n-1)^{th}$ pulse. This value is chosen as it has been shown to result in optimal cancellation of unwanted transverse coherences [10], since it does not share integer multiples with $360°$ for low n [11].

Once TR and θ have been chosen, balancing the need for adequate signal-to-noise ratio (SNR) against time constraints, TE may be chosen to achieve the balance between T_1-weighting, which is most prominent at very short TE, and T_2^* weighting, which is best seen when TE$\sim T_2^*$ ($\sim 33/27$ ms in grey/white matter at 7T, see Table 1 [4]).

Figure 3-11 shows a schematic representation of the FLASH sequence, divided into sections a, b, c and d. The slice select gradient and RF excitation pulse are shown in a, the frequency and phase encoding gradients in b, the readout gradients and gradient echo signal in c, and the gradient spoiling in d.

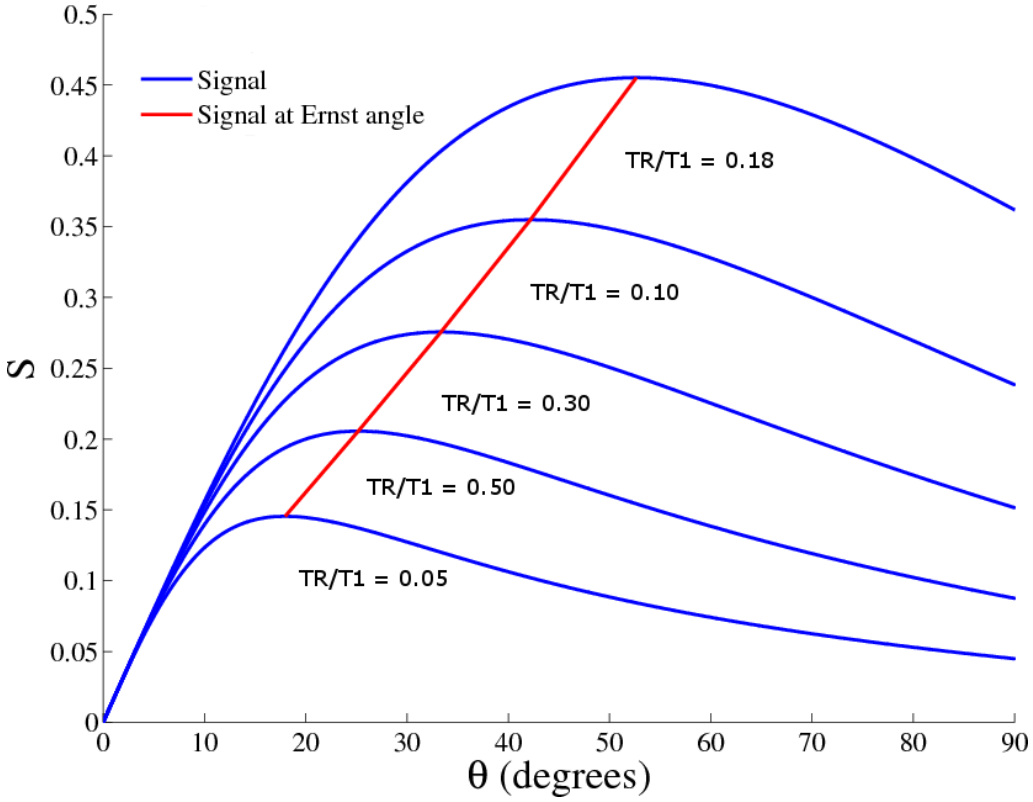

Figure 3-10 – Signal strength as a function of flip angle for varying values of TR/T_1

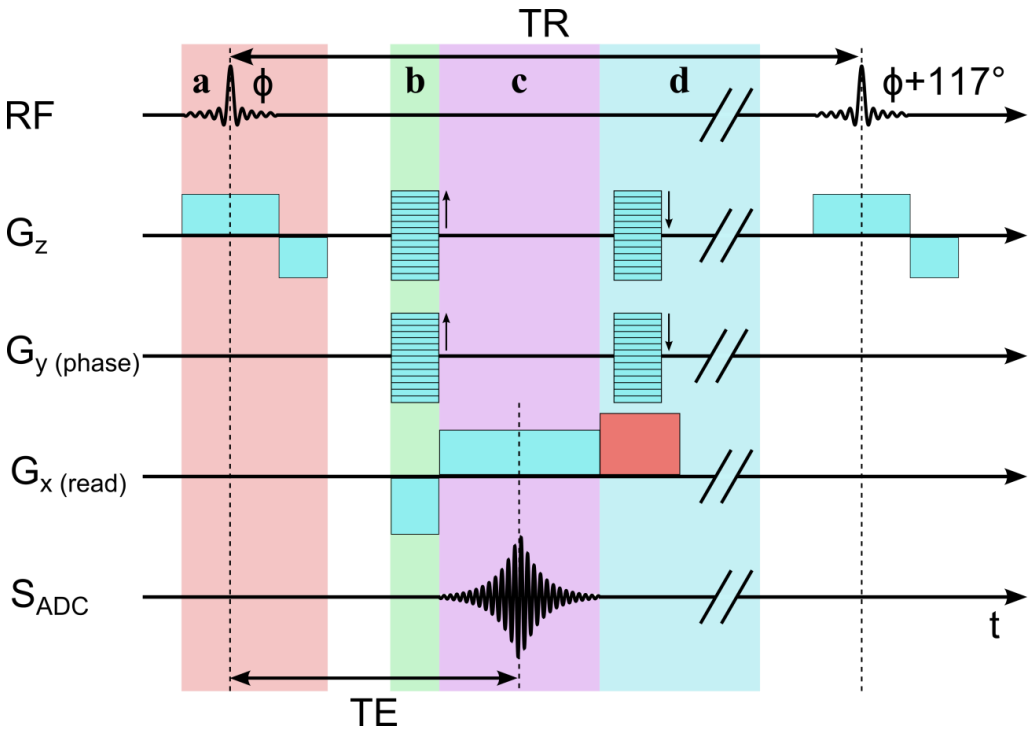

Figure 3-11 – The FLASH pulse sequence

3.4.5 Further Acceleration of FLASH Imaging: EPI Factors and Parallel Imaging

In addition to the reduction in TR made possible by steady-state imaging sequences such as FLASH, further acceleration of image acquisition can be achieved through the use of EPI factors and parallel imaging.

Gradient echo-based imaging sequences such as FLASH may be further accelerated by the acquisition of multiple lines of k-space during each TR period. While full echo planar imaging involves the acquisition of an entire k-space plane in a single TR period, SNR and acquisition time can be balanced by collecting more than one line of k-space in a single TR period, but not extending this to a full EPI acquisition. The number of lines collected is often referred to as the EPI factor, and the imaging time will be reduced by this factor.

Parallel imaging methods accelerate the acquisition of MR images by the systematic under-sampling of k-space in the phase encode direction while acquiring the data using an array of independent receiver channels, and subsequent reconstruction of a single corrected image from these under sampled data through the application of an appropriate algorithm [12].

In the work presented in Chapter 2, sensitivity encoding (SENSE) [13] parallel imaging was used in the acquisition of the FLASH images. SENSE utilises data acquired at a lower resolution in the phase encoding direction in k-space, which leads to aliasing in the resulting images from the individual receive channels. In MR images, aliasing (also known as 'ghosting' or 'wraparound') is the projection of any signal-producing volume falling outside of the FOV of the image back into the opposite side of the image. Aliasing occurs due to the reduction of the image-space FOV due to the decrease in the k-space resolution (see Eq. 3.18) below the Nyquist limit, and is a consequence of the periodic nature of the Fourier transform [1]. The SENSE algorithm takes advantage of the known spatial sensitivity of each independent receiver channel, which must be measured for each subject or object through a separate reference scan, to create an unaliased image from a weighted combination of the individual aliased images.

In the work presented in Chapter 2, data were acquired at 0.5 mm resolution using a FLASH sequence with TR = 150 ms, with an EPI factor of 3 and a SENSE factor of 2. For the same $200 \times 200 \times 100$ mm ROI considered at the beginning of this

section, the acquisition time would be reduced from over 273 hours for the simple 90 degree gradient echo sequence to 8.3 minutes using these parameters.

3.4.6 T_1-weighted Imaging

T_1-weighting is commonly used in anatomical imaging of the brain as it can offer good contrast between grey matter (GM), white matter (WM), and cerebrospinal fluid (CSF). One method of generating strong T_1-weighting is the combination of an inversion recovery sequence with a conventional gradient or spin-echo readout sequence. A common T_1-weighted imaging sequence is the magnetisation-prepared rapid-acquisition gradient echo (MPRAGE) [14].

3.4.6.1 Magnetisation-Prepared Rapid-Acquisition Gradient Echo (MPRAGE) Imaging

A schematic of an MPRAGE sequence is shown in Figure 3-12. A 180˚ inversion pulse is applied across the sample to invert the magnetisation from the $+\hat{\mathbf{z}}$ to the $-\hat{\mathbf{z}}$ direction. The magnetisation then recovers according to Eq. 2.8, with the magnetisation in GM, WM, and CSF recovering at different rates, as shown in Figure 3-13. At a time TI after the inversion pulse a FLASH readout is used to acquire the T_1-weighted image. TI may be varied to generate optimum contrast between two tissue types, or to null the signal from one tissue, commonly CSF. The echo time of the readout sequence is kept as short as possible to maximise T_1-weighting, as shown in Table 2.

MPRAGE images are sensitive only to the magnitude of the magnetisation in each voxel. If TI is chosen such that GM and WM have magnetisations of equal magnitude but opposite polarity, there will be no contrast between them in the resulting image. However, in voxels containing both GM and WM, signal loss will be observed where the contribution from the two magnetisations cancel, leading to a dark line artefact where regions of GM and WM meet. This effect can be exploited using phase sensitive inversion recovery (PSIR) and null-point imaging [15, 16].

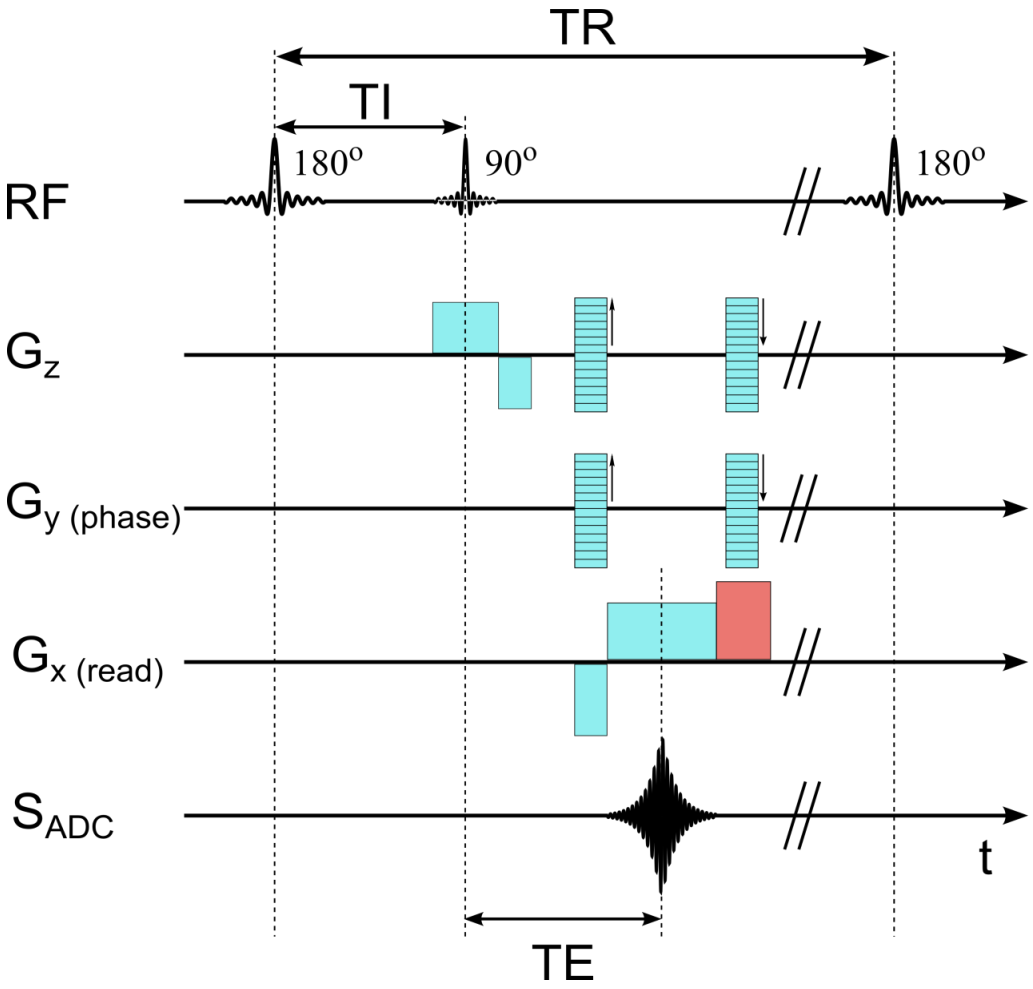

Figure 3-12 – A schematic representation of an MPRAGE imaging sequence

3.5 T1, T2 and T2* Measurements Using MRI

Conventional MRI is typically based on mapping the magnitude of the signal from each voxel in the ROI, measured at fixed point in time. While the relative signal levels between voxels may be weighted by or manipulated, based on sensitivity to the relaxation times in different media, the absolute intensity of the final image is often arbitrary, varying between subjects, with changes in imaging parameters, and between scanners. Quantitative MRI techniques, in theory, create images whose intensity and contrast is based on quantitative measures of local variations in some property of the media under investigation.

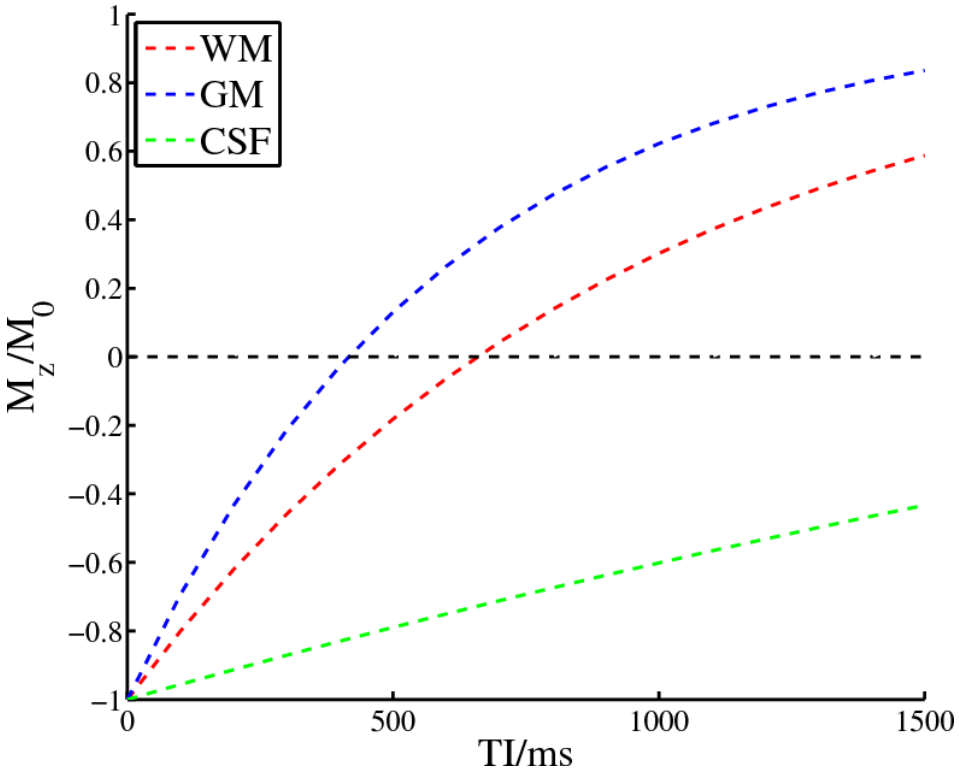

Figure 3-13 – Longitudinal recovery of the magnetisation in grey matter (GM), white matter (WM) and cerebrospinal fluid (CSF)* at 1.5 T

*The CSF T1 used here related to a field strength of 1.5 T, as no published value for T1 in CSF at 7 T was available. However, T1 in CSF varies very little with field strength relative to GM and WM.

Such measurement allows direct quantitative comparison between subjects, and the drawing of inferences regarding sub-voxel level tissue composition and structure.

One group of parameters that are commonly quantified using MR are the relaxation times T_1, T_2, and T_2^* (often expressed as relaxation rates, which are simply the inverse of these times). These values in turn may be linked to factors such as iron and myelin content in tissues, oxygenation in blood, and diffusion.

T_1, T_2, and T_2^*-weighted images can be acquired through the use of inversion recovery, spin echo, and gradient echo based sequences respectively. In such sequences, T_1-weighting is controlled by varying the inversion time TI, and T_2- and T_2^*-weighting are determined by the echo time TE. These relaxation times can be calculated by the acquisition of multiple images while varying TI or TE, and voxel-wise fitting of the resulting images to Eq. 2.10 and Eq. 3.6.

Figures 3-14, 3-15 and 3-16 show examples of T_2^*-weighted magnitude images and quantitative R_2^* maps of a post-mortem chimpanzee brain. Data were acquired at 0.3 mm isotropic resolution using a multi-echo FLASH sequence at 7 T using a 32-channel RF receive coil (TE=8.0/21.5/35.0 ms, TR=200 ms, FOV=75x134x134 mm^3, scan duration = 6 hours and 20 minutes). The R_2^* map was calculated from the multi echo data in MATLAB. These images were acquired for collaborators at the University of Nottingham School of Veterinary Medicine and Science, who were interested in investigating changes in iron levels in the deep grey matter during aging in captive chimpanzees. Unfortunately this project did not proceed due to the small number of samples available, and the poor condition of some of these samples. Theses figures, however, show striking examples of the post-mortem image quality achievable at 7 T with standard hardware for *in vivo* human imaging.

Darker areas in the T_2^*-weighted magnitude appear bright in the quantitative R_2^* maps, with the iron rich red nuclei appearing clearly as dark circles in the T_2^*-weighted image and bright circles in the R_2^* map in Figure 3-16. Field perturbations due to paramagnetic iron cause signal dephasing which results in a shorter T_2^* and therefore higher R_2^*.

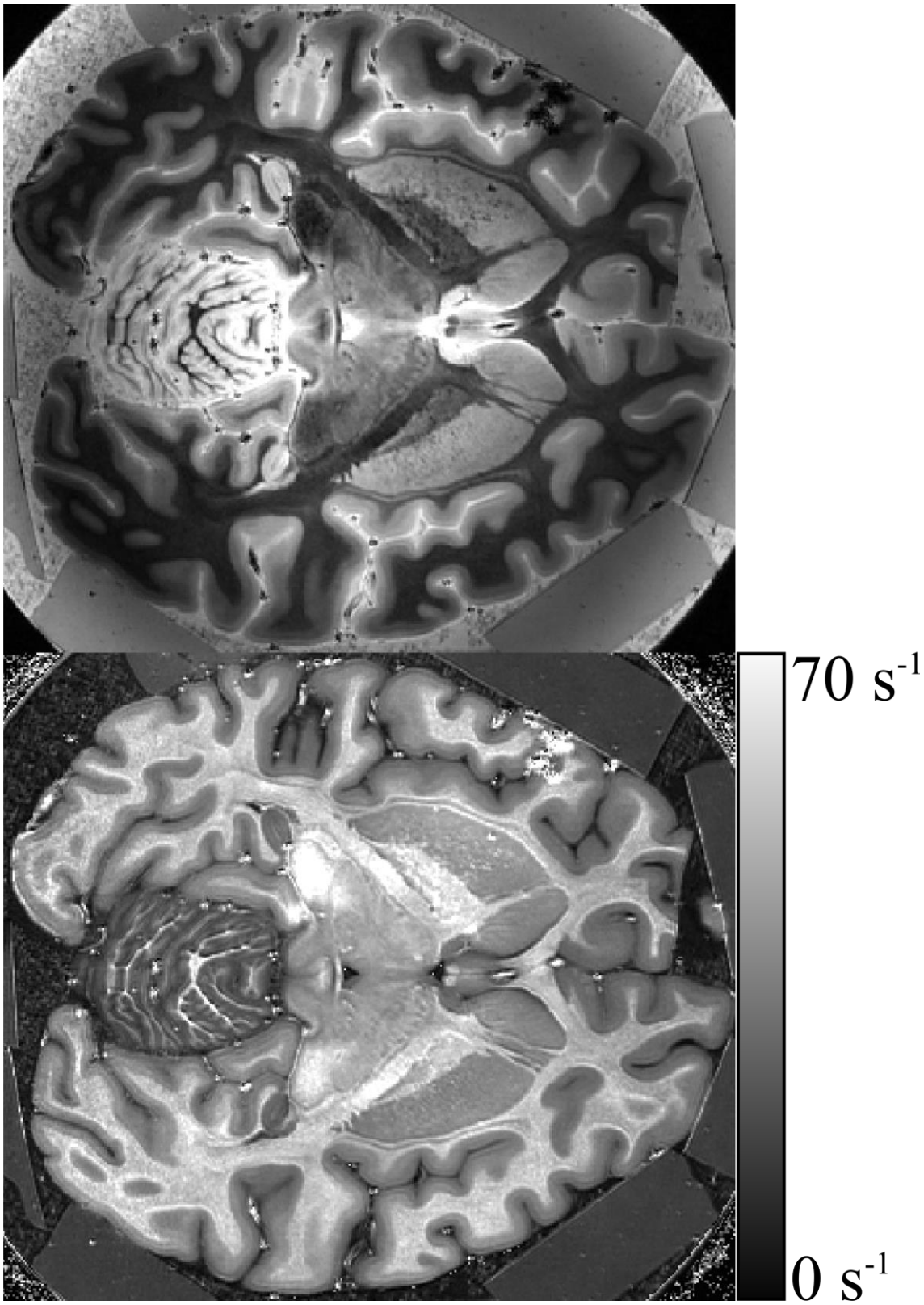

Figure 3-14 – Transverse T_2^*-weighted magnitude (top) and quantitative R_2^* (bottom) images of a post-mortem chimpanzee brain. Three magnitude images were acquired using a multi-echo FLASH sequence, at 0.3 mm isotropic resolution, with a total scan duration of 380 minutes

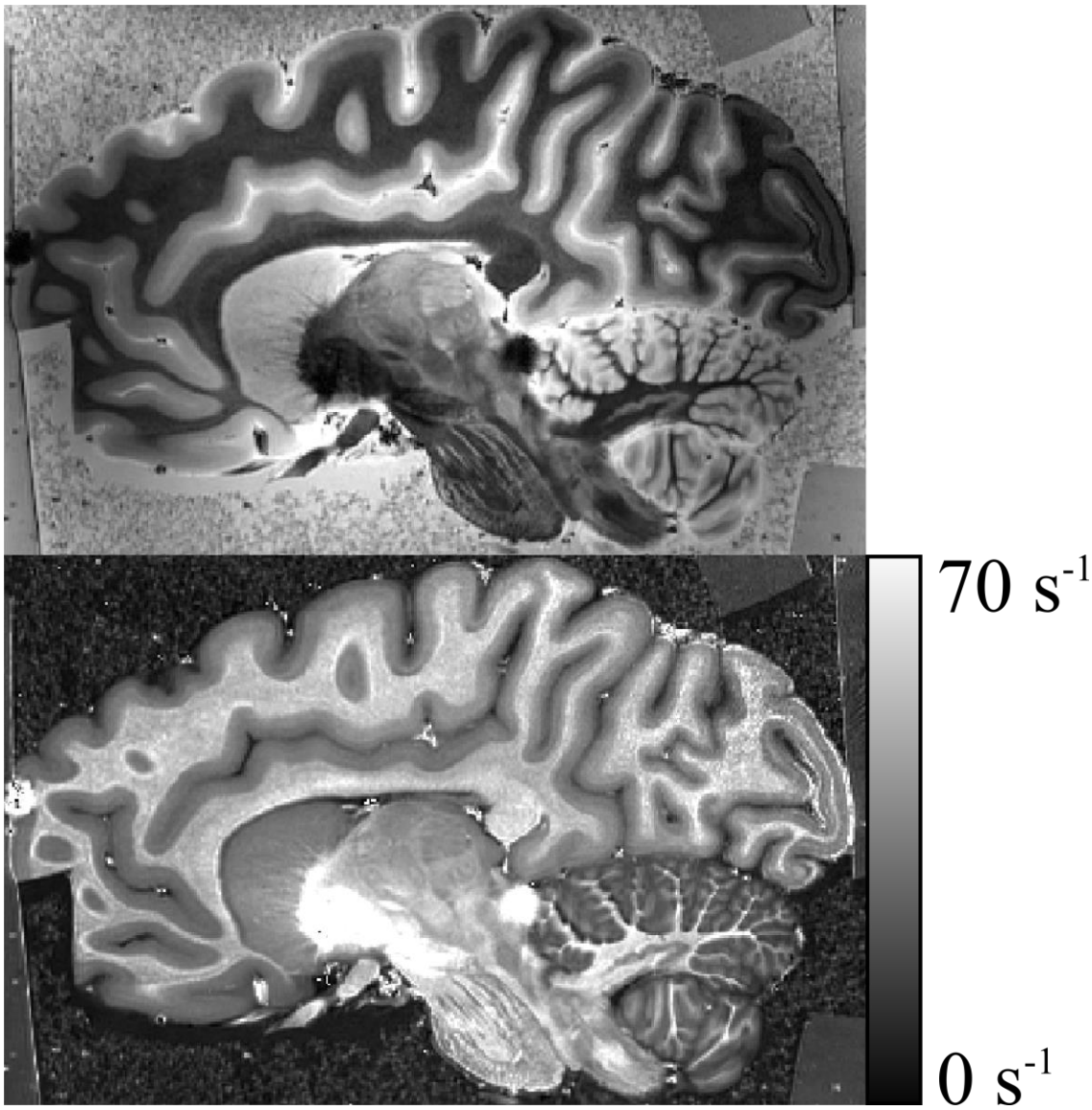

Figure 3-15 – Sagittal T_2^*-weighted magnitude (top) and quantitative R_2^* (bottom) images of a post-mortem chimpanzee brain. Three magnitude images were acquired using a multi-echo FLASH sequence, at 0.3 mm isotropic resolution, with a total scan duration of 380 minutes

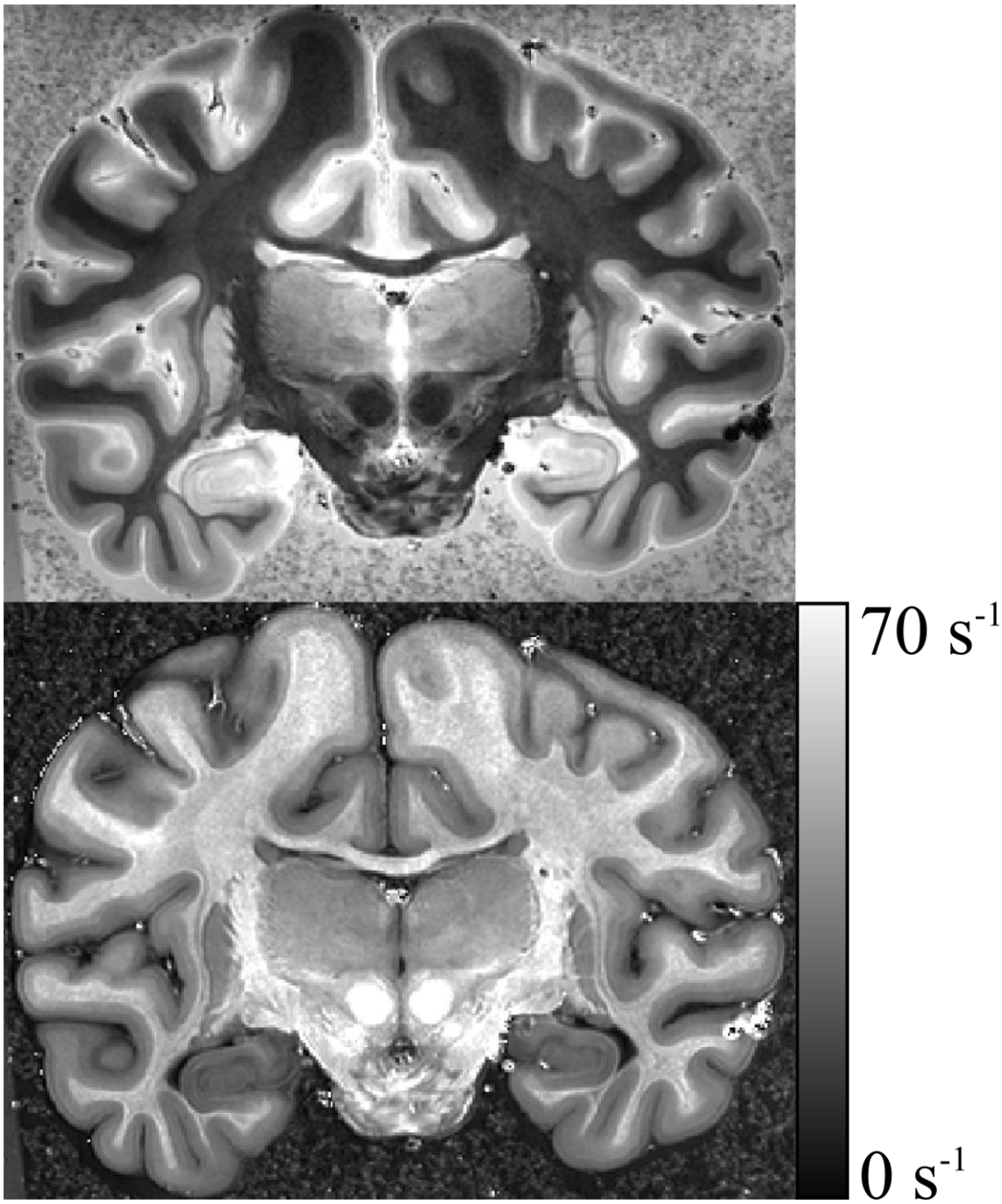

Figure 3-16 – Coronal T_2^*-weighted magnitude (top) and quantitative R_2^* (bottom) images of a post-mortem chimpanzee brain. Three magnitude images were acquired using a multi-echo FLASH sequence, at 0.3 mm isotropic resolution, with a total scan duration of 380 minutes. The iron-rich red nuclei can be clearly seen as dark (T_2^*-wt.) or bright (R_2^* map) circles in the lower mid section of the images.

3.6 References

1. Brown, R.W., et al., *Magnetic resonance imaging: physical principles and sequence design*. 2014: John Wiley & Sons.
2. Wright, P.J., et al., *Water proton T 1 measurements in brain tissue at 7, 3, and 1.5T using IR-EPI, IR-TSE, and MPRAGE: results and optimization.* Magnetic Resonance Materials in Physics, Biology and Medicine, 2008. **21**(1-2): p. 121-130.
3. Cox, E.F. and P.A. Gowland, *Simultaneous quantification of T2 and T' 2 using a combined gradient echo-spin echo sequence at ultrahigh field.* Magnetic Resonance in Medicine, 2010. **64**(5): p. 1440-1445.
4. Peters, A.M., et al., *T2* measurements in human brain at 1.5, 3 and 7 T.* Magnetic Resonance Imaging, 2007. **25**(6): p. 748-753.
5. Mansfield, P., *Multi-planar image formation using NMR spin echoes.* Journal of Physics C: Solid State Physics, 1977. **10**(3): p. L55.
6. Stehling, M.K., R. Turner, and P. Mansfield, *Echo-planar imaging: magnetic resonance imaging in a fraction of a second.* Science, 1991. **254**(5028): p. 43-50.
7. Frahm, J., A. Haase, and D. Matthaei, *Rapid three-dimensional MR imaging using the FLASH technique.* Journal of computer assisted tomography, 1986. **10**(2): p. 363-368.
8. Mansfield, P. and A.A. Maudsley, *Medical imaging by NMR.* The British Journal of Radiology, 1977. **50**(591): p. 188-194.
9. Jezzard, P. and R.S. Balaban, *Correction for geometric distortion in echo planar images from B0 field variations.* Magnetic Resonance in Medicine, 1995. **34**(1): p. 65-73.
10. Duyn, J.H., *Steady state effects in fast gradient echo magnetic resonance imaging.* Magnetic Resonance in Medicine, 1997. **37**(4): p. 559-568.
11. Bernstein, M.A., X.J. Zhou, and K.F. King, *Handbook of MRI pulse sequences*. 2004, Amsterdam ; Boston: Academic Press. xxii, 1017
12. Deshmane, A., et al., *Parallel MR imaging.* Journal of Magnetic Resonance Imaging, 2012. **36**(1): p. 55-72.
13. Pruessmann, K.P., et al., *SENSE: sensitivity encoding for fast MRI.* Magnetic Resonance in Medicine, 1999. **42**(5): p. 952-962.
14. Brant-Zawadzki, M., G.D. Gillan, and W.R. Nitz, *MP RAGE: a three-dimensional, T1-weighted, gradient-echo sequence--initial experience in the brain.* Radiology, 1992. **182**(3): p. 769-775.
15. Hou, P., et al., *Phase-sensitive T1 inversion recovery imaging: a time-efficient interleaved technique for improved tissue contrast in neuroimaging.* American Journal of Neuroradiology, 2005. **26**(6): p. 1432-1438.
16. Pitiot, A., J. Totman, and P. Gowland, *Null point imaging: a joint acquisition/analysis paradigm for MR classification*, in *Medical Image Computing and Computer-Assisted Intervention–MICCAI 2007*. 2007, Springer. p. 759-766.

4 QUANTITATIVE SUSCEPTIBILITY MAPPING

In addition to the quantification of relaxation times through measurement of the decay of MR signal magnitude, novel contrast and additional quantitative measurements can be made by considering the signal phase, both in combination with the magnitude signal and on its own. Signal phase is increasingly of interest as variations in signal phase are linked to local variations in the B_0 field caused by the magnetisation of molecules within the sample with non-zero magnetic susceptibility. As well as simple phase imaging, techniques such as susceptibility-weighted imaging (SWI) [1], quantitative susceptibility mapping (QSM) [2-10], and frequency difference mapping [11] have become prominent in the investigation of a number of diseases and attempts to probe sub voxel level microstructure.

In SWI, T_2^*-weighted magnitude images are multiplied by a weighted mask derived from the phase data. Phase data is unwrapped and high-pass filtered using a high-pass filtered using a Hanning window, and a mask generated which varies between 0 and 1, with positive phase values being set to 1, and values from $-\pi$ to 0 varying from 0 to 1, either linearly or by a power function. These images highlight areas of high susceptibility such as veins, iron stores, and haemorrhages [1]. While SWI processing is simple and its results can be sued to highlight clinically important features, it limited by its reliance on non-local, orientation dependent phase effects, and as such SWI contrast does not correlate with local magnetic susceptibility.

Quantitative susceptibility mapping (QSM) refers to a number of techniques used to map the variation in the relative magnetic susceptibility within an object based on the measured MR signal phase. Such measurements are particularly useful in biological tissue such as the brain, as magnetic susceptibility is directly linked to iron and myelin content [6, 12-14], and QSM is increasingly used in the study of neurodegenerative conditions such as multiple sclerosis (MS), where iron deposition and demyelination are believed to play important roles [15-20]. QSM processing is more complex than SWI processing, but QSM images offer the advantage of quantitative, local contrast, directly linked to the local magnetic susceptibility, and so inferences may be drawn about local tissue content.

4.1 Susceptibility and Magnetisation

When a molecule is placed in a magnetic field, a magnetic moment is induced in it, which is either parallel or antiparallel to the external field. If the net spin and orbital angular momentum of the electrons in a molecule both cancel, the molecule has no intrinsic magnetic moment. However when an external magnetic field is applied to the molecule, precession of the orbital moments is induced, producing a magnetic moment which is opposed to the applied field [21]. This effect is known as diamagnetism. If the net spin and orbital angular momentums of the electrons do not cancel both then molecules possess an intrinsic magnetic moment which is greater than the induced diamagnetic moment, and when exposed to a magnetic field on average adopt a least-energy state with the dipoles aligned with the applied field. This effect is known as paramagnetism. The net magnetic moment per unit volume of a material is known as the magnetisation, **M**. The magnetisation is quantified by an intrinsic property of the material known as the magnetic susceptibility, χ, and is related to an the applied magnetic field by

$$\mathbf{M} = \chi \mathbf{H} \quad ,$$

Eq. 4.1

where **H** is the magnetic field expressed in Am^{-1}. χ is positive for paramagnetic materials and negative for diamagnetic materials. A magnetised material will produce its own magnetic field which adds linearly to the externally applied field causing spatial field perturbations.

In magnetostatics, the magnetic field **H** and the magnetic induction **B** follow the Maxwell relations

$$\boldsymbol{\nabla} \cdot \mathbf{B} = 0$$

Eq. 4.2

and

$$\boldsymbol{\nabla} \times \mathbf{H} = \mathbf{J} \quad ,$$

Eq. 4.3

where **J** is the current density. In the absence of current, Eq. 4.3 becomes

$$\boldsymbol{\nabla} \times \mathbf{H} = 0 \quad ,$$

Eq. 4.4

and **H** may be defined in terms of a magnetic scalar potential $\Phi(\mathbf{r})$, such that

$$\mathbf{H} = -\boldsymbol{\nabla}\Phi(\mathbf{r}) \quad .$$

Eq. 4.5

The magnetic field and magnetic induction are related by $\mathbf{B} = \mu_0(\mathbf{H} + \mathbf{M})$, and so Eq 4.2 may be written as

$$\boldsymbol{\nabla} \cdot \mathbf{B} = \boldsymbol{\nabla} \cdot \mu_0(\mathbf{H} + \mathbf{M}) = 0 \quad .$$

Eq. 4.6

Therefore, using Eq. 4.5,

$$\boldsymbol{\nabla^2}\Phi(\mathbf{r}) = -\boldsymbol{\nabla} \cdot \mathbf{M} = -\rho_M \quad ,$$

Eq. 4.7

where $\rho_M = -\boldsymbol{\nabla} \cdot \mathbf{M}$ is the effective magnetic charge density. The solution for $\Phi(\mathbf{r})$ in the absence of boundary surfaces is given by [21]

$$\Phi(\mathbf{r}) = -\frac{1}{4\pi} \int_V \frac{\boldsymbol{\nabla}' \cdot \mathbf{M}(\mathbf{r}')}{|\mathbf{r} - \mathbf{r}'|} d^3r' \quad .$$

Eq. 4.8

If the magnetization distribution contains boundary surfaces, these surfaces may be idealized as discontinuities in the magnetization distribution, and boundary conditions imposed to find $\Phi(\mathbf{r})$. Application of the divergence in a Gaussian pillbox at the surface gives an effective surface charge density of [21]

$$\sigma_M = \mathbf{n} \cdot \mathbf{M} \quad ,$$

Eq. 4.9

where $\mathbf{n}$ is a unit vector normal to the surface directed outward. In the presence of such boundary surfaces, Eq. 4.9 becomes

$$\Phi(\mathbf{r}) = -\frac{1}{4\pi} \int_V \frac{\nabla' \cdot \mathbf{M}(\mathbf{r}')}{|\mathbf{r} - \mathbf{r}'|} d^3r' + \frac{1}{4\pi} \oint_S \frac{\mathbf{n}' \cdot \mathbf{M}(\mathbf{r}')}{|\mathbf{r} - \mathbf{r}'|} dS'$$

Eq. 4.10

Eq. 4.10 may be solved analytically for uniformly magnetised objects whose geometry fits with a particular coordinate system such as spherical and cylindrical polar coordinates, or ellipsoidal coordinates, allowing easy calculation of the magnetic field $\mathbf{H}$ or the magnetic induction $\mathbf{B}$, which are related by $\mathbf{B} = \mu_0\mathbf{H} + \mathbf{M}$, where μ_0 is the permeability of free space. However, outside of these special cases the field perturbation must be calculated numerically. Direct calculation of numerical solutions to Eq. 4.10 over any significant number of points is computationally intensive, and impractical or impossible in many cases.

4.2 Fourier-based Calculation of Magnetic Field Perturbations

Several methods have been proposed to calculate field perturbations due to heterogeneous magnetic susceptibility distributions. These include iterative methods [22-26] and convolution based methods [27-30]. The Fourier-based method introduced by Marques and Bowtell [29] provides a fast, computationally efficient means of calculating the magnetic field perturbation due to an arbitrary distribution of magnetic susceptibility. This method directly includes the sphere of Lorentz correction [31-33]. The sphere of Lorentz is a theoretical construction in which each nucleus is imagined to be at the centre of a sphere of zero susceptibility outside of which the surrounding molecules form a homogenous medium with constant

magnetic susceptibility, and is required to accurately calculate the magnetic field experienced by the nucleus.

If a strong magnetic field $B_0\hat{\mathbf{z}}$ is applied to an object with spatially varying magnetic susceptibility $\chi(\mathbf{r})$, the z-component of the induced magnetisation is given by

$$M_z(\mathbf{r}) = \chi(\mathbf{r})\frac{B_0}{\mu_0\mu_r(\mathbf{r})} = \chi(\mathbf{r})\frac{B_0}{\mu_0(1+\chi(\mathbf{r}))} \approx \chi(\mathbf{r})\frac{B_0}{\mu_0}$$

Eq. 4.11

where μ_0 is the permeability of free space, $\mu_r = (1+\chi)$ is the permeability of the medium, and $\chi \ll 1$. Each element of the magnetization distribution creates a dipolar field perturbation. The total field perturbation at a point $\mathbf{r}$ is given by the sum of these contributions. In real space, this is a complex expression, given by [29]

$$\Delta\mathbf{B}(\mathbf{r}) = \frac{\mu_0}{4\pi}\int \frac{1}{|\mathbf{r}-\mathbf{r}'|^3} \times \left(3\frac{\mathbf{M}(\mathbf{r}')\cdot(\mathbf{r}-\mathbf{r}')}{|\mathbf{r}-\mathbf{r}'|^2}(\mathbf{r}-\mathbf{r}') - \mathbf{M}(\mathbf{r}')\right) d^3\mathbf{r}'$$

Eq. 4.12

The expression for the z-component of the field, ΔB_z, becomes simple and local when expressed in k-space, where [29]

$$\Delta B_z(\mathbf{k}) = -\mu_0\left(\cos^2(\beta) - \frac{1}{3}\right) M_z(\mathbf{k})$$

Eq. 4.13

where $\mathbf{k}$ is the k-space coordinate, β is the angle between the main magnetic field and $\mathbf{k}$, and $M_z(\mathbf{k})$ is the 3D Fourier transforms of $M_z(\mathbf{r})$. We can consequently define a dipole kernel $d(\mathbf{k})$

$$d(\boldsymbol{k}) = (3\cos^2(\beta) - 1) = \left(3\frac{k_z^2}{k_x^2 + k_y^2 + k_z^2} - 1\right)$$

Eq. 4.14

such that

$$\Delta B_z(\mathbf{k}) = \frac{\mu_0}{3} M_z(\mathbf{k}) \cdot d(\mathbf{k}) \quad .$$

Eq. 4.15

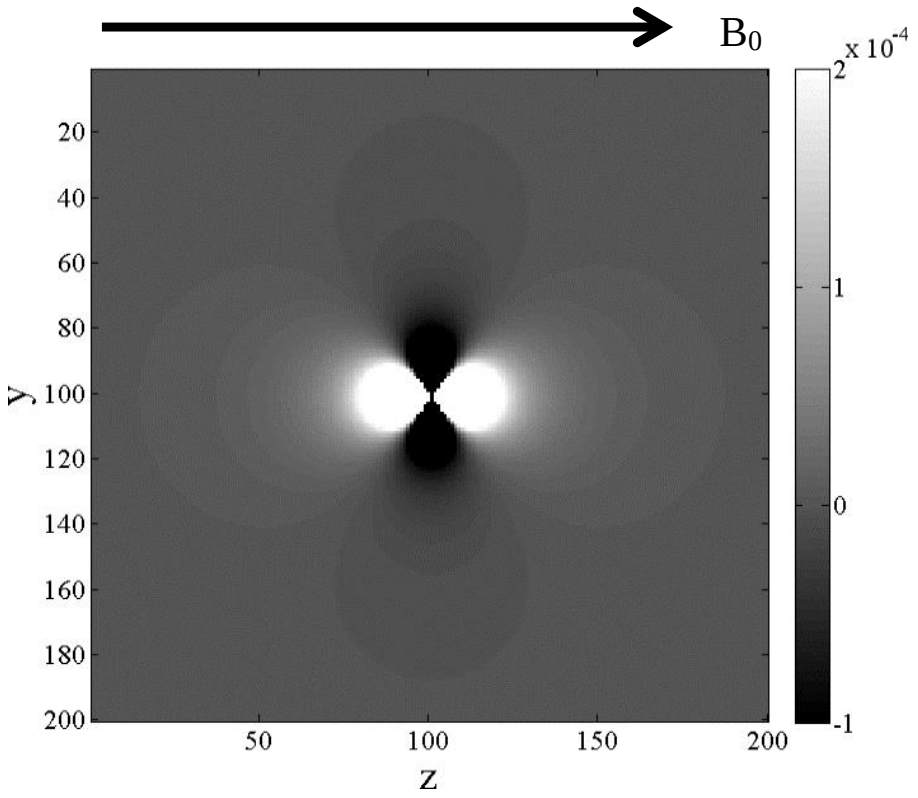

Figure 4-1 – A unit dipole kernel defined over a (200 mm)3 matrix in real space

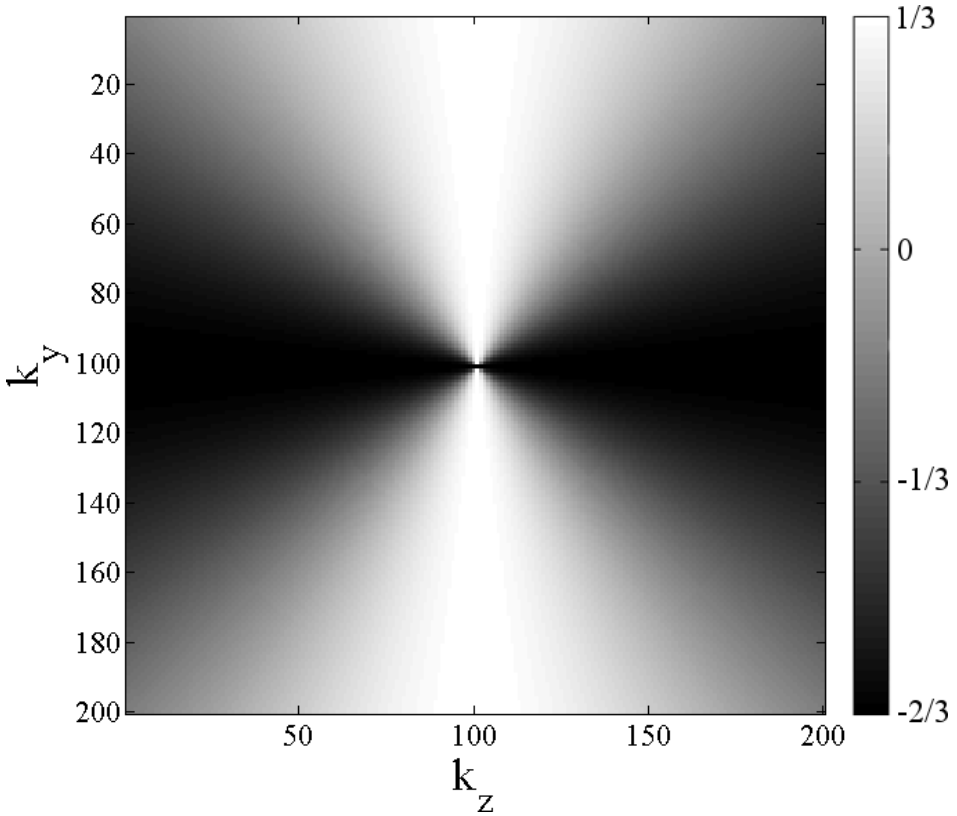

Figure 4-2 – The dipole kernel defined over a 1000 mm-3 matrix in k-space

$\Delta B_z(\mathbf{r})$ may then be calculated using an inverse Fourier transform. Eq. 4.14 is equivalent to the Fourier transform of a unit dipole in real space, as shown in Figures 4-1 and 4-2 .

This method can be validated by the comparison of its result with structures for which the analytical form of the field perturbation is known. Figures 4-3, 4-4 and 4-5 show the field perturbation due to a sphere with a magnetic susceptibility of -9 ppm residing in a vacuum and exposed to a z-directed magnetic field. The sagittal images show a close correspondence between the analytical and Fourier forms of the field perturbation, with a slight distortion at the edge of the image due to the periodic nature of the Fourier transform. This distortion can be made insignificant by ensuring that the size of the matrix is sufficiently large relative to the perturbing structures. In real world use, this can be achieved by zero-padding the image data before performing calculation involving Fourier transforms. The 1D profile through the image also shows slight deviations of the Fourier model from the analytical solution at the boundary of the sphere, caused by truncation and discretisation effects inherent in the discrete fast Fourier transform used in the calculation [29].

Quantitative susceptibility mapping is based upon the inversion of Eq. 4.13 to map the distribution of magnetic susceptibilities in an object based on a measured field perturbation.

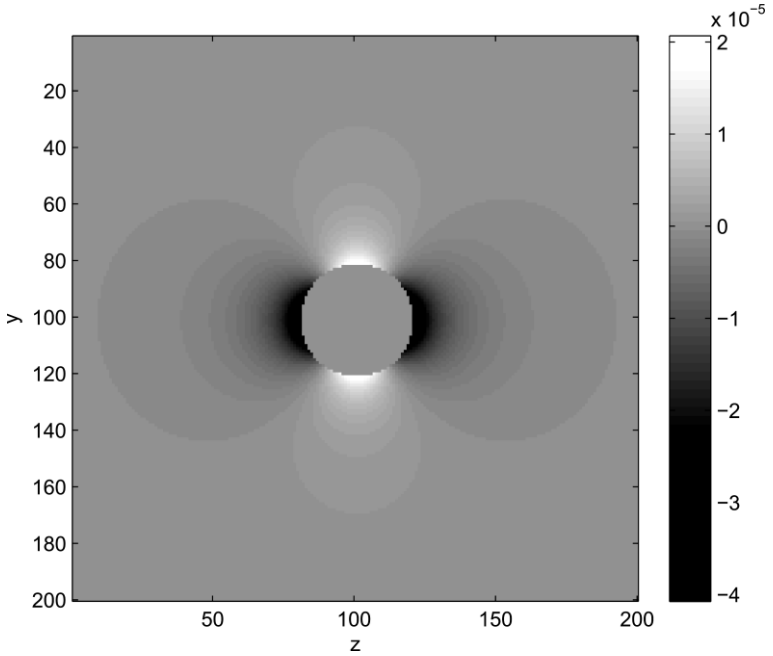

Figure 4-3 – Sagittal image of the analytical form of the field perturbation in Tesla due to a spherical perturber with a 20 voxel radius and $\chi = -9$ ppm exposed to a B_0 field of 7 T.

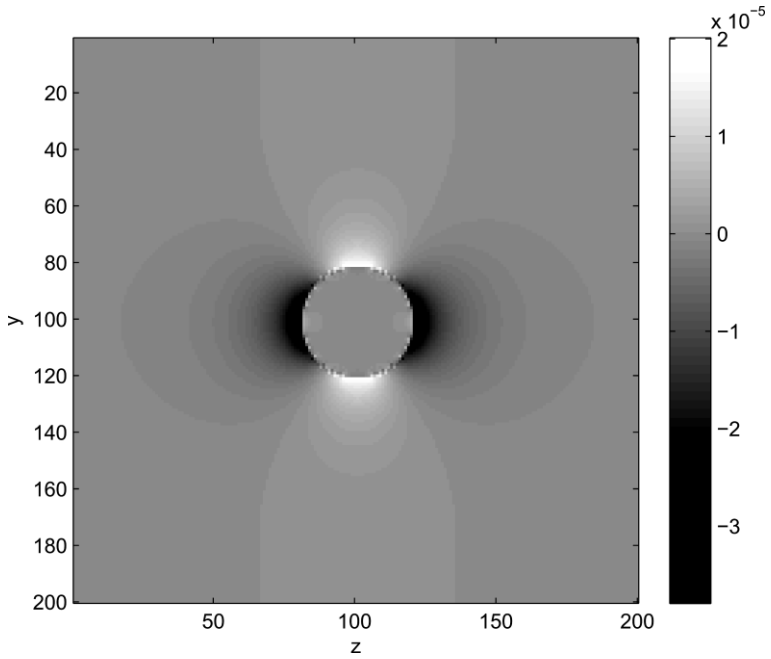

Figure 4-4 – Sagittal image of the field perturbation in Tesla due to a spherical perturber with a 20 voxel radius and $\chi = -9$ ppm exposed to a B_0 field of 7 T, calculated using the Fourier calculation in Eq. 4.15.

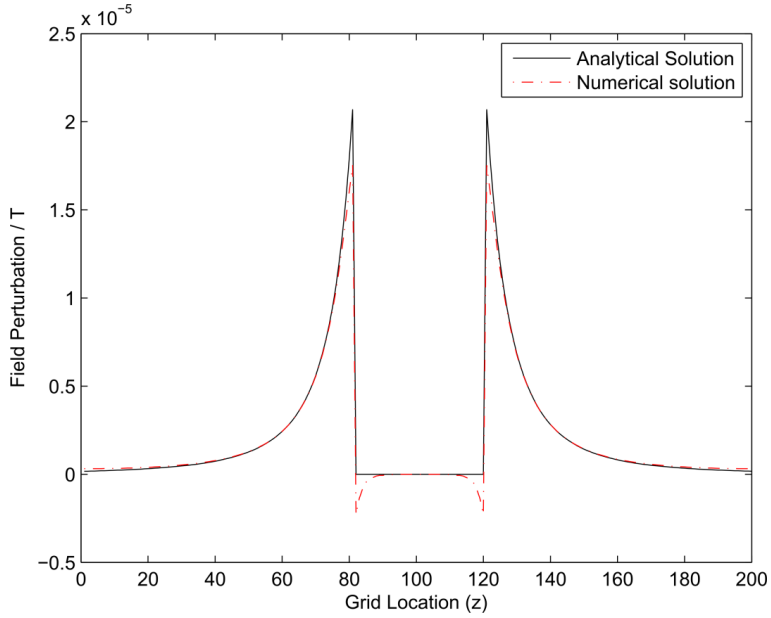

Figure 4-5 – 1D profile through analytic and numerically calculated field perturbations due to a sphere with $\chi = -9$ ppm and $B_0 = 7$ T

4.3 Calculation of Field Perturbations from MRI Phase Data

Modern MRI systems increasingly use multiple receiver coils to sample the MR signal in order to increase SNR throughout the image and accelerate image acquisition using parallel imaging techniques. Prior to further processing, the phase signal from each coil must be properly combined to form a single image. This is optimally performed by weighting coil values in each voxel by the complex sensitivity of the coil at that position. Accurate sensitivity maps may be acquired dividing the complex data acquired using each coil with complex data acquired using a volume reference coil [34] For the data presented in this thesis, coil sensitivity maps were acquired as part of all imaging protocols and data from each coil was combined automatically by the scanner.

In order to invert Eq. 4.13 and calculate $\chi(\mathbf{r})$, it is necessary to measure the field perturbation $\Delta B_z(\mathbf{r})$ caused by this distribution. While the relationship between MR phase accumulation and the local magnetic field is presumed to be linear for the purposes of QSM, measurement of $\Delta B_z(\mathbf{r})$ is confounded by the presence of large field perturbations caused by susceptibility variations outside of the object being imaged, and by the wrapping of the phase recorded by the scanner. In order to overcome these issues, the phase must be unwrapped, filtered to remove background fields, and divided by TE to yield a frequency map, which can then be related to the local magnetic field by $\omega = \gamma B_o$.

4.3.1 Unwrapping MRI Phase Data

A number of algorithms exist for the unwrapping of MRI phase data. Readily available software, such as PRELUDE in FSL [35], identifies regions with similar phase values and merges them by adding or subtracting integer multiples of 2π at the boundaries where wraps occur. This method is robust, however high-resolution MRI datasets may take several hours to process [36].

For the work presented in this thesis, a Laplacian-based phase unwrapping algorithm was used [6, 37]. This algorithm exploits the inherent insensitivity of the Laplacian operator to phase wraps, allowing the expression of the unwrapped phase purely in terms of the wrapped phase. It is computationally efficient, taking ~ 4 s to unwrap a 384x384x170 element volume on a desktop computer (3.40 GHz Intel Core i7-3770 CPU, 8.00 GB RAM, Windows 7 64-bit operating system).

The true phase, $\phi(\mathbf{r})$, of a continuous function wrapped about $\pm\pi$ at a point $\mathbf{r}$ relative to the origin of coordinates may be expressed in terms of the wrapped phase $\phi_w(\mathbf{r})$, calculated from the real and imaginary signals recorded by the ADC and an integer $n(\mathbf{r})$ as

$$\phi(\mathbf{r}) = \phi_w(\mathbf{r}) + 2\pi n(\mathbf{r})$$

Eq. 4.16

Applying the Laplacian operator to both sides of Eq. 4.16 and rearranging, $n(\mathbf{r})$ may be expressed as

$$n(\mathbf{r}) = \frac{1}{2\pi}\nabla^{-2}[\nabla^2\phi(\mathbf{r}) - \nabla^2\phi_w(\mathbf{r})]$$

Eq. 4.17

Now we define a function $P(\mathbf{r})$ where

$$P(\mathbf{r}) = exp\big(i\phi_w(\mathbf{r})\big) = exp\big(i\phi(\mathbf{r}) - i2\pi n(\mathbf{r})\big)$$
$$= \frac{exp\big(i\phi(\mathbf{r})\big)}{exp(i2\pi n(\mathbf{r}))} = exp\big(i\phi(\mathbf{r})\big)$$

Eq. 4.18

First, considering a simple 1D wrapped function, $\phi(\mathbf{r}) = \phi(x)$, $\phi_w(\mathbf{r}) = \phi_w(x)$. If $P(\mathbf{r}) = \exp\big(i\phi(x)\big) = \exp(i\phi)$, then

$$\frac{\partial^2}{\partial x^2}P = \frac{\partial^2}{\partial x^2}\exp(i\phi) = \frac{\partial^2}{\partial x^2}(\cos(\phi) + i\sin(\phi))$$
$$= \frac{\partial}{\partial x}\left(-\sin(\phi)\frac{\partial\phi}{\partial x} + i\cos\frac{\partial\phi}{\partial x}\right)$$
$$= -\frac{\partial^2\phi}{\partial x^2}\sin(\phi) - \cos(\phi)\left(\frac{\partial\phi}{\partial x}\right)^2 + i\cos(\phi)\frac{\partial^2\phi}{\partial x^2}$$
$$- i\sin(\phi)\left(\frac{\partial\phi}{\partial x}\right)^2$$
$$= -\left(\frac{\partial\phi}{\partial x}\right)^2(\cos(\phi) + i\sin(\phi)) + i\frac{\partial^2\phi}{\partial x^2}(\cos(\phi) + i\sin(\phi))$$
$$= -\left(\frac{\partial\phi}{\partial x}\right)^2\exp(i\phi) + i\frac{\partial^2\phi}{\partial x^2}\exp(i\phi)$$

Eq. 4.19

and we can also write

$$\frac{1}{P}\nabla^2 P = -\exp(-i\phi)\left(\frac{\partial\phi}{\partial x}\right)^2 \exp(i\phi) + i\exp(-i\phi)\frac{\partial^2\phi}{\partial x^2}\exp(i\phi)$$
$$= \left(\frac{\partial\phi}{\partial x}\right)^2 + i\frac{\partial^2}{\partial x^2}\phi$$

Eq. 4.20

so that

$$Im\left[\frac{1}{P}\nabla^2 P\right] = \nabla^2\phi \quad .$$

Eq. 4.21

Now, if we express Eq. 4.20 and Eq. 4.21 in terms of trigonometric functions we find that

$$\frac{1}{P}\nabla^2 P = (\cos(\phi) - i\sin(\phi))(\nabla^2\cos(\phi) + \nabla^2 i\sin(\phi))$$
$$= \cos(\phi)\,\nabla^2\cos(\phi) + i\cos(\phi)\,\nabla^2\sin(\phi)$$
$$- i\sin(\phi)\,\nabla^2\cos(\phi) + \sin(\phi)\,\nabla^2\sin(\phi)$$

Eq. 4.22

and

$$Im\left[\frac{1}{P}\nabla^2 P\right] = \cos(\phi)\,\nabla^2\sin(\phi) - \sin(\phi)\,\nabla^2\cos(\phi) \quad .$$

Eq. 4.23

Using Eq. 4.18, Eq. 4.21, and Eq. 4.23 we can express the Laplacian of the unwrapped function ϕ entirely as a function of the wrapped function ϕ_w, giving

$$\nabla^2\phi = \cos(\phi_w)\,\nabla^2\sin(\phi_w) - \sin(\phi_w)\,\nabla^2\cos(\phi_w)$$

Eq. 4.24

Although we initially considered ϕ to be a one-dimensional function of x, these expressions also apply in two and three dimensions.

To unwrap MRI phase data using Eq. 4.24, we apply fast Fourier techniques exploiting the convolution theorem to apply the discrete Laplace operator, so that for arbitrary functions f and g

$$\nabla^2 f = -\frac{4\pi^2}{N^2}\,\mathrm{FFT}^{-1}\left[|\mathbf{k}|^2\mathrm{FFT}[f]\right] \quad ; \quad \nabla^{-2} g = -\frac{N^2}{4\pi^2}\,\mathrm{FFT}^{-1}\left[\frac{\mathrm{FFT}[g]}{|\mathbf{k}|^2}\right]$$

Eq. 4.25

Applying Eq. 4.25 to Eq. 4.24, we find that

$$\nabla^2\phi = -\frac{4\pi^2}{N^2}\Big(\cos(\phi_w)\,\mathrm{FFT}^{-1}\big[|\mathbf{k}|^2\mathrm{FFT}[\sin(\phi_w)]\big] - \sin(\phi_w)\,\mathrm{FFT}^{-1}\big[|\mathbf{k}|^2\mathrm{FFT}[\cos(\phi_w)]\big]\Big)$$

Eq. 4.26

and the unwrapped phase ϕ is then given by

$$\phi = \nabla^{-2}\nabla^2\phi = \mathrm{FFT}^{-1}\left[\frac{1}{|\mathbf{k}|^2}\mathrm{FFT}\left[\cos(\phi_w)\,\mathrm{FFT}^{-1}\big[|\mathbf{k}|^2\mathrm{FFT}[\sin(\phi_w)]\big] - \sin(\phi_w)\,\mathrm{FFT}^{-1}\big[|\mathbf{k}|^2\mathrm{FFT}[\cos(\phi_w)]\big]\right]\right]$$

Eq. 4.27

4.3.2 Removing Background Fields from Unwrapped Phase Data

In order to reconstruct a map of the susceptibility within the object being imaged, it is necessary to remove field perturbations generated by external sources. In the human brain, these include sources such as the lungs and the air-tissue interface at the surface of the skull. Various methods have been proposed and used to remove these fields.

A high-pass filtering approach to phase filtering was proposed by Haacke *et al* in their work on susceptibility weighted imaging (SWI), in which unwrapped and filtered phase data is used to weight the magnitude image [1]. Complex data is convolved with a Hanning window to create a low-pass filtered image, and the subsequent complex division of this into the unfiltered complex data and calculation of the phase of the result creates a high-pass filtered image. This removes slowly varying field perturbations generated by sources outside of the object, whilst mostly

preserving those generated by the local susceptibility variations. Appropriate filter width selection can be used to remove most phase wraps from the image. This method is limited, however, as it fails to discriminate properly between fields generated inside and outside of the object, and so some useful information is lost.

Another method is the projection onto dipole fields (PDF) algorithm [3, 38]. In the PDF algorithm, the measured field offset inside of the ROI is fitted to fields generated by dipolar sources outside of the ROI, and the result subtracted from the measured phase.

4.3.3 Sophisticated Harmonic Artefact Reduction for Phase Data (SHARP)

The phase filtering method used in this thesis is the sophisticated harmonic artefact reduction for phase data (SHARP) algorithm [39]. Like the phase unwrapping algorithm described above, the SHARP algorithm exploits the properties of the Laplacian operator. If the measured field perturbation is composed of fields generated by sources inside (ΔB_{int}) and outside (ΔB_{ext}) the region of interest, it can be expressed as

$$\Delta B = \Delta B_{int} + \Delta B_{ext}$$

Eq. 4.28

ΔB_{ext} is harmonic throughout the ROI, and as such it satisfies Laplace's equation throughout the ROI [40, 41], so

$$\nabla^2 \Delta B_{ext} = 0$$

Eq. 4.29

and

$$\nabla^2 \Delta B = \nabla^2 \Delta B_{int} + \nabla^2 \Delta B_{ext} = \nabla^2 \Delta B_{int} \quad .$$

Eq. 4.30

Eq. 4.30 may be solved for ΔB_{int} by exploiting the mean value property of harmonic functions [42]. This property means that a harmonic function $a(\mathbf{r})$ is unchanged by convolution with any non-negative, radially symmetric, normalised function $b(\mathbf{r})$, so that [43]:

$$a(\mathbf{r}) = b(\mathbf{r}) \otimes a(\mathbf{r})$$

Eq. 4.31

where $\otimes$ is the 3D convolution operator. This allows the elimination of harmonic components of ΔB as follows

$$\begin{aligned} \Delta\widehat{B} &= \Delta B - b(\boldsymbol{r}) \otimes \Delta B \\ &= \Delta B_{ext} + \Delta B_{int} - b(r) \otimes \Delta B_{ext} - b(r) \otimes \Delta B_{int} \\ &= \Delta B_{int} - b(r) \otimes \Delta B_{int} \end{aligned}$$

Eq.4.32

If δ is a unit impulse at the centre of a radial function, Eq. 4.32 may be re-written as

$$\begin{aligned} \Delta\widehat{B} &= \Delta B_{\text{int}} - b(\boldsymbol{r}) \otimes \Delta B_{int} \\ &= \big(\delta - b(\boldsymbol{r})\big) \otimes \Delta B_{int} \end{aligned}$$

Eq. 4.33

ΔB_{int} may then be recovered from Eq. 4.33 by deconvolution of $\Delta\widehat{B}$ with the kernel $\big(\delta - b(\boldsymbol{r})\big)$

$$\Delta B_{int} = \big(\delta - b(\boldsymbol{r})\big) \otimes^{-1} \Delta\widehat{B}$$

Eq. 4.34

In the work presented in Chapter 5, the function $b(\boldsymbol{r})$ was chosen to be a normalised sphere of radius 1.5 mm. SHARP filtering of phase data is limited by convolution artefacts at the edges of the VOI over which it is applied. However, this region can be limited to a few voxels in thickness by the appropriate choice of deconvolution kernel.

4.4 Calculation of Magnetic Susceptibility from Measured Field Perturbations

As discussed in section 4.2, the relationship between an arbitrary magnetic susceptibility distribution and the z-component of the resulting magnetic field perturbation is shown by Eq. 4.15 to be the result of a simple pointwise multiplication in the Fourier domain between the magnetisation $M_z(\mathbf{k})$ and a dipole kernel $d(\boldsymbol{k}) = 3\cos^2(\beta) - 1$, where β is the angle between $\mathbf{k}$ and the z-axis. While

this calculation is simple and well defined, inversion of this problem is ill-posed due to the presence of zeros in the Fourier-space dipole kernel where $\beta \approx 54.7°$ or $125.3°$, known as the magic angle. The susceptibility distribution $\chi(\mathbf{r})$ cannot therefore be recovered by simple deconvolution (division in the Fourier domain) of a measured field perturbation by the dipole kernel, as the inverse kernel tends to infinity at the magic angle. This division by small numbers causes severe amplification of noise and streaking artefacts in the deconvolved susceptibility map.

Quantitative susceptibility mapping is therefore reliant on the regularisation of this problem to extract meaningful information about $\chi(\mathbf{r})$. Various algorithms have been proposed to achieve this, including threshold-based k-space division methods [3, 8, 9], multiple orientation methods [2, 10], and iterative methods [4, 5, 44].

4.4.1 Quantitative Susceptibility Mapping using Threshold-based k-space Division

The simplest methods of susceptibility mapping involve the modification of the inverse dipole kernel in k-space to remove or replace regions where it approaches infinity. If a threshold parameter α is chosen, the deconvolution kernel $C(\mathbf{k}) = [d(\mathbf{k})]^{-1}$ may be set to either α [9] or 0 [3] where $|C| > \alpha$. Studies using doped agar phantoms [3] and in vivo [3, 9] and ex vivo [9] tissue show that this method can generate susceptibility maps which agree well with known object susceptibilities [3] and estimated tissue iron concentrations [3, 9]. Care must be taken in choosing the threshold parameter, however. High values of α provide more accurate susceptibility estimates, as a lower volume of k-space is excluded around the conical surfaces at the magic angle. However, this comes at the expense of amplified noise and streaking artefacts, which obscure the resulting image. Conversely, reducing α reduces artefacts, but also leads to less accurate susceptibility estimates as an increasing amount of information is lost from the image. Optimum values for α lie in the range of 2 – 5 [9] to 15 [3], with lower values being more appropriate for images with a low SNR which are more sensitive to noise amplification.

Another threshold-based approach to QSM is presented as part of the superfast dipole inversion (SDI) algorithm [8]. This algorithm was used to generate QSM data presented in Chapter 5 of this thesis, and is shown schematically in Figure 4-6. The SDI algorithm combines the Laplacian-based phase unwrapping and SHARP phase

filtering algorithms described in Sections 4.3.2 and 4.3.3 with thresholded k-space division using a modified dipole kernel. The modified dipole kernel is defined such that

$$d'(\mathbf{k}) = \begin{cases} \frac{1}{3} & d(\mathbf{k}) > 0 \\ -\frac{2}{3} & d(\mathbf{k}) < 0 \end{cases}$$

Eq. 4.35

This modified kernel can now be used to generate an inverse kernel $C'(\mathbf{k}) = d'(\mathbf{k})^{-1}$ which is well defined for all $\mathbf{k}$. The application of this dipole modification introduces a point spread function (PSF) whose effects must be corrected. The correction factor may be calculated by the inversion of a simulated field map due to a delta function at the origin of coordinates, and deconvolution of this by the modified dipole kernel. The degree to which this function is underestimated in the calculated susceptibility map gives the correction factor which must be applied to all data calculated using this method. This algorithm produces susceptibility maps which have slightly increased noise, but relatively good agreement with images generated using the gold-standard COSMOS algorithm [2], described in section 4.4.2.

4.4.2 Calculation of Susceptibility through Multiple Orientation Sampling (COSMOS)

The COSMOS algorithm [2] stabilises the inversion problem using data acquired with the susceptibility distribution at multiple orientations to B_0, thus allowing the entirety of k-space to be sampled and represented in the resulting susceptibility map. If k-space coordinates are defined in the frame of reference of the object, and the object is imaged at N angles produced by rotations about the x-axis in the frame of reference of the scanner, Eq. 4.15 becomes [2]

$$\begin{bmatrix} \left(\frac{1}{3} - \frac{\left(k_z \cos(\theta_1) + k_y \sin(\theta_1)\right)^2}{k^2}\right) \\ \left(\frac{1}{3} - \frac{\left(k_z \cos(\theta_2) + k_y \sin(\theta_2)\right)^2}{k^2}\right) \\ \vdots \\ \left(\frac{1}{3} - \frac{\left(k_z \cos(\theta_N) + k_y \sin(\theta_N)\right)^2}{k^2}\right) \end{bmatrix} \cdot M(\mathbf{k}) = \begin{bmatrix} \Delta B_1 \\ \Delta B_2 \\ \vdots \\ \Delta B_N \end{bmatrix}$$

Eq. 4.36

Direct inversion of this expression in k-space is possible so long as no nonzero element exists in $\left(1/3 - k_{axis_N}^2/k^2\right)$, $n = 1, 2, \ldots, N$. A set of angles $\theta_1, \ldots, \theta_N$ which satisfy this condition exist for every point in k-space when $N \geq 3$ [2]. An exception to this solution exists at the origin of coordinates, where the dipole kernel is not defined, however this point may simply be set to zero in the inversion as it only defines a constant offset in the image. The best results from COSMOS are achieved when $\theta_1/\theta_2/\theta_3 = -60°/0°/60°$ [2]. While COSMOS allows the complete sampling of k-space, and so provides a gold standard for QSM calculations,

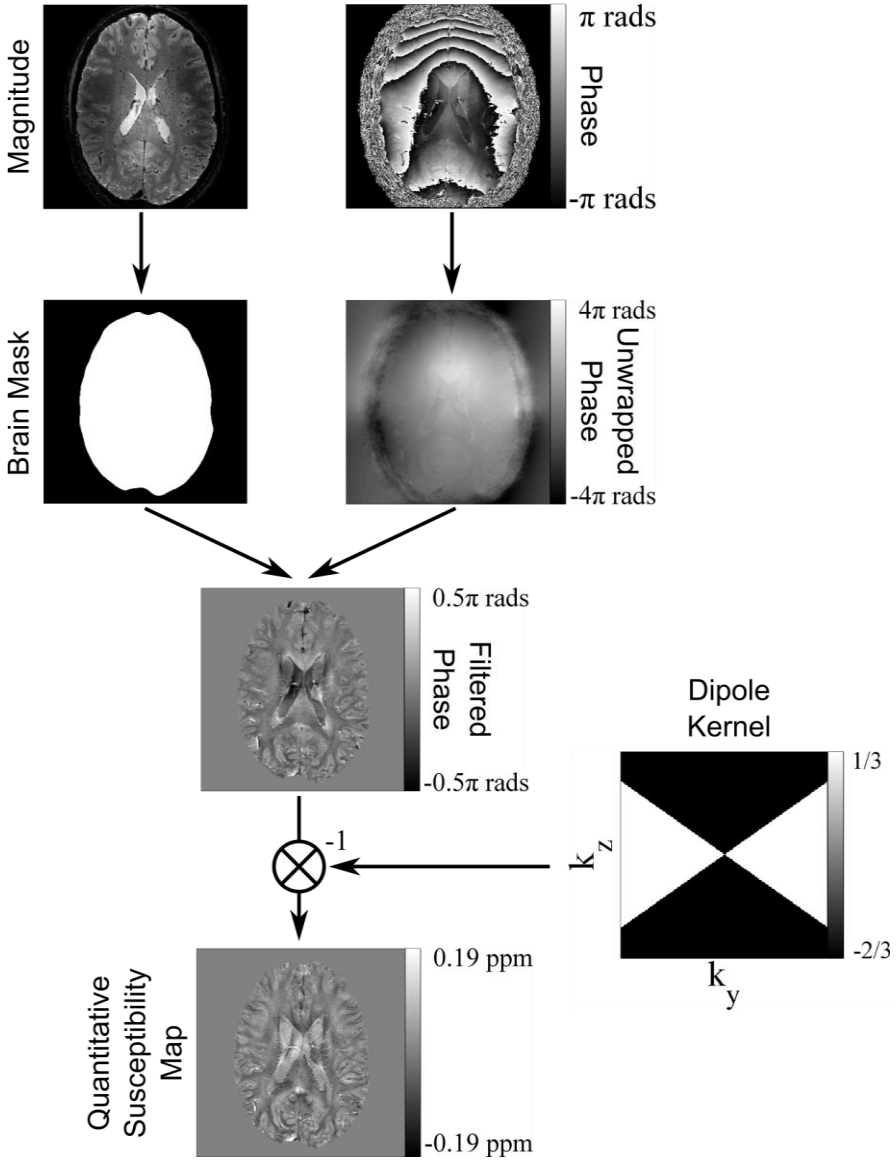

Figure 4-6 – Schematic representation of QSM processing using Laplacian unwrapping, SHARP filtering and deconvolution with the modified dipole kernel proposed in [1].

it is impractical in many applications, particularly *in vivo*, due to the need for multiple image acquisitions and large rotations which may be uncomfortable or impractical for the subject to perform. The required range of motion may be reduced by making combined rotations about the x- and y-axes [3]. While COSMOS remains impractical in many experimental settings, it provides a useful standard against which other single-acquisition based QSM algorithms may be compared [3, 5, 8, 10].

4.4.3 Quantitative Susceptibility Mapping using Iterative Inversion Methods

Alternatives to QSM by direct k-space inversion of the fast forward calculation exist in the form of iterative methods. These methods involve applying the forward calculation to guessed solutions of the susceptibility distribution, comparing this result to the measured field perturbation and adjusting the guess based on this comparison to yield a more accurate result.

A simple iterative solution to the QSM inversion involves the solution of a least-squares minimisation of the form

$$\min_x \|Ax - b\|^2$$

Eq. 4.37

where b is the measured data, x is the unknown quantity, A is a matrix representing an operation, and $\|...\|$ is the Euclidian or L2 norm given by

$$\|y\| = \sqrt{\sum_{i=1}^{n} (y_i)^2}$$

Eq. 4.38

In QSM Eq. 4.37 takes the form

$$\min_\chi \|C\chi - \Delta B\|^2$$

Eq. 4.39

where

$$C\chi(\mathbf{r}) = \text{FFT}^{-1}\left(d(\mathbf{k}) \cdot \text{FFT}\left(\chi(\mathbf{r})\right)\right)$$

Eq. 4.40

In problems where Ax is a simple pointwise multiplication, Eq. 4.37 may be solved by single value decomposition [45] or application of the Moore-Penrose pseudo inversion [46] to A. However in QSM, the operation in question is a 3D convolution over a sizeable matrix (400 x 400 x 200 points for both the kernel and image for a 200 x 200 x 100 mm volume imaged at 0.5 mm isotropic resolution) making such a direct inversion extremely computationally inefficient, and impractical in most settings. Other algorithms must therefore be used, such as the conjugate gradient method [47], which only require knowledge of the product Ax rather than the explicit form of A.

Morphology enabled dipole inversion (MEDI) [5, 48] is a more complicated iterative QSM algorithm involving a weighted L1 norm or least absolute errors (LAE) minimisation based on spatial priors derived from the magnitude image. MEDI assumes that uniform-appearing tissue compartments in the T_2^*-weighted magnitude image most likely correspond to regions of uniform magnetic susceptibility. This assumption is expressed in the MEDI algorithm by the minimization of the number of edges in the QSM that do not exist in the magnitude image. A structural weighting matrix M is derived from the gradient of the magnitude, and is given by

$$M = \begin{cases} 0 & |Gm| \geq \mu \\ 1 & |Gm| < \mu \end{cases}$$

Eq. 4.41

where m is the magnitude image, G is the gradient operator and μ is a threshold parameter related to the image noise level. The MEDI L1 norm minimisation is then given by

$$\min_{\chi} \|MG\chi\|_1 \quad \text{subject to} \quad \|W(C\chi - \Delta B)\|_2^2 \leq \varepsilon$$

Eq. 4.42

where W is a weighting matrix proportional to the signal magnitude to compensate for noise variation in ΔB, and ε is the noise power used to control the fidelity of the reconstruction to the data.

MEDI has been used in a number of QSM applications, including the investigation of multiple sclerosis [16], intracranial calcifications and haemorrhages [49], cerebral microbleeds [50] and iron quantification [51].

4.5 References

1. Haacke, E.M., et al., *Susceptibility weighted imaging (SWI).* Magnetic resonance in medicine : official journal of the Society of Magnetic Resonance in Medicine / Society of Magnetic Resonance in Medicine, 2004. **52**: p. 612-8.
2. Liu, T., et al., *Calculation of susceptibility through multiple orientation sampling (COSMOS): a method for conditioning the inverse problem from measured magnetic field map to susceptibility source image in MRI.* Magnetic resonance in medicine : official journal of the Society of Magnetic Resonance in Medicine / Society of Magnetic Resonance in Medicine, 2009. **61**: p. 196-204.
3. Wharton, S., A. Schäfer, and R. Bowtell, *Susceptibility mapping in the human brain using threshold-based k-space division.* Magnetic resonance in medicine : official journal of the Society of Magnetic Resonance in Medicine / Society of Magnetic Resonance in Medicine, 2010. **63**: p. 1292-304.
4. de Rochefort, L., et al., *Quantitative susceptibility map reconstruction from MR phase data using bayesian regularization: validation and application to brain imaging.* Magnetic resonance in medicine : official journal of the Society of Magnetic Resonance in Medicine / Society of Magnetic Resonance in Medicine, 2010. **63**: p. 194-206.
5. Liu, T., et al., *Morphology enabled dipole inversion (MEDI) from a single-angle acquisition: Comparison with COSMOS in human brain imaging.* Magnetic Resonance in Medicine, 2011. **66**(3): p. 777-783.
6. Li, W., B. Wu, and C. Liu, *Quantitative susceptibility mapping of human brain reflects spatial variation in tissue composition.* NeuroImage, 2011. **55**: p. 1645-56.
7. Tang, J., et al., *Improving susceptibility mapping using a threshold-based K-space/image domain iterative reconstruction approach.* Magnetic Resonance in Medicine, 2013. **69**(5): p. 1396-1407.
8. Schweser, F., et al., *Toward online reconstruction of quantitative susceptibility maps: Superfast dipole inversion.* Magnetic Resonance in Medicine, 2013. **69**(6): p. 1581-1593.
9. Shmueli, K., et al., *Magnetic susceptibility mapping of brain tissue in vivo using MRI phase data.* Magnetic resonance in medicine : official journal of the Society of Magnetic Resonance in Medicine / Society of Magnetic Resonance in Medicine, 2009. **62**: p. 1510-22.
10. Wharton, S. and R. Bowtell, *Whole-brain susceptibility mapping at high field: a comparison of multiple-and single-orientation methods.* NeuroImage, 2010. **53**(2): p. 515-525.
11. Wharton, S. and R. Bowtell, *Fiber orientation-dependent white matter contrast in gradient echo MRI.* Proc Natl Acad Sci U S A, 2012. **109**(45): p. 18559-64.
12. Schweser, F., et al., *Quantitative imaging of intrinsic magnetic tissue properties using MRI signal phase: an approach to in vivo brain iron metabolism?* NeuroImage, 2011. **54**: p. 2789-807.

13. Deistung, A., et al., *Toward in vivo histology: A comparison of quantitative susceptibility mapping (QSM) with magnitude-, phase-, and* R2* *imaging at ultra-high magnetic field strength.* NeuroImage, 2013. **65**: p. 299-314.

14. Argyridis, I., et al., *Quantitative magnetic susceptibility of the developing mouse brain reveals microstructural changes in the white matter.* NeuroImage, 2014. **88**: p. 134-142.

15. Al-Radaideh, A.M., et al., *Increased iron accumulation occurs in the earliest stages of demyelinating disease: an ultra-high field susceptibility mapping study in Clinically Isolated Syndrome.* Multiple Sclerosis Journal, 2012, 19(7), 896-903.

16. Langkammer, C., et al., *Quantitative Susceptibility Mapping in Multiple Sclerosis.* Radiology, 2013.

17. Chen, W., et al., *Quantitative Susceptibility Mapping of Multiple Sclerosis Lesions at Various Ages.* Radiology, 2013. **271**(1): p. 183-192.

18. Eskreis-Winkler, S., et al., *Multiple sclerosis lesion geometry in quantitative susceptibility mapping (QSM) and phase imaging.* Journal of Magnetic Resonance Imaging, 2014. DOI: 10.1002/jmri.24745

19. Wisnieff, C., et al., *Quantitative susceptibility mapping (QSM) of white matter multiple sclerosis lesions: Interpreting positive susceptibility and the presence of iron.* Magn Reson Med, 2014. DOI: 10.1002/mrm.25420

20. Rudko, D.A., et al., *Multiple Sclerosis: Improved Identification of Disease-relevant Changes in Gray and White Matter by Using Susceptibility-based MR Imaging.* Radiology, 2014. **272**(3): p. 851-864.

21. Jackson, J., *Classical Electrodynamics Third Edition*. 1998: Wiley.

22. Bhagwandien, R., et al., *Numerical analysis of the magnetic field for arbitrary magnetic susceptibility distributions in 2D.* Magnetic Resonance Imaging, 1992. **10**(2): p. 299-313.

23. Bhagwandien, R., et al., *Numerical analysis of the magnetic field for arbitrary magnetic susceptibility distributions in 3D.* Magnetic Resonance Imaging, 1994. **12**(1): p. 101-107.

24. Li, S., et al., *Three-dimensional mapping of the static magnetic field inside the human head.* Magnetic Resonance in Medicine, 1996. **36**(5): p. 705-714.

25. Collins, C.M., et al., *Numerical calculations of the static magnetic field in three-dimensional multi-tissue models of the human head.* Magnetic Resonance Imaging, 2002. **20**(5): p. 413-424.

26. Truong, T.-K., et al., *Three-dimensional numerical simulations of susceptibility-induced magnetic field inhomogeneities in the human head.* Magnetic Resonance Imaging, 2002. **20**(10): p. 759-770.

27. Jenkinson, M., J.L. Wilson, and P. Jezzard. *Perturbation calculation of B0 field for non-conducting materials*. in *Proc. Int. Soc. of Magnetic Resonance in Medicine*. 2002.

28. Jenkinson, M., J.L. Wilson, and P. Jezzard, *Perturbation method for magnetic field calculations of nonconductive objects.* Magnetic Resonance in Medicine, 2004. **52**(3): p. 471-477.

29. Marques, J.P. and R. Bowtell, *Application of a Fourier-based method for rapid calculation of field inhomogeneity due to spatial variation of magnetic susceptibility.* Concepts in Magnetic Resonance Part B: Magnetic Resonance Engineering, 2005. **25B**: p. 65-78.

30. Salomir, R., B.D. de Senneville, and C.T.W. Moonen, *A fast calculation method for magnetic field inhomogeneity due to an arbitrary distribution of bulk susceptibility.* Concepts in Magnetic Resonance Part B: Magnetic Resonance Engineering, 2003. **19B**(1): p. 26-34.

31. Lorentz, H.A., *The theory of electrons and its applications to the phenomena of light and radiant heat*. Vol. 29. 1916: BG Teubner.

32. Dickinson, W., *The time average magnetic field at the nucleus in nuclear magnetic resonance experiments.* Physical Review, 1951. **81**(5): p. 717.

33. Chu, K., et al., *Bulk magnetic susceptibility shifts in NMR studies of compartmentalized samples: use of paramagnetic reagents.* Magnetic Resonance in Medicine, 1990. **13**(2): p. 239-262.

34. Robinson, S., et al., *Combining phase images from multi-channel RF coils using 3D phase offset maps derived from a dual-echo scan.* Magnetic Resonance in Medicine, 2011. **65**(6): p. 1638-1648.

35. Jenkinson, M., *Fast, automated, N-dimensional phase-unwrapping algorithm.* Magnetic Resonance in Medicine, 2003. **49**(1): p. 193-197.

36. Wharton, S., *Susceptibility Mapping in High Field MRI*. 2011. p. 190.

37. Schofield, M.A. and Y. Zhu, *Fast phase unwrapping algorithm for interferometric applications.* Optics letters, 2003. **28**(14): p. 1194-1196.

38. Liu, T., et al., *A novel background field removal method for MRI using projection onto dipole fields (PDF).* NMR in biomedicine, 2011: p. 1129-1136.

39. Schweser, F., et al., *Quantitative imaging of intrinsic magnetic tissue properties using MRI signal phase: An approach to in vivo brain iron metabolism?* NeuroImage, 2011. **54**(4): p. 2789-2807.

40. Li, L. and J.S. Leigh, *High-precision mapping of the magnetic field utilizing the harmonic function mean value property.* Journal of magnetic resonance, 2001. **148**(2): p. 442-448.

41. Li, L. and J.S. Leigh, *Quantifying arbitrary magnetic susceptibility distributions with MR.* Magnetic Resonance in Medicine, 2004. **51**(5): p. 1077-1082.

42. Roy, K.K., *Green's Theorem in Potential Theory*, in *Potential Theory in Applied Geophysics*. 2008, Springer. p. 307-327.

43. Kim, J. and M. Wong, *Invariant mean value property and harmonic functions.* Complex Variables, Theory and Application: An International Journal, 2005. **50**(14): p. 1049-1059.

44. Kressler, B., et al., *Nonlinear regularization for per voxel estimation of magnetic susceptibility distributions from MRI field maps.* Medical Imaging, IEEE Transactions on, 2010. **29**(2): p. 273-281.

45. Golub, G.H. and C. Reinsch, *Singular value decomposition and least squares solutions.* Numerische Mathematik, 1970. **14**(5): p. 403-420.

46. Penrose, R. and J.A. Todd. *On best approximate solutions of linear matrix equations*. in *Mathematical Proceedings of the Cambridge Philosophical Society*. 1956. Cambridge Univ Press.

47. Hestenes, M.R. and E. Stiefel, *Methods of conjugate gradients for solving linear systems.* 1952.

48. Liu, J., et al., *Morphology enabled dipole inversion for quantitative susceptibility mapping using structural consistency between the magnitude image and the susceptibility map.* NeuroImage, 2012. **59**(3): p. 2560-2568.

49. Chen, W., et al., *Intracranial calcifications and hemorrhages: characterization with quantitative susceptibility mapping.* Radiology, 2014. **270**(2): p. 496-505.

50. Liu, T., et al., *Cerebral microbleeds: burden assessment by using quantitative susceptibility mapping.* Radiology, 2012. **262**(1): p. 269-278.

51. Lim, I.A.L., et al., *Human brain atlas for automated region of interest selection in quantitative susceptibility mapping: application to determine iron content in deep gray matter structures.* NeuroImage, 2013. **82**: p. 449-469.

5 A COMPARISON OF PHASE IMAGING AND QUANTITATIVE SUSCEPTIBILITY MAPPING OF MULTIPLE SCLEROSIS LESIONS AT 7T

In vivo quantification of brain tissue properties is increasingly of interest in the investigation of neurodegenerative diseases, particularly due to the changes in the chemical and structural composition of brain tissue associated with such disease pathologies. The inherent sensitivity of MRI to such changes makes it a powerful tool in the diagnosis and investigation of such conditions, however it is important to understand the strengths and limitations of specific imaging protocols and techniques in order to be able to draw reliable inferences and measurements from data.

A prominent application of MRI in neurological research is the diagnosis and investigation of multiple sclerosis (MS). T_2^*-weighted gradient echo sequences are often used to study MS due to the high signal to noise ratio (SNR) and good contrast [1-10] that they provide. With the increasing availability of high and ultra-high field

MRI systems, the phase data associated with the T2*-weighted magnitude images are increasingly being used both as an adjunct to conventional magnitude images [10-13], or in combination with them to produce susceptibility-weighted (SWI) images [7, 14, 15], as they provide a complimentary contrast mechanism.

In recent years, phase and SWI images have been used to study the variation in iron levels in different anatomical brain regions with age and gender [13, 16], as well as changes in iron levels in MS [3, 7, 10]. However, the use of phase contrast as a qualitative or quantitative measure of iron content assumes a direct relationship between signal phase and local iron levels. This assumption is flawed since a magnetic susceptibility perturbation, such as a local increase in iron concentration, produces a change in the magnetic field (and hence phase) that is not localised to the susceptibility perturbation, but instead is dipolar in nature, causing both positive and negative field/phase perturbations in the surrounding region [14]. This effect can lead to incorrect inferences being drawn about local iron levels based on phase or SWI images. The non-local nature of the phase contrast can be overcome by the application of quantitative susceptibility mapping (QSM) [17-19] algorithms to the data, producing maps of the local variations in the bulk susceptibility of the tissue that are responsible for the measured phase changes. The QSM technique has, amongst other applications, been used *in vivo* to measure changes in the magnetic susceptibility of the basal ganglia in MS patients [1, 2]. While these techniques offer a local contrast directly linked to the physical property of magnetic susceptibility, they rely on accurate measurement of the local field perturbations originating only within the imaging volume. For this reason, care must still be taken in the choice of filtering algorithms and parameters for processing of the phase data.

The white matter lesions occurring in MS are sometimes surrounded by rings on T_2^*-weighted magnitude and phase images and it has been suggested that these rings may be a marker of local changes in iron content [5, 7, 10]. However, this MR signature could also result from a local variation of the myelin density, or even from changes in tissue microstructure [20], and so the origin of peripheral rings remains a matter of some debate. The ability to detect iron changes around lesions would be useful in understanding the pathogenesis of MS lesions and in tracking disease progression. In previous work, phase and SWI images have been used to investigate the prevalence and nature of peripheral rings in MS lesions [3, 7, 10].

The aim of the work described here was to compare the depiction of white matter MS lesions in high resolution (0.5 mm, isotropic) phase and QSM images. The prevalence of peripheral rings was measured across a cohort of 39 MS patients in order to compare the effectiveness of phase and QSM images in such identification. More detailed analysis was applied to a subset of 6 lesions with peripheral rings, in order to establish the sources of the contrast in each image type, including comparison of the effects of SHARP and high-pass (SWI) phase filtering algorithms on phase and QSM contrast. Simulated field maps were generated for models of a solid and shell-like susceptibility distribution based on one lesion, in order to illustrate the field patterns that such structures produce.

5.1 Methods

5.1.1 Data Acquisition

Data were drawn from previous studies conducted at the Sir Peter Mansfield Imaging Centre (SPMIC) investigating the prevalence of central veins in white matter lesions, and iron deposition in the deep grey matter in multiple sclerosis. These studies were led by Dr Nikos Evangelou and Dr Cris Constantinescu at the SPMIC Queen's Medical Centre site, and Professor Penny Gowland at the SPMIC University Park site. To acquire the data used in this study, 39 patients with multiple sclerosis were scanned using a Philips Achieva 7T system equipped with a either a 16 or 32 channel receiver head coil. Different head coils were used as the system hardware was upgraded during the period over which these data were acquired. Data for susceptibility mapping were acquired using a multi-stack, spoiled 3D T_2^*-weighted. FLASH sequence with 4 stacks, overlapping by 10 voxels at each interface, and 0.5 mm isotropic resolution (TE=20 ms, TR=150 ms, FOV=196x164x85 mm^3, EPI factor=3, SENSE factor=2). As the imaging protocol was designed several years before the inception of the study presented here, and so without regard for the most up-to-date practices in the field of QSM, these images were acquired with a single echo rather than the multi-echo acquisitions often used to calculate MRI signal frequency. MPRAGE images were acquired for segmentation at 0.6x0.5x0.6 mm^3 resolution and reconstructed at 0.5 mm isotropic resolution (TE=5.89 ms, TR=15 ms, TI= 1186 ms, shot interval = 3000 ms, FOV=192x156x163.2 mm^3, SENSE factor=2).

5.1.2 Lesion Selection

In order to establish the prevalence of peripheral rings in the cohort, up to 11 WM lesions were identified by the author on the axial T_2^*-weighted magnitude images for each subject. Binary masks were generated using MRIcro (www.mricro.com), identifying an approximately central voxel in lesions as images were viewed in the axial plane starting at the top of the head. In total, 305 lesions were identified in the 39 subjects. In addition, 6 well-isolated lesions with peripheral rings in the axial phase images were identified in 4 subjects for more detailed analysis.

5.1.3 Image Processing

For all subjects, the T_2^*-weighted magnitude and phase images from the 4 stacks were merged using software written in-house in MATLAB (Mathworks Inc., Massachusetts, USA). As the signal to noise ratio is worst at the edge of the stack, the overlapping regions were combined using a linearly-weighted sum, so that

$$w = exp(-n^2/20) \quad ,$$

$$M_{merged}(n) = \frac{\left(w(n) \times M_{st1}(n) + w(11-n) \times M_{st2}(n)\right)}{w(n) + w(11-n)} \quad ,$$

$$P_{merged} = arctan\left(\frac{Re\left(w(n) \times e^{i \times p_{st1}(n)} + w(n) \times e^{i \times p_{st2}(n)}\right)}{Im(w(n) \times e^{i \times p_{st1}(n)} + w(n) \times e^{i \times p_{st2}(n)})}\right) \quad .$$

Eq. 5.1

Here, n is the number of the slice in the overlapping region of each stack counting from the edge of the stack in the overlapping region; w is a weighting factor; $M_{merged}(n)$ and $P_{merged}(n)$ are the magnitude and phase in the merged slice; $M_{st1}(n)$ and $P_{st1}(n)$ are the signal magnitude and phase in the n^{th} slice from the top of the head in the overlapping region in the upper stack (closest to the top of the head), and $M_{st1}(n)$ and $P_{st1}(n)$ are the signal magnitude and phase in the first slice in the overlapping region from the top of the volume in the lower stack (closest to the feet).

5.1.3.1 Phase Data Processing

For all subjects, the phase data were first unwrapped using the Laplacian-based method [21, 22] described in Chapter 4. A binary brain mask was generated from the T_2^*-weighted magnitude data using the brain extraction tool (BET) in FSL [23]. This

mask was then zero-padded with 8 voxels at each edge and eroded to ensure the exclusion of unreliable phase data from outside of the brain after which padding was removed. Mask erosion was carried out using two iterations of Matlab's imerode tool using a 3x3x3 voxel erosion kernel. Background fields from sources outside of the brain were removed using the SHARP algorithm [18] described in section 4.3.3, using a spherical SHARP kernel with a radius of 3 voxels (1.5 mm) and a truncation value of 0.015. Each element of the SHARP kernel was set to 1, with the exception of the voxel at the origin which was set to 0. The kernel was then normalized so that the sum of its elements was equal to 1.

Additionally, the phase images from the 4 subjects from whom lesions were selected for more detailed analysis were unwrapped and filtered slice by slice in 2D using a standard high-pass filtering algorithm employed in SWI processing [24]. Low-pass filtered phase images were created by constructing a 2D square Hanning window in k-space. The original phase images were then complex-divided by the low pass filtered data to create unwrapped, high-pass filtered images. In order to establish the optimum filter width for this data, one dataset was processed using filter widths of 0.063, 0.094, 0.125 and 0.199 (using the definition described by Walsh and Wilman [25]), and a filter width of 0.094 was chosen as a compromise between maximising the removal of the effects of background fields from the data while preserving as much structural contrast as possible.

5.1.3.2 Quantitative Susceptibility Mapping

In this study, quantitative susceptibility mapping was carried out using the threshold-based k-space division method [26, 27] using the modified dipole kernel from the superfast dipole inversion algorithm [28], described in section 4.4.1. The SHARP-filtering and QSM formation is described schematically in Figure 4-6. The TKD method was chosen as rotation of the head was impractical in a patient study, making the COSMOS algorithm [19] unsuitable. Also, since there is no clear consensus regarding the nature of the susceptibility offsets associated with MS lesions and their consistency with the magnitude data, the spatial constraints enforced by the MEDI algorithm [29, 30] were not appropriate for this study.

Quantitative susceptibility maps for all subjects were calculated from the SHARP filtered phase data. The data were Fourier transformed and divided in k-space by the modified Fourier domain dipole kernel $\tilde{d}(\boldsymbol{k})$, where

$$\tilde{d}(\boldsymbol{k}) = \frac{1}{3} \quad [d(\boldsymbol{k}) \geq 0]$$

$$\tilde{d}(\boldsymbol{k}) = -\frac{2}{3} \quad [d(\boldsymbol{k}) < 0]$$

Eq. 5.2

and $d(\boldsymbol{k})$ represents the unmodified dipole kernel defined in Eq. 4.7. The result was then inverse Fourier transformed to yield a susceptibility map. Finally, the map was divided by a correction factor of 0.502 to compensate for the global underestimation inherent in this inversion method [28]. This QSM method was computationally efficient, taking approximately 1 minute to run on a PC (3.1 GHz Intel Core i3, 4GB RAM, 64-bit Linux OS) including the unwrapping and filtering steps described above.

QSM data were also generated using the high-pass filtered phase images containing the lesions identified for detailed analysis using the same method described above.

5.1.3.3 Whole Cohort Lesion Analysis

Following QSM processing, the lesions identified across all subjects were examined in the axial, sagittal and coronal planes intersecting the voxel marked in the T_2^*-weighted magnitude, SHARP-filtered phase and QSM images. Lesions were not examined in the high-pass filtered phase images, as SHARP-filtered phase gives a more accurate representation of the fields generated within the ROI. The appearance of lesions in the phase and QSM images was classified as either (i) showing hyperintense contrast relative to normal appearing white matter (NAWM) with a hyperintense peripheral ring, (ii) showing hyperintense contrast relative to NAWM without a peripheral ring, (iii) showing no contrast, or (iv) as unclassifiable. It was additionally noted if there was a distinguishable external dipolar pattern surrounding the lesion.

5.1.3.4 Detailed Individual Lesion Analysis

In addition to the visual analysis described above, the six well-isolated individual lesions were further assessed in each image type by the generation of 1D profiles of

mean voxel intensity in the lesion and surrounding white matter (WM). This process is shown in Figure 5-1. MPRAGE images were coregistered onto the T_2^*-weighted magnitude images using FLIRT in FSL. Lesion masks were drawn on the T_2*-weighted images, and white matter masks were drawn on MPRAGE images, using MRIcro. To ensure consistent lesion edges, the lesion was counted as white matter when drawing the WM mask, and the lesion mask was later subtracted from this. Profiles of the mean voxel intensity in the WM and in the lesion as a function of radial distance to the nearest point on the edge of the lesion mask were generated by convolution of the voxels in the ROIs with a spherical kernel whose elements were set to the radial distance of the voxel from the centre of the sphere, rounded to the nearest integer.

The distance of each voxel was set to the value of the kernel element that overlapped with the lesions mask (for voxels outside of the lesion) or WM mask (for voxels inside of the lesion). for T_2^*-weighted magnitude images, phase images and susceptibility maps (generated from both SHARP and high-pass filtered phase) using code written in-house in MATLAB. The magnitude data were normalized to the mean voxel intensity 3 mm from the lesion edge.

The QSM and phase images were normalized relative to the susceptibility and phase value in CSF averaged over two 6x6x10 voxel ROIs, one placed centrally in each ventricle.

One lesion was used as a model to simulate the effect of a relevant susceptibility distribution on phase distortion. For that lesion, masks of the peripheral ring and of its central core were created from the magnitude image data. These masks were assigned a nominal susceptibility of 0.15 ppm (the approximate magnitude of voxels in the ring in the QSM image of the lesion relative to the surrounding white matter) and the phase shifts caused by the resulting susceptibility distributions were modelled using the Fourier method [31]. The images were then processed with both high-pass and SHARP filtering methods to allow qualitative comparison with the measured phase shift patterns, and the SHARP filtered phase shift was inverted to form a susceptibility map using the TKD method.

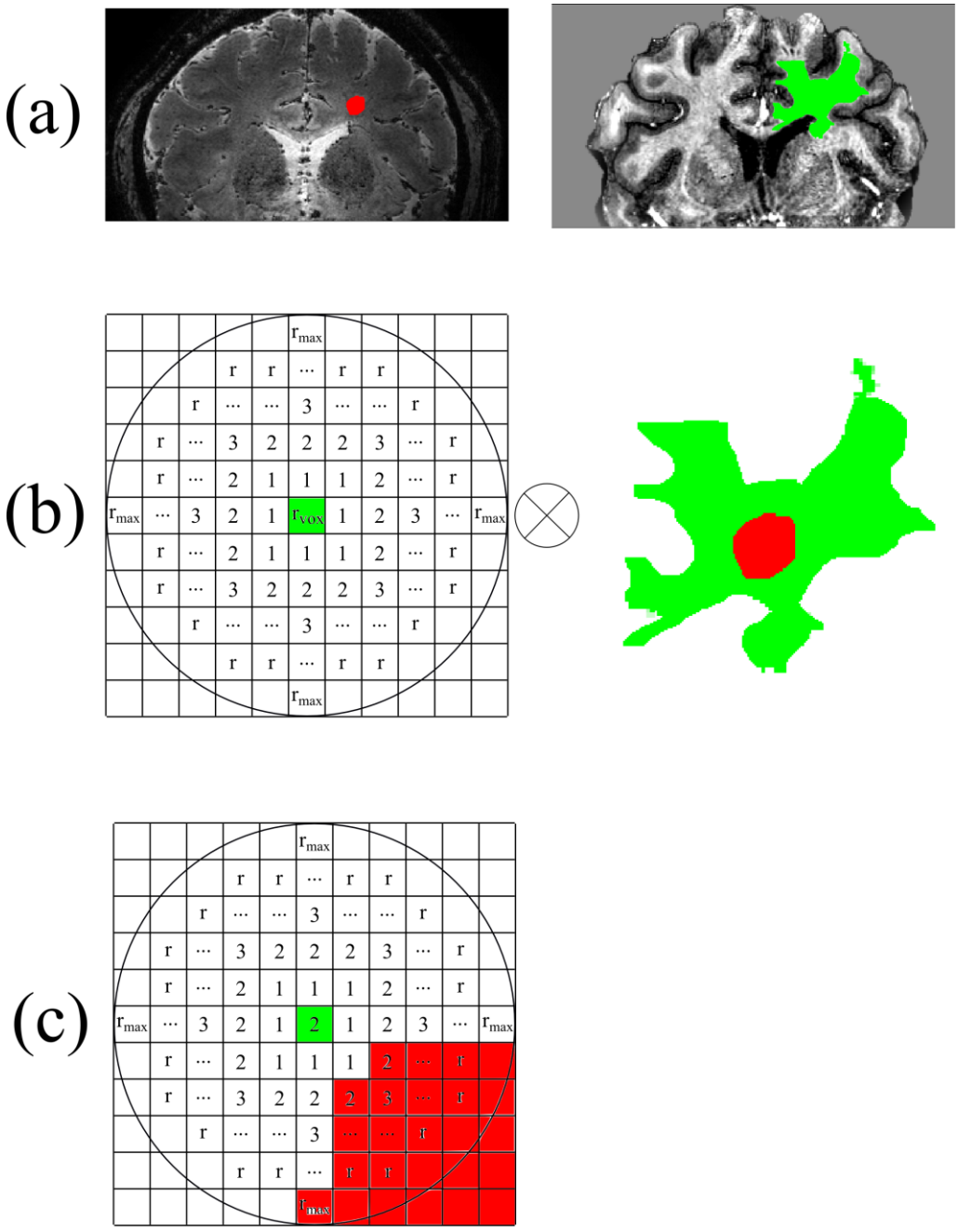

Figure 5-1 – Voxelwise distance mapping was carried out by: (a) Masking of the lesion on the T_2^*-weighted magnitude image and surrounding white matter on the MPRAGE; (b) Convolution of the masked region with a 3D radial distance kernel; (c) allocation of an integer distance value to each voxel in the

5.2 Results

5.2.1 Optimisation of Hanning Window Width for Phase Unwrapping and Filtering

Figure 5-2 shows phase images of a WM lesion with visible external dipolar contrast, unwrapped using a Laplacian-based method with no filter applied in the top row, and unwrapped and filtered using a Hanning window with filter widths of 0.063, 0.094, 0.125 and 0.199 in the remaining rows. The external dipolar contrast is clearly present in the unfiltered image; however most of the image is dominated by the large, slowly varying fields generated by field sources outside of the brain. As the filter width increases, the filtered images show remaining phase wraps visible on the right hand side of the axial and coronal images, as well as an overall flattening of the image and reduction in the visible external dipolar contrast as the range of spatial frequencies attenuated in the image increases.

5.2.2 Visual Analysis of White Matter Lesions with Peripheral Rings

Figures 5-3, 5-4 and 5-5 show different individual WM lesions in magnitude, SHARP filtered (SF) and high-pass filtered (HF) phase images, along with the corresponding susceptibility maps, for axial, sagittal and coronal slices cutting through the centre of the lesion. In the axial plane, the SF images display hyper-intense rings at the periphery of the lesion, consistent with the boundaries seen in the magnitude images. In Figures 5-3 and 5-4, the ring in the axial SF image is surrounded by a distinct, hypo-intense region located outside of the lesion. In the sagittal and coronal planes, the dipolar nature of the field perturbation underlying the phase contrast due to the lesion is more apparent. Figure 5-5 shows an example of a lesion with a less distinct boundary in the magnitude image. In the SF image, the dipole field is still present, and the hyper-intense periphery is also evident in the susceptibility map. However these features are less visually striking than in Figures 5-2 and 5-3. Dipolar patterns in the phase are observed around all three lesions, extending significantly beyond the boundaries of the lesions observed in the magnitude images, as indicated by arrows. The intensity of these patterns is reduced in the HF images compared to the SF images due to the effect of the high-pass spatial filtering. The susceptibility maps show hyper-intense rings at the lesion boundaries in all 3 planes, without significant external offsets.

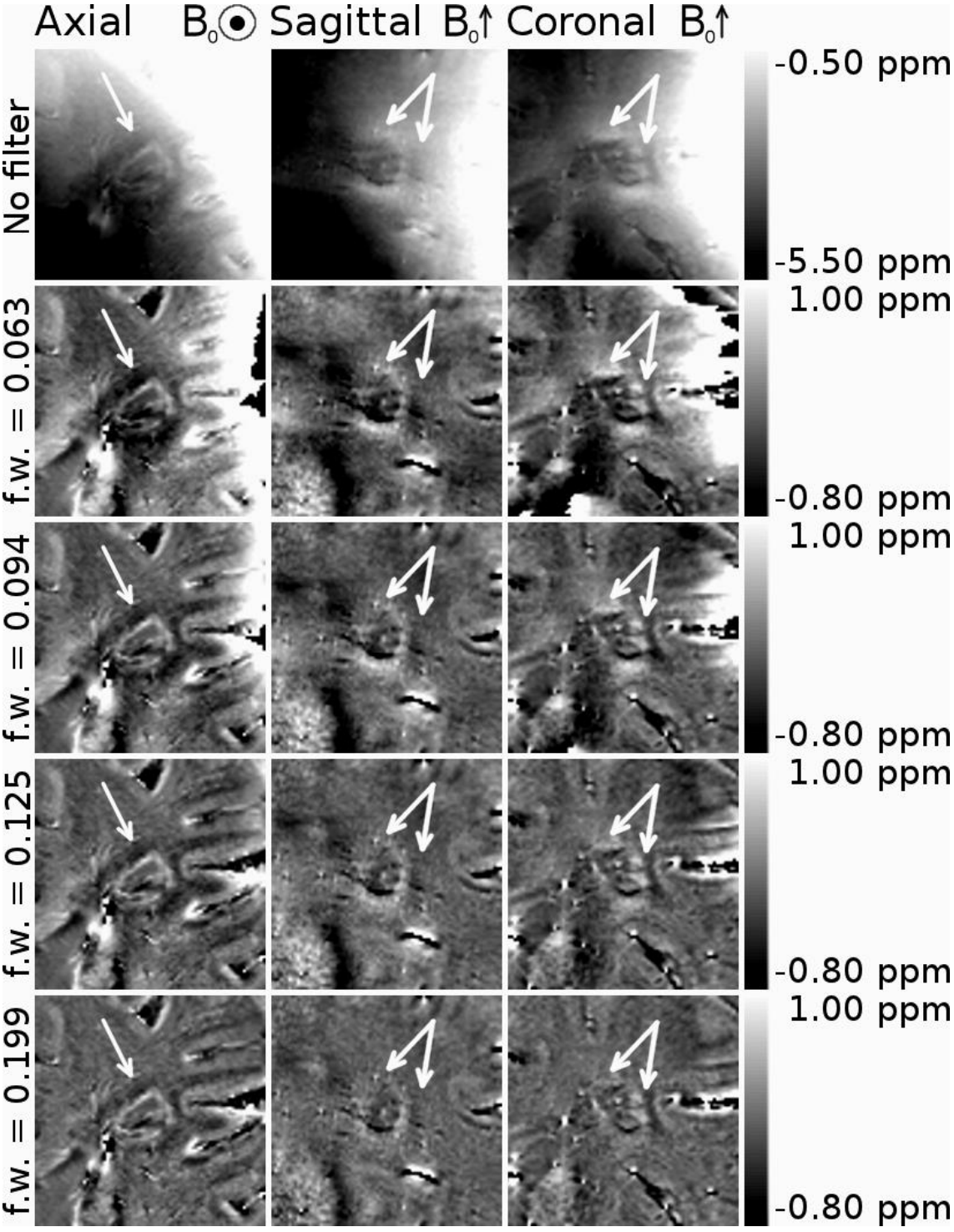

Figure 5-2 – Phase images of a white matter MS lesion with a peripheral ring and visible external dipolar pattern (indicated by the white arrows). The raw, wrapped phase image is shown, along with images that have been filtered in k-space using Hanning windows with widths of 0.063, 0.094 0.125 and 0.199.

The presence of material with heterogeneous paramagnetic susceptibility is evident inside the lesions from the hyper-intensity seen in the susceptibility maps although this feature is slightly less prominent in Figure 5-5.

Figure 5-3 also shows images of an additional axial slice located above the lesion. The magnitude image of this slice shows only normal-appearing white matter, while in the SF and HF images, a hyper-intense offset can be seen in the white matter region overlying the lesion. This corresponds to the region where the plane cuts the hyper-intense lobe of the dipole field projected above the lesion. The susceptibility map shows no such offset.

Figure 5-6 shows sagittal images (magnitude, phase and susceptibility contrast) from an MS patient which span a larger field of view. Several lesions are indicated, and the phase and susceptibility images show similar contrast behaviour to that seen in Figures 5-1 – 5-3. As in the previous figures, the contrast in the HF image appears flatter than in the SF image.

Figure 5-7 shows simulated phase images produced from forward field calculations based on a mask of the peripheral ring of the lesion shown in Figure 5-3, and on a mask of the entire lesion, in both cases assuming a constant susceptibility difference of 0.15 ppm in the mask region relative to the rest of the tissue. The simulated phase images were then processed with the same high-pass and SHARP filtering methods that were applied to the real data. Susceptibility maps were calculated from these phase images using the TKD method. Both the shell and solid models produced a dipolar phase pattern, shown in the sagittal plane, which is consistent with the pattern observed in the sagittal phase images in the measured data. The amplitude of the dipolar field is reduced in the HF phase compared to the SF phase, as observed in the real data, and some lateral distortion can be seen in the HF images. As would be expected, the external phase perturbation is larger in magnitude for the solid model since the dipole moment is stronger in this case. In addition, the solid model yields a more significant overall perturbation of the internal phase for this non-spherical lesion shape. In the shell model, while a dipolar perturbation is observed outside of the ring, there is also a phase shift within the shell itself of opposite polarity to the adjacent dipole lobe.

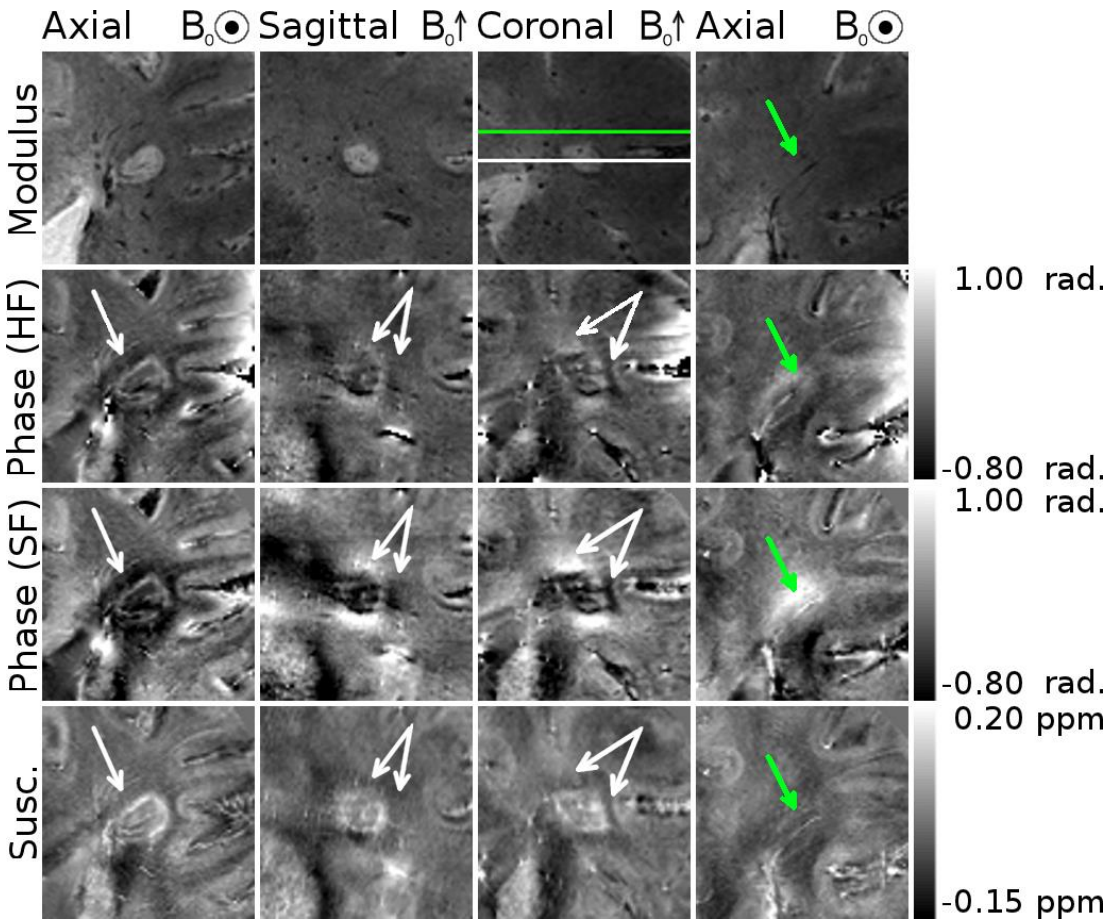

Figure 5-3 - Magnitude, phase and QSM images of a white matter MS lesion with a peripheral ring. The first three columns show cross-sectional images through the lesions, with the plane of the axial images indicated on the coronal magnitude image in white, and with the location of the projected dipolar field lobes (identified from the phase images) indicated with white arrows on the phase and QSM images. A hyper-intense peripheral ring is visible on the QSM images. The fourth column shows axial images in the plane indicated in green on the coronal magnitude image, with the location of the projected dipolar field indicated with green arrows on the phase and QSM images.

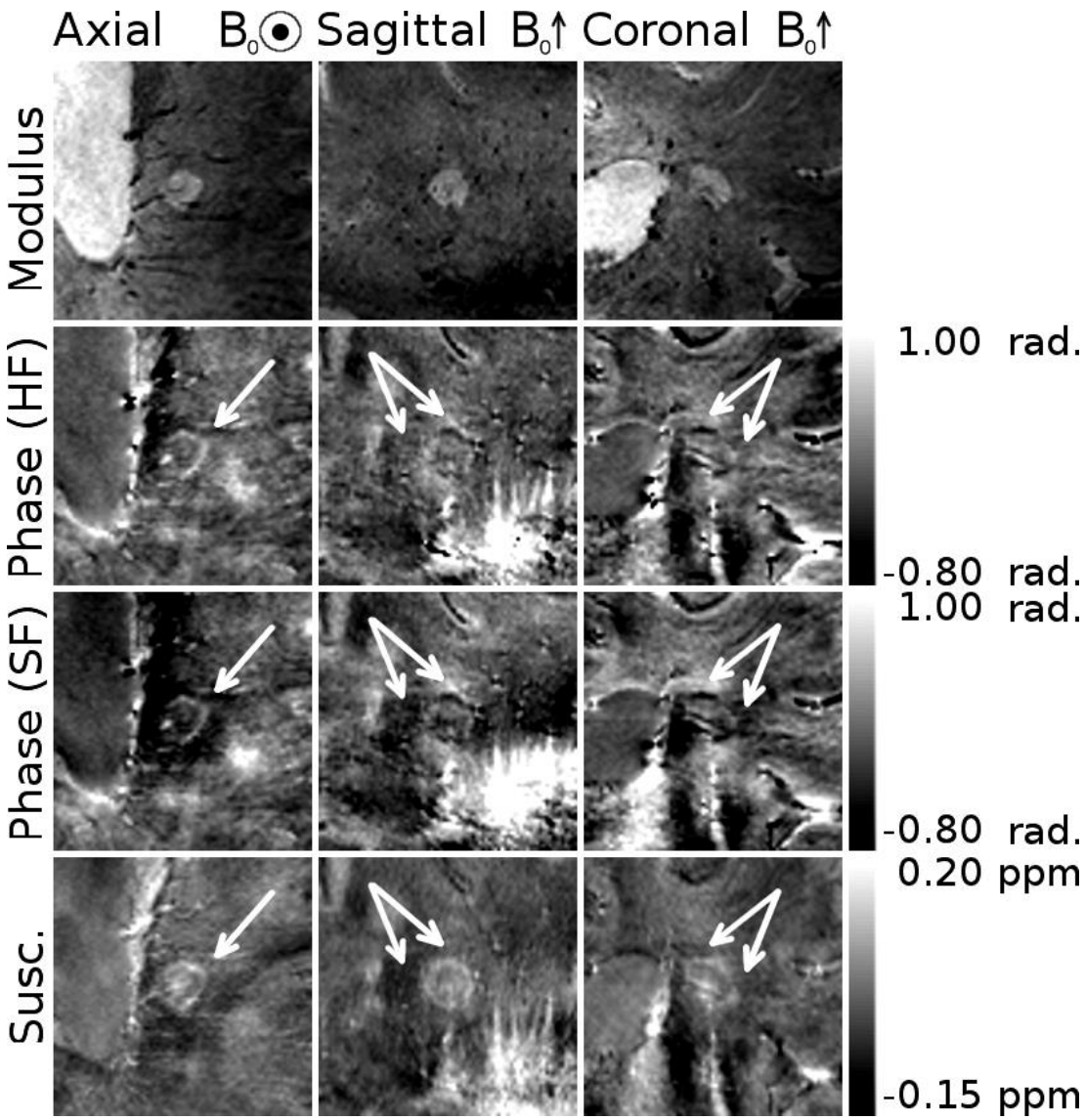

Figure 5-4 - A second example of a white matter MS lesion with a peripheral ring. The location of the projected dipolar field lobes is indicated with white arrows on the phase and QSM images. A hyper-intense ring can be seen at the periphery of the lesion in the QSM images.

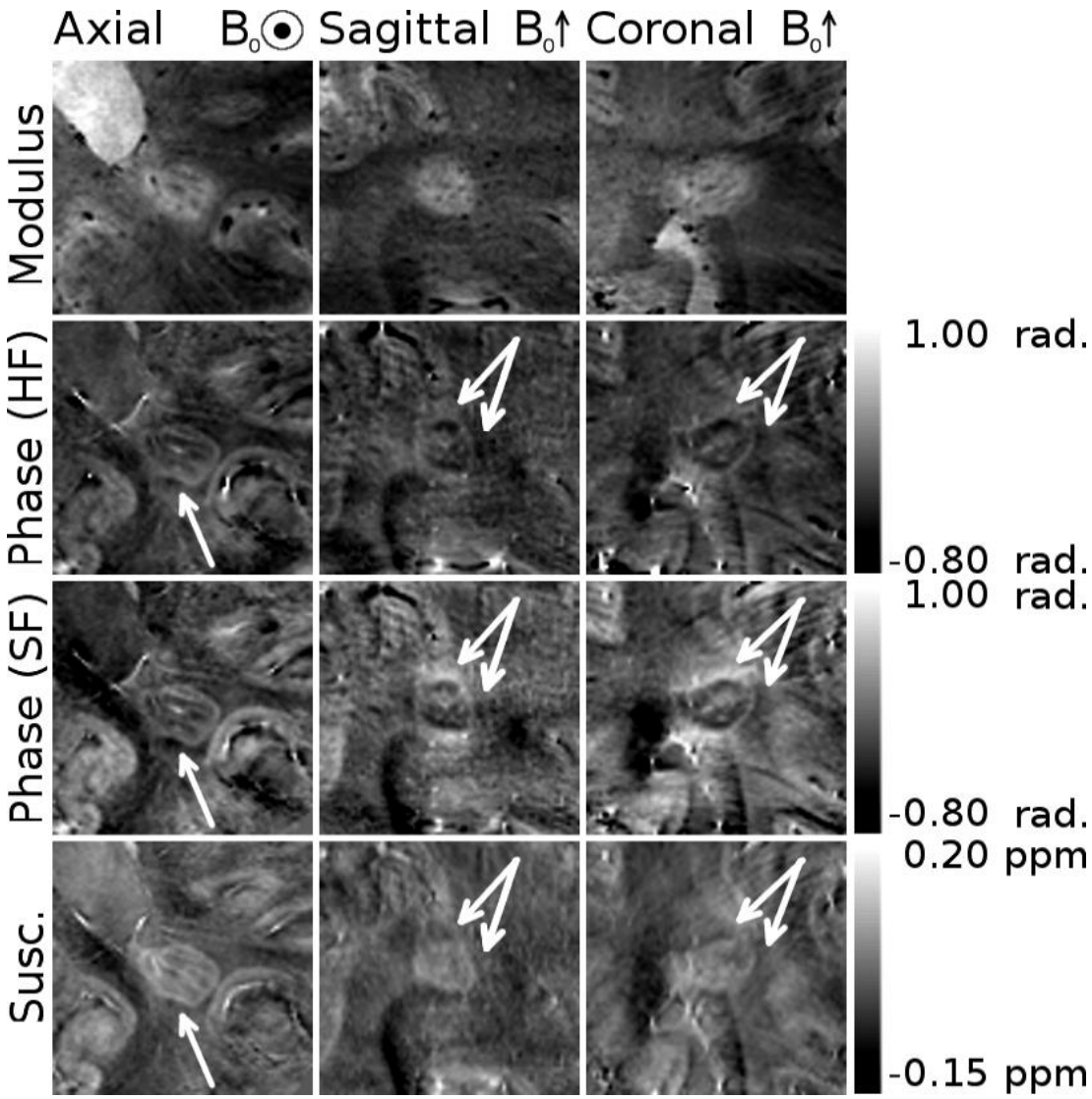

Figure 5-5 - A white matter MS ring with a less distinct boundary in the magnitude image than those seen in Figures 5-1 and 5-2. A weaker, but still present dipolar field is visible in the SF phase images, and its location is indicated by white arrows on the phase and QSM images. A hyper-intense ring can be seen at the periphery of the lesion in the QSM images.

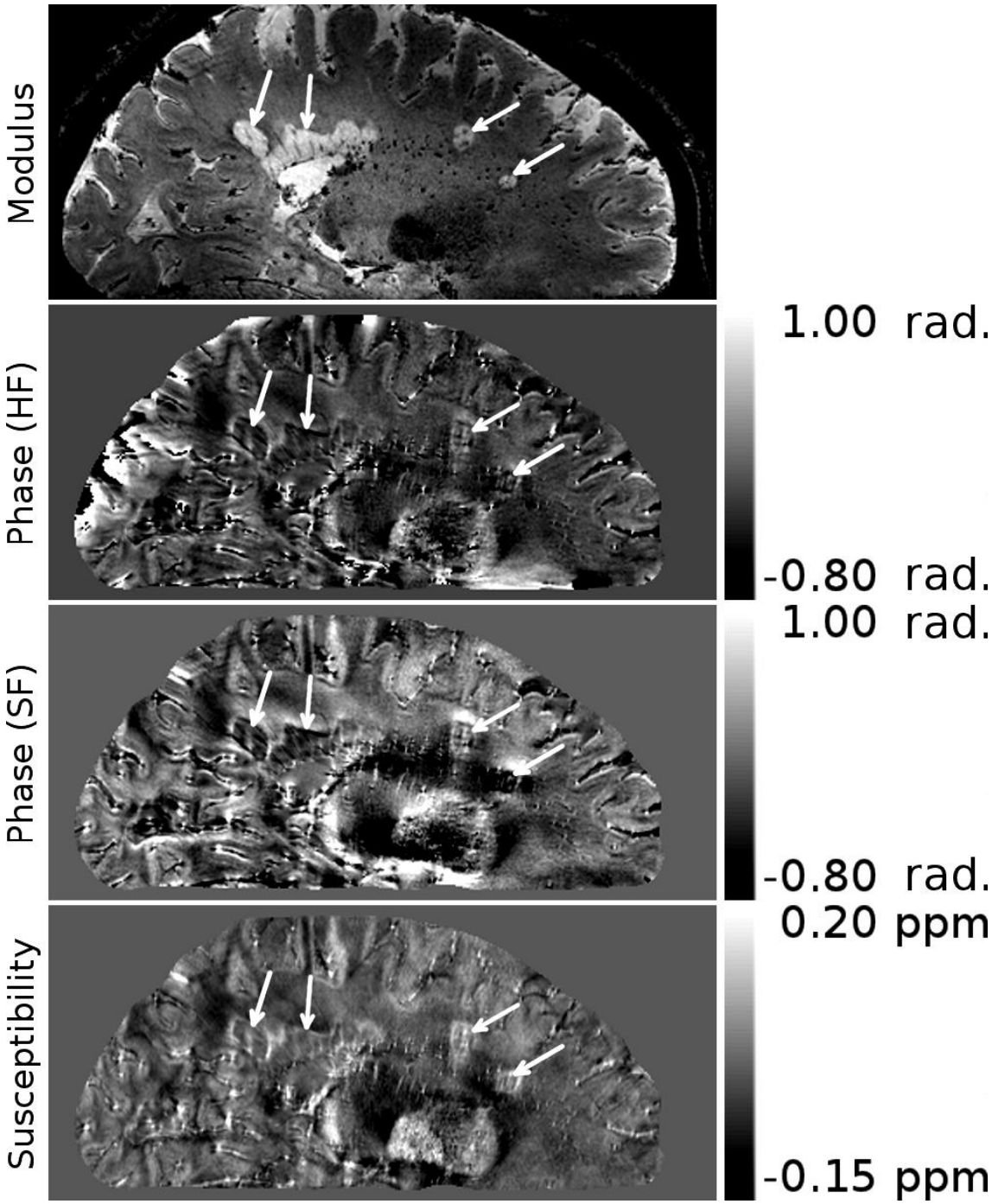

Figure 5-6 - Whole head sagittal images of a patient with multiple sclerosis showing several white matter lesions, indicated by white arrows, with peripheral rings. Dipolar fields are apparent in the phase image, but do not appear in the QSM image.

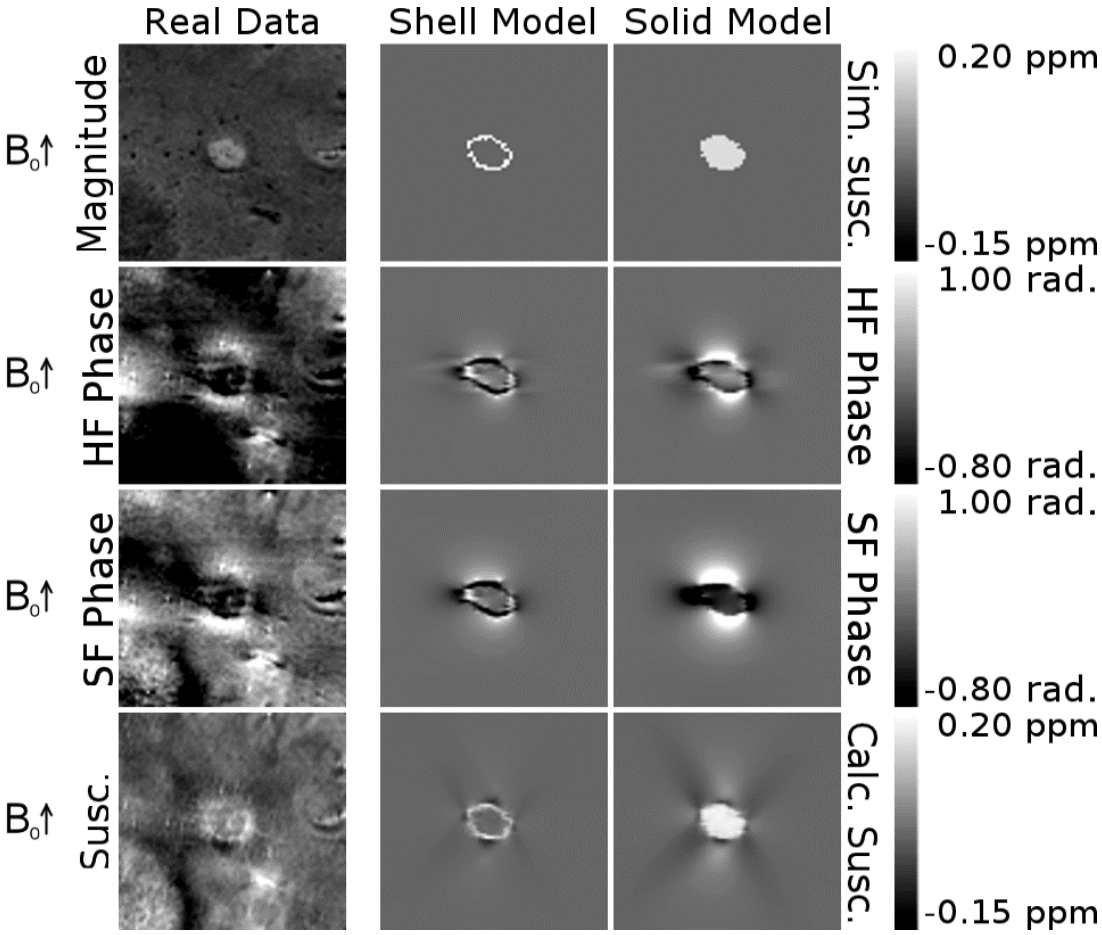

Figure 5-7 – Sagittal susceptibility masks, simulated phase patterns, and QSM images generated using the TKD method, based on the lesion shown in Figure 5-2. The first column shows corresponding experimental data. The top row shows susceptibility masks based on shell-like and solid representations of the lesion, shown in the second and third columns, respectively. The second and third rows show the result of a simulation of the high-pass filtered and SHARP-filtered phase data, respectively. The fourth row shows quantitative susceptibility maps generated from the SHARP-filtered phase data.

5.2.3 Average Voxel Intensity Profile in Ringed WM Lesions in Magnitude, Phase and QSM Images

Figures 5-8 and 5-9 show the average variation with distance from the lesion edge of the signal magnitude, high-pass (HP) and SHARP-filtered (SF) signal phase, and susceptibility derived from both HP and SF phase images in the lesions and

surrounding WM. The mean and standard deviation of the phase and susceptibility used to normalise the lesion profiles is shown in Table 5-1.

Figure 5-8 shows the mean (and standard deviation in) intensity variation around all 6 lesions, while the inset graphs show the profiles for each individual lesion. In the phase and susceptibility maps, the mean standard deviation in the ROIs used to normalise the data is also shown, giving an indication of the relative precision of measurements taken relative to these 'zero' points. The magnitude profile is hyper-intense inside the lesions, falling monotonically to a constant lower level in the external WM. The phase data show relatively flat mean profiles, with both the lesions and the external WM being hyper-intense relative to CSF, and with consistent profiles for individual lesions. The mean SF phase profile is consistently higher relative to the CSF and has a greater variation between individual lesions than the HF phase. In contrast, the susceptibility profile has a consistent internal hyper-intense offset, shows a peak at the lesion boundary, and falls monotonically to a constant level in the external WM.

The mean susceptibility profiles show a consistent trend, but the susceptibility variation seen in the data generated from the HF phase is lower in magnitude and flatter than the profile generated from the SF phase. The mean and standard deviation of the phase values in the CSF ROIs is of a similar magnitude for both the HF and SF data and is of significant magnitude relative to the mean phase profiles. The standard deviation of the mean profiles is greater in the SF phase than the HF phase. Similarly, the standard deviation of the susceptibility in the CSF is also significant in magnitude relative to the mean profiles. The standard deviation of the individual susceptibility profiles is decreased inside the lesions and beyond ~2 mm outside of the lesions in the HF data relative to the SF data.

The individual lesion profiles in Figure 5-9 show trends that are consistent with the mean profiles. In the SF phase profiles, lesion 6 has a susceptibility profile similar in behaviour but markedly higher in absolute value relative to CSF than the other lesions. Additionally, lesion 5 has a more negative interior phase and more positive external phase between 2 and 4 mm outside of the lesion then lesion 1-4. In the susceptibility profiles, lesion 5 has a greater susceptibility difference between inside and outside of the lesion relative to the other lesions. The raised phase profile of the lesion 6 may be explained by the more negative mean phase measured in the CSF

relating to this lesion relative to the lesions represented by lesion 1-4. It is possible that either through the proximity of a structure such as a blood vessel to the ROI, or the orientation of the head in the scanner. The standard deviation of the phase values in the CSF ROI is also ~2x the standard deviation in those relating lesion 1-4, which may suggest the presence of a relatively strong phase gradient across the ROI from an outside source. The phase and susceptibility profiles of lesion 5 may be interpreted similarly. The mean phase in the CSF is again more negative than that relating to lesions 1-4, which causes the phase profile to appear high relative to those others. The more negative phase inside the lesion may be a real product of the relatively strong susceptibility of the lesion, as seen in the susceptibility profiles. As no lesion is perfectly spherical, phase offsets will be caused both inside and outside of the lesion due to its heterogeneous susceptibility distribution. The susceptibility profile supports this explanation, showing a significantly larger difference in susceptibility between the lesion and external white matter. While the susceptibility profile seems to suggest a lower susceptibility in the external white matter surrounding this lesion and a similar susceptibility within the lesion compared to the mean susceptibility profile, the mean susceptibility in the CSF for this lesion is high and positive relative to the other lesions. If this is due to a higher susceptibility being present in the CSF ROI (due to blood vessels, for example), then it may be inferred that the susceptibility within this lesion is in fact higher than the other lesions, rather than the external susceptibility being lower.

Table 5-1 – Mean and standard deviation of phase and susceptibility in CSF ROIs.

	Mean CSF Phase ± Std. Dev.	**Mean CSF Susc. ± Std. Dev.**
Lesion 1 & Lesion 2	-0.009±0.003 ppm	-0.012±0.017 ppm
Lesion 3 & Lesion 4	-0.008±0.003 ppm	0.001±0.034 ppm
Lesion 5	-0.015±0.004 ppm	0.003±0.023 ppm
Lesion 6	-0.017±0.006 ppm	-0.014±0.034 ppm

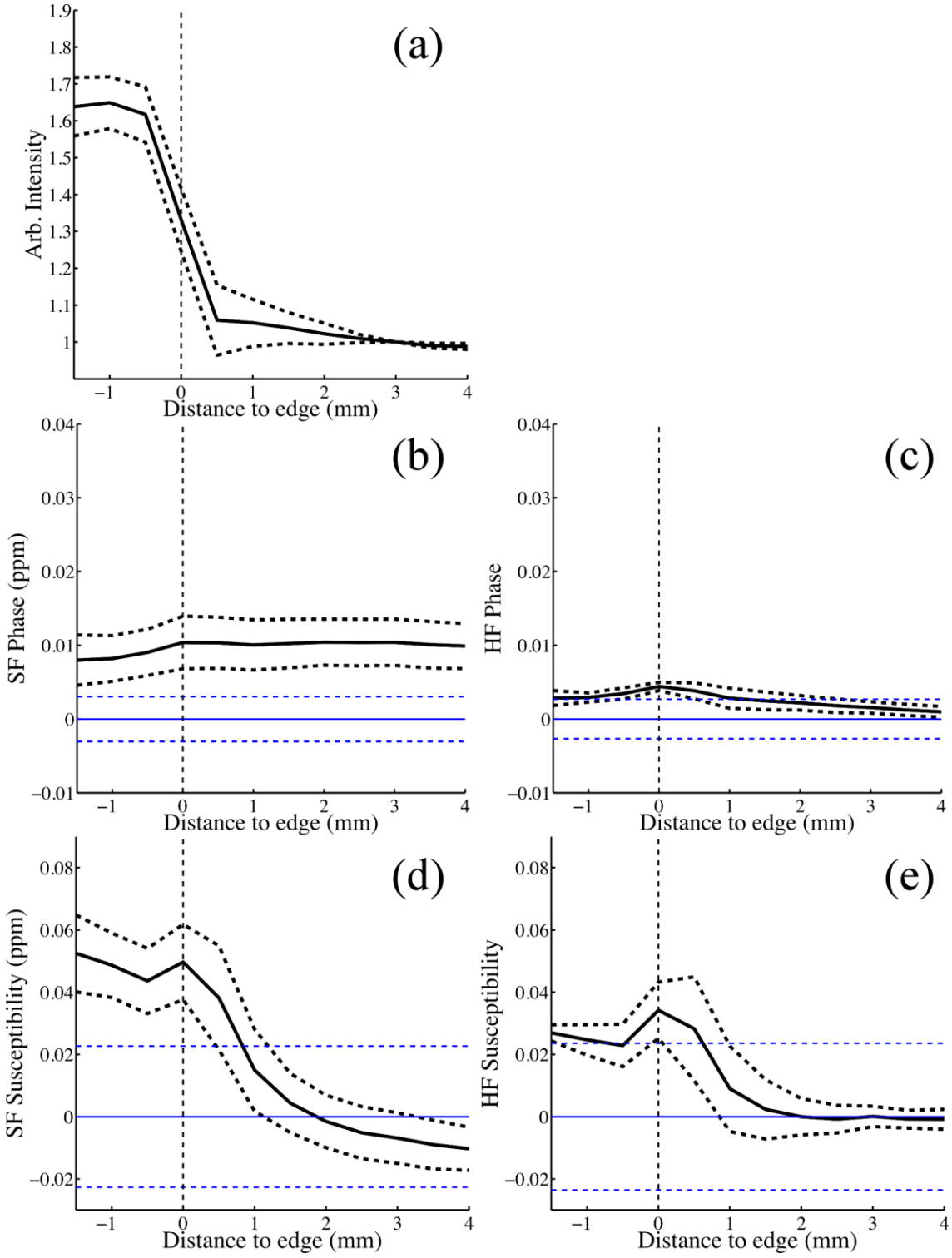

Figure 5-8 - Profiles of the mean voxel intensity in the white matter as a function of distance to the nearest point at the edge of the lesion in:(a) T_2^*-weighted magnitude images (b) SHARP-filtered phase images (c) high-pass filtered phase images, (d) QSM images generated from SF phase data, (e) QSM images generated from HF phase data - showing mean values (solid black lines) with standard deviations (dashed black lines). Phase and QSM data were normalised relative to CSF, and the mean of the standard deviations calculated within the individual CSF ROIs is shown by the horizontal dashed blue lines.

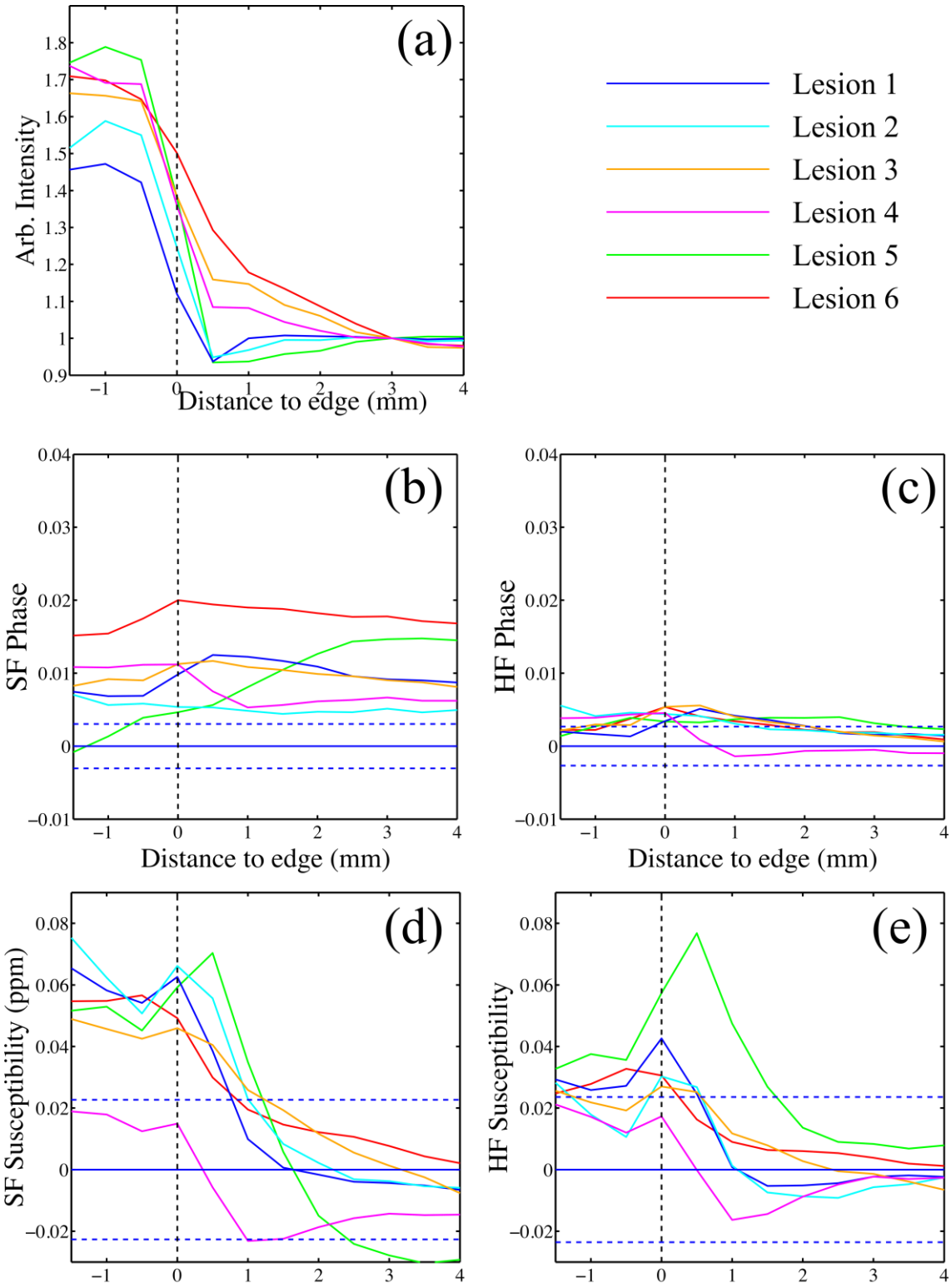

Figure 5-9 - Profiles of the voxel intensity in the white matter as a function of distance to the nearest point at the edge of individual lesions in:(a) T_2^*-weighted magnitude images (b) SHARP-filtered phase images (c) high-pass filtered phase images, (d) QSM images generated from SF phase data, (e) QSM images generated from HF phase data - The mea of the standard deviations calculated within the individual CSF ROIs is shown by the horizontal dashed blue lines.

5.2.4 Whole Cohort Lesion Analysis

Figures 5-10 and 5-11 show the results of the analysis of the 305 lesions identified on the T_2^*-weighted magnitude images of the 39 subjects included in this study. Of these lesions, one was excluded as it was deemed unclassifiable in the sagittal and coronal planes of the T_2^*-weighted magnitude images. In all image types, lesions were considered unclassifiable if the contrast was not isointense, but the presence or absence of a focal lesion was ambiguous to the observer. Of the remaining 304 lesions, 60 (20%) were visible in the SHARP filtered phase (SF) images and 69 (23%) were visible in the QSM images. 144 lesions (47%) were not visible on SF phase or QSM images. A further 81 (27%) of selected lesions were unclassifiable in the SF phase images, and 67 (22%) were unclassifiable in the QSM images. Of the 60 lesions visible in the SF phase images, 37 (62%) displayed evidence of a peripheral ring, and 23 (38%) had no peripheral ring. 19 (32%) of the lesions visible in the SF phase images displayed visible, external dipolar contrast. Of the lesions visible in the QSM images, 30 (43%) displayed evidence of a peripheral ring, 39 (57%) had no peripheral ring, and no lesions displayed external dipolar contrast. 12 (4%) lesions were visible on SF phase images but invisible or unclassifiable in QSM data, 21 (7%) were visible on QSM images but invisible or unclassifiable on SF phase data. 45 lesions (15%) were unclassifiable in both SF phase and QSM images. Of the 48 lesions visible in both SF phase and QSM images, 27 (56%) had peripheral rings and 21 (44%) had no rings on QSM, 34 (71%) had peripheral rings and 14 (29%) had no rings on SF phase images. Of the 34 lesions with peripheral rings on SF phase images, 27 (79%) had rings on the QSM images while 7 (21%) did not. Of the 27 of these 48 lesions in QSM images with peripheral rings, all had peripheral rings in the SF phase images.

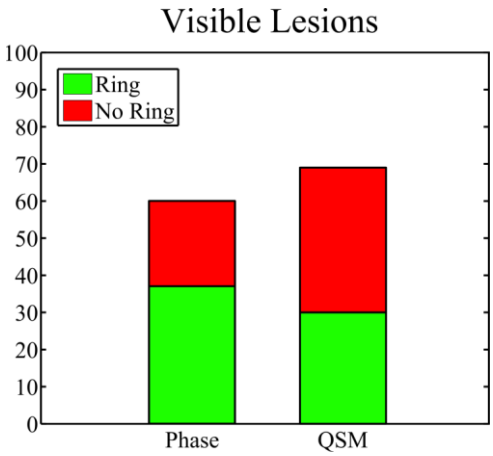

Figure 5-10 – Total number of lesions identified in the SHARP-filtered phase and QSM images from a total of 305 lesions identified in the T_2^*-weighted magnitude, alongside total number of lesions identified with and without peripheral rings.

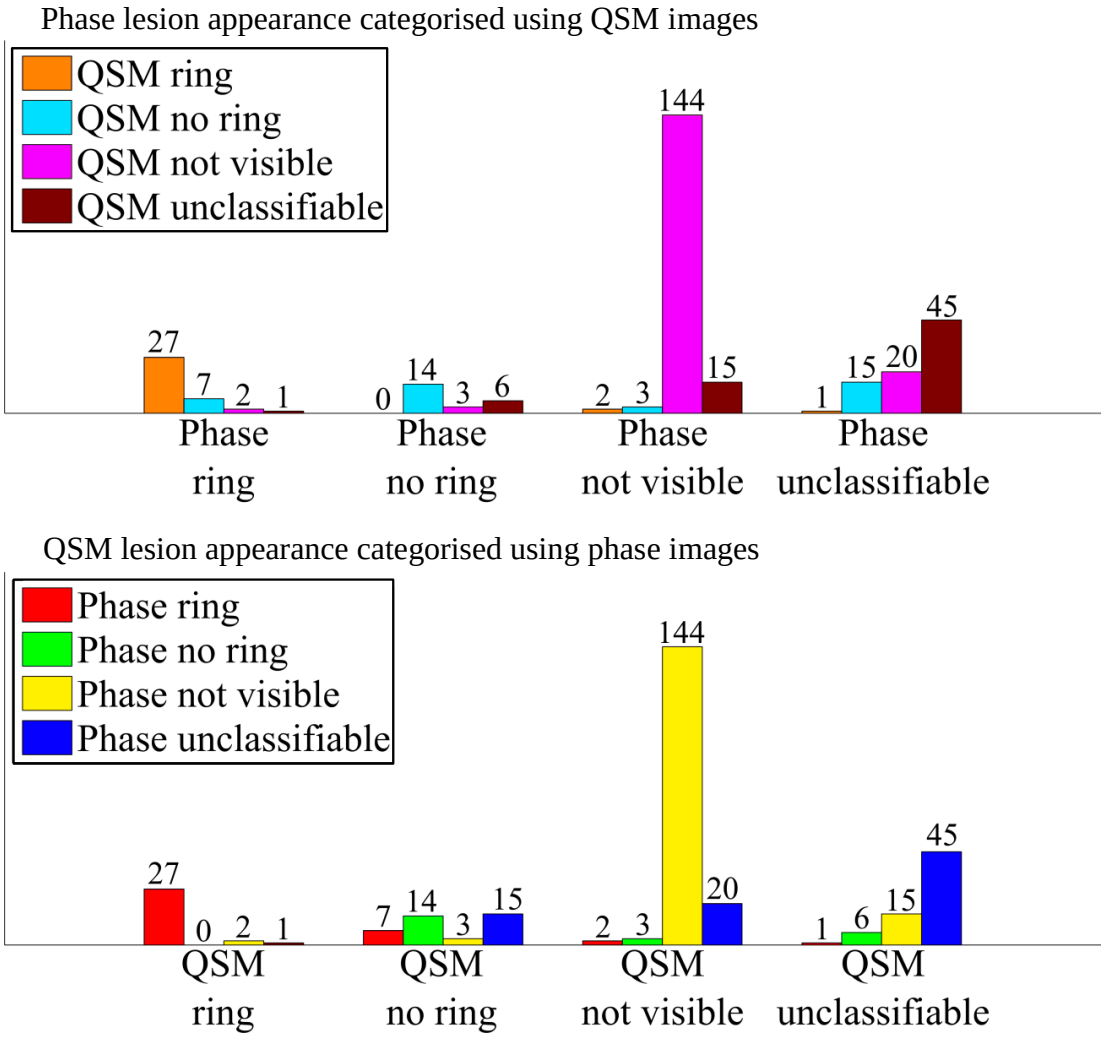

Figure 5-11 – Appearance of lesions in SHARP-filtered phase images subdivided according to appearance in QSM, and appearance of lesions in QSM images subdivided according to appearance in SHARP-filtered phase.

5.3 Discussion

In this study, the use of ultra-high field MRI has allowed comparison of the appearance of white matter MS lesions with peripheral rings in high resolution magnitude, phase and QSM images, as well as facilitating the representation of the lesions using 1D plots of voxel intensity with respect to distance from the lesion boundary. Axial and coronal phase images showed obvious dipolar patterns surrounding some lesions: patterns that are not consistent with any expected distribution of iron in or around MS lesions if phase offsets are considered to be a

locally generated. Quantitative susceptibility maps showed lesion structures that are more consistent with the tissue changes known to occur in MS from post-mortem studies [5, 32], where iron bearing macrophages have been identified at the boundary of ringed lesions. Comparison between phase data unwrapped and filtered using a Hanning window and data unwrapped using a Laplacian-based method and filtered using the SHARP technique highlighted the sensitivity of both phase and QSM images to processing methods. Visual analysis of a subset of 304 lesions gave an indication of the prevalence of peripheral rings in phase and QSM images, and the variable morphology of individual lesions when their appearance is compared in phase and QSM images.

Histological studies have linked the paramagnetic rings surrounding some MS lesions to the presence of iron-rich macrophages at the periphery of the lesions [5, 10]. *In vivo* quantification of such features is clearly desirable, and the effect of such features on tissue susceptibility makes susceptibility-sensitive MRI contrast an obvious tool for such research. Using phase contrast rather than QSM to investigate changes in tissue susceptibility in MS poses the risk that images will be misinterpreted, especially if the lesion is not viewed in the sagittal or coronal planes where the non-local, dipolar nature of phase contrast is most obvious. For example, if phase contrast were simply used as a measure of the iron level surrounding these lesions, the presence of raised iron levels above and below the lesion would mistakenly be inferred, while reduced levels would be assigned to the region surrounding the lesion in central axial planes, as can be seen clearly in Figures 5-2, 5-3 and 5-4. The exact appearance of lesions in the phase images depends on the spatial filtering that is applied to the phase data. The use of high-pass filtering reduces the amplitude of the phase variation due to the external field perturbations when compared to the SHARP filtered phase. However, as can be seen in Figure 5-2, the degree of attenuation will depend on the size of the lesion relative to that of the filter window and such filtering also obviously leads to underestimation of the phase effects due to structures with large susceptibilities. Non-local effects generally also confound the use of the phase measured in a lesion relative to the phase of nearby normal appearing white matter as a means of characterising tissue changes and mean that, in general, reliable quantitative information about tissue composition cannot be measured from local phase contrast.

In contrast, quantitative susceptibility maps show features that are consistent with the physical extent of the lesion and with the occurrence of normal appearing WM around the lesion. Locally elevated susceptibility can also be seen to occur with varying degrees inside the lesion, and consistently in the peripheral ring, as expected from histology [5].

Iron levels cannot be directly quantified from a susceptibility map alone, particularly due to the negative contribution of myelin, which is diamagnetic, to the bulk susceptibility, although techniques for quantifying iron by combining information from susceptibility and R_2^* maps have been proposed [33, 34]. Recently, it is also been suggested that the presence of iron in tissue can be inferred from QSM images if the bulk susceptibility measured relative to that of the CSF are greater than zero [35, 36]. Both decreased myelin levels and increased iron levels lead to a positive increase in the net magnetic susceptibility [37-39]. Complete demyelination in a voxel would not be expected to increase the bulk susceptibility above that of CSF, and so any further increase in susceptibility is argued to be related to iron. As shown in Figures 5-8 and 5-9, profiles through the lesions in T_2^*-weighted images show that T_2^* is increased inside the lesion and reduced at the lesion boundary before levelling off at the value for external normal appearing white matter. This variation is consistent with either myelin or iron loss within the lesion, but is most probably due to myelin loss and the destruction of normal tissue. On some T_2^*-weighted images (Figures 5-2, 5-3 and 5-4), hypo-intensity can be seen at the lesion edge, which would be consistent with increased iron (or myelin) in that region, although this is not detected on the averaged radial profiles (Figure 5-9), probably due to the competing effects of reduced myelination and increased iron deposition in this region. The average phase profile in both the HF and SF phase is slightly reduced inside the lesions, rising at the edge of the lesion, and remaining level (SF) or reducing slightly (HF) in the external WM, giving little, if any, indication of a change in tissue composition internally or externally because of the non-local, dipolar nature of phase contrast [14]. In contrast, the susceptibility profiles are higher inside the lesion than outside, and display a peak at the lesion edge, reflecting structure consistent with that observed in the magnitude images. When normalised to CSF, a positive susceptibility measured within the lesions is consistent with an internal loss of myelin and the presence of iron, and the peak at the lesion edge is

suggestive of a peak in iron levels. The T_2*-weighted and susceptibility profiles are therefore consistent with recently reported results from histology [5] which suggest that myelin levels are reduced inside lesions relative to the surrounding WM, while iron levels are increased at the lesion boundaries.

The magnitude of the phase variation relative to CSF was clearly reduced in the HF phase images when compared to the SF phase images. The SF phase in the lesions is consistently positive relative to the CSF however the mean standard deviation of the voxels in the CSF ROIs overlaps considerably with the phase profile in the HF data. This indicates both that normalised phase values are highly sensitive to the specific filtering applied to the data, and that attempts to quantify phase variation relative to CSF are somewhat confounded by variability of values found within the 'zero' region defined in the CSF.

The susceptibility calculated from the SF phase shows a more positive susceptibility within the lesion and a more negative susceptibility in the external WM than the susceptibility calculated form the HF phase. This may indicate a systematic underestimation of the magnetic susceptibility calculated using QSM due to the flattening effect of the high-pass filtering on the phase data, and suggests that the choice `information in phase data and calculating quantitative susceptibility maps. There is also a large variability in the susceptibility measured within the CSF, as shown by the large mean standard deviation in these regions. This indicates that even with the application of QSM, care must be taken in drawing conclusions from these measurements, as the 'zero' point is poorly defined so there is still a significant degree of uncertainty in the quantitative values measured.

Variation in susceptibility distribution can be seen between the lesions, for example, the smaller increase in susceptibility inside the lesion shown in Figure 5-4 could be due to that lesion having undergone less demyelination than the lesions shown in Figure 5-3 and Figure 5-5.

Figure 5-7 shows the phase shift caused by a simulated shell of raised susceptibility at the periphery of a lesion, and also that produced by a uniform increase in susceptibility of the region lying within the same lesion boundary. The simulated phases can be seen after both high-pass and SHARP filters have been applied. In both cases the resulting external phase shifts are consistent in polarity and orientation

to the pattern observed in the real phase data. In the shell model, it can be seen that in addition to an external dipole, a local field shift is generated on the inner surface of the shell, with opposite polarity to the adjacent external dipole lobes. This feature can also be seen in the real phase images in Figures 5-2, 5-3 and 5-4. The solid model produces a dipole of greater magnitude, but without this feature. The susceptibility of the shell and solid object were based on the susceptibility of the shells observed in experimentally acquired susceptibility maps, but the magnitude of the dipole produced by the shell model appears reduced compared to the real data whereas the solid model generates a dipole of similar magnitude to the real data. This suggests that the experimental maps are consistent with a shell of high susceptibility with an additional contribution from internal material with susceptibility that is greater than that of the surrounding white matter, but lower than the susceptibility of the shell. As noted in the discussion of Figures 5-2, 5-3 and 5-4, the amplitude of the dipolar phase patterns is reduced in the HF phase relative to the SF phase data. Additionally, some lateral distortion can be seen in the HF phase images as a result of the filter being applied in 2D to axial slices of the data, further demonstrating that images processed in this way must be interpreted with care. The calculation of susceptibility maps from phase images is an ill-posed problem, whereas the forward calculation used in the simulation is well conditioned, so this result strengthens the interpretations made from the QSM images. The susceptibility distribution calculated from the simulated phase data is approximately consistent with the simulated susceptibility distribution, although there are some streaking and other artefacts present due to the imperfect inversion resulting from the truncated k-space filter used in the TKD implementation. This effect may account for the hypo-intense region seen immediately below the lesion in the susceptibility map, indicating that, even when using QSM, care must be taken when drawing inferences from small variations in contrast, despite the strong localisation of contrast that QSM displays in comparison to phase imaging.

An indication of the relative prevalence and variable appearance of white matter lesions in SHARP filtered phase and QSM images can be seen in Figures 5-10 and 5-11. Of the 304 lesions marked on the T_2^*-weighted magnitude images, 20% were visible in phase images. This is lower than the prevalence reported in previous studies which included similar analysis [7, 10, 32, 40], in which 40-78% of lesions in

magnitude data were found to be visible in phase images. These figures could be affected by a number of factors, including the field strength of the scanner used, the resolution of the data acquired, the criteria by which lesions were identified for comparison and the number of planes in which lesions were compared. Further variation would be expected due to the subjective nature of visual comparison and the lack of consistent criteria for categorization of lesions across different studies. Our data were acquired at an ultra-high field strength of 7 T with a high isotropic resolution of 0.5x0.5x0.5 mm^3, and images were compared in the axial, sagittal and coronal planes. In contrast, images used for lesion identification in previous studies were typically acquired with high in-plane resolution, but with slice thicknesses of 2-3 mm [7, 10, 32, 40], and only axial images are reported. In one case the lesions used for comparison were specifically selected for their large size [40]. For this reason, smaller lesions (<3 mm in diameter) would be less likely to be selected for comparison. A systematic bias towards larger lesions in previous analyses may explain the increase in the proportion of lesions found to be visible in phase images, as smaller lesions may have different levels or distributions of iron deposition or demyelination. As small lesions may be early indicators of new disease activity, investigation of them has been recognised as an important area of future focus [40], making the use of high, isotropic resolution acquisitions a potentially important improvement on previous imaging protocols.

The absolute number of lesions identified was greater in the QSM images than in the phase data. The majority of this difference is due to lesions with no ring in the QSM images, and are unclassifiable in the phase images. In contrast, the majority of lesions which presented rings in the QSM also appeared in the phase images. This suggests that lesions with peripheral rings are more likely to have a relatively consistent appearance in the phase and QSM images, possibly indicating that the changes in tissue composition in these lesions is greater relative to the surrounding white matter than lesions with no ring. Lesions with less pronounced changes in microstructure relative to the surrounding white matter may be more obscured by the distortion inherent in phase imaging, making them unclassifiable or undefined, while the correction of this distortion in QSM may allow a greater proportion of such lesions to be identified.

Of the 48 lesions visible on both phase and QSM images, 27 (56%) had rings on both phase and QSM images, 14 (29%) did not display rings in the phase or QSM images, 7 (15%) displayed rings in the phase, but not the QSM images, and no lesions displayed rings in the QSM images, but not in phase images. Recently published work has highlighted that solid, nodular distributions of magnetic susceptibility can lead to shell-like patterns in phase images [40]. Such an effect may explain the 7 lesions found in our data which displayed rings in the phase images but not in QSM images. In contrast, the fact that no ringed lesions were found in QSM images where no ring had been found in the phase data suggests that QSM may offer improved specificity in the identification of peripheral rings in white matter lesions compared with phase images. This further highlights the importance of using QSM when trying to quantify such features. As our data was acquired during a single visit for each patient and without the use of contrast, our ability to establish any significance of the presence or absence of peripheral rings in the severity of progression of MS symptoms was limited.

5.4 Conclusions

In this study, isotropic high-resolution, whole head T_2^*-weighted images acquired at 7T were used to compare phase imaging and QSM as a means of investigating white matter MS lesions with peripheral rings. Phase images were shown to be dominated by non-local dipolar field effects, causing both positive and negative shifts in the contrast, even in the axial plane. These effects have the potential to be misleading when interpreting phase images and preclude the use of phase contrast in studying tissue composition. However, QSM techniques can be applied to phase data to yield susceptibility maps showing contrast that is much more closely linked to the local tissue composition. Although the susceptibility values are affected by both myelin and iron, the use of susceptibility maps in combination with T_2*-weighted data allow inferences to be drawn about changes in tissue composition and comparison to be made to histology. The peripheral rings and visible dipolar field pattern apparent in some phase images were shown to appear in both SHARP and high-pass filtered data, although high-pass filtering sufficient to remove phase wraps was found to systematically yield lower susceptibility values both inside and outside of lesions when processed using QSM. The prevalence of peripheral rings in phase and QSM data was found to be lower than previously reported [7, 10, 32, 40], however this

could be attributed to the high isotropic resolution images used in this study, which may have resulted in the identification of smaller lesions in the magnitude data than those identified in other studies.

5.5 References

1. Al-Radaideh, A.M., et al., *Increased iron accumulation occurs in the earliest stages of demyelinating disease: an ultra-high field susceptibility mapping study in Clinically Isolated Syndrome*. Multiple Sclerosis Journal, 2012, **19**(7), 896-903.
2. Langkammer, C., et al., *Quantitative Susceptibility Mapping in Multiple Sclerosis*. Radiology, 2013, **267**(2), 551-559.
3. Walsh, A.J., et al., *Multiple Sclerosis: Validation of MR Imaging for Quantification and Detection of Iron*. Radiology, 2013, **267**(2), p. 531-542
4. Zivadinov, R., et al., *Abnormal subcortical deep-gray matter susceptibility-weighted imaging filtered phase measurements in patients with multiple sclerosis: a case-control study*. NeuroImage, 2012. **59**: p. 331-9.
5. Bagnato, F., et al., *Tracking iron in multiple sclerosis: a combined imaging and histopathological study at 7 Tesla*. Brain : a journal of neurology, 2011. **134**: p. 3602-15.
6. Hopp, K., et al., *Brain iron detected by SWI high pass filtered phase calibrated with synchrotron X-ray fluorescence*. Journal of Magnetic Resonance Imaging, 2010. **31**(6): p. 1346-1354.
7. Haacke, E.M., et al., *Characterizing iron deposition in multiple sclerosis lesions using susceptibility weighted imaging*. Journal of magnetic resonance imaging : JMRI, 2009. **29**: p. 537-44.
8. Eissa, A., et al., *Detecting lesions in multiple sclerosis at 4.7 tesla using phase susceptibility-weighting and T2-weighting*. Journal of magnetic resonance imaging : JMRI, 2009. **30**: p. 737-42.
9. Ge, Y., et al., *Diminished visibility of cerebral venous vasculature in multiple clerosis by susceptibility-weighted imaging at 3.0 Tesla*. Journal of magnetic resonance imaging : JMRI, 2009. **29**: p. 1190-4.
10. Hammond, K.E., et al., *Quantitative in vivo magnetic resonance imaging of multiple sclerosis at 7 Tesla with sensitivity to iron*. Annals of neurology, 2008. **64**: p. 707-13.
11. Duyn, J.H., et al., *High-field MRI of brain cortical substructure based on signal phase.* Proceedings of the National Academy of Sciences of the United States of America, 2007. **104**: p. 11796-801.
12. Hammond, K.E., et al., *Development of a robust method for generating 7.0 T multichannel phase images of the brain with application to normal volunteers and patients with neurological diseases*. NeuroImage, 2008. **39**: p. 1682-92.

13. Haacke, E.M., et al., *Establishing a baseline phase behavior in magnetic resonance imaging to determine normal vs. abnormal iron content in the brain*. Journal of Magnetic Resonance Imaging, 2007. **26**(2): p. 256-264.

14. Schäfer, A., et al., *Using magnetic field simulation to study susceptibility-related phase contrast in gradient echo MRI*. NeuroImage, 2009. **48**: p. 126-37.

15. Grabner, G., et al., *Analysis of multiple sclerosis lesions using a fusion of 3.0 T FLAIR and 7.0 T SWI phase: FLAIR SWI*. Journal of magnetic resonance imaging : JMRI, 2011. **33**: p. 543-9.

16. Xu, X., Q. Wang, and M. Zhang, *Age, gender, and hemispheric differences in iron deposition in the human brain: An in vivo MRI study*. NeuroImage, 2008. **40**(1): p. 35-42.

17. Wharton, S. and R. Bowtell, *Whole-brain susceptibility mapping at high field: a comparison of multiple-and single-orientation methods*. NeuroImage, 2010. **53**(2): p. 515-525.

18. Schweser, F., et al., *Quantitative imaging of intrinsic magnetic tissue properties using MRI signal phase: an approach to in vivo brain iron metabolism?* NeuroImage, 2011. **54**: p. 2789-807.

19. Liu, T., et al., *Calculation of susceptibility through multiple orientation sampling (COSMOS): a method for conditioning the inverse problem from measured magnetic field map to susceptibility source image in MRI*. Magnetic resonance in medicine : official journal of the Society of Magnetic Resonance in Medicine / Society of Magnetic Resonance in Medicine, 2009. **61**: p. 196-204.

20. Yablonskiy, D.a., et al., *Biophysical mechanisms of MRI signal frequency contrast in multiple sclerosis.* Proceedings of the National Academy of Sciences of the United States of America, 2012. **109**: p. 14212-7.

21. Li, W., B. Wu, and C. Liu, *Quantitative susceptibility mapping of human brain reflects spatial variation in tissue composition*. NeuroImage, 2011. **55**: p. 1645-56.

22. Schofield, M.A. and Y. Zhu, *Fast phase unwrapping algorithm for interferometric applications.* Optics letters, 2003. **28**(14): p. 1194-1196.

23. Smith, S.M., *Fast robust automated brain extraction.* Human brain mapping, 2002. **17**(3): p. 143-155.

24. Haacke, E.M., et al., *Susceptibility weighted imaging (SWI).* Magnetic Resonance in Medicine, 2004. **52**(3): p. 612-618.

25. Walsh, A.J. and A.H. Wilman, *Susceptibility phase imaging with comparison to R2 mapping of iron-rich deep grey matter*. NeuroImage, 2011. **57**: p. 452-61.

26. Wharton, S., A. Schäfer, and R. Bowtell, *Susceptibility mapping in the human brain using threshold-based k-space division.* Magnetic resonance in medicine : official journal of the Society of Magnetic Resonance in Medicine / Society of Magnetic Resonance in Medicine, 2010. **63**: p. 1292-304.

27. Shmueli, K., et al., *Magnetic susceptibility mapping of brain tissue in vivo using MRI phase data.* Magnetic resonance in medicine : official journal of the Society of Magnetic Resonance in Medicine / Society of Magnetic Resonance in Medicine, 2009. **62**: p. 1510-22.

28. Schweser, F., et al., *Toward online reconstruction of quantitative susceptibility maps: Superfast dipole inversion*. Magnetic Resonance in Medicine, 2013. **69**(6): p. 1581-1593.

29. Liu, T., et al., *Morphology enabled dipole inversion (MEDI) from a single-angle acquisition: Comparison with COSMOS in human brain imaging*. Magnetic Resonance in Medicine, 2011. **66**(3): p. 777-783.

30. Liu, J., et al., *Morphology enabled dipole inversion for quantitative susceptibility mapping using structural consistency between the magnitude image and the susceptibility map*. NeuroImage, 2012. **59**(3): p. 2560-2568.

31. Marques, J.P. and R. Bowtell, *Application of a Fourier-based method for rapid calculation of field inhomogeneity due to spatial variation of magnetic susceptibility*. Concepts in Magnetic Resonance Part B: Magnetic Resonance Engineering, 2005. **25B**: p. 65-78.

32. Yao, B., et al., *Chronic Multiple Sclerosis Lesions: Characterization with High-Field-Strength MR Imaging*. Radiology, 2012. **262**(1): p. 206-15.

33. Schweser, F., et al. *SEMI-TWInS: simultaneous extraction of myelin and iron using a T2*-weighted imaging sequence*. in Proc Intl Soc Mag Reson Med. 2011.

34. Schweser, F., et al., *Disentangling contributions from iron and myelin architecture to brain tissue magnetic susceptibility by combining Quantitative Susceptibility Mapping (QSM) and R2* relaxation rate mapping, in DPMG*. 2012: Jena, Germany. p. p60.

35. Wisnieff, C., et al., *Quantitative susceptibility mapping (QSM) of white matter multiple sclerosis lesions: Interpreting positive susceptibility and the presence of iron*. Magn Reson Med, 2014.

36. Chen, W., et al., *Quantitative susceptibility mapping of multiple sclerosis lesions at various ages*. Radiology, 2014. **271**(1): p. 183-92.

37. Lee, J., et al., *The contribution of myelin to magnetic susceptibility-weighted contrasts in high-field MRI of the brain*. NeuroImage, 2012. **59**(4): p. 3967-3975.

38. Langkammer, C., et al., *Quantitative susceptibility mapping (QSM) as a means to measure brain iron? A post mortem validation study*. NeuroImage, 2012.

39. Yao, B., et al., *Susceptibility contrast in high field MRI of human brain as a function of tissue iron content*. NeuroImage, 2009. **44**(4): p. 1259-1266.

40. Eskreis-Winkler, S., et al., *Multiple sclerosis lesion geometry in quantitative susceptibility mapping (QSM) and phase imaging*. Journal of Magnetic Resonance Imaging, 2014. DOI: 10.1002/jmri.24745

6 INVESTIGATING MRI FREQUENCY SHIFTS DUE TO STRUCTURES WITH ANISOTROPIC MAGNETIC SUSCEPTIBILITY

6.1 Introduction

The uptake of high and ultra-high field strength MRI systems in clinical and research settings has led to an increasing exploitation of new MR contrast mechanisms. In particular, novel contrast based on local variations in the Larmor frequency, ω_0, caused by the heterogeneity of tissue magnetic susceptibility, χ, has been used to generate frequency maps and susceptibility-weighted magnitude images, as well as quantitative susceptibility maps [1]. The resulting images give insight into microscopic tissue composition *in vivo*, providing a valuable tool in the non-invasive assessment of changes in tissue composition in various medical conditions, including neurodegenerative diseases such as multiple sclerosis [2-5].

In order to exploit fully the information provided in susceptibility-based contrast, it is essential to understand the microscopic basis of the macroscopic measurements of MR frequency taken at the voxel level. Early attempts at quantifying magnetic

susceptibility from MRI assumed that each voxel created a dipolar field perturbation whose strength was governed by the average scalar susceptibility of the tissue within the voxel, and that frequency maps calculated from the signal phase simply reflected the superposition of the perturbations generated by all of the voxels in the image (assuming fields generated outside of the region of interest had been removed through appropriate filtering). However, some biological materials such as lipids have been shown to have an anisotropic magnetic susceptibility, which particularly leads to unusual field effects being observed due to ordered structures, such as lipoproteins [6] and myelinated axons [7-12]. The latter effect forms the basis for susceptibility tensor imaging and novel susceptibility-based methods for fibre tracking [12-16].

Although correct mathematical expressions for calculating the field perturbation due to structures composed of materials with anisotropic susceptibility have been described [9, 13], the effects of such structures have often been modelled using a simplified approach in which the anisotropy is represented by allocating the material an isotropic susceptibility whose magnitude depends on its orientation with respect to the field [7, 14]. Here we demonstrate using theory and experiment that this approximation leads to errors in predicting the frequency perturbation due to anisotropic structures, and also show that a tensor model of magnetic susceptibility anisotropy yields correct expressions for these perturbations. In addition, we show that the correct calculation predicts interesting behaviour in a hollow cylinder model of myelinated nerve fibres, and in spherical shell models, whose behaviour could form the basis for creating tuneable contrast in MRI.

Pyrolytic graphite is a material composed of highly-ordered layers of graphite, making it both highly diamagnetic and anisotropic, giving it an anisotropic magnetic susceptibility. It is most strongly diamagnetic when the applied magnetic field is normal to the plane of the sheet. As a result of its strong diamagnetism, this material has previously been used in MRI as a passive shimming material, which was placed in the mouth, to reduce susceptibility artefacts when imaging the inferior frontal cortex [17]. Pyrolytic graphite sheet (PGS) is made from a highly ordered polymer graphite film, and is readily available for use in heat transfer applications. Here, we use PGS to form point-like regions of anisotropic magnetic susceptibility, as well as cylindrical and spherical shells. While previous studies have used mathematical

models to explain the MR signal acquired from protons within and surrounding microscopic biological structures [6, 10], here we use macroscopic phantoms which allow direct separate measurement of the field perturbations in the internal and external compartments, allowing a more detailed comparison of theory and experimental results. Measurements of the field perturbations generated by these structures made using MRI at 3 T allowed validation of the tensor model.

6.2 Theory

The magnetic susceptibility of an anisotropic material can be represented by a cylindrically-symmetric, second-order tensor of the form

$$\underline{\underline{\chi}} = \chi_I \underline{\underline{I}} + \begin{bmatrix} -\chi_a/2 & 0 & 0 \\ 0 & -\chi_a/2 & 0 \\ 0 & 0 & \chi_a \end{bmatrix} \quad , \qquad \text{Eq. 6.1}$$

where χ_I and χ_a ($<< 1$) represent the isotropic and anisotropic components of the susceptibility, and $\underline{\underline{I}}$ is the identity matrix. Here we have assumed that the principal axes of the susceptibility tensor are aligned with the Cartesian x-, y-, and z-axes, and that the axis of symmetry is aligned with the z-axis. If a structure made from such a material is exposed to an applied magnetic field, **H**, the magnetization, **M**, is given by $\mathbf{M} = \underline{\underline{\chi}}\mathbf{H}$. The field perturbation due to this magnetization can then be calculated by evaluation of the magnetic scalar potential, $\Phi(\mathbf{r})$, which is related to the field perturbation by $\mathbf{H} = -\nabla\Phi$, and given by [18]

$$\Phi(\mathbf{r}) = -\frac{1}{4\pi}\int_V \frac{\nabla' \cdot \mathbf{M}(\mathbf{r}')}{|\mathbf{r}-\mathbf{r}'|} d^3\mathbf{r}' + \frac{1}{4\pi}\oint_S \frac{\mathbf{n}' \cdot \mathbf{M}(\mathbf{r}')}{|\mathbf{r}-\mathbf{r}'|} dS' \quad , \qquad \text{Eq. 6.2}$$

where $\mathbf{n}'$ is a unit vector, which is locally normal to the surface of the perturbing structure. This expression can be solved analytically in structures with spherical or cylindrical symmetry. Here we consider the field perturbation produced inside and outside of hollow spherical and cylindrical shells with a radially-oriented,

cylindrically-symmetric susceptibility tensor, as described in Eq. 6.1, as well as the field perturbation due to a point source of anisotropic susceptibility

6.2.1 Field Perturbation due to a Point Source of Anisotropic Magnetic Susceptibility

To compare the representation of anisotropic susceptibility as an orientation-dependent scalar value [7, 14] with the tensor model used in this work, we approximate the field perturbation due to a small solid cylinder of material with anisotropic susceptibility as that of a point-like susceptibility inclusion producing a dipolar field perturbation whose strength and orientation depend on the magnetization induced by a magnetic field $\mathbf{H}_{Applied} = H_0\hat{\boldsymbol{z}}$, applied in the laboratory frame of reference. We consider a Cartesian coordinate system in the frame of the susceptibility tensor (x', y', z'). If the tensor is rotated by an angle Θ about the x-axis in the y-z plane of the laboratory frame, as shown in Figure 6-1, $z' = z$ when $\Theta = 0$ and $z' = y$ when $\Theta = 90°$.

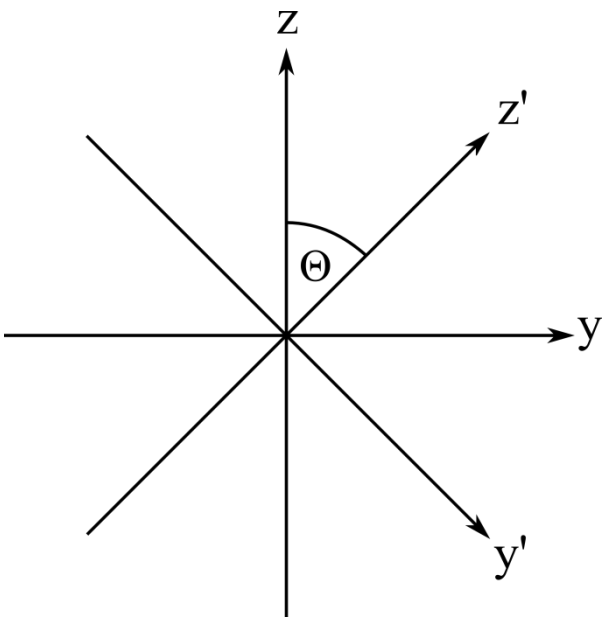

Figure 6-1 – Orientation of the tensor coordinates y' and z' relative to the laboratory-frame coordinates y and z.

In the frame of the tensor, the applied field is

$$\mathbf{H}_{Applied} = \begin{bmatrix} 0 \\ -H_0 \sin\Theta \\ H_0 \cos\Theta \end{bmatrix} \quad .$$

Eq. 6.3

This field induces volume magnetization of the susceptibility, in the frame of the tensor which is given by

$$\mathbf{M}_{Tensor} = -H_0 \left(\chi_I - \frac{\chi_a}{2}\right) \sin\Theta\, \hat{\mathbf{y}}' + H_0(\chi_I + \chi_a) \cos\Theta\, \hat{\mathbf{z}}' \quad .$$

Eq. 6.4

This can be expressed in the laboratory frame as

$$\mathbf{M}_{Lab} = H_0 \sin\Theta \cos\Theta \frac{3\chi_a}{2} \hat{\mathbf{y}} + H_0 \left(\chi_I + \chi_a \left(1 - \frac{3}{2}\sin^2\Theta\right)\right) \hat{\mathbf{z}} \quad .$$

Eq. 6.5

If this magnetization is placed at the origin, the magnetic field perturbation induced at a point **r** will be

$$\Delta\mathbf{H}(\mathbf{r}) = \frac{1}{4\pi}\left(\frac{3\mathbf{r}(\mathbf{m}\cdot\mathbf{r})}{|\mathbf{r}|^5} - \frac{\mathbf{m}}{|\mathbf{r}|^3}\right) \quad ,$$

Eq. 6.6

where $\mathbf{m} = \boldsymbol{M}\delta V$, and δV is the volume of the magnetised material. As the MR frequency depends only on the z-component of the field perturbation, we note that

$$\Delta\mathbf{H}\cdot\hat{\mathbf{z}} = \frac{1}{4\pi}\left(\frac{3z\left(M_y y + M_z z\right)}{|\mathbf{r}|^5} - \frac{M_z}{|\mathbf{r}|^3}\right)\delta V \quad .$$

Eq. 6.7

Separating the contributions due to M_y and M_z and expressing the result in spherical polar coordinates (r, θ, ϕ), in the laboratory frame we find that

$$\begin{aligned}\Delta H_z(M_y) &= \frac{3}{8\pi|\mathbf{r}|^3}(\sin 2\theta \sin\phi) M_y \delta V \\ \Delta H_z(M_z) &= \frac{3}{4\pi|\mathbf{r}|^3}\left(\cos^2\theta - \frac{1}{3}\right) M_z \delta V\end{aligned} \quad , \qquad \text{Eq. 6.8}$$

and therefore, using Eq. 6.5

$$\begin{aligned}\Delta B_z(M_y) &= \frac{3\mu_0}{8\pi|\mathbf{r}|^3}(\sin 2\theta \sin\phi) M_y \delta V \\ &= \frac{9B_0 \delta V \chi_a}{16\pi|\mathbf{r}|^3}(\sin 2\theta \sin\phi)\sin\Theta\cos\Theta \\ \Delta B_z(M_z) &= \frac{3\mu_0}{4\pi|\mathbf{r}|^3}\left(\cos^2\theta - \frac{1}{3}\right) M_z \delta V \\ &= \frac{3B_0\delta V}{4\pi|\mathbf{r}|^3}\left(\cos^2\theta - \frac{1}{3}\right)\left(\chi_I + \chi_a\left(1 - \frac{3}{2}\sin^2\Theta\right)\right)\end{aligned} \quad . \qquad \text{Eq. 6.9}$$

In comparison, if we represent the effect of the anisotropic susceptibility by allocating the material an effective isotropic susceptibility of $\left(\chi_I + \chi_A(1 - 3/2\sin^2\Theta)\right)$, the predicted field perturbation follows $\Delta B(M_Z)$ only.

6.2.2 Field Perturbation due to a Cylindrical Shell with Radial Anisotropic Magnetic Susceptibility

The field perturbation due to a cylindrical shell with radial anisotropic susceptibility has been considered in previous work for modelling the effect of the myelin sheath [10]. We consider a hollow cylinder centred at the origin and rotated in the x-z plane of the laboratory reference frame, such that the cylinder's axis makes an angle Θ to the z-direction.

If a uniform applied magnetic field $\mathbf{H}_{Applied} = H_0\hat{\boldsymbol{z}}$ is applied in the laboratory frame, the field and induced magnetization can be defined in the local frame of the shell using cylindrical coordinates (ρ, ϕ, z') as

$$\mathrm{H}_{\mathrm{Applied}} = \mathrm{H}_0 \sin\Theta\cos\phi\,\hat{\boldsymbol{\rho}} - \mathrm{H}_0 \sin\Theta\sin\phi\,\hat{\boldsymbol{\phi}} + \mathrm{H}_0\cos\Theta\,\hat{\mathbf{z}}'$$
$$= \begin{bmatrix} \mathrm{H}_0 \sin\Theta\cos\phi \\ -\mathrm{H}_0 \sin\Theta\sin\phi \\ \mathrm{H}_0\cos\Theta \end{bmatrix} \quad .$$

Eq. 6.10

If the principal axis of the cylindrically symmetric tensor is radially oriented, we can write

$$\underline{\underline{\chi}} = \chi_I \underline{\underline{I}} + \begin{bmatrix} \chi_a & 0 & 0 \\ 0 & -\chi_a/2 & 0 \\ 0 & 0 & -\chi_a/2 \end{bmatrix}$$

Eq. 6.11

in this instance so that

$$\mathrm{M_I} = \mathrm{H_0}\chi_\mathrm{I} \begin{bmatrix} \sin\Theta\cos\phi \\ -\sin\Theta\sin\phi \\ \cos\Theta \end{bmatrix}$$
$$\mathrm{M_A} = \mathrm{H_0}\chi_\mathrm{a} \begin{bmatrix} \sin\Theta\cos\phi \\ \frac{1}{2}\sin\Theta\sin\phi \\ -\frac{1}{2}\cos\Theta \end{bmatrix} \quad .$$

Eq. 6.12

First we consider the scalar potential due to $\boldsymbol{M}_A$. We define the internal and external radii of the shell as ρ_i and ρ_o respectively, as shown in Figure 6-2. Using Eq. 6.2 and Eq. 6.12, noting that in cylindrical coordinates $\mathbf{n}' = \hat{\boldsymbol{\rho}}$ at the outer surface of the shell and $\mathbf{n}' = -\hat{\boldsymbol{\rho}}$ at the inner surface, using the Green's function expansion in cylindrical coordinates of $|\mathbf{r} - \mathbf{r}'|^{-1}$, and integrating over ϕ' and z' we find that [10]

$$\Phi_\mathrm{s}(\mathbf{r}) = \mathrm{H_0}\chi_\mathrm{a} \sin\Theta\cos\phi \left(\frac{\rho_{<_\mathrm{o}}}{2\rho_{>_\mathrm{o}}}\rho_\mathrm{o} - \frac{\rho_{<_\mathrm{i}}}{2\rho_{>_\mathrm{i}}}\rho_\mathrm{i} \right) \quad .$$

Eq. 6.13

This gives, inside the shell ($\rho < \rho_i$):

$$\Phi_s(\boldsymbol{r}) = 0 \quad ,$$

Eq. 6.14

and outside the shell ($\rho > \rho_o$):

$$\Phi_s(\boldsymbol{r}) = H_0 \chi_a \sin\Theta \cos\phi \frac{(\rho_0^2 - \rho_i^2)}{2\rho}$$

Eq. 6.15

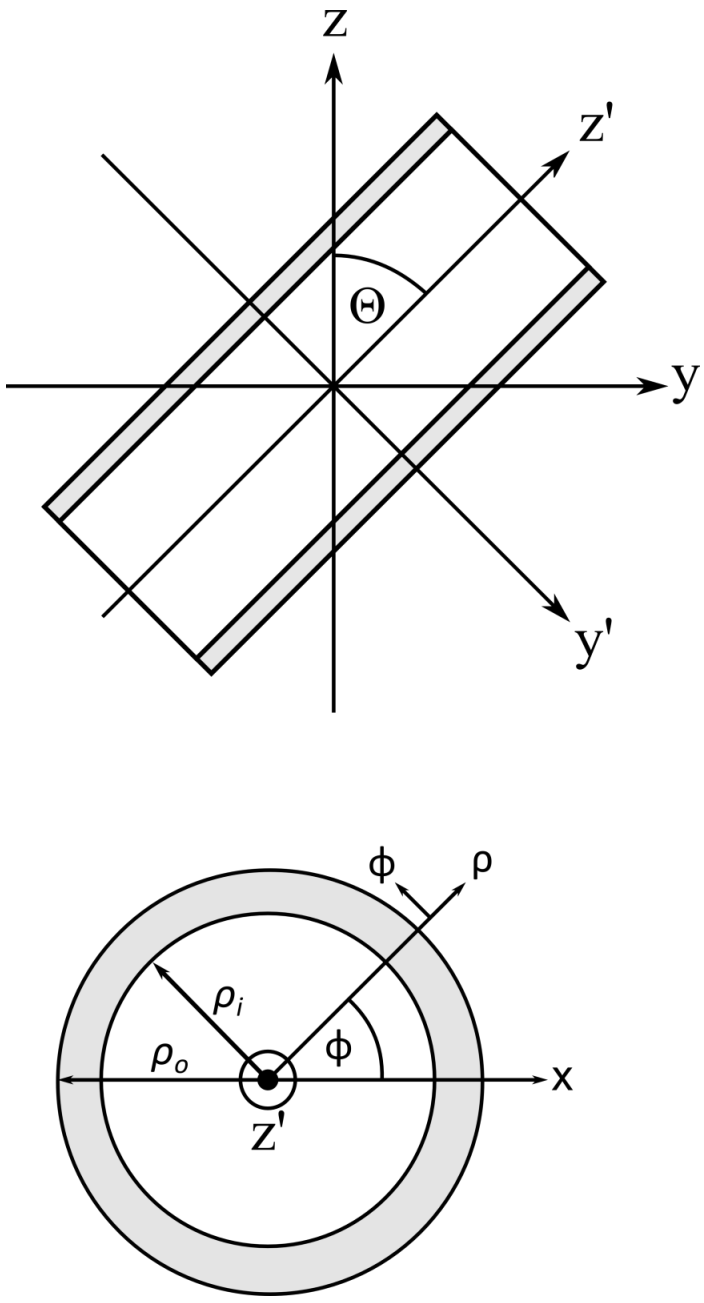

Figure 6-2 – A schematic representation of the cylindrical shell, showing the local Cartesian coordinates (x',y',z') relative to the laboratory coordinates (x,y,z), and their relation to the local cylindrical coordinates (ρ,ϕ,z')

Taking the divergence of the magnetization using the cylindrical polar form of $\boldsymbol{\nabla}$ and integrating using the Green's function expansion we find that the contributions of the volume integral in Eq. 6.2 are [10]

Inside the shell ($\rho < \rho_i$):

$$\Phi_v(\mathbf{r}) = -\frac{3}{4} H_0 \chi_a \sin\Theta \cos\phi \, \rho \ln\left(\frac{\rho_o}{\rho_i}\right) \quad ,$$

Eq. 6.16

and outside the shell ($\rho > \rho_o$):

$$\Phi_v(\mathbf{r}) = -\frac{3}{8} H_0 \chi_a \sin\Theta \cos\phi \frac{(\rho_o^2 - \rho_i^2)}{\rho} \quad .$$

Eq. 6.17

Consequently, the total scalar potential, $\Phi_A(\mathbf{r})$, due to the anisotropic magnetic susceptibility is

$$\Phi_A(\mathbf{r}) = \begin{cases} -\frac{3}{4} H_0 \chi_a \sin\Theta \cos\phi \, \rho \ln\left(\frac{\rho_o}{\rho_i}\right) & (\rho < \rho_i) \\ \frac{1}{8} H_0 \chi_a \sin\Theta \cos\phi \frac{(\rho_o^2 - \rho_i^2)}{\rho} & (\rho > \rho_o) \end{cases}$$

Eq. 6.18

Taking the gradient of the potential yields magnetic field shifts both inside and outside of the cylinder due to the magnetic susceptibility anisotropy in the frame of reference of the cylinder

$$\Delta\mathbf{H_A}(\mathbf{r}) = \begin{cases} \frac{3}{4} H_0 \chi_a \ln\left(\frac{\rho_o}{\rho_i}\right) \sin\Theta \left(cos\,\phi\,\hat{\boldsymbol{\rho}} - sin\,\phi\,\hat{\boldsymbol{\phi}}\right) & (\rho < \rho_i) \\ \frac{1}{8} H_0 \chi_a \sin\Theta \frac{(\rho_o^2 - \rho_i^2)}{\rho^2} \left(cos\,\phi\,\hat{\boldsymbol{\rho}} + sin\,\phi\,\hat{\boldsymbol{\phi}}\right) & (\rho > \rho_o) \end{cases}$$

Eq. 6.19

Taking the projection of $\Delta\mathbf{H}_A(\mathbf{r})$ onto the z-axis in the laboratory frame, and assuming $t \ll \rho_i, \rho_o$ so that $\ln(\rho_o/\rho_i) \approx t/\rho_i$, we find

$$\Delta H_{A_z} = \begin{cases} \frac{3}{4} H_0 \chi_a \frac{t}{\rho_i} \sin^2\Theta & (\rho < \rho_i) \\ \frac{1}{8} H_0 \chi_a \sin^2\Theta \cos 2\phi \frac{(\rho_o^2 - \rho_i^2)}{\rho^2} & (\rho > \rho_o) \end{cases},$$

Eq. 6.20

$$\Delta B_{A_z} = \begin{cases} \frac{3}{4} B_0 \chi_a \frac{t}{\rho_i} \sin^2\Theta & (\rho < \rho_i) \\ \frac{1}{8} B_0 \chi_a \sin^2\Theta \cos 2\phi \frac{(\rho_0^2 - \rho_i^2)}{\rho^2} & (\rho > \rho_0) \end{cases}.$$

Eq. 6.21

Applying the same method to calculate the z-component of the field perturbation due to $\mathbf{M}_I$, we find that

$$\Delta B_{I_z} = \begin{cases} 0 & (\rho < \rho_i) \\ \frac{1}{2} B_0 \chi_I \sin^2\Theta \cos 2\phi \frac{(\rho_o^2 - \rho_i^2)}{\rho^2} & (\rho > \rho_i) \end{cases}.$$

Eq. 6.22

The total field perturbation due to the isotropic and anisotropic components of the magnetic susceptibility is therefore

$$\Delta \mathrm{B}_z = \begin{cases} \frac{3}{4} B_0 \chi_a \frac{t}{\rho_i} \sin^2\Theta & (\rho < \rho_i) \\ \left(\frac{\chi_I}{2} + \frac{\chi_a}{8}\right) B_0 \sin^2\Theta \cos 2\phi \frac{(\rho_o^2 - \rho_i^2)}{\rho^2} & (\rho > \rho_o) \end{cases},$$

Eq. 6.23

where $(\rho_0^2 - \rho_i^2) \sim 2\rho_i t$ for $t \ll \rho_i, \rho_o$. Note that allocating an orientation-dependent value of χ_I in Eq. 6.43, varying as $\sin^2\Theta$, would lead one to erroneously predict that the external field perturbation would scale as $\sin^4\Theta$.

6.2.3 Field Perturbation due to a Spherical Shell with Radial Anisotropic Susceptibility

We consider a spherical shell with radial anisotropic susceptibility, centred at the origin with internal radius, r_i, and external radius, r_o, as shown in Figure 6-3.

If a uniform applied magnetic field $\mathbf{H}_{Applied} = H_0\hat{\boldsymbol{z}}$ is applied in the laboratory frame, the field and induced magnetization due to the isotropic and anisotropic components of the susceptibility can be defined in the local frame of the shell using spherical polar coordinates (r, θ, ϕ) as

$$H_{Applied} = H_0 \cos\theta\, \hat{\mathbf{r}} - H_0 \sin\theta\, \hat{\boldsymbol{\theta}} = \begin{bmatrix} H_0 \cos\theta \\ -H_0 \sin\theta \\ 0 \end{bmatrix} \quad ,$$

Eq. 6.24

and using $\mathbf{M} = \underline{\underline{\chi}}\mathbf{H}$ with

$$\underline{\underline{\chi}} = \chi_I \underline{\underline{I}} + \begin{bmatrix} \chi_a & 0 & 0 \\ 0 & -\chi_a/2 & 0 \\ 0 & 0 & -\chi_a/2 \end{bmatrix} \quad ,$$

Eq. 6.25

such that the principal component of the susceptibility tensor is along the radial direction, we find that the magnetization, M_I, due to the isotropic susceptibility and, M_A, due to the anisotropic susceptibility are given by

$$\left.\begin{aligned} M_I &= H_0\chi_I \begin{bmatrix} \cos\theta \\ -\sin\theta \\ 0 \end{bmatrix} \\ M_A &= H_0\chi_a \begin{bmatrix} \cos\theta \\ \frac{1}{2}\sin\theta \\ 0 \end{bmatrix} \end{aligned}\right\} \quad .$$

Eq. 6.26

We now evaluate the scalar potential given by Eq. 6.2 in the region inside the spherical cavity $(r < r_i)$ and outside the shell $(r > r_o)$. First, we consider the scalar potential $\Phi_A(\mathbf{r})$ due to M_A. Considering the surface integral term

$$\phi_s = 1/4\pi \int \frac{\mathbf{n}' \cdot \mathbf{M}(\mathbf{r}')}{|\mathbf{r} - \mathbf{r}'|} dS' \quad ,$$

Eq. 6.27

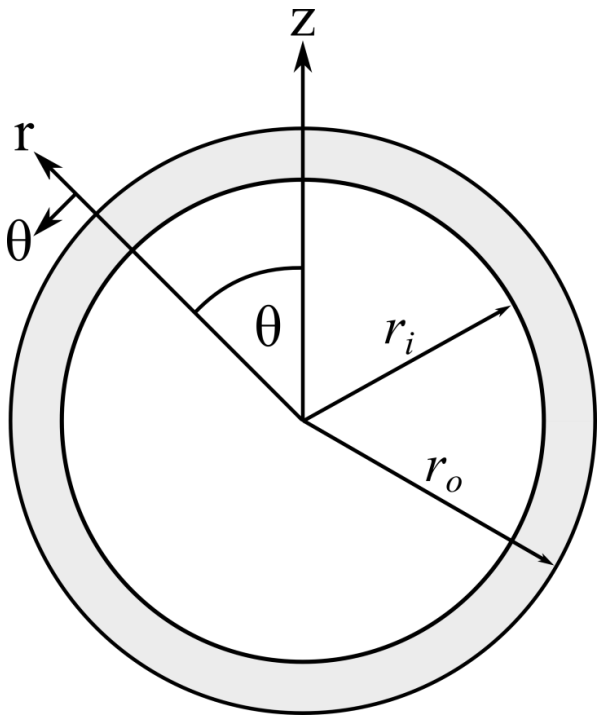

Figure 6-3 – A schematic representation of the spherical shell, showing the Cartesian z-axis and the spherical polar vectors r and θ.

we note that $\mathbf{n}' = \hat{\mathbf{r}}$ at the outer surface of the shell and $\mathbf{n}' = -\hat{\mathbf{r}}$ at the inner surface, so that $\mathbf{n}' \cdot \mathbf{M} = \pm H_0 \chi_A \cos\theta$. The Green's function expansion in spherical coordinates of $|\mathbf{r} - \mathbf{r}'|^{-1}$ is given by

$$\frac{1}{|\mathbf{r}-\mathbf{r}'|} = 4\pi \sum_{l=0}^{\infty} \sum_{m=-l}^{m=l} \frac{1}{2l+1} \frac{r_<^l}{r_>^{l+1}} Y_{l,m}^*(\theta', \phi') Y_{l,m}(\theta, \phi) \quad ,$$

Eq. 6.28

where $Y_{l,m}(\theta, \phi)$ are spherical harmonic functions [18] , and

$$r_< = \begin{cases} r & (r < r_s) \\ r_s & (r > r_s) \end{cases}$$
$$r_> = \begin{cases} r_s & (r < r_s) \\ r & (r > r_s) \end{cases} \quad ,$$

Eq. 6.29

where r_s is the radius of the surface of integration. Then by symmetry only the term with $m = 0$ and $l = 1$, $Y_{1,0}(\theta, \phi) = \sqrt{\frac{3}{4\pi}} \cos\theta$, gives a non-zero integral with respect to θ and ϕ in Eq. 6.27.

Since $\int_0^{2\pi} d\phi' \int_0^{\pi} d\theta' \, Y_{10}(\theta,\phi) Y_{10}(\theta',\phi') \cos\theta' \sin\theta' = \cos\theta$, the contribution to the scalar potential from the surface integral is given by

$$\Phi_s(\mathbf{r}) = \frac{H_0\chi_a}{3}\left(\frac{r_{<_o}}{r_{>_o}^2} r_o^2 - \frac{r_{<_i}}{r_{>_i}^2} r_i^2\right)\cos\theta \quad .$$

Eq. 6.30

Now, following the same approach, the volume integral in Eq. 6.2 can be evaluated using the spherical polar form of $\boldsymbol{\nabla}$ and the Green's function expansion, yielding

$$\Phi_v(\mathbf{r}) = -H_0\chi_a \cos\theta \int_{r_i}^{r_o} \frac{r_<}{r_>^2} r' dr' \quad .$$

Eq. 6.31

Then evaluating and we find that inside the shell ($r < r_i$):

$$\left.\begin{aligned} \Phi_s(\mathbf{r}) &= 0 \\ \Phi_v(\mathbf{r}) &= -H_0\chi_a \cos\theta \, r \ln\left(\frac{r_o}{r_i}\right) \end{aligned}\right\} \quad ,$$

Eq. 6.32

while outside the the shell ($r > r_o$):

$$\left.\begin{aligned} \Phi_s(\mathbf{r}) &= \frac{H_0\chi_a}{3}(r_o^3 - r_i^3)\frac{\cos\theta}{r^2} \\ \Phi_v(\mathbf{r}) &= -\frac{H_0\chi_a}{3}(r_o^3 - r_i^3)\frac{\cos\theta}{r^2} \end{aligned}\right\}$$

Eq. 6.33

The scalar potential, $\Phi_A(\mathbf{r})$, due to the magnetic susceptibility is therefore

$$\Phi_A(\mathbf{r}) = \begin{cases} -H_0\chi_a \cos\theta \, r \ln\left(\frac{r_o}{r_i}\right) & (r < r_i) \\ 0 & (r > r_o) \end{cases} \quad .$$

Eq. 6.34

Taking the gradient of Eq. 6.34, and noting that $\Delta\mathbf{H}_A = -\boldsymbol{\nabla}\Phi_A$, we find that the field perturbation due to the anisotropy

$$\Delta\mathbf{H}_A(\mathbf{r}) = \begin{cases} H_0\chi_a \ln\left(\frac{r_o}{r_i}\right)\left(cos\,\theta\,\hat{\mathbf{r}} - sin\,\theta\,\widehat{\boldsymbol{\theta}}\right) & (r < r_i) \\ 0 & (r > r_o) \end{cases} .$$

Eq. 6.35

We are only interested in the component of the field perturbation which is aligned with the main magnetic field. Taking the projection of $\Delta\mathbf{H}_A(\mathbf{r})$ onto the z-axis in the laboratory frame, we find that

$$\Delta\mathrm{H}_{A_z} = \hat{\mathbf{z}} \cdot \Delta\mathbf{H}_{\boldsymbol{A}} = H_0\chi_a \ln\left(\frac{r_o}{r_i}\right) ,$$

Eq. 6.36

and in fact the components of the field perturbation along the y and z axes are zero. If $r_o = r_i + t$, where t is the thickness of the shell, the z-component of the field, $\Delta\mathrm{H}_{A_z}$ may be written in Cartesian coordinates as

$$\Delta\mathrm{H}_{A_z} = H_0\chi_a \ln\left(\frac{r_i + t}{r_i}\right) = H_0\chi_a \ln\left(1 + \frac{t}{r_i}\right) \quad (r < r_i)$$

Eq. 6.37

If the thickness of the shell is much less than its radius, such that $t \ll r_i$, we may use the approximation $\ln(1 + x) \approx x \quad (x \ll 1)$ and so becomes

$$\Delta\mathrm{H}_{A_z} = H_0\chi_a \frac{t}{r_i} \quad (r < r_i) .$$

Eq. 6.38

The magnetic induction **B** is related to the magnetic field **H** and the magnetization **M** by $\mathbf{B} = \mu_0(\mathbf{H} + \mathbf{M})$ where μ_0 is the permeability of free space. As $\mathbf{M} = \mathbf{0}$ when $(r < r_i)$, this yields

$$\begin{aligned} \Delta\mathrm{B}_{A_z} &= \mu_0 H_0\chi_a \frac{t}{r_i} \quad (r < r_i) \\ &= B_0\chi_a \frac{t}{r_i} \qquad (r < r_i) \\ &= 0 \qquad\qquad (r > r_o) \end{aligned}$$

Eq. 6.39

Now, considering the magnetization due to χ_I, the contribution to the scalar potential from the surface integral is given by

$$\Phi_s(\mathbf{r}) = \frac{H_0\chi_I}{3}\left(\frac{r_{<_o}}{r_{>_o}^2}r_o^2 - \frac{r_{<_i}}{r_{>_i}^2}r_i^2\right)\cos\theta \quad ,$$

Eq. 6.40

and the contribution to the scalar potential from the volume integral

$$\Phi_v(\mathbf{r}) = 0 \quad .$$

Eq. 6.41

Evaluating the potential inside and outside of the shell yields a potential

$$\Phi(\mathbf{r}) = \begin{cases} 0 & (r < r_i) \\ \frac{H_0\chi_I}{3}(r_o^3 - r_i^3)\frac{\cos\theta}{r^2} & (r > r_o) \end{cases} .$$

Eq. 6.42

The potential outside of the sphere is thus that of a unit dipole along the z-direction, with dipole moment [18]

$$\mathbf{m} = \frac{4\pi M_I}{3}(r_o^3 - r_i^3)\hat{\mathbf{z}} \quad ,$$

Eq. 6.43

where $M_I = H_0\chi_I$. The total field perturbation due to the isotropic and anisotropic susceptibility contributions is therefore given by

$$\Delta \mathrm{B}_z = \begin{cases} \frac{B_0\chi_I}{r^3}(r_o^3 - r_i^3)\left(\cos^2\theta - \frac{1}{3}\right) & (r > r_o) \\ B_0\chi_a\frac{t}{r_i} & (r < r_i) \end{cases} ,$$

Eq. 6.44

where $(r_0^3 - r_i^3) \sim 3r_i^2 t$, when $t \ll r_i, r_o$.

6.3 Methods

In order to test the theoretical predictions of the tensor model of anisotropic magnetic susceptibility, we went on to measure experimentally the field perturbations

produced by such susceptibility distributions. Different structures were produced from 25 or 70 μm thick pyrolytic graphite sheet (PGS) (Panasonic EYGS121803 / EYGS121807). Image data were acquired using a Philips Achieva 3T MRI system. Frequency maps were measured using a dual-echo field mapping sequence acquired at 1.5 mm isotropic resolution. For the spherical and cylindrical shell phantoms, the imaging parameters were: TE/TR = 3/40 ms, ΔTE = 1 ms, flip angle = 18°. For the PGS stacks, the imaging parameters were: TE/TR = 3/7.4 ms, ΔTE = 2 ms, flip angle = 8°.

6.3.1 Measuring the External Field Perturbation due to a Small Point-like PGS Stack

Disks of nominally 25 μm thick PGS with a diameter of 4.95 mm were stuck together using cyanoacrylate glue to form a cylindrical stack of ~5 mm in height, using 65.960 ± 0.030 mg of pre-cut disks with a mean mass of 0.984 ± 0.006 mg per disk. The mean thickness of the PGS, measured using a micrometer over 5 sets of 10 disks, was found to be 29.0 ± 0.5 μm. The volume, δV, of PGS in the stack was then calculated to be $\delta V = (3.74 \pm 0.22) \times 10^{-8}$ m^3. The stack was then embedded in an agar-filled perspex sphere with a diameter of 180 mm. Field maps were then generated with the stack at 5 different angles (Θ) to the field. In each case, the field variation in a spherical shell with an internal radius of $r_i = 10$ mm and external radius $r_o = 15$ mm around the stack was analysed to identify the amplitude of the field components due to M_z and M_x. The field variation was then fitted to $\sin 2\Theta$ or $\sin^2 \Theta$ to allow evaluation of the magnitude of χ_I and χ_a, respectively, as defined in Eq. 6.9. Construction of the PGS stacks was carried out by the author.

6.3.2 Measuring the Internal Field Perturbation due to Cylindrical Shells of 25 μm PGS

Glass tubes with three different external diameters (5, 10 and 15 mm) were covered with a layer of nominally 25 μm thick PGS producing a hollow cylinder structure. Narrow slots running lengthwise down the cylinder were left uncovered to reduce any potential RF shielding of the agar inside of the tubes by the PGS coating. The tubes were filled with agar and embedded in a 180 mm diameter spherical agar phantom, as shown in Figure 6-4. Field maps were generated with the tubes at

angles (Θ) of $1°, 17°, 33°, 49°, 59°, 73°,$ and $89°$ with respect to the magnetic field. ROIs were drawn inside each cylinder and in a cylindrical annulus (length $= 15$ mm and inner/outer radii $\approx$ 7.5/15, 6.0/13.5, and $4.5/12.0$ mm for the $15, 10$ and 5 mm diameter cylinders respectively) surrounding the cylinder at each angle to the field using MRIcro (http://www.mricro.com).

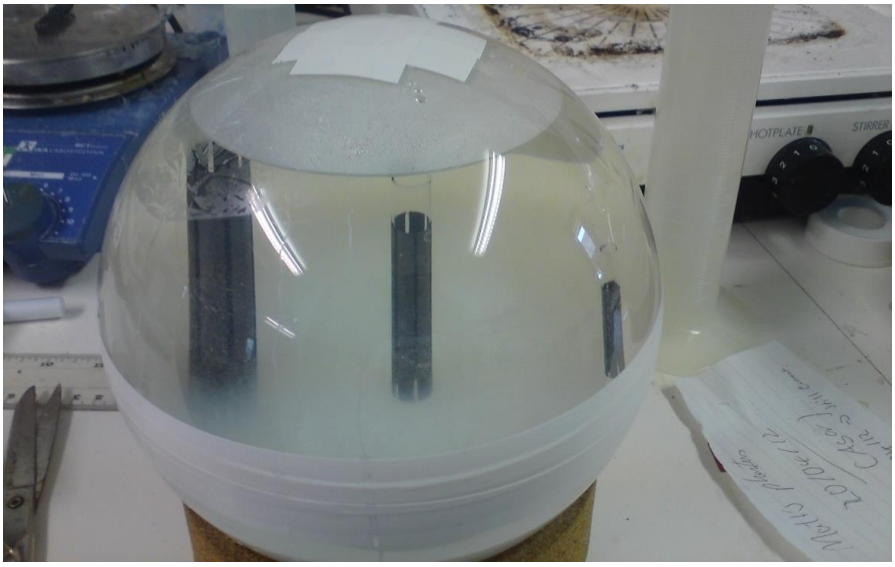

Figure 6-4 – Agar phantom containing 5, 10 and 15 mm diameter glass tubes coated in nominally 25 μm pyrolytic graphite sheet.

Mean internal field shifts were calculated for each cylinder at each angle relative to the mean field in the surrounding cylindrical shell ROI in order to minimize errors due to B_1 phase or imperfect shimming, and compared to values predicted from Eq 6.44. The standard deviation of points in the internal ROI was taken for each measurement as an indication of the uniformity of the internal field shift. Coating of the glass cylinders with PGS was carried out by Ian Thexton in the SPMIC workshop. Construction of the agar phantom was carried out by the author.

6.3.3 Measuring the External Field Perturbation due to a Cylindrical Shell of PGS

Two agar filled glass tubes of 15 mm diameter were embedded in a 180 mm diameter spherical agar phantom. One tube was covered in a layer of 70 μm thick PGS. Field maps were generated with the tubes at angles of $4°, 37°, 48°, 62°, 78°,$ and $90°$ with respect to the field. Cylindrical annuli with an internal radius of $r_i = 7.5$ mm and external radius $r_o = 10$ mm were generated surrounding each

tube at each angle to the field in MATLAB. The mean external field perturbation in the ROI was measured as a function of the angle, ϕ, about the axis of the cylinders, and a linear polynomial fit of the perturbation as a function of $\cos 2\phi$ was calculated, reflecting the variation expected from . The amplitude of the perturbation surrounding the uncoated glass tube was subtracted from that surrounding the PGS coated tube, resulting in corrected amplitude of the field perturbation due to the PGS shell. This amplitude was then plotted as a function of $\sin^2 \Theta$, where Θ is the angle formed between the principal axis of the cylinder and B_0. Coating of the glass cylinders with PGS was carried out by Ian Thexton in the SPMIC workshop. Construction of the agar phantom was carried out by the author.

6.3.4 Measuring the Field Perturbation due to Spherical Shells of 25 µm PGS

Five thin-walled plastic spheres with radii, r, of 5, 10, 12.5, 19 and 25 mm were covered with a layer of nominally 25-µm-thick PGS, filled with water, and set in a 180 mm diameter spherical agar phantom, as shown in Figure 6-5.

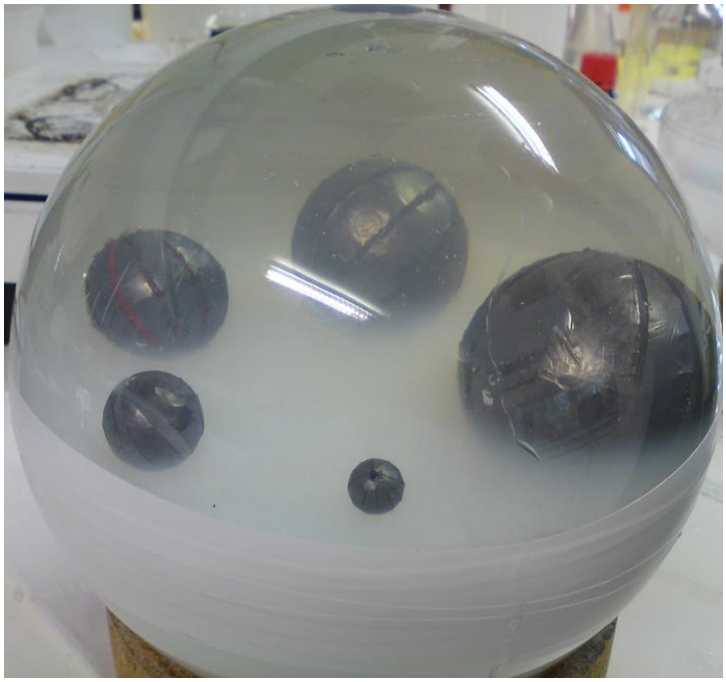

Figure 6-5 – Agar phantom containing plastic spheres with radii of 5, 10, 12.5, 19 and 25mm, coated in nominally 25 µm pyrolytic graphite sheet.

A field map was then generated of the phantom. ROIs were generated inside the spheres and in a spherical shell outside of each sphere in MATLAB, with inner/outer radii = $10.5/18, 18/25.5, 22.5/30, 31.5/39$, and $40.5/48$ mm for the 5, 10, 12.5,

19 and 25 mm radius spheres respectively. The mean field in the internal ROI relative to that in the external ROI was calculated for each sphere. A first order polynomial fit of these values with respect to 1/r was then calculated, reflecting the field variation expected from . Coating of the plastic spheres with PGS was carried out by Ian Thexton in the SPMIC workshop. Construction of the agar phantom was carried out by the author with assistance from Dr Sam Wharton.

6.4 Results

6.4.1 Measuring the External Field Perturbation due to a Small Point-like PGS Stack

Figure 6-6 shows 48×48 mm^2 sections of the measured field maps in the y-z plane through the centre of a PGS stack orientated at different angles to B_0. Also shown are simulated field maps generated using the tensor model of anisotropy, and simulated field maps generated using an orientation-dependent isotropic susceptibility model. The simulations were carried out with susceptibility values of $\chi_I = -135$ ppm and $\chi_a = -260$ ppm, and a perturber volume of 3.289×10^{-8}m^3, representing similar values to those of the PGS stack. A field perturbation following a standard dipolar field pattern $(3\cos^2\theta - 1)$, aligned with B_0, is evident when the normal to the stack is nearly parallel (2˚) or perpendicular (90˚) to the field, with the amplitude being greater in the parallel case. At the intermediate angle (64˚) the field contribution from M_y is evident from the rotation of the field pattern. This rotated field pattern is predicted by the tensor model, but not by the orientation-dependent isotropic model.

M_y and M_z were determined by measuring the amplitude of the field variation in a spherical shell around the stack. From Eq. 6.9, the z-component of the field perturbation (in Hz) may be expressed as $\Delta B_z = A_y(3/2|\mathbf{r}^3|)(\sin 2\theta \sin\phi) + A_z(3/|\mathbf{r}^3|)\left(\cos^2\theta - \frac{1}{3}\right)$, where $A_y = \gamma M_y \delta V \mu_0/4\pi$, and $A_z = \gamma M_z \delta V \mu_0/4\pi$, where $\gamma = 42.576$ MHz T^{-1}. To measure A_y the field was first normalised to remove the variation with $|\boldsymbol{r}|^{-3}$ and $\sin\phi$, and its amplitude then plotted as a function of $1.5\sin 2\theta$. To measure A_z the field was normalised to remove the variation with $|\mathbf{r}|^{-3}$, and its amplitude then plotted as a function of $3\cos^2\theta - 1$.

These plots are shown in Figure 6-7. Linear regression of these plots then yielded values for A_y and A_z at each orientation.

We therefore plot $A_y/(\gamma B_0 \delta V/4\pi)$ vs. $1.5 \sin\Theta \cos\Theta$ and find χ_a from the slope of the plot and also plot $A_z/(\gamma B_0 \delta V/4\pi)$ vs. $1 - 1.5 \sin^2\Theta$ and find χ_a from the slope of the plot and χ_I from the y-intercept. Here, $(\gamma B_0 \delta V/4\pi) = 0.3801$ Hz m^{-3}.

Figures 6-8 and 6-9 show plots of A_y and A_z with $1.5 \sin\Theta \cos\Theta$ and $1 - 1.5 \sin^2\Theta$, indicating a good agreement with theory. Linear regression of the variation of M_y gave $\chi_a = -257 \pm 21$ ppm, and regression of the variation of M_z gave $\chi_I = -121 \pm 10$ ppm and $\chi_a = -234 \pm 18$ ppm.

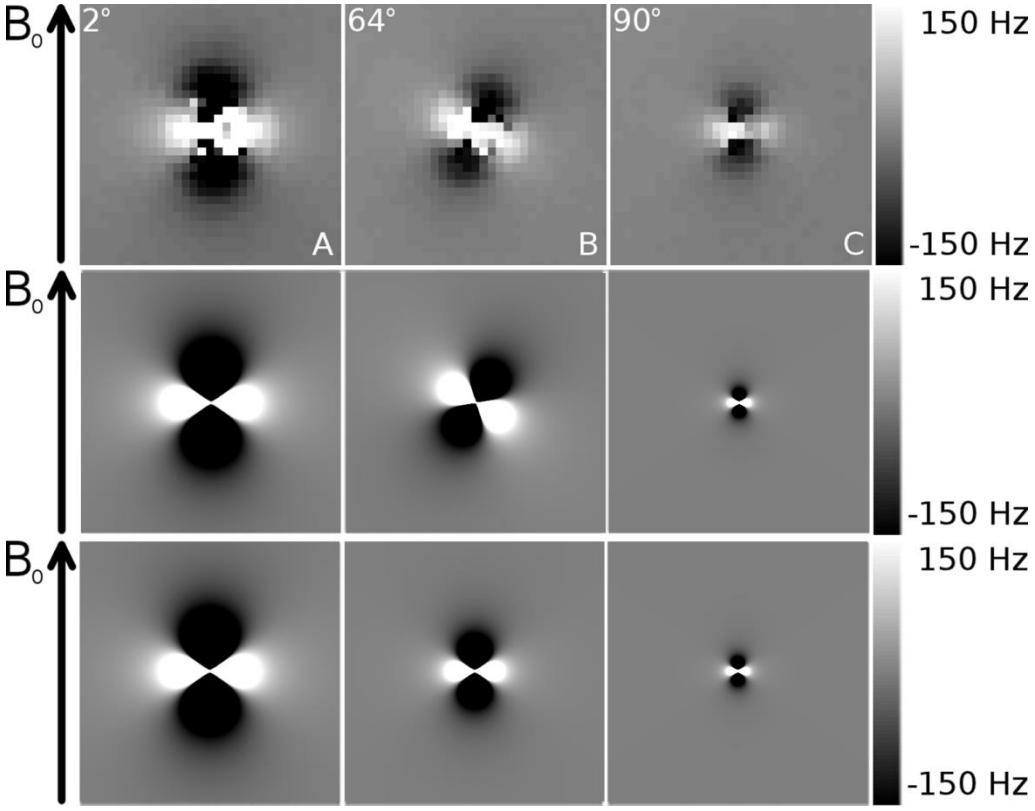

Figure 6-6 Field maps in the y-z plane through the centre of a PGS stack orientated at 2˚, 64˚, and 90˚ toB_0. The top row shows the measured field maps from the phantom, the middle row shows simulated field maps generated using the full tensor model, and the bottom row shows simulated field maps generated using an orientation-dependent isotropic susceptibility model.

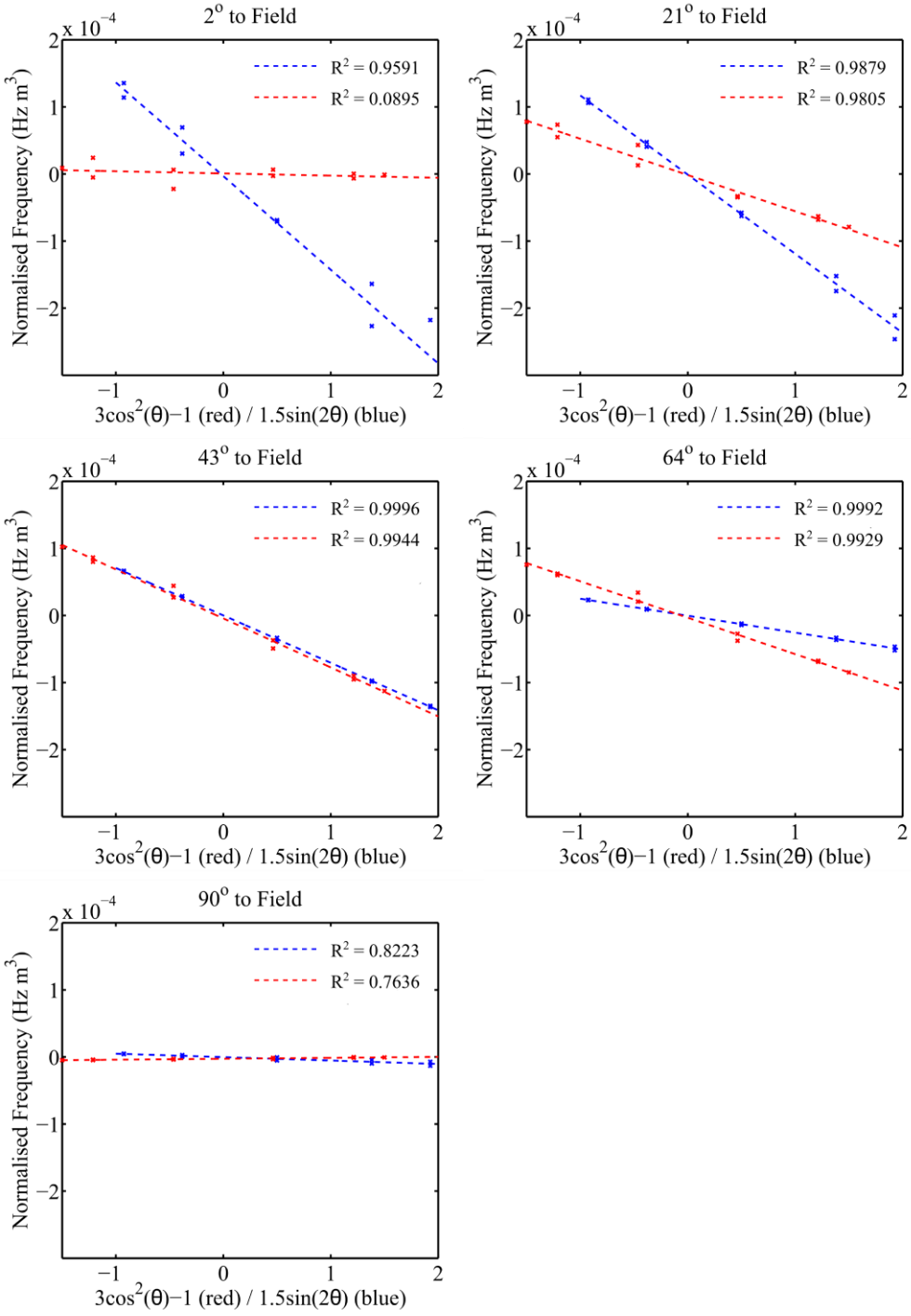

Figure 6-7 – Amplitudes A_y (blue) and A_z (red) of the normalised frequency variation around the PG stack.

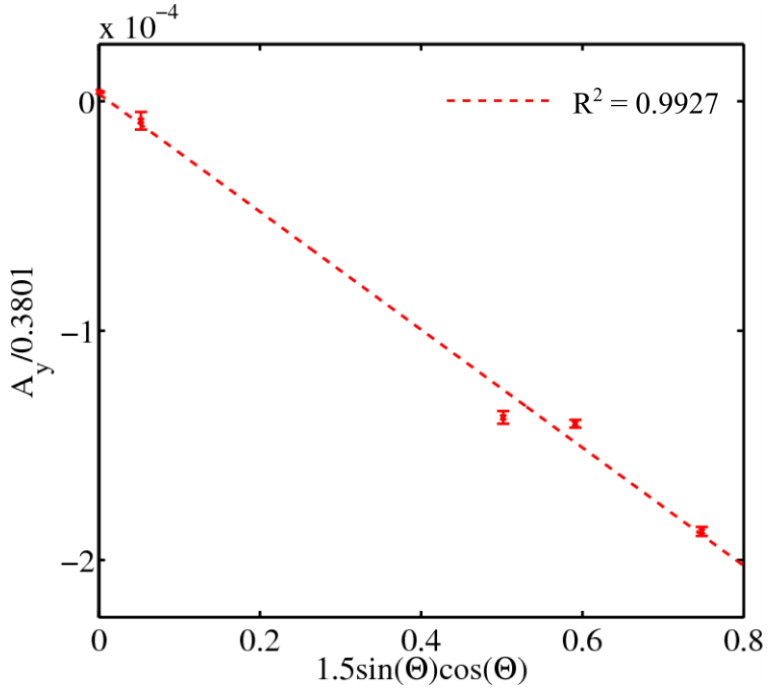

Figure 6-8 – Variation of A_y with respect to $1.5 \sin\Theta \cos\Theta$

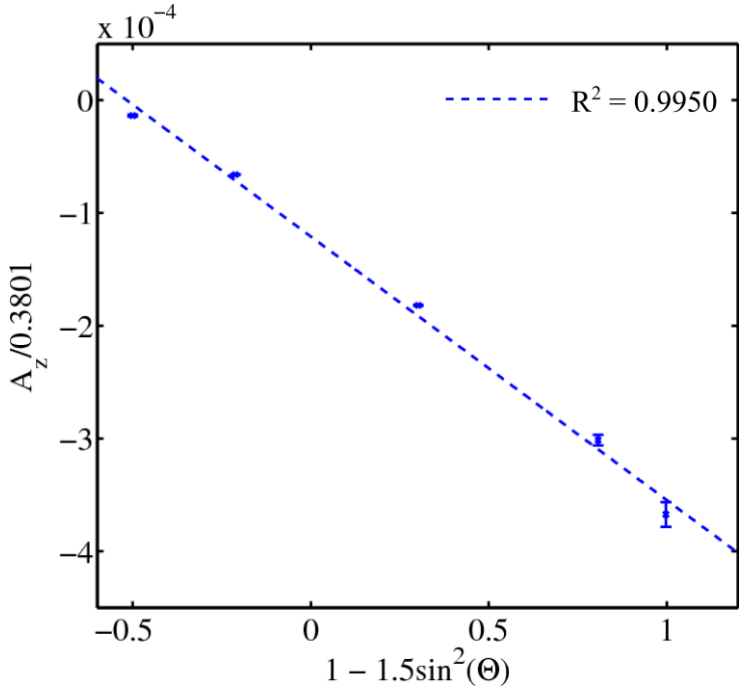

Figure 6-9 – Variation of A_z with respect to $1 - 1.5 \sin^2\Theta$

6.4.2 Measuring the Internal Field Perturbation due to Cylindrical Shells of 25 µm PGS

Figure 6-10 shows a $46.5 \times 149\ \text{mm}^2$ section of the field map acquired with the three PGS covered tubes oriented perpendicular to B_0. A negative frequency offset, whose magnitude increases with decreasing tube radius is evident in the map, as predicted by Eq. 6.23. Figure 6-11 shows plots of the average field offset inside the tubes as a function of $\sin^2\Theta$. This indicates that the frequency offset scales linearly with $\sin^2\Theta$ with a constant of proportionality which increases in magnitude as r decreases.

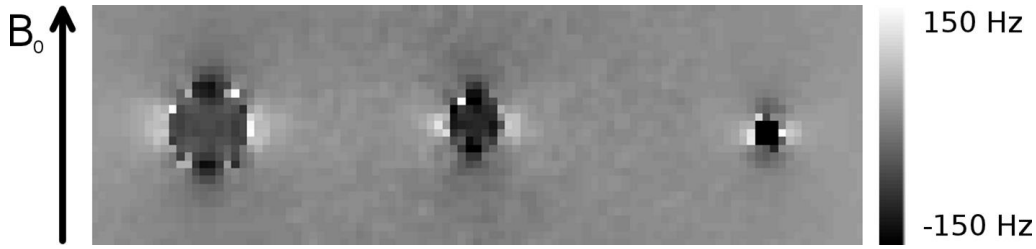

Figure 6-10 – Field map showing the internal field shifts (in Hz) of the PGS-covered tubes with diameters (from left to right) of 5, 10 and 15 mm, with the tubes orientated perpendicular to $\mathbf{B}_0$.

The tH

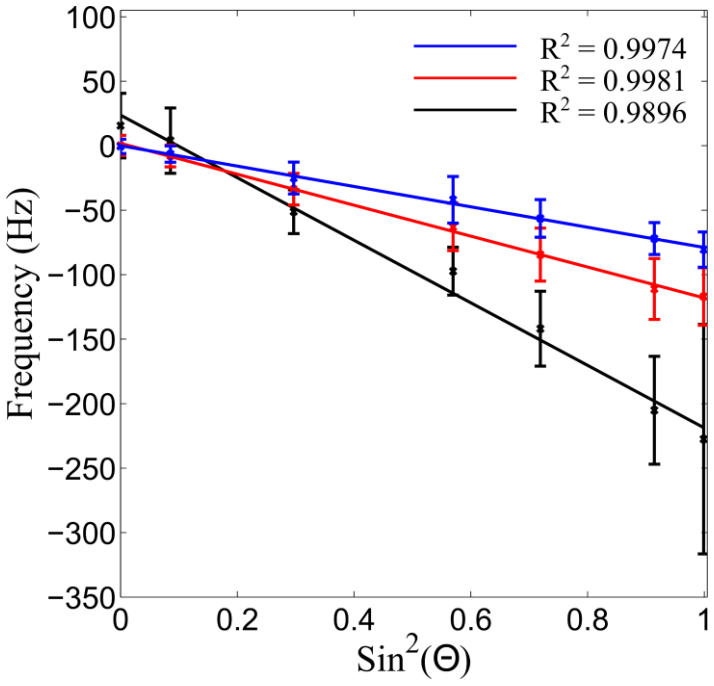

Figure 6-11 - Mean internal frequency due to 5mm (black), 10mm(red) and 15mm (blue) cylindrical shells of PGS, as a function of $\sin^2\Theta$, where Θ is the angle with respect to the field. Error bars show the standard deviation from the mean for the ROI chosen inside each cylinder.

The linear variation of the field offsets with $\sin^2\Theta$ agrees with the theoretical prediction given by Eq. 6.23. Figure 6-12 shows the gradient of the slopes shown in Figure 6-11 as a function of the inverse radius of the cylinders. Linear regression gave a good fit to the data ($R^2 > 0.99$), confirming the linear relationship predicted by , and gave a value of $\chi_a = -221 \pm 11$ ppm.

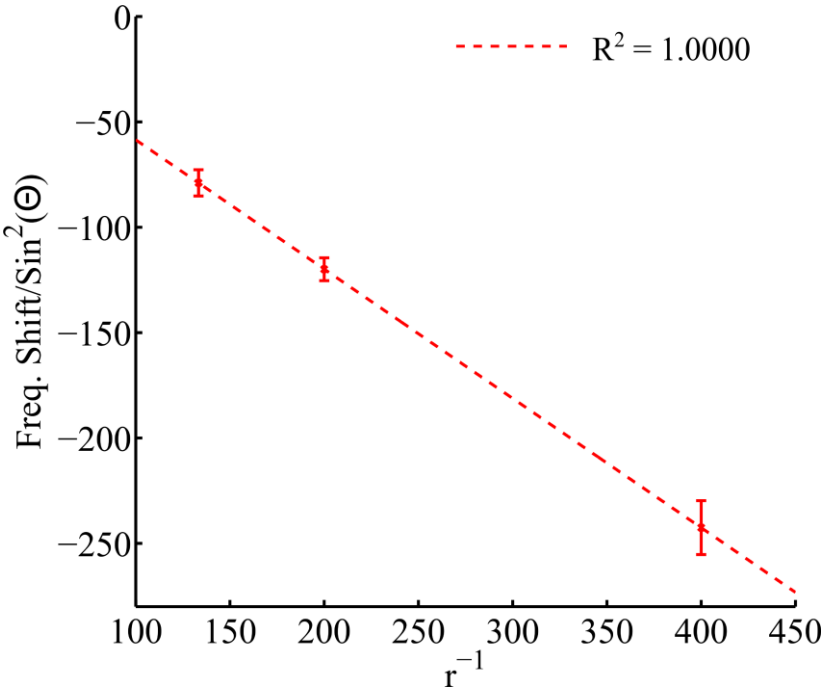

Figure 6-12 – Internal frequency offset normalised for variation with $\sin^2\Theta$ and plotted as a function of inverse radius. Error bars show the 68% confidence interval for the fit to each line shown in Figure 6-11

6.4.3 Measuring the External Field Perturbation due to a Cylindrical Shell of PGS

Figure 6-13 shows a cross section through a field map spanning two glass tubes, with and without PGS coating, with the tubes oriented perpendicular to B_0. The field outside the tubes varies as $\cos 2\phi$, as predicted by Eq. 6.23. Linear regression of the amplitude of this field perturbation with $\sin^2\Theta$, shown in Figure 6-14, gave a good fit to the data ($R^2 > 0.99$). An F-test showed no evidence of any significant improvement in the model with the addition of a $\sin^4\Theta$ term predicted if an orientation-dependent value for χ_I were used in Eq. 6.43 (F=2.4083, P = 0.2481).

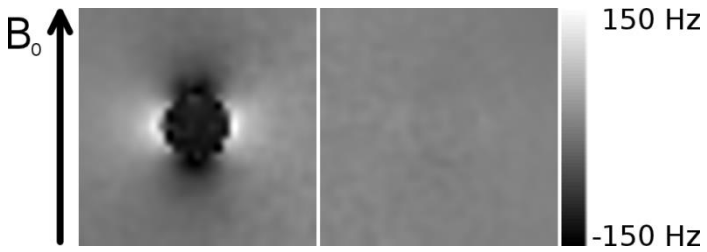

Figure 6-13 – Field map showing the field perturbation in Hz due to the two 15 mm diameter glass tubes, with (left) and without (right) PGS coating, with their principal axes orientated perpendicular to $\mathbf{B}_0$.

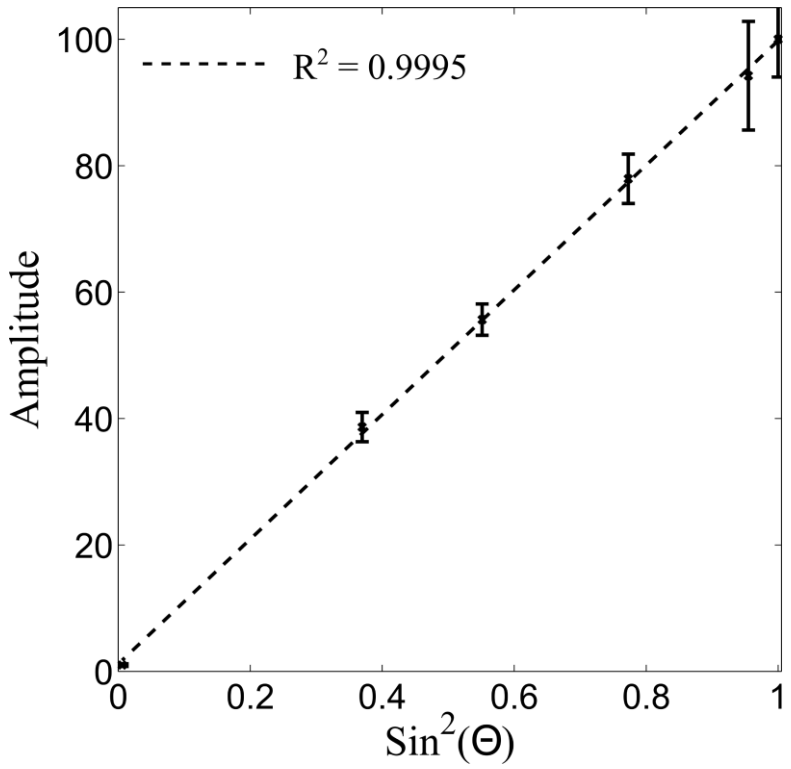

Figure 6-14 – Amplitude of the $\cos 2\phi$ external field perturbation due to a cylindrical shell of PGS, as a function of $\sin^2\Theta$. Error bars show the uncertainty in the amplitude of the field at each orientation.

6.4.4 Measuring the Field Perturbation due to Spherical Shells of 25 µm PGS

Figure 6-15 shows an axial cross-section through the field map spanning the centres of the five spheres. It shows a uniform field offset inside each sphere, with a magnitude that is inversely proportional to the radius, as predicted by Eq. 6.44. The field outside each sphere is relatively homogeneous, indicating that the external dipolar field perturbation is weak.

Figure 6-16 shows the variation of the mean internal field shift with $1/r_i$. Linear regression yields a fit with $R^2 > 0.99$, showing that inside the shells $\Delta\mathbf{B} \propto r_i^{-1}$, as predicted by Eq. 6.44. The slope of the plot is $\gamma B_0 t \chi_a / 2\pi$, yielding a value $\chi_a = -212 \pm 16$ ppm, shown in Table 1.

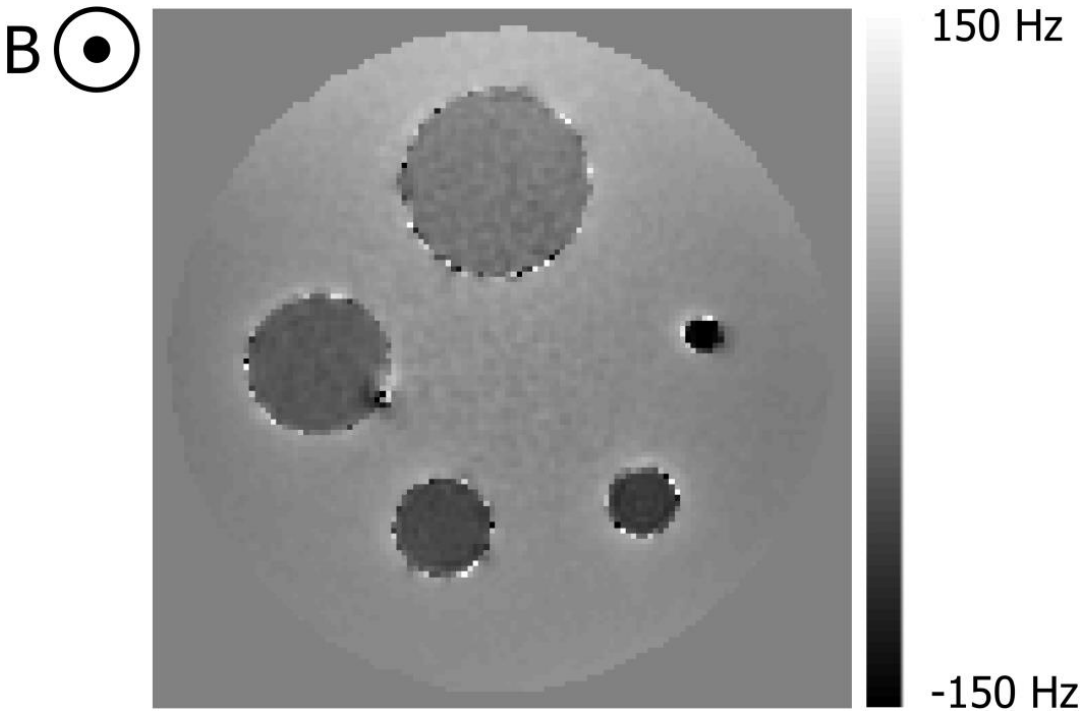

Figure 6-15 – Field map showing the field shifts due to 5 spheres coated in nominally 25µm PGS. A uniform field offset can be seen inside each shell.

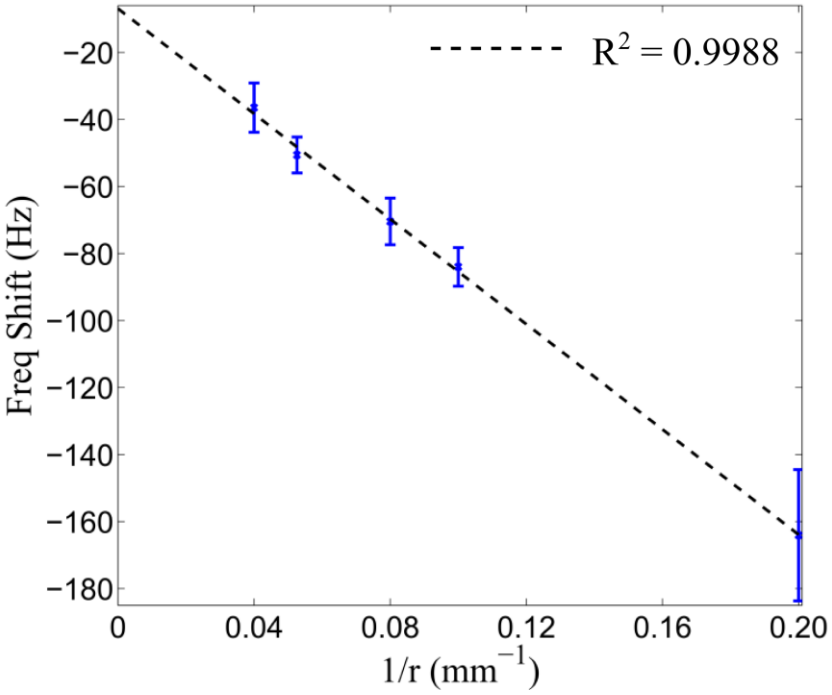

Figure 6-16 – Mean internal field shift due to spherical shells of nominally 25 μm thick PGS, varying as a function of 1/r. Error bars show the standard deviation from the mean for the ROI chosen in each shell.

6.4.5 Summary of Measured Susceptibility Values

Table 1 shows a summary of the susceptibility values measured in experiments 1, 2 and 4.

Table 1 – Calculated Susceptibility Values

Structure	χ_A**/ppm**	χ_I**/ppm**
Stack M_y	-257±21	N/A
Stack M_z	-234±18	-121±10
Cylinders	-221±11	N/A
Spheres	-212±16	N/A

6.5 Discussion

These results confirm the importance of using the full tensor representation of magnetic susceptibility when modelling the effects of structures formed from materials with anisotropic magnetic susceptibility.

If anisotropic magnetic susceptibility is simply modelled as an orientation dependent isotropic property, the contributions from M_y in Eq. 6.5 and χ_a in and would vanish completely, predicting no $\sin 2\theta \sin \phi$ variation about a point source, and no internal field perturbation in spherical or cylindrical shells. The experimental data presented here clearly demonstrates the presence of such field shifts.

The comparison of simulated and experimental data show that the contribution to the field perturbation which varies as $\sin 2\theta \sin \phi$ resulting from the effect of M_y (predicted by Eq. 6.5 & 6.9) is apparent in Figure 6-6, and supported numerically by the high R^2-value of the fit to this model.

The uniform, orientation- and radius-dependent internal field shift demonstrated with the cylindrical 25 μm PGS shells, and the $\sin^2 \Theta \cos 2\phi$ dependent external field shift demonstrated with the 75 μm PGS shell are consistent with and the previously published work by Wharton and Bowtell regarding fibre orientation-dependent MR contrast in white matter [10]. The F-test comparison of first and second order polynomial fits of the external field amplitude to $\sin^2 \Theta$ showed no significant improvement to the model with the addition of a $\sin^4 \Theta$ term, which has been proposed in other models which assume that the effect of anisotropy can be represented by using an orientation-dependent isotropic susceptibility [14].

The radius-dependent internal field perturbation demonstrated with the spherical 25 μm PGS shells is consistent both with and previously published work by Lounila et al regarding the particle size dependence of the NMR line position of signals from spherical lipoproteins [6]. The large internal field shift and relatively small external field perturbation observed suggest that if such structures could be formed on a microscopic scale, and an MR signal be obtained from a water pool contained within them, this may be exploited to form the basis of tunable MR contrast. Contrast materials based on precisely-dimensioned small particles have previously been proposed by Zabow et al in the form of micrometer-sized gold-plated iron and nickel disks, and cylindrical nanoshells [19, 20].

The values of χ_I and χ_a obtained from the work presented here can be seen in Table 1. The measured values for χ_a are consistent between models and with the order of magnitude of previously reported values of the susceptibility of pyrolytic graphite [17], with the exception of the value calculated from the fit to the field perturbation due to M_y in experiment 1. The values for χ_a measured from the PGS stack are higher than those found from spherical and cylindrical shells. This may be explained by the material removed from our cylindrical and spherical shells to ensure detection of the signal from within the structures.

6.6 Conclusions

This work demonstrates the importance of the use of a full tensor model in the modelling of anisotropic magnetic susceptibility in order to accurately predict the magnetic field perturbations produced. The results presented are consistent with previously published observations based on biological systems [6, 10], and may provide an interesting basis for future research.

6.7 References

1. Liu, C., et al., *Susceptibility‐weighted imaging and quantitative susceptibility mapping in the brain*. Journal of Magnetic Resonance Imaging, 2014. DOI: 10.1002/jmri.24768
2. Chen, W., et al., *Quantitative susceptibility mapping of multiple sclerosis lesions at various ages*. Radiology, 2014. **271**(1): p. 183-92.
3. Rudko, D.A., et al., *Multiple Sclerosis: Improved Identification of Disease-relevant Changes in Gray and White Matter by Using Susceptibility-based MR Imaging*. Radiology, 2014. **272**(3): p. 851-864.
4. Wisnieff, C., et al., *Quantitative susceptibility mapping (QSM) of white matter multiple sclerosis lesions: Interpreting positive susceptibility and the presence of iron.* Magn Reson Med, 2014. DOI: 10.1002/mrm.25420
5. Yao, B., et al., *Susceptibility contrast in high field MRI of human brain as a function of tissue iron content*. NeuroImage, 2009. **44**(4): p. 1259-1266.
6. Lounila, J., et al., *Effects of orientational order and particle size on the NMR line positions of lipoproteins*. Phys Rev Lett, 1994. **72**(25): p. 4049-4052.
7. Lee, J., et al., *Sensitivity of MRI resonance frequency to the orientation of brain tissue microstructure*. Proceedings of the National Academy of Sciences, 2010. **107**(11): p. 5130-5135.
8. Schweser, F., et al., *Quantitative imaging of intrinsic magnetic tissue properties using MRI signal phase: an approach to in vivo brain iron metabolism?* NeuroImage, 2011. **54**: p. 2789-807.

9. Li, W., et al., *Magnetic susceptibility anisotropy of human brain in vivo and its molecular underpinnings*. NeuroImage, 2012. **59**(3): p. 2088-2097.

10. Wharton, S. and R. Bowtell, *Fiber orientation-dependent white matter contrast in gradient echo MRI.* Proc Natl Acad Sci U S A, 2012. **109**(45): p. 18559-64.

11. van Gelderen, P., et al., *A torque balance measurement of anisotropy of the magnetic susceptibility in white matter*. Magn Reson Med, 2014. DOI: 10.1002/mrm.25524

12. Wharton, S. and R. Bowtell, *Gradient echo based fiber orientation mapping using R2* and frequency difference measurements*. NeuroImage, 2013. **83**: p. 1011-1023.

13. Liu, C., *Susceptibility tensor imaging.* Magnetic Resonance in Medicine, 2010. **63**(6): p. 1471-1477.

14. Lee, J., et al., *T2*-based fiber orientation mapping.* NeuroImage, 2011. **57**(1): p. 225-234.

15. Liu, C., et al., *3D fiber tractography with susceptibility tensor imaging.* NeuroImage, 2012. **59**(2): p. 1290-1298.

16. Wisnieff, C., et al., *Magnetic susceptibility anisotropy: Cylindrical symmetry from macroscopically ordered anisotropic molecules and accuracy of MRI measurements using few orientations*. NeuroImage, 2013. **70**(0): p. 363-376.

17. Wilson, J.L., M. Jenkinson, and P. Jezzard, *Optimization of static field homogeneity in human brain using diamagnetic passive shims.* Magnetic Resonance in Medicine, 2002. **48**(5): p. 906-914.

18. Jackson, J., *Classical Electrodynamics Third Edition*. 1998: Wiley.

19. Zabow, G., et al., *The fabrication of uniform cylindrical nanoshells and their use as spectrally tunable MRI contrast agents*. Nanotechnology, 2009. **20**(38): p. 385301.

20. Zabow, G., et al., *Microfabricated high-moment micrometer-sized MRI contrast agents.* Magnetic Resonance in Medicine, 2011. **65**(3): p. 645-655.

7 INVESTIGATING THE EFFECTS OF NMR INVISIBLE ORIENTED SPHEROID PERTURBERS ON SIGNAL PHASE

7.1 Introduction

The growing use of magnetic resonance imaging techniques based on the phase of gradient signals means that it is increasingly important to understand the nature of phase contrast and to be cautious in drawing direct inferences from phase measurements or using them as a basis for further calculations. As discussed in Chapter 5, unguarded interpretation of the contrast shown in techniques such as phase imaging and susceptibility-weighted imaging (SWI) may lead to incorrect inferences being made about the underlying tissue composition due to the non-local nature of the phase offsets caused by variations in magnetic susceptibility. Quantitative susceptibility mapping (QSM) was shown to offer an effective remedy to this problem in the imaging of white matter lesions in multiple sclerosis. However, QSM as a technique still relies on certain assumptions about the measured signal phase. For example, in some implementations of QSM, the phase measured in

a voxel is assumed to be linearly proportional to the product of the local magnetic field and echo time. This assumption is immediately confounded by phase variation at $TE = 0$ caused by variation in the phase of B_1, the magnetic component of the RF pulse used to excite the sample. The impact of this may be mitigated by the use of high-pass filtering in QSM, or additionally by measuring the phase accumulation between echoes of a multi-echo FLASH sequence. Removing the effect of B_1 phase variation does not, however, always result in a consistent linear phase evolution being measured in vivo. Recent studies have observed non-linear, orientation-dependent phase evolution in the white matter of the brain [1-6]. This effect has been attributed to sub-voxel level, compartmentalised contributions to the signal from water pools experiencing different magnetic fields due to the structure and anisotropic susceptibility of myelinated nerve fibers [1-3, 5, 6], as well as the shape of microscopic and mesoscopic susceptibility inclusions, in the form of proteins, lipids, deoxyhemoglobin, and other magnetic iron-bearing inclusions [4, 7-10]. The observations relating to myelin structure have been exploited in the development of novel fiber orientation mapping and tractography techniques [3, 11, 12], while the broader effects of susceptibility inclusions and tissue structure have been investigated both using theory and simulation and by experiment, and considered as a source of frequency contrast in multiple sclerosis [7, 9, 13]. Developing a clear understanding of the tissue content and microstructure underlying measured phase evolution is evidently key in extracting useful information about tissue at a sub-voxel level and driving advances in the development of quantitative MRI techniques.

In this study we consider the phase evolution of spins surrounding oriented NMR-invisible spheroids, both in the static regime and in the presence of diffusion. Such structures can exist *in vivo* in the form of inclusions such as oligodendrocytes, myelin sheaths, red blood cells, muscle fibres and extramyocellular lipids. Here, using Monte-Carlo simulations, we consider only a simple model of uniform spheroids with susceptibility χ_i orientated along the direction of an applied magnetic field $\mathbf{B} = B_0\hat{\mathbf{z}}$, surrounded by a randomly distributed ensemble of particles. Using this model, we investigate the effect of variations in the shape and volume fraction of the perturber, and the rate of diffusion of the particles. We demonstrate that the rate of phase accumulation is non-linear in time, and is strongly dependent upon the system parameters. These results reaffirm the complexity of phase behaviour in

media whose content and structure is non-uniform at a sub-voxel level, and show that care must be taken in the interpretation of data based on MRI phase measurements.

7.2 Field Perturbations due to Magnetized Spheroids

As described in Chapter 6, if a magnetic field **H** is applied to a structure with magnetic susceptibility, χ, a magnetization $\mathbf{M} = \chi\mathbf{H}$ is induced in the structure. The magnetic field cause by this magnetization at a position **r** can then be calculated by evaluation of the magnetic scalar potential, $\Phi(\mathbf{r})$ [14].

$$\Phi(\mathbf{r}) = -\frac{1}{4\pi}\int_V \frac{\nabla' \cdot \mathbf{M}(\mathbf{r}')}{|\mathbf{r}-\mathbf{r}'|} d^3r' + \frac{1}{4\pi}\oint_S \frac{\mathbf{n}' \cdot \mathbf{M}(\mathbf{r}')}{|\mathbf{r}-\mathbf{r}'|} dS' \quad .$$

Eq. 7.1

This equation may be solved analytically for structures whose surfaces coincide with a coordinate surface in a curvilinear coordinate system. Such solutions for spherical and cylindrical shells were described in Chapter 6 using spherical and cylindrical polar coordinates, respectively.

In this study we consider field perturbations due to magnetized spheroids. A spheroid is a 3D object based on the rotation of an ellipse with semi-axes a and c about its principal axis, as shown in Figure 7-1 and Figure 7-2. The scalar potential may be solved analytically for a magnetized spheroid using spheroidal coordinates, defined relative to the particular shape in question. Such a solution has previously been described by Sukstanskii and Yablonskiy [7].

Any point on the surface of a spheroid can be defined in terms of the spheroidal coordinates σ, τ, and φ. These coordinates are related to the Cartesian coordinates x, y, and z by

$$\begin{aligned} x &= l[(\sigma^2 \pm 1)(1-\tau^2)]^{1/2}\cos\varphi \\ y &= l[(\sigma^2 \pm 1)(1-\tau^2)]^{1/2}\sin\varphi \\ z &= l\sigma\tau \end{aligned} \quad .$$

Eq. 7.2

Here, and in the following equations, + and – relate to oblate and prolate spheroidal coordinates respectively.

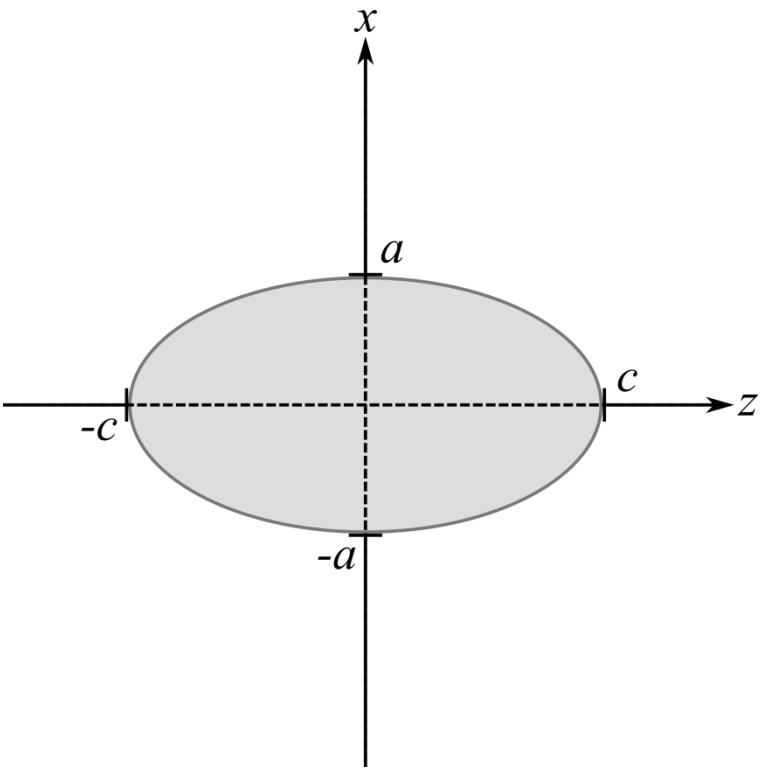

Figure 7-1 – An ellipse with semi-axes a and c.

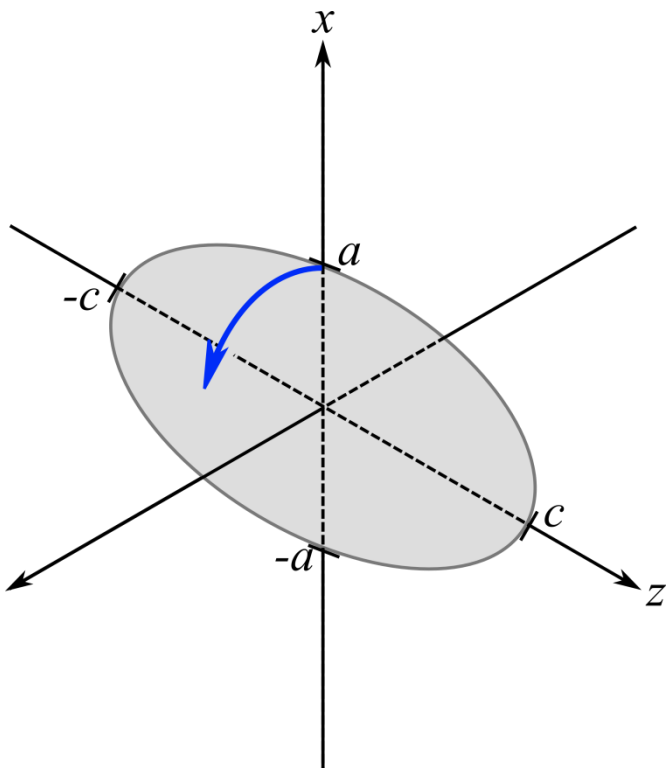

Figure 7-2 – Rotation of an ellipse to create a spheroid

These coordinates cover space via a manifold of confocal spheroids centred on the origin of coordinates with rotational symmetry about the Cartesian z-axis, and with a distance between foci of $2l$, lying on the z-axis for prolate spheroids and in the x-y plane for oblate spheroids [7].

The range of the coordinates σ, τ, and φ is

$$1 \leq \sigma \leq \infty \quad -1 \leq \tau \leq 1 \quad 0 \leq \varphi \leq 2\pi$$

Eq. 7.3

for prolate spheroidal coordinates, and

$$0 \leq \sigma \leq \infty \quad -1 \leq \tau \leq 1 \quad 0 \leq \varphi \leq 2\pi$$

Eq. 7.4

for oblate spheroidal coordinates [7].

The spheroidal surfaces in Cartesian coordinates at which σ is constant are given by

$$\frac{x^2 + y^2}{l^2(\sigma^2 \pm 1)} + \frac{z^2}{l^2\sigma^2} = 1 \quad ,$$

Eq. 7.5

and if we consider a spheroid based on the rotation about the z-axis of an ellipse with semi-axes a and c, $l = |a^2 - c^2|^{1/2}$. The surface of such a spheroid coincides with the σ-surface where

$$\sigma = \sigma_0 = \begin{cases} [1 - (a/c)^2]^{-1/2}, & \begin{cases} a = l(\sigma_0^2 - 1)^{1/2} \\ c = l\sigma_0 \end{cases}, \quad c > a \ (Prolate) \\ [(a/c)^2 - 1]^{-1/2}, & \begin{cases} a = l(\sigma_0^2 + 1)^{1/2} \\ c = l\sigma_0 \end{cases}, \quad c < a \ (Oblate) \end{cases} .$$

Eq. 7.6

Coordinates, therefore, lie within the spheroid when $\sigma < \sigma_0$ and outside of the spheroid when $\sigma > \sigma_0$.

The spheroidal coordinates based on a spheroid with dimensions as described above may be expressed in terms of Cartesian coordinates, l, and the radial coordinate $r = (x^2 + y^2 + z^2)^{1/2}$ as follows

$$\sigma = \left(\frac{1}{2}\left(\left(1+\frac{r^2}{l^2}\right)+\left(\left(1+\frac{r^2}{l^2}\right)^2-\frac{4z^2}{l^2}\right)^{1/2}\right)\right)^{1/2}$$

$$\tau = \left(\frac{1}{2}\left(\left(1+\frac{r^2}{l^2}\right)-\left(\left(1+\frac{r^2}{l^2}\right)^2-\frac{4z^2}{l^2}\right)^{1/2}\right)\right)^{1/2}$$

$$\varphi = \tan^{-1}\frac{y}{x}$$

Eq. 7.7

for prolate spheroidal coordinates, and

$$\sigma = \left(\frac{1}{2}\left(\left(\frac{r^2}{l^2}-1\right)+\left(\left(\frac{r^2}{l^2}-1\right)^2+\frac{4z^2}{l^2}\right)^{-1/2}\right)\right)^{-1/2}$$

$$\tau = \left(\frac{1}{2}\left(\left(1-\frac{r^2}{l^2}\right)+\left(\left(\frac{r^2}{l^2}-1\right)^2+\frac{4z^2}{l^2}\right)^{-1/2}\right)\right)^{-1/2}$$

$$\varphi = \tan^{-1}\frac{y}{x}$$

Eq. 7.8

for oblate coordinates.

Laplace's equation for the magnetic scalar potential, Φ, in spheroidal coordinates is given by [7]

$$\frac{\partial}{\partial\sigma}\left[(\sigma^2 \pm 1)\frac{\partial\Phi}{\partial\sigma}\right] + \frac{\partial}{\partial\tau}\left[(1-\tau^2)\frac{\partial\Phi}{\partial\tau}\right] + \frac{(\sigma^2 \pm \tau^2)}{(\sigma^2 \pm 1)(1-\tau^2)}\frac{\partial^2\Phi}{\partial\varphi^2} = 0 \quad .$$

Eq. 7.9

This equation may be solved with appropriate boundary conditions [15], and the MR frequency shift $\delta\omega$ due to the field perturbation outside the spheroid caused by the magnetized spheroid with susceptibility χ_i in a uniform background matrix with susceptibility χ_e, can then be expressed as

$$\delta\omega_{\pm} = \delta\omega_s\sigma_0(\sigma_0^2 \pm 1)h_{\pm} \quad ,$$

Eq. 7.10

where

$$\delta\omega_s = \gamma B_0(\chi_i - \chi_e)$$

Eq. 7.11

is the characteristic frequency shift,

$$h_+ = \cot^{-1}\sigma - \frac{\sigma}{\sigma^2 + \tau^2} \quad ,$$

and

$$h_- = \frac{\sigma}{\sigma^2 - \tau^2} - \coth^{-1}\sigma \quad .$$

Eq. 7.12

The frequency offset inside the spheroid is given by $\delta\omega = -\delta\omega_s(D_{ze} - 1/3)$, where D_{ze} is the spheroid's demagnetizing factor [16]. In the case of spheroids with semi-axes $a = b$ and $c = qa$, where q is a scalar multiplier relating the lengths of a and c, the demagnetizing factor may be expressed as a function of q, so that [17]

$$D_{ze}(q) = \frac{q\ln\left(q + \sqrt{q^2 - 1}\right)}{(q^2 - 1)^{3/2}} - \frac{1}{q^2 - 1} \quad .$$

Eq. 7.13

D_{ze} consequently varies from ~0 for a long, thin, prolate spheroid, to $1/3$ for a sphere and to ~1 for a flat, oblate spheroid.

A plot of D_{ze} vs q for the shapes considered in this study is shown in Figure 7-3. The mean magnetic field in a spherical region surrounding a spheroidal perturber with fixed volume fraction varies linearly with $D_{ze} - 1/3$.

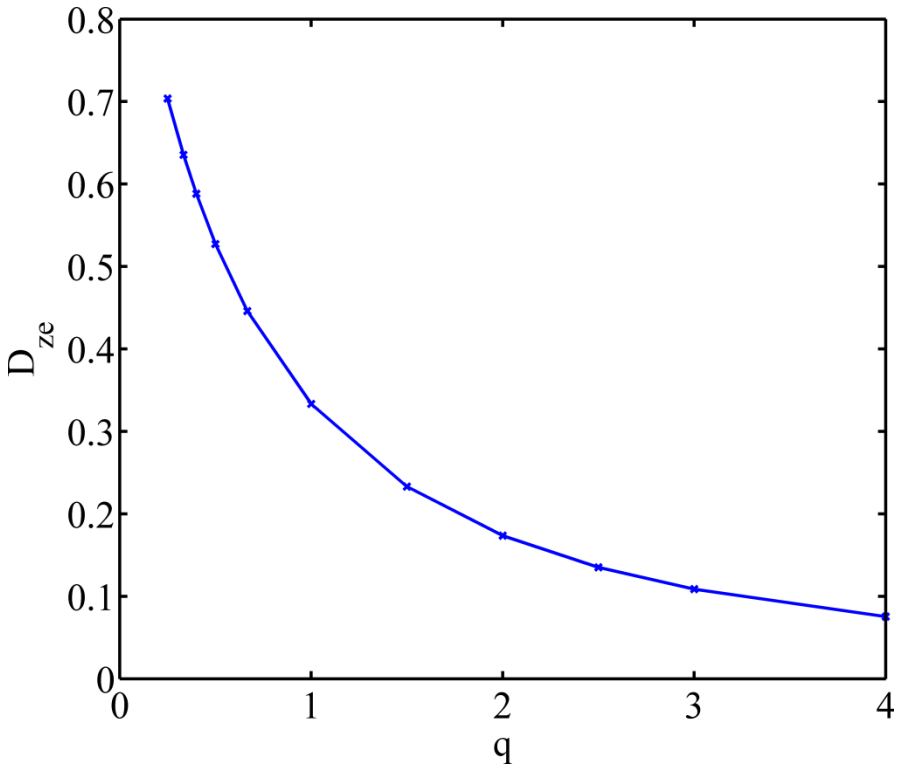

Figure 7-3 – The relationship between D_{ze} and q.

7.3 Simulating the Effects of Spheroidal Perturbers on MR Signal Phase Evolution

In order to carry out a detailed evaluation of the effect of oriented spheroids on the signal phase, Monte Carlo simulations were written in Matlab to simulate the signal from 1,000,000 point-like 'particles' prescessing at the local Larmor frequency in a spherical volume surrounding an impermeable, NMR-invisible, paramagnetic spheroid. A single perturber in a spherical region was used to represent randomly distributed perturbers of low volume fraction in a computationally efficient manner.

The field perturbation due to a spheroid perturber centred on the origin of coordinates of a $300 \times 300 \times 300$ voxel matrix was calculated with $(\chi_i - \chi_e) = 0.1$ ppm according to Eq. 7.10, an example of which is shown in Figure 7-4.

A binary spherical mask centred on the origin with a radius of 300 voxels was created, with the volume of the perturber excluded. This mask defined the region within which the particles were allowed to exist. 1,000,000 particles were then randomly seeded within this volume. These particles then underwent a random walk. At t = 0 s, each particle was assigned a phase of 0. After each step, each particle accumulated a phase increment $\Delta\phi = \gamma \Delta B \, \Delta t / N$, where ΔB is the local field perturbation t the location of the particle, Δt is a time increment and N is the number of steps per time increment. The complex signal S generated by the ensemble was then taken to be

$$S = \sum_{j=1}^{1,000,000} \exp(i\phi_j) \quad ,$$

Eq. 7.14

where ϕ_j is the cumulative phase of particle j, and the amplitude of the signal generated by each particle is 1, and remains constant throughout the simulation. The signal magnitude and phase were then calculated by taking the magnitude and phase of S. In order to give an indication of the size of the region within which significant signal cancellation due to dephasing had occurred, the maximum radial distance, r_π, from the centre of the perturber at which a static particle external to the perturber would have accumulated a phase $\geq \pi$ was recorded after each step. r_π will also be referred to as the dephasing radius. The frequency of the ensemble at each time point was calculated by taking the gradient of the phase evolution to find its rate of change in time at each step.

While the volume fraction was set to be a known constant, and the spheroid was always oriented parallel to the field, the exact position of surrounding spheroids was assumed to be unknown. To reflect this, when a particle attempted to leave the allowed spherical volume surrounding the perturber, it was re-seeded at a random point on the outer surface of the volume.

In order to maintain generality in our simulations, the diffusion length D can be defined in terms of the voxel size δ_Δ, the radius, r_a, of a spherical perturber with a volume equal to that of the spheroid under consideration, and the number of voxels, n, across r_a, such that

$$r_a = n\delta_\Delta \quad .$$

Eq. 7.15

The diffusion length D for a random walk may then be expressed as

$$D = \frac{\delta_\Delta^2 N}{2\Delta t} = \frac{r_a^2 N}{2n^2 \Delta t} \quad ,$$

Eq. 7.16

where N is the number of steps per time interval, Δt, with a step size of $\pm\delta_\Delta$ in each dimension.

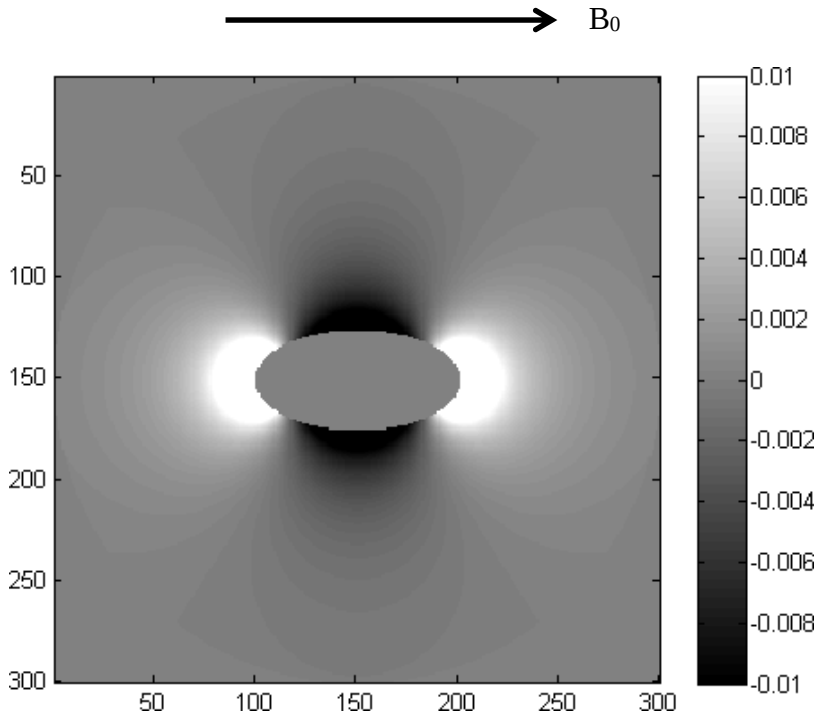

Figure 7-4 – Field perturbation in ppm due to a magnetized spheroid with $(\chi_i - \chi_e) = 0.1$ ppm and $q = 2.00$ /$D_{ze} = 0.1736$

We now define a dimensionless variable, α, so that

$$\alpha = \frac{D}{\delta\omega_s r_a^2} = \frac{N}{2n^2\delta\omega_s\Delta t} \quad ,$$

Eq. 7.17

and β, a dimensionless time variable, where

$$\beta = \delta\omega_s t \quad .$$

Eq. 7.18

The RMS displacement $\langle r^2 \rangle$ of a particle at time t is then given by

$$R = \sqrt{\langle r^2 \rangle} = \sqrt{6Dt} = \sqrt{6\alpha\delta\omega_s r_a^2 t} = r_a\sqrt{6\alpha\beta} \quad .$$

Eq. 7.19

Figures 7-5 and 7-6 show the summed phase and frequency evolution from the particles surrounding a prolate perturber with $q = 2.00$ / $D_{ze} = 0.1736$ in the absence of diffusion.

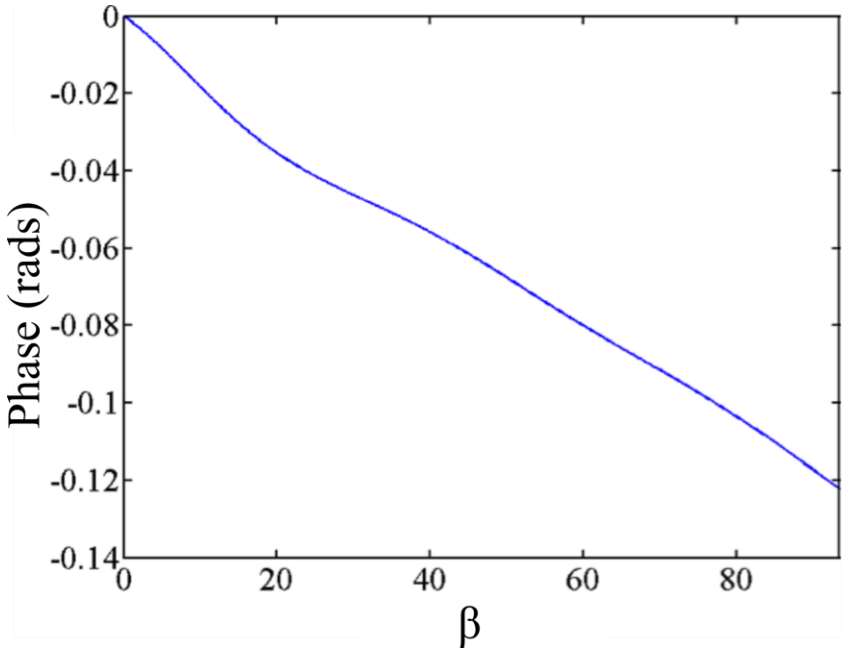

Figure 7-5– Phase evoluation vs. scaled time for the signal sampled from a population of 1,000,000 precessing particles surrounding a prolate perturber with $q = 2.00$ /$D_{ze} = 0.1736$.

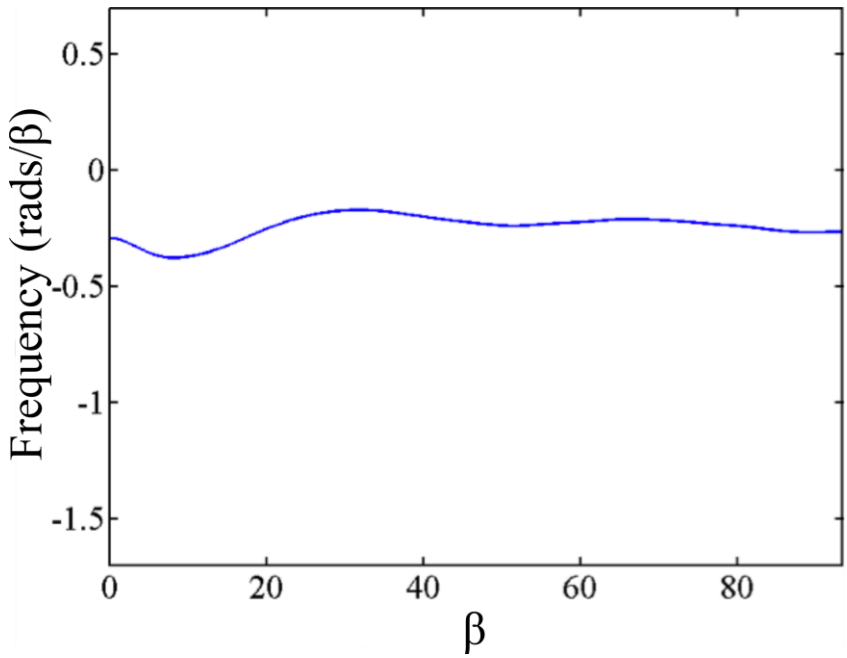

Figure 7-6 – Instantaneous frequency of the phase evolution shown in Figure 7-5.

In our simulations, $\delta\omega_s$ was fixed at $187.26\ \mathrm{s}^{-1}$ representative of a perturber with a susceptibility of 0.1 ppm in a static applied field, where $B_0 = 7$ T. The time interval Δt was set at 1 ms, and simulations were run out to times $t = 500$ ms, so that $0 \leq \beta \leq 93.5$. β provides a measure of the phase accumulated at the surface of the perturber, while α provides a measure of the mean squared displacement due to diffusion in units of r_a on a timescale of $1/\delta\omega_s$. The scaled RMS displacement R/r_a is approximately equal to 4 when $\alpha^{1/2}\beta^{1/2} = \pi$.

To characterise the system, three additional key variables were considered: the volume fraction of the perturber relative to the surrounding medium, the diffusion rate of the particles precessing in the field, and the shape of the spheroidal perturber, characterised by the demagnetizing factor.

As the radius of the total volume under consideration in these simulations is fixed at 150 voxels, the volume fraction and diffusion rate may be altered by varying n and N respectively. To investigate the effect of altering the volume fraction, n was set to values of 32 and 41, corresponding to volume fractions of 1% and 2% respectively. For each volume fraction, N was set to $0, 1, 4, 16, 32$ and 64.

The demagnetizing factor D_{ze} dictates the average field perturbation in a spherical volume surrounding the perturber [18]. This in turn dictates the average frequency

of precession of the individual particles in the field, although it is important to note that this is not necessarily the rate of accumulation of the summed signal phase due to wrapping of the phase accumulated by individual particles about $\pm\pi$ when expressed in complex form. To investigate the effect of perturber shape, the simulation was repeated for a range of perturbers with q values ranging from 0.25 to 4.0 for both volume fractions and the range of N values. The full range of q values and the corresponding demagnetizing factors are shown in Table 7-1, and the full range of combinations of n and N and corresponding α values are shown in Table 7-2.

For each combination of the 3 parameters, data were plotted against the dimensionless time variable β.

The phase evolution for $N = 0, 16, \text{and}, 64$ was plotted against β along with the linear phase evolution that would be expected if the phase simply evolved according to the mean field perturbation in the volume.

q	D_{ze}	$D_{ze} - 1/3$
0.25	0.7036	0.3703
0.33	0.6354	0.3021
0.40	0.5882	2549
0.50	0.5272	0.1939
0.66	0.4459	0.1126
1.0	0.3333	0.0000
1.5	0.2330	-0.1003
2.0	0.1736	-0.1597
2.5	0.1352	-0.1981
3.0	0.1087	-0.2246
4.0	0.0754	-0.2579

Table 7-1 – Aspect ratio q and demagnetizing factor for the range of prolate (q>1) and oblate (q<1) spheroid perturbers considered in this work.

	$\boldsymbol{n = 32}$	$\boldsymbol{n = 41}$
$\boldsymbol{N = 0}$	$\alpha = 0.0000$	$\alpha = 0.0000$
$\boldsymbol{N = 1}$	$\alpha = 0.0026$	$\alpha = 0.0016$
$\boldsymbol{N = 4}$	$\alpha = 0.0104$	$\alpha = 0.0064$
$\boldsymbol{N = 16}$	$\alpha = 0.0418$	$\alpha = 0.0255$
$\boldsymbol{N = 32}$	$\alpha = 0.0836$	$\alpha = 0.0509$
$\boldsymbol{N = 64}$	$\alpha = 0.1671$	$\alpha = 0.1018$

Table 7-2 – Variation of α with diffusion variable *N* and base perturber radius *n*.

A normalised frequency was generated to remove the effect of volume fraction, B_0, and $(\chi_i - \chi_e)$, defined as

$$Normalised\ Frequency\ (NF) = \frac{Frequency}{\delta\omega_s \times VF} \quad ,$$

Eq. 7.20

to allow comparison of the effects of perturber shape and diffusion rate in isolation, and was also plotted against β.

The RMS displacement, R, and dephasing radius, r_π, were also plotted against β to give an indication of the scale of the average displacement of the particles relative to the radius within which the contribution of static particles to the summed phase would be significantly diminished due to strong dephasing.

In order to compare the effect of volume fraction, the non-normalised frequency was also plotted against β for every shape for $N = 0$.

Simulations were carried out on a desktop computer with a 64-bit Linux OS, 3.60 GHz Intel core i7 CPU, and 32 GB of RAM. Each simulation required ~3.52 GB of RAM, and simulation times ranged from ~30 minutes when N = 0 or 1 increasing approximately linearly to ~30 hours when N = 64. The memory- and processor-intensive nature of these simulations means that extending this model to more closely

resemble a biologically realistic *in vivo* scenario, for example by explicitly simulating multiple perturbers of varying shape, size, or distribution in a larger volume, is impractical without access to significantly higher performance computers.

7.4 Results

7.4.1 Field Perturbations due to Varying Spheroid Shape

Figure 7-7 shows the imaginary part of the signal measured at t = 250 ms in the absence of diffusion. Rapid variation of the imaginary signal indicates regions in which the phase varies rapidly. B_0 runs left to right, and as such the positive poles of the dipole-like fields are to the left and right of the perturbers, while the negative poles are above and below.

The relative volume covered by the positive field perturbation reduces progressively between the most oblate (q=0.25) and most prolate (q=4.00) perturbers, while the rate of variation of the positive field offset near the perturber increases. Conversely, the relative volume covered by the negative field perturbation increases progressively between the most oblate (q=0.25) and most prolate (q=4.00) perturbers, while the rate of variation of the negative field offset near the perturber decreases.

7.4.2 Evolution of Signal Phase and Frequency with Varying Demagnetization Factor and Diffusion Rate

Figures 7-8 to 7-18 show the variation of phase, normalised frequency, RMS displacement and dephasing radius as a function of β for perturbers with the full range of q values $(0.25 \text{ to } 4)$, and a volume fraction of 2% (n = 41). The phase is displayed for diffusion rates where $\alpha = 0, 0.0254,$ and 0.1018. In addition, the phase expected from the mean field offset is shown. The normalised frequency evolution is shown for $\alpha = 0, 0.0016, 0.0064, 0.0254, 0.0509$ and 0.1018. The RMS displacement and is displayed for $\alpha = 0.0016, 0.0064, 0.0254, 0.0509$ and 0.1018 alongside the dephasing radius. The distances R and r_π are expressed in units of r_a.

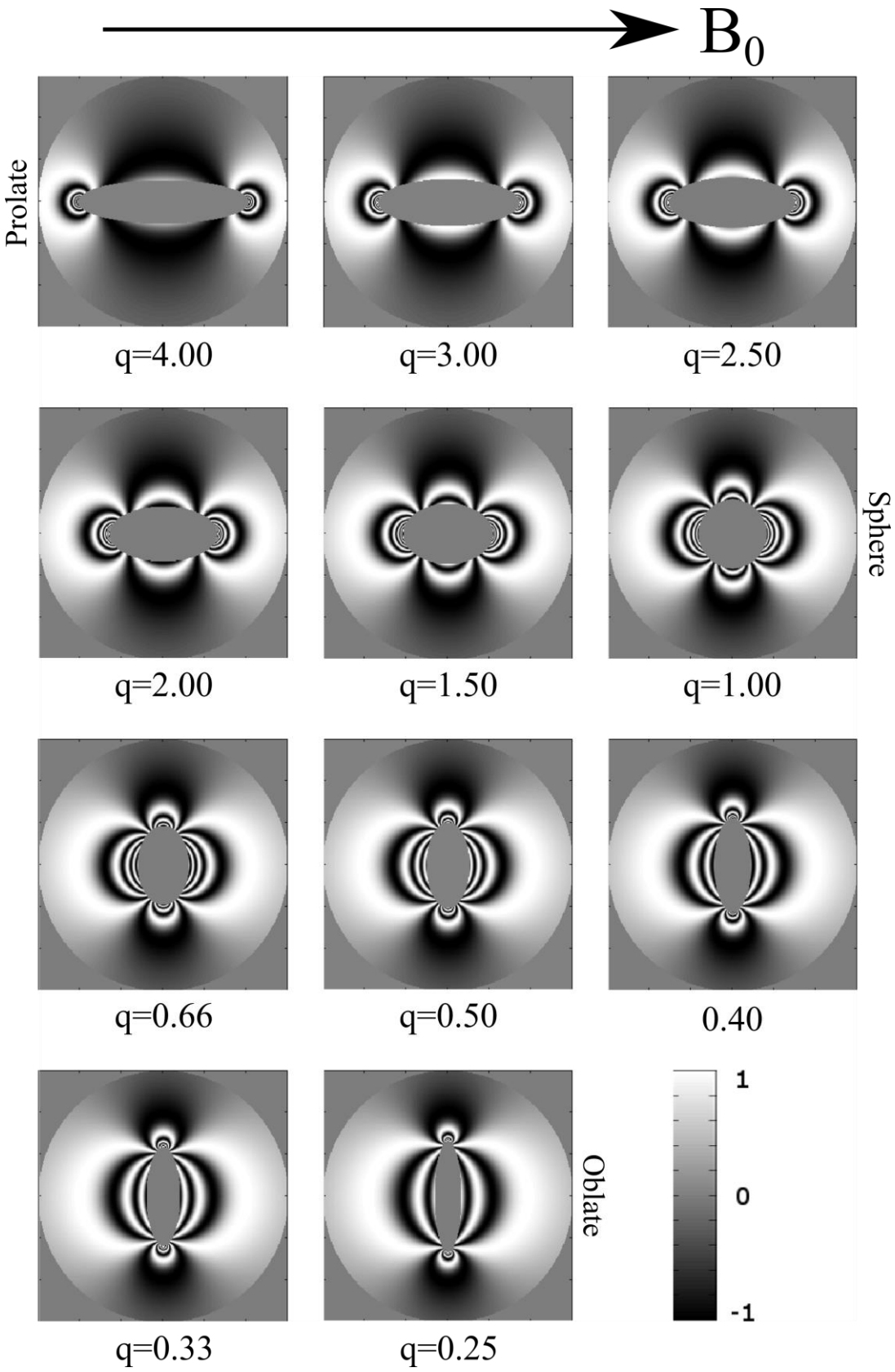

Figure 7-7 – Imaginary component of the complex signal measured at t = 250 ms in the static regime where N = 0 for perturbers with different q-factors and a VF of 2 %.

7.4.2.1 Phase Evolution

The rate of phase accumulation predicted by the mean field perturbation (and shown by the frequency when t = 0 s) is proportional to $D_{ze} - 1/3$, as expected from theory [17] and as shown in Figure 7-21. For all perturbers, the calculated phase evolution differed from that predicted by the mean field perturbation, with the difference greatest where there is no diffusion ($\alpha = 0$). The calculated phase evolution tended increasingly towards that predicted by the mean field perturbation as the rate of diffusion increased ($\alpha = 0.0254$ and $\alpha = 0.1018$). The deviation of the calculated phase evolution from the predicted phase is greatest for the flattest oblate spheroid perturber with $q = 0.25$ /$D_{ze} = 0.7036$, reducing with D_{ze} to a minimum with the longest prolate perturber with $q = 4.00$ /$D_{ze} = 0.0754$.

7.4.2.2 Frequency Evolution

The normalised frequency (NF) evolution displays a strong dependence on the shape of the perturber. This shape dependence is most pronounced in the static regime where $\alpha = 0$.

The frequency of the subsequent oscillation of the NF in the absence of diffusion increases as D_{ze} decreases, and the perturber becomes more spherical, the magnitude of the oscillations decreases and the rate of damping increases, revealing a gradual downward trend in the NF over time. In contrast, there is little variation in the magnitude of the initial fall in NF in the static regime between the sphere and the most prolate perturber with $q = 4.00$ / $D_{ze} = 0.0754$. The magnitude of the subsequent oscillation increases slightly between the sphere and the prolate perturber with $q = 1.50$ /$D_{ze} = 0.2330$, and then remains fairly constant as D_{ze} decreases. In all but the longest prolate perturber, the magnitude of the oscillation is greater than that of the initial fall in NF, causing the NF to increase above its initial value at $\beta = 0$ at some points in time. The frequency of the oscillation reduces with D_{ze} as the perturber is progressively elongated.

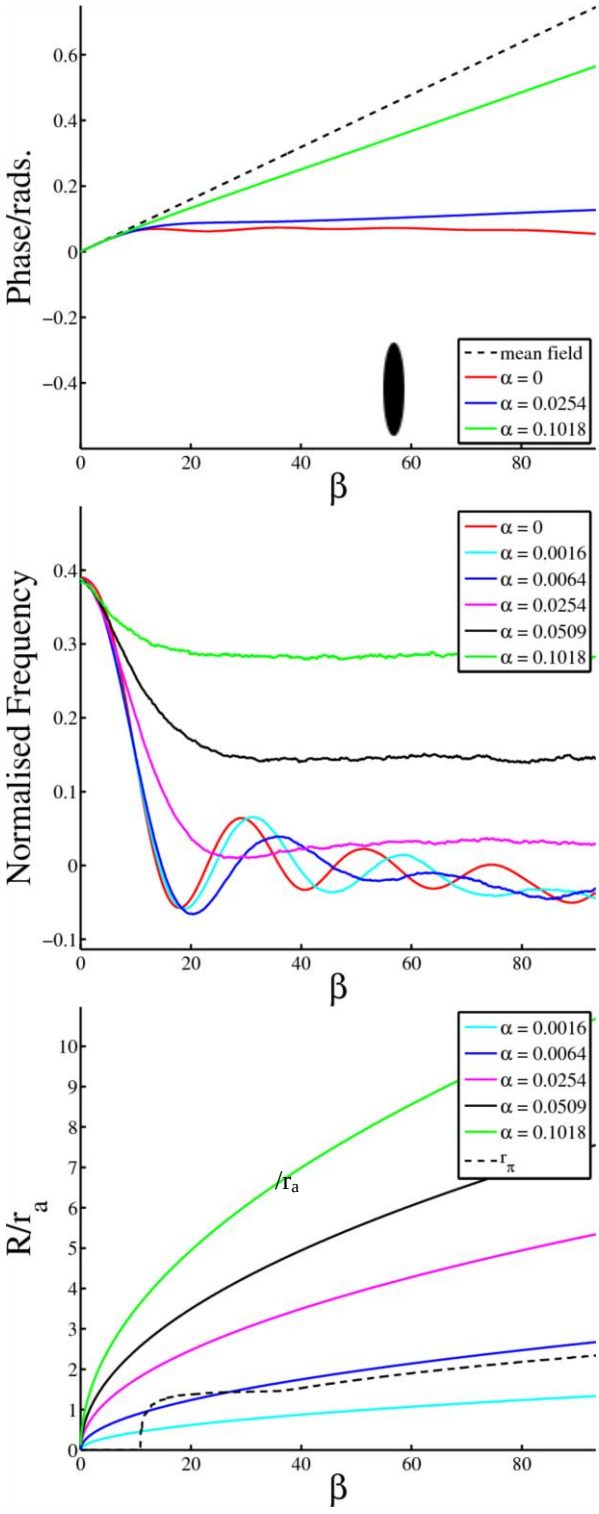

Figure 7-8 Oblate perturber $q = 0.25$ / $D_{ze} = 0.7036$. When α = 0, the phase deviates rapidly from that predicted by the mean field when β > ~10. The frequency falls before oscillating with a gradually decreasing magnitude. A α increases, the phase converges on that predicted by the mean field, and the frequency oscillations are damped before the normalised frequency begins to converge on its initial value of ~0.4 when β = 0.

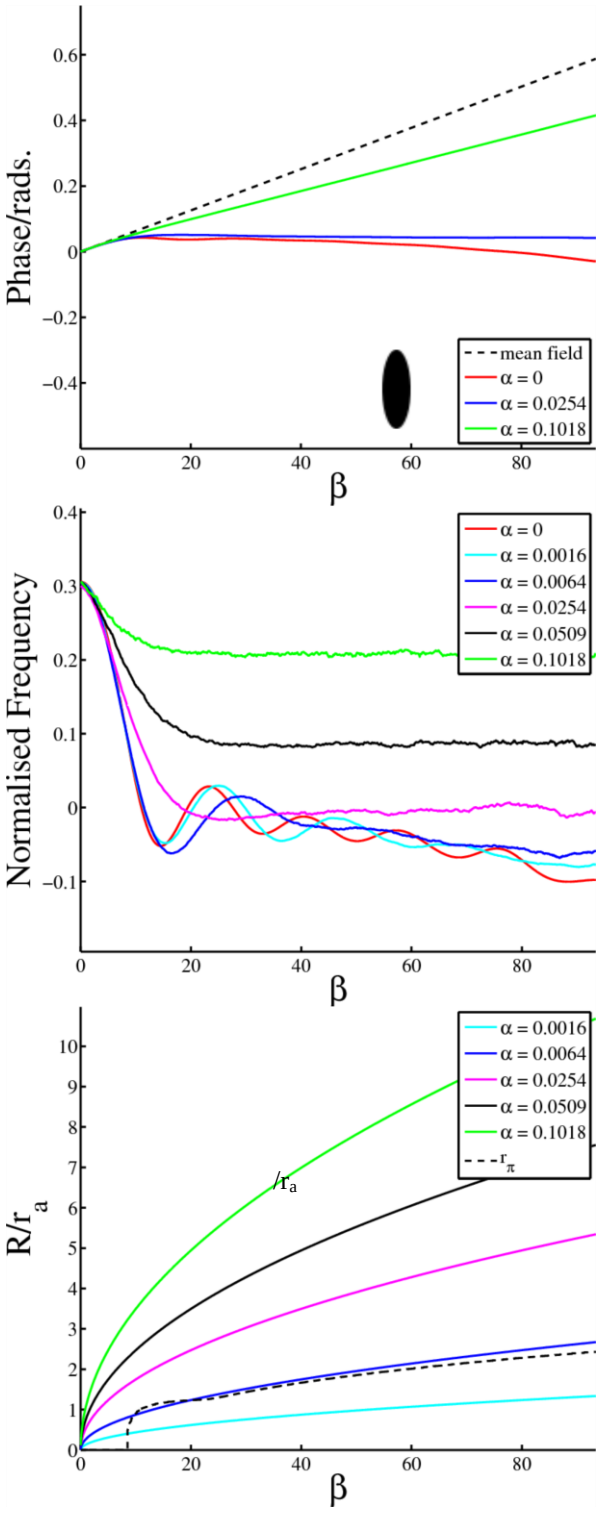

Figure 7-9 – Oblate perturber $q = 0.33$ /$D_{ze} = 0.6354$. When α = 0, the phase deviates rapidly from that predicted by the mean field when β > ~10. The frequency falls before oscillating with a gradually decreasing magnitude while continuing a slight downwards trend. A α increases, the phase converges on that predicted by the mean field, and the frequency oscillations are damped before the normalised frequency begins to converge on its initial value of ~0.3 when β = 0.

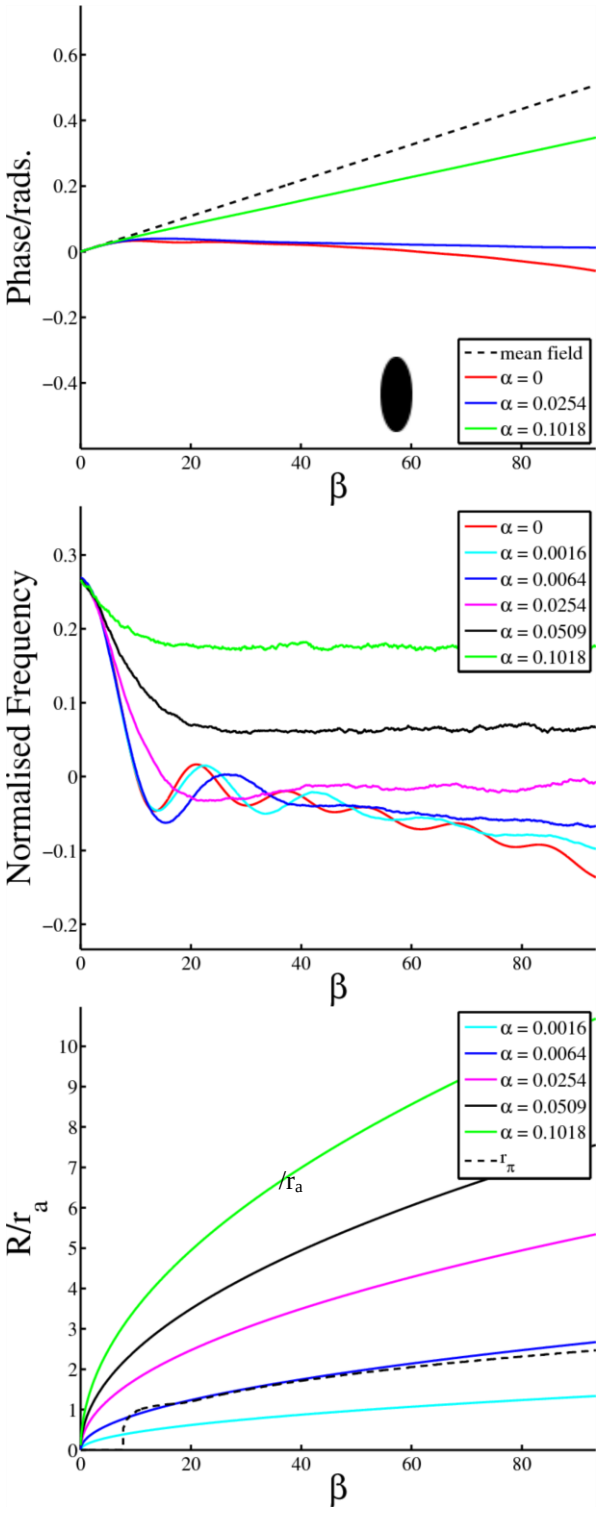

Figure 7-10 – Oblate perturber $q = 0.40$ /$D_{ze} = 0.5882$. When α = 0, the phase deviates rapidly from that predicted by the mean field when β > ~10. The frequency falls before oscillating with a gradually decreasing magnitude while continuing a slight downwards trend. A α increases, the phase converges on that predicted by the mean field, and the frequency oscillations are damped before the normalised frequency begins to converge on its initial value of ~0.27 when β = 0.

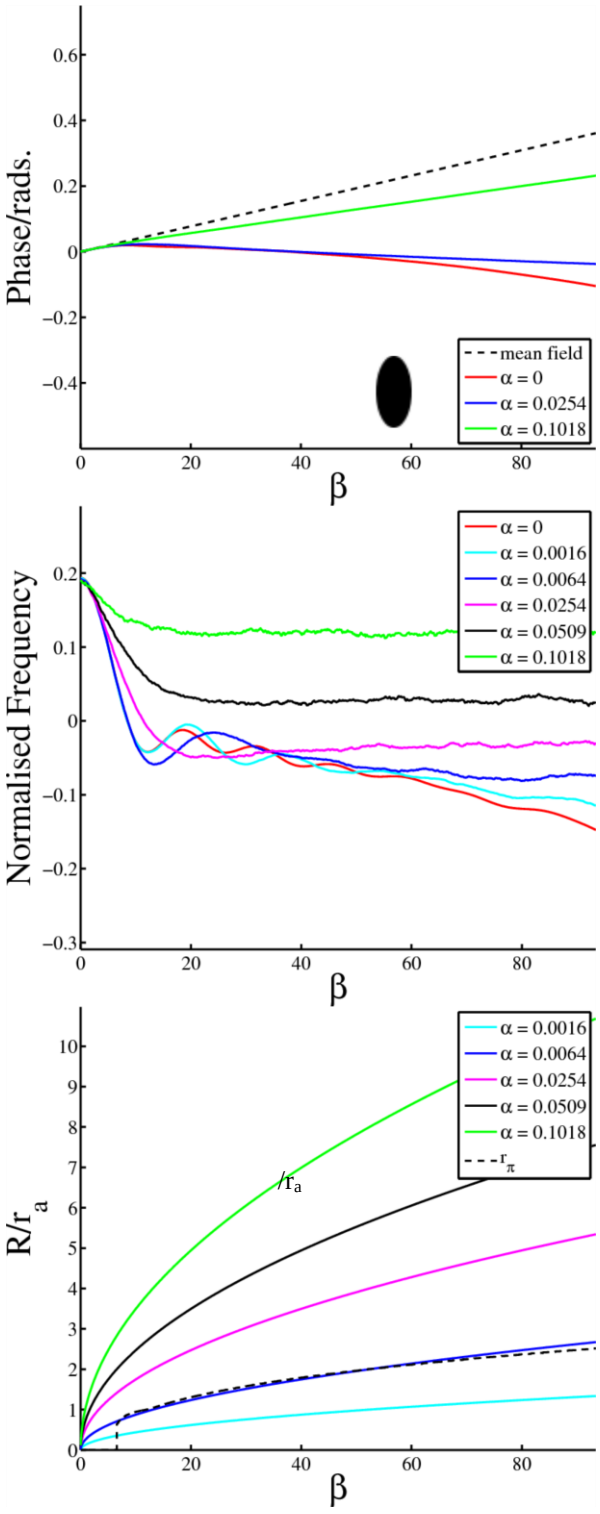

Figure 7-11 – Oblate perturber $q = 0.50$ /$D_{ze} = 0.5272$. When α = 0, the phase deviates rapidly from that predicted by the mean field when β > ~10. The frequency falls before oscillating with a gradually decreasing magnitude while continuing a slight downwards trend. A α increases, the phase converges on that predicted by the mean field, and the frequency oscillations are damped before the normalised frequency begins to converge on its initial value of ~0.2 when β = 0.

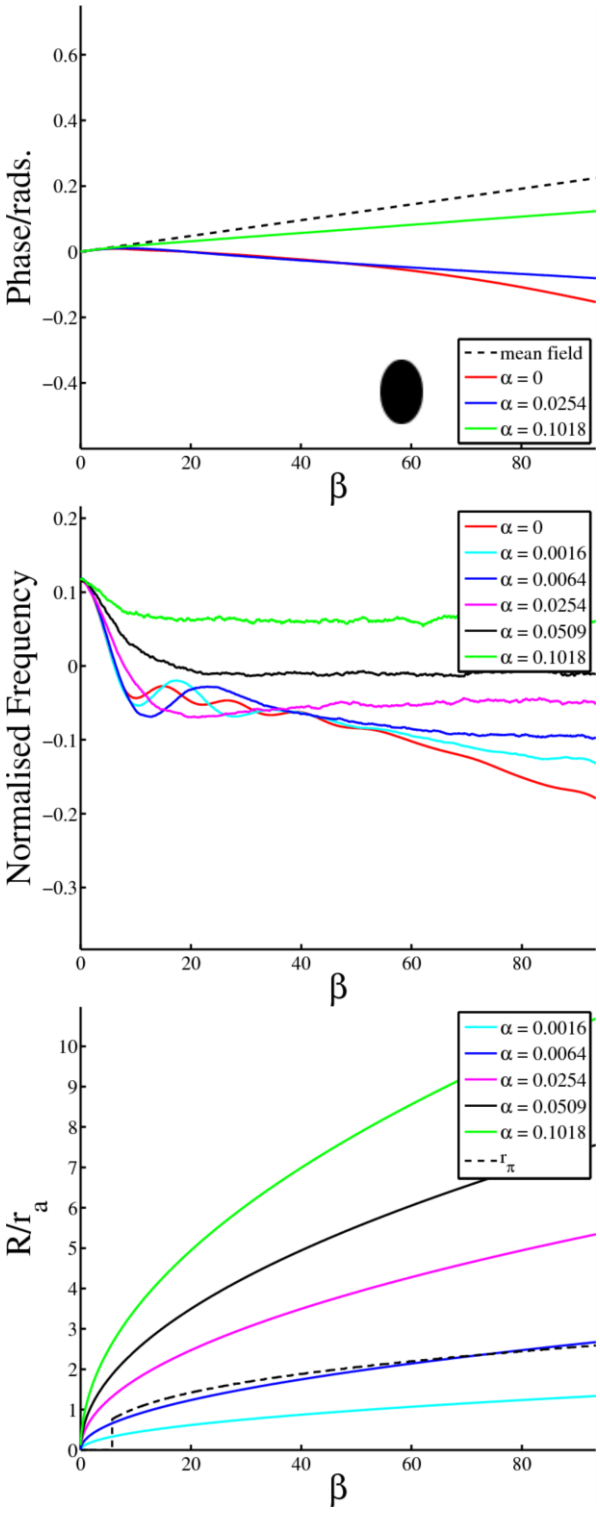

Figure 7-12 – Oblate perturber $q = 0.66$ /$D_{ze} = 0.4459$. When α = 0, the phase deviates from that predicted by the mean field when β > ~10. The frequency falls before oscillating with a gradually decreasing magnitude while continuing a downwards trend. A α increases, the phase converges on that predicted by the mean field, and the frequency oscillations are damped before the normalised frequency begins to converge on its initial value of ~0.1 when β = 0.

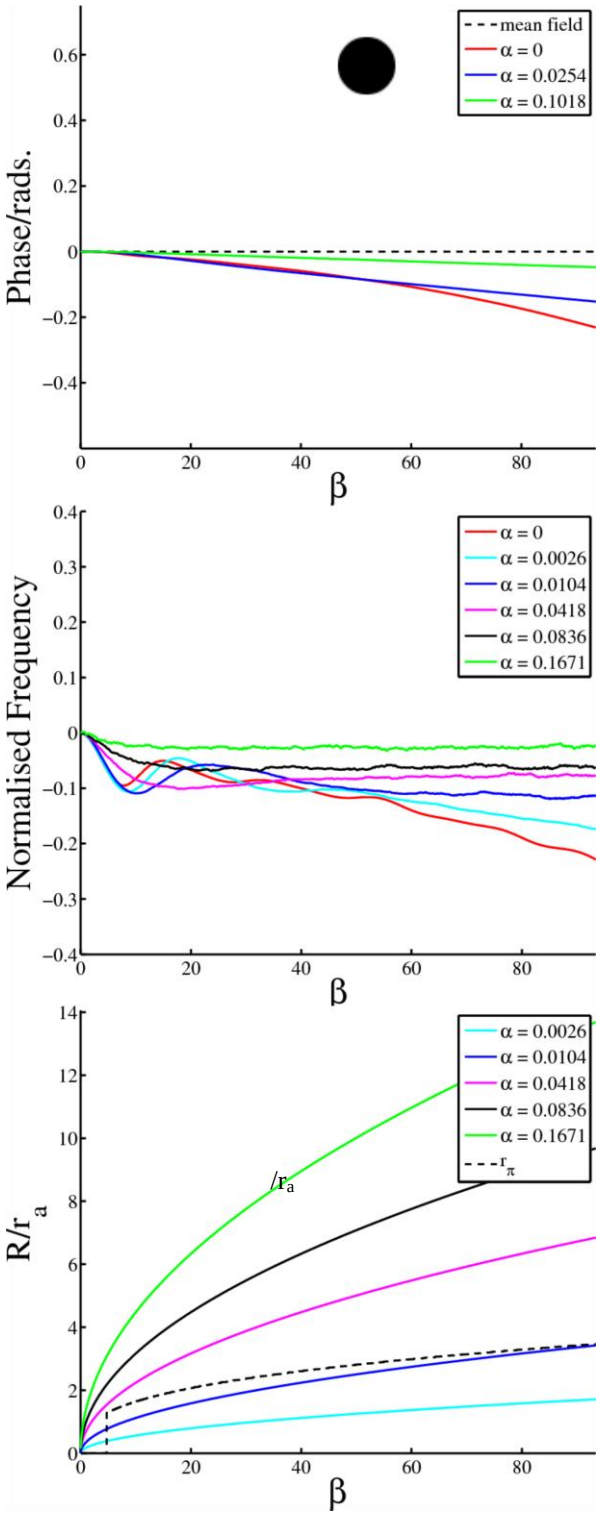

Figure 7-13 – Spherical perturber $q = 1.00$ /$D_{ze} = 0.3333$. When α = 0, the phase deviates from that predicted by the mean field when β > ~10. The frequency falls before oscillating with a gradually decreasing magnitude while continuing a slight downwards trend. A α increases, the phase converges on that predicted by the mean field, and the frequency oscillations are damped before the normalised frequency begins to converge on its initial value of ~0 when β = 0.

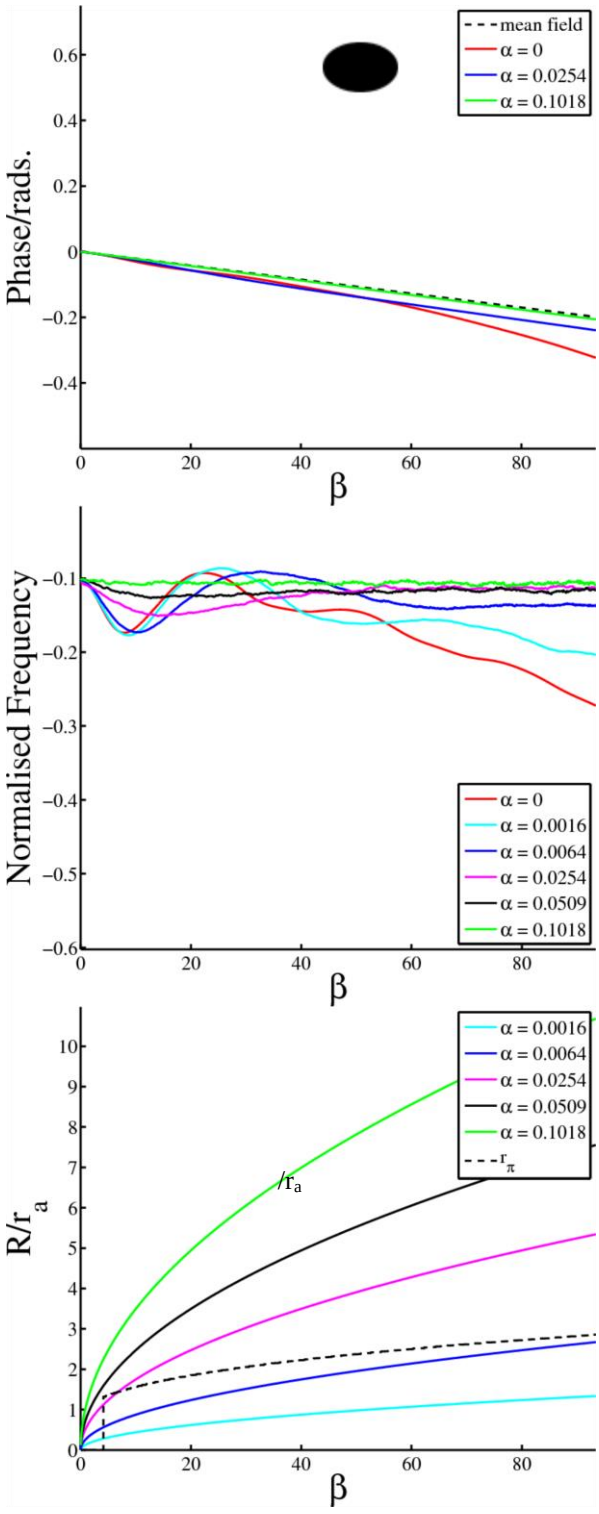

Figure 7-14 – Prolate perturber $q = 1.50$ /$D_{ze} = 0.2330$. When α = 0, the phase deviates rapidly from that predicted by the mean field when β > ~10. The frequency falls before oscillating with a gradually decreasing magnitude with a slight downwards trend when β > ~40. A α increases, the phase converges on that predicted by the mean field, and the frequency oscillations are damped before the normalised frequency begins to converge on its initial value of ~-0.1 when β = 0.

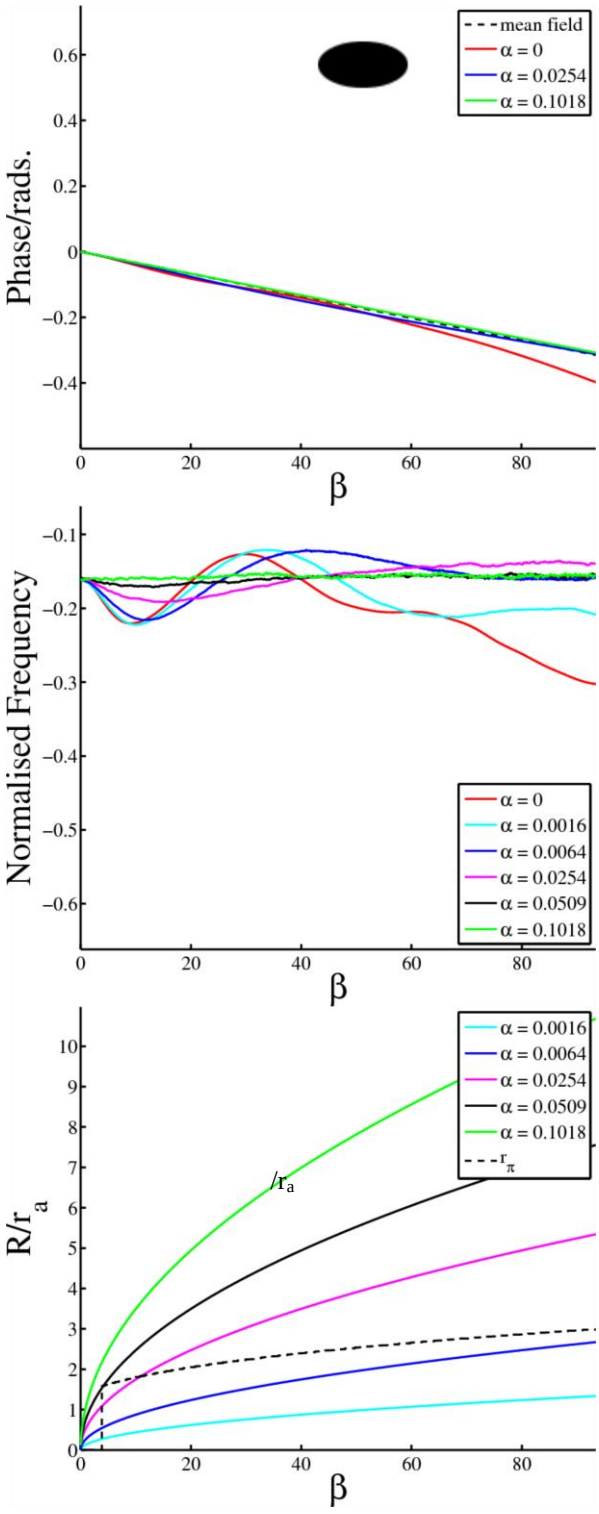

Figure 7-15 – Prolate perturber $q = 2.00$ /$D_{ze} = 0.1736$. When α = 0, the phase deviates gradually from that predicted by the mean field when β > ~60. The frequency falls before oscillating with a gradually decreasing magnitude while continuing a slight downwards trend. A α increases, the phase converges on that predicted by the mean field, and the frequency oscillations are damped before the normalised frequency begins to converge on its initial value of ~-0.16 when β = 0.

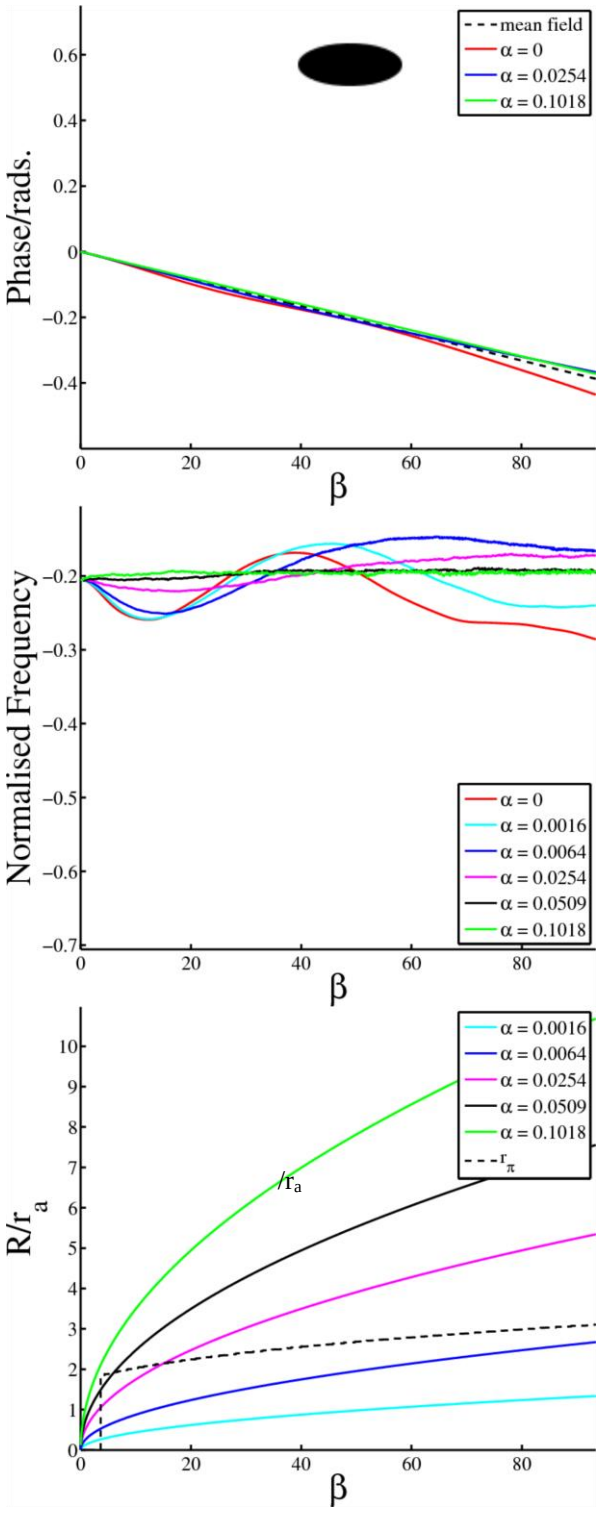

Figure 7-16 – Prolate perturber $q = 2.50$ /$D_{ze} = 0.1352$. When α = 0, the phase deviates gradually from that predicted by the mean field when β > ~60. The frequency falls before oscillating with a gradually decreasing magnitude while continuing a slight downwards trend. A α increases, the phase converges on that predicted by the mean field, and the frequency oscillations are damped before the normalised frequency begins to converge on its initial value of ~-0.2 when β = 0.

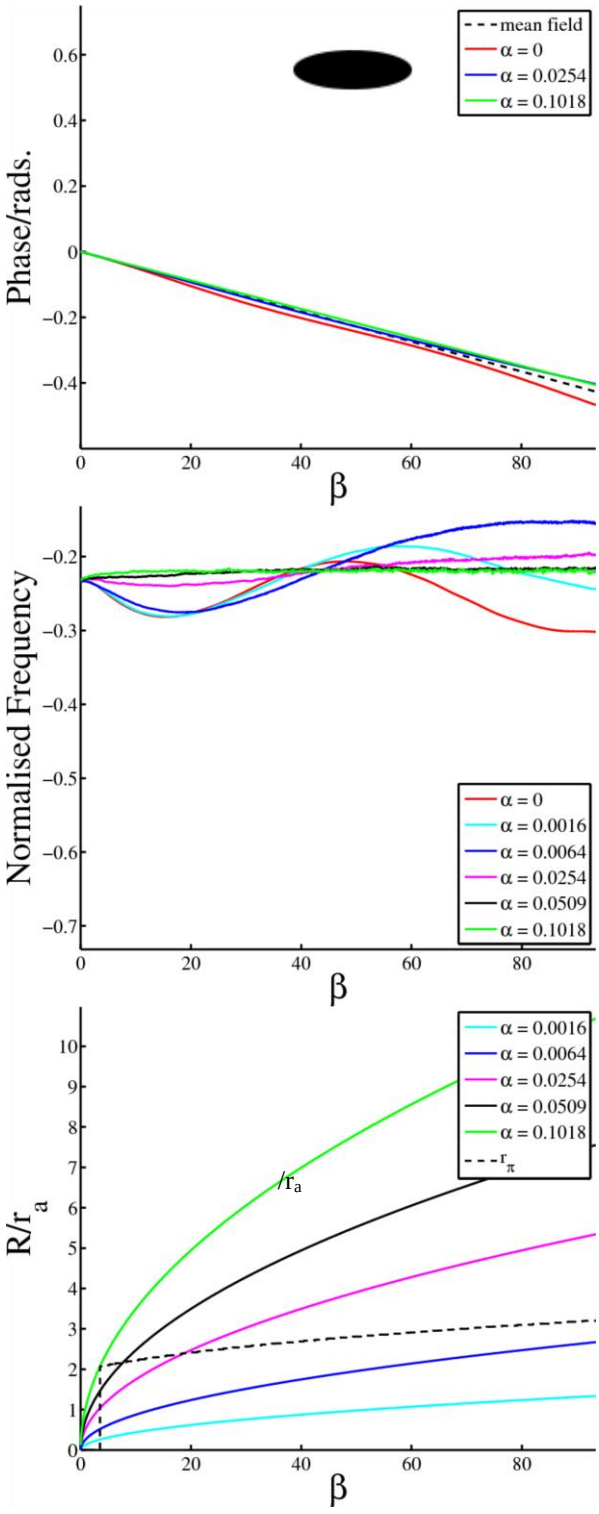

Figure 7-17 – Prolate perturber $q = 3.00$ /$D_{ze} = 0.1087$. When α = 0, the phase decreases slightly from that predicted by the mean field when β > ~10. The frequency slowly oscillates with a slight downwards trend. A α increases, the phase converges on that predicted by the mean field, and the frequency of the normalised frequency oscillations decreases and the downward trend disappears, before the normalised frequency begins to converge on its initial value of ~-2.2 when β = 0.

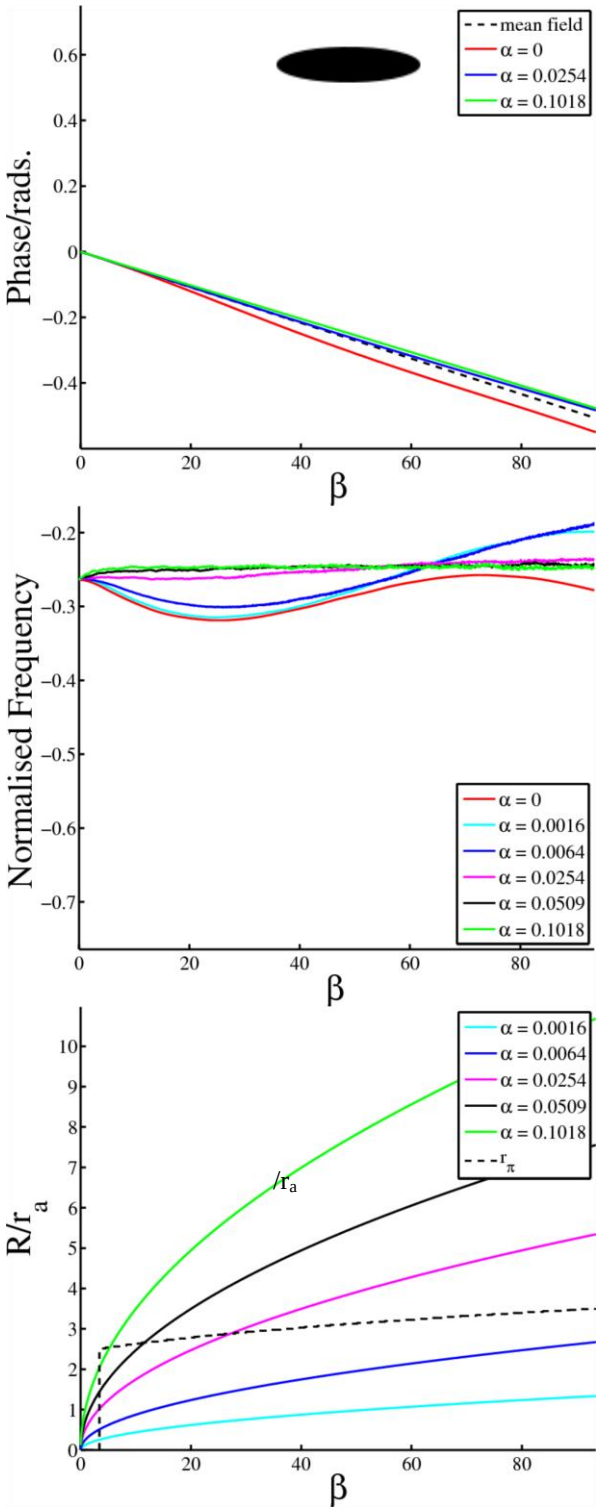

Figure 7-18 – Prolate perturber $q = 4.00$ /$D_{ze} = 0.0754$. When α = 0, the phase deviates gradually from that predicted by the mean field when β > ~10, and the frequency slowly oscillates with a slight downwards trend. A α increases, the phase converges on that predicted by the mean field, and the frequency of the normalised frequency oscillations decreases and the downward trend disappears, before the normalised frequency begins to converge on its initial value of ~-2.5 when β = 0.

For all perturber shapes, as diffusion increases, the oscillation of the NF occurring after the initial reduction is damped. The magnitude of the initial decrease in NF is also attenuated. In the case of the oblate perturbers and the sphere, the NF reaches a steady state when $\alpha \geq 0.0254$. For higher α values, the NF in the steady state converges on the NF when $\beta = 0$. In the case of the prolate perturber with $q = 1.50$ $/D_{ze} = 0.2330$, the NF when $\alpha = 0.0254$ reaches a steady state when β~40-45. When $\alpha = 0.0509$ the NF drops slightly initially before reaching a steady state just below the NF at β =0. When $\alpha = 0.1018$ the NF remains approximately constant throughout the simulation. For the remaining prolate perturbers, slight oscillation of the NF is still apparent when $\alpha = 0.0254$. At short times (β~ 0-40), when $\alpha =$ 0.0509 the NF falls slightly below that seen when $\alpha = 0.1018$, with this difference reducing with D_{ze}, and vanishing completely for the most prolate perturber. When $q = 3.00$ $/D_{ze} = 0.1087$ and $\alpha = 0.1018$, and also when $q = 4.00$ $/D_{ze} = 0.0754$ and $\alpha = 0.0509/0.1018$, the NF rises slightly at very low β, before entering a steady state.

Comparison of the evolution of the NF with the RMS displacement, $R = \sqrt{\langle r^2 \rangle}$ at each diffusion rate with the dephasing radius shows that the NF evolution falls broadly into three diffusion-dependent regimes.

For all perturbers, when $\alpha = 0,$ or 0.0016, the low rate of diffusion means that $R <$ r_π throughout the simulation (with the exception of very low β values, where no static particle has yet accumulated a phase $\geq \pi$). At these diffusion rates, oscillation is apparent in the evolution of the NF, which does not reach a steady state.

When $\alpha = 0.0509$ or 0.01018, $R > r_\pi$ for all but very low β values in the case of prolate ellipsoids where $q > 2.00$ $/D_{ze} > 0.1736$, where the radial distance of the strongest field perturbation from the centre of the spheroid is greatest. At these diffusion rates, the NF does not oscillate after the initial decrease, and reaches a steady state.

When $\alpha = 0.0254$, $R > r_\pi$ throughout the simulation for the oblate spheroids and the sphere, but for the prolate spheroids, $R < r_\pi$ when β~5-20, before , R overtakes r_π. For the oblate spheroids and sphere, the NF does not oscillate after the initial decrease, and reaches a steady state. For the prolate spheroids, slight oscillation is evident in the NF.

When $\alpha = 0.0064$, $R \sim r_\pi$ over most of the range of β values for the oblate spheroids and the sphere, and $R < r_\pi$ for the prolate spheroids, with a difference which increases as D_{ze} decreases. In the case of the most oblate spheroid with $q = 0.25$ /$D_{ze} = 0.7036$, the initial decrease in NF is followed by oscillation, however these oscillations are rapidly damped as β increases. For the remaining oblate spheroids and the sphere, the initial decrease in NF is followed by oscillation, however a steady state is reached at large β values. For the prolate spheroids with $q \leq 2.00$ /$D_{ze} \leq 0.1736$, the evolution of the NF follows that observed in the oblate spheroids and sphere, with the steady state reached at increasingly large β values. For the remaining profdlate spheroids, the oscillation persists throughout the simulation, and no steady state is achieved.

7.4.3 Variation of Initial and Final Frequency with Demagnetizing Factor, Diffusion Rate, and Volume Fraction

Figures 7-19 and 7-20 show the variation of the normalised frequency (NF) as a function of $D_{ze} - 1/3$ at $t = 0$ for $N = 0$ and at $t = 500$ ms for $N = 0, 16$ and 64, for perturbers with volume fractions of 2% and 1% respectively. The normalised frequency $t = 0$ varies linearly with $D_{ze} - 1/3$ for both volume fractions. These *NF* values reflect the average field perturbation in the spherical volume surrounding the perturber, as expected. When $t = 500$ ms, the relationship between normalised frequency and $D_{ze} - 1/3$ becomes non-linear in the absence of diffusion, due strong dephasing of the signal in regions where the field offset is strong and spatially varying. The relationship becomes more linear and approaches the NF values at $t =$ 0 ms as the rate of diffusion is increased by increasing N to 16 and then 64. For the perturbers with a 1% volume fraction and $D_{ze} - 1/3 \leq 0$, the NF at $t = 500$ ms with $N = 64$ does not deviate significantly ($> 10\%$) from its value when $t = 0$ ms in the static regime. For perturbers with a 2% volume fraction, the NF at $t =$ 500 ms deviates more significantly strongly from its value when $t = 0$ ms in the static regime for all shapes other than the most prolate perturber with $D_{ze} - 1/3 = -0.2579$. Figure 7-21 shows the non-normalised frequency of the perturbers with both 1% and 2% volume fractions when *t* = 0 ms. The frequency offset in both cases varies linearly with $D_{ze} - 1/3$ at each volume fraction, and scales in proportion to the volume fraction for each shape.

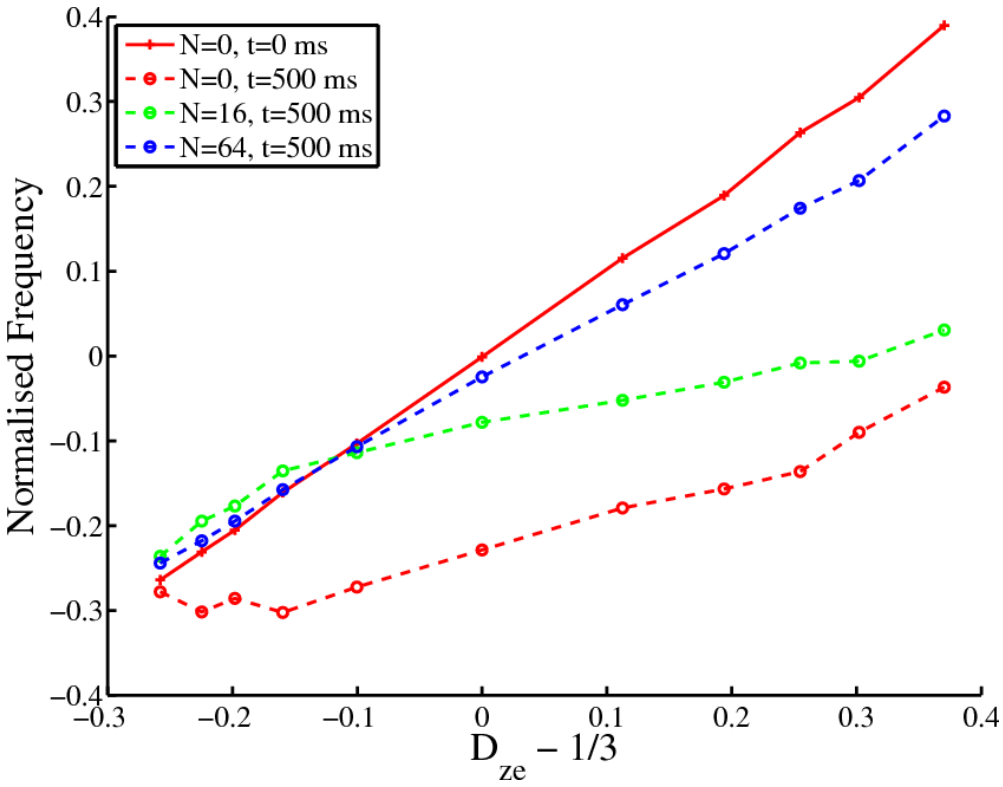

Figure 7-19 – Normalised frequency variation for perturbers with 2% VF as a function of $D_{ze} - 1/3$ at t = 0 ms for N = 0 and at t = 500 ms for the N = 0, 16 and 64.

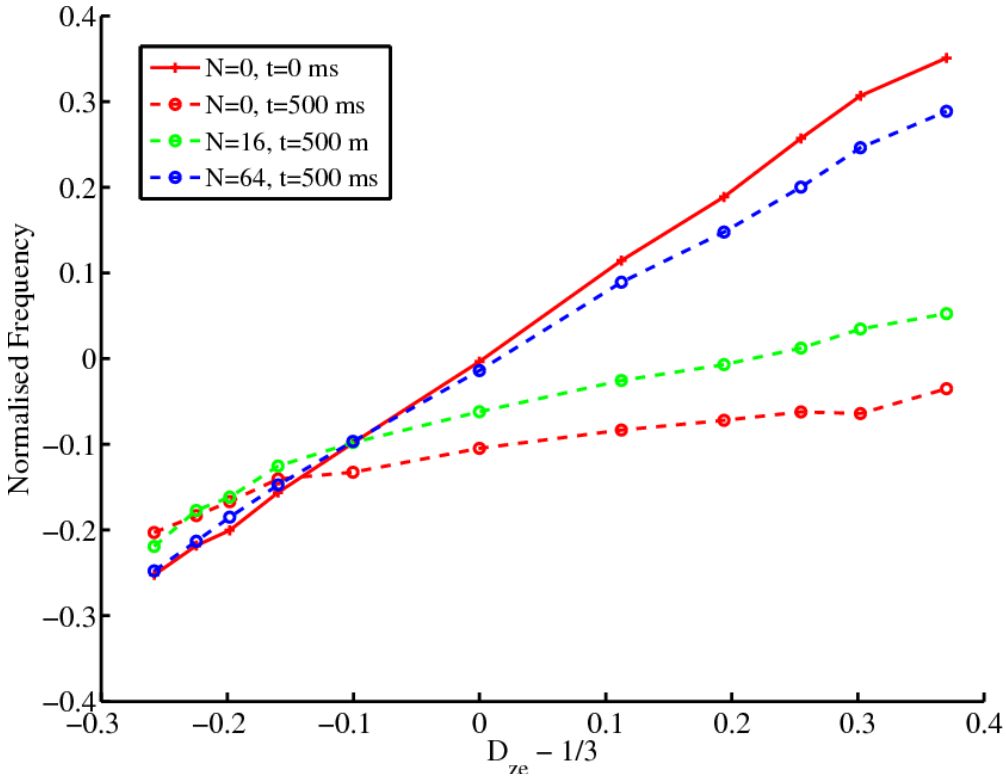

Figure 7-20 – Normalised frequency variation for perturbers with 1% VF as a function of $D_{ze} - 1/3$ at t = 0 ms for N = 0 and at t = 500 ms for the N = 0, 16 and 64.

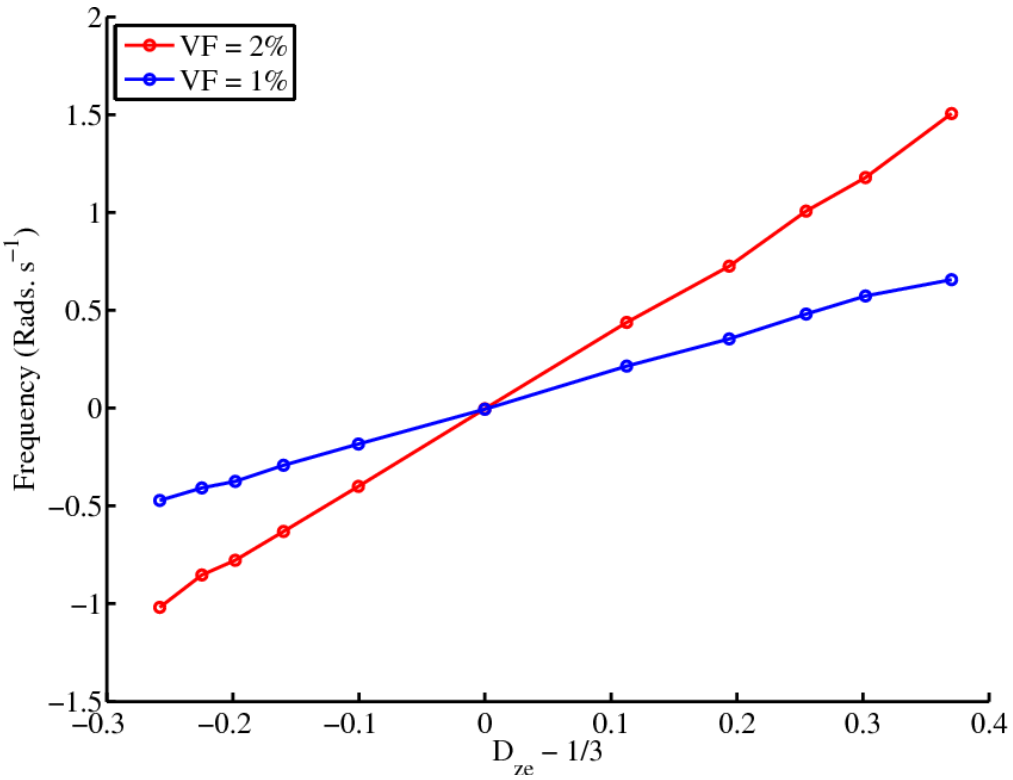

Figure 7-21 – Comparison of the variation of signal frequency at t = 0 ms for perturbers with 1% and 2% volume fractions.

7.4.4 Effect of Varying Volume Fraction

Figures 7-22 and 7-23 show the absolute (non-normalised) frequency evolution in the absence of diffusion for the full range of perturber shapes with volume fractions of 1% and 2%. The frequency when $\beta = 0$ is proportional to volume fraction as well as $D_{ze} - 1/3$, as shown in Figure 7-21. While the evolution of the frequency at both volume fractions reflects similar trends, they are not simply scaled copies of one another. While the initial decrease in frequency for each shape appears to simply scale with volume fraction, the frequency of the subsequent oscillation appears to vary between volume fractions for the two most oblate perturbers ($q = 0.25$ /$D_{ze} = 0.7036$ and $q = 0.33$ /$D_{ze} = 0.6354$), where the magnitude of such oscillations is greatest. The frequency of oscillation appears consistent between volume fractions for the remainder of the perturbers. For the perturbers with a 1% volume fraction, an initial decrease in frequency is followed by oscillation of the frequency about an approximately constant value. In the case of the prolate perturbers, the initial drop in frequency becomes very small and the frequency oscillates slowly about the frequency when $\beta = 0$. However, for the perturbers with a 2% volume fraction, the frequency continues to decline slowly as it oscillates after its initial decrease.

Figures 7-24 to 7-26 show the variation of phase, normalised frequency, RMS displacement, and r_π for the most oblate ($q = 0.25$ /$D_{ze} = 0.7036$), spherical ($q = 1$ /$D_{ze} = 0.3333$), and most prolate ($q = 4.00$ /$D_{ze} = 0.0754$) perturbers with both 1% and 2% volume fractions. The normalised frequency should be independent of volume fraction when $\beta = 0$, however it appears slightly lower for a volume fraction of 1% when compared to the corresponding spheroid with a volume fraction of 2% for the oblate perturbers. While the NF evolution follows similar trends for corresponding shapes and diffusion rates at each volume fraction, it is not identical. In the case of the oblate perturber, the magnitude of the oscillations in the NF are reduced when the volume fraction is 1%, and the damping of the oscillations through time is greater. Increasing rates of diffusion cause a more rapid convergence of the NF towards its starting value for the 1% volume fraction when compared to the 2% volume fraction. The pi dephasing radius is reduced for the 1% volume fraction, reflecting the smaller size of the perturber. When $\alpha = 0.0064$ (2%)/0.0104 (1%), the difference between R and r_π is significantly increased for the 1% volume fraction, and the NF reaches a steady state when $\beta > 60$, whereas no such state is achieved for the 2% volume fraction.

In the case of the sphere, the magnitude of the oscillations remains similar between the 1% and 2% volume fractions. The damping of the oscillations also appears to be similar. The rate at which the NF converges on its starting value increases slightly for the 1% volume fraction relative to the 2% volume fraction. When $\alpha = 0$, 0.0016 (2%)/0.0026 (1%), or 0.0064 (2%)/0.0104 (1%), the downward trend in NF apparent when $\beta > \sim 50$ is significantly reduced for the 1% volume fraction relative to the 2% volume fraction.

For the prolate perturber, the initial decrease in NF is slightly reduced for the 1% volume fraction relative to the 2%. The amplitude of the oscillation when $\alpha = 0$ or 0.0016 (2%)/0.0026 (1%) is slightly increased, and they appear to be more centred on the initial NF for the 1% volume fraction than the 2%. In both cases, the NF remains in a steady state throughout when $\alpha = 0.0509$ (2%) / 0.0836 (1%) or 0.1018 (2%) / 0.1671 (1%) , and oscillate very slightly when $\alpha = 0.0254$ (2%)/0.0418 (1%).

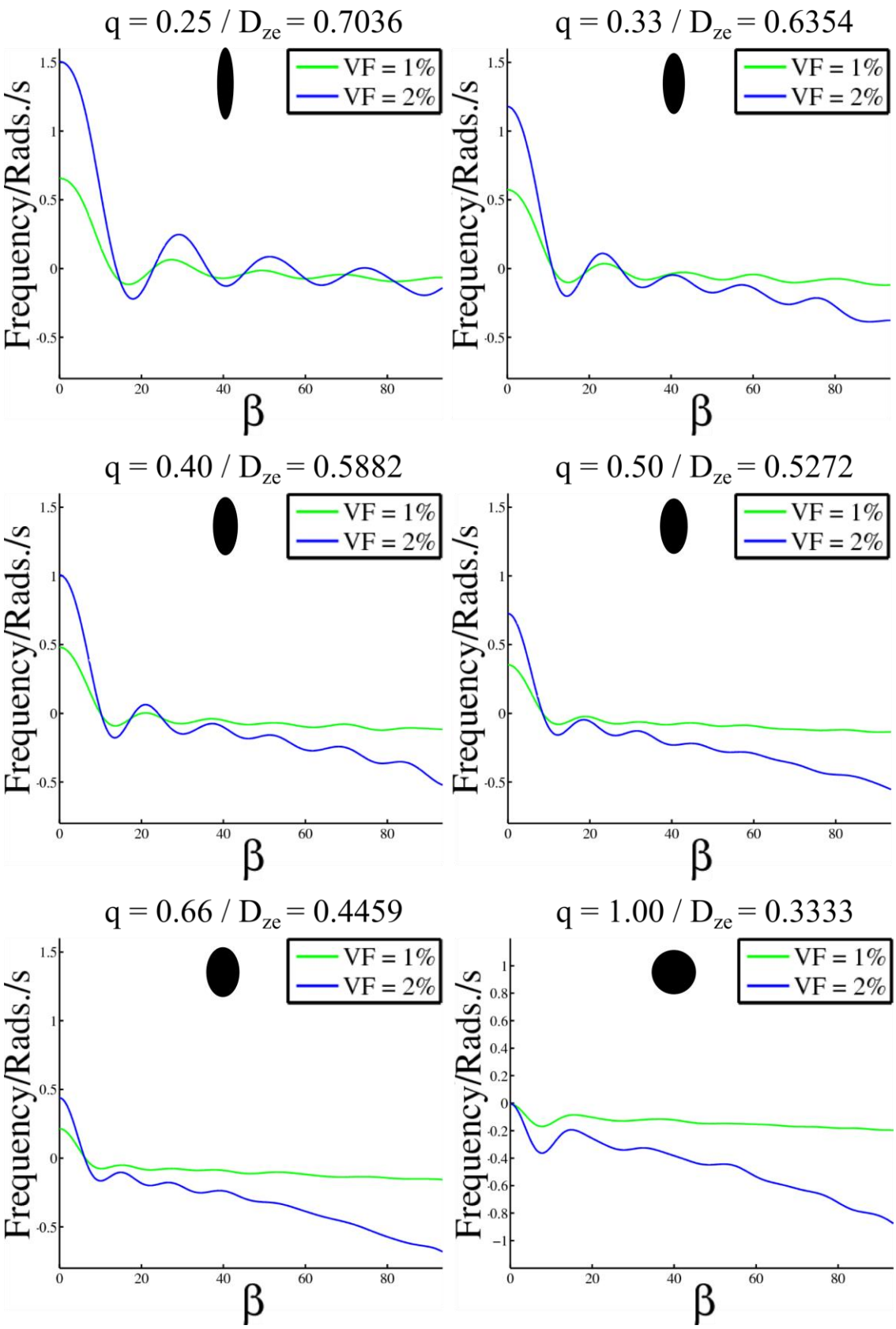

Figure 7-22 – Non-normalised frequency evolution in the absence of diffusion for the oblate and spherical perturbers with *q* ranging from 0.25 to 1.00.

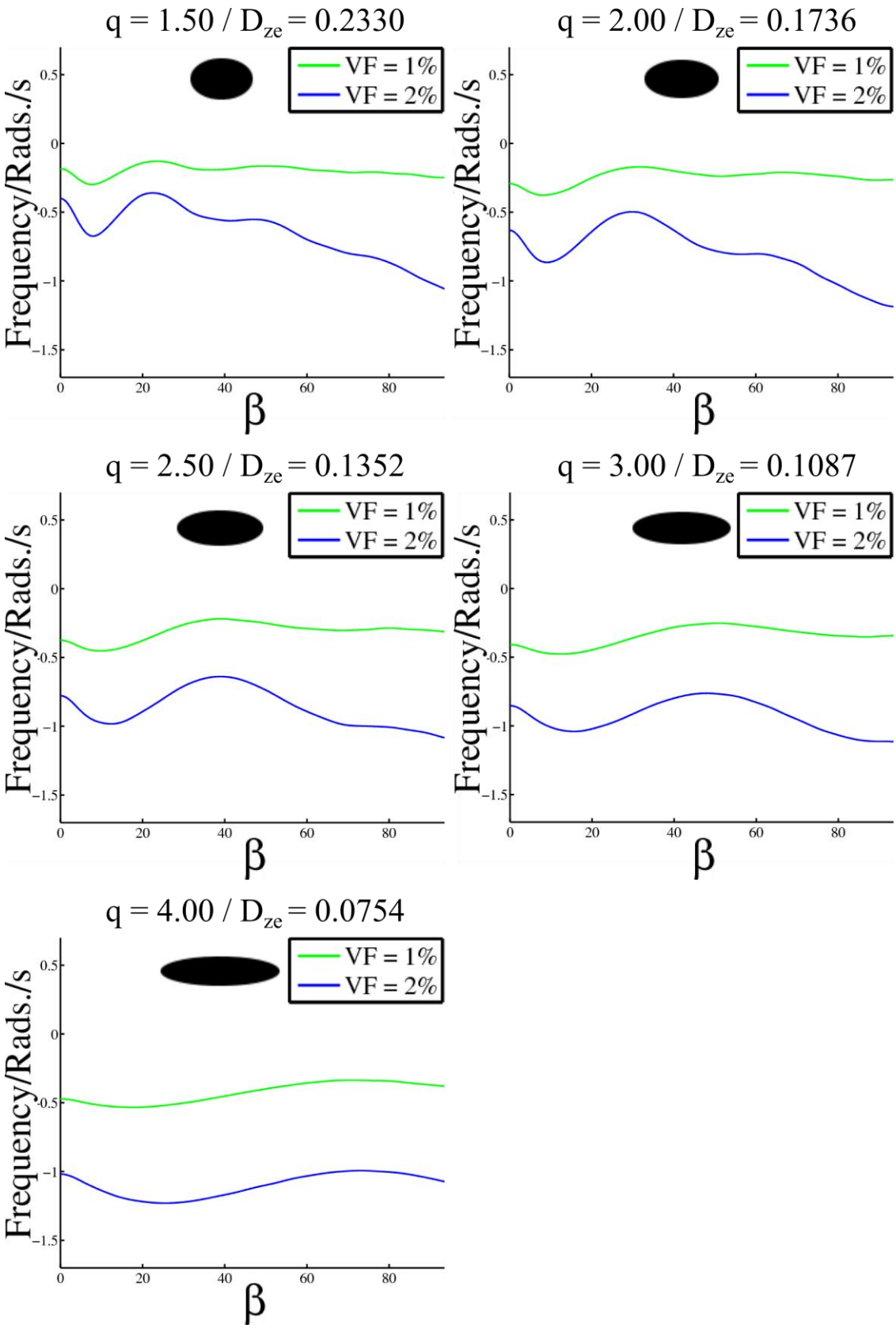

Figure 7-23 - Non-normalised frequency evolution in the absence of diffusion for the prolate perturbers with *q* ranging from 1.50 to 4.00.

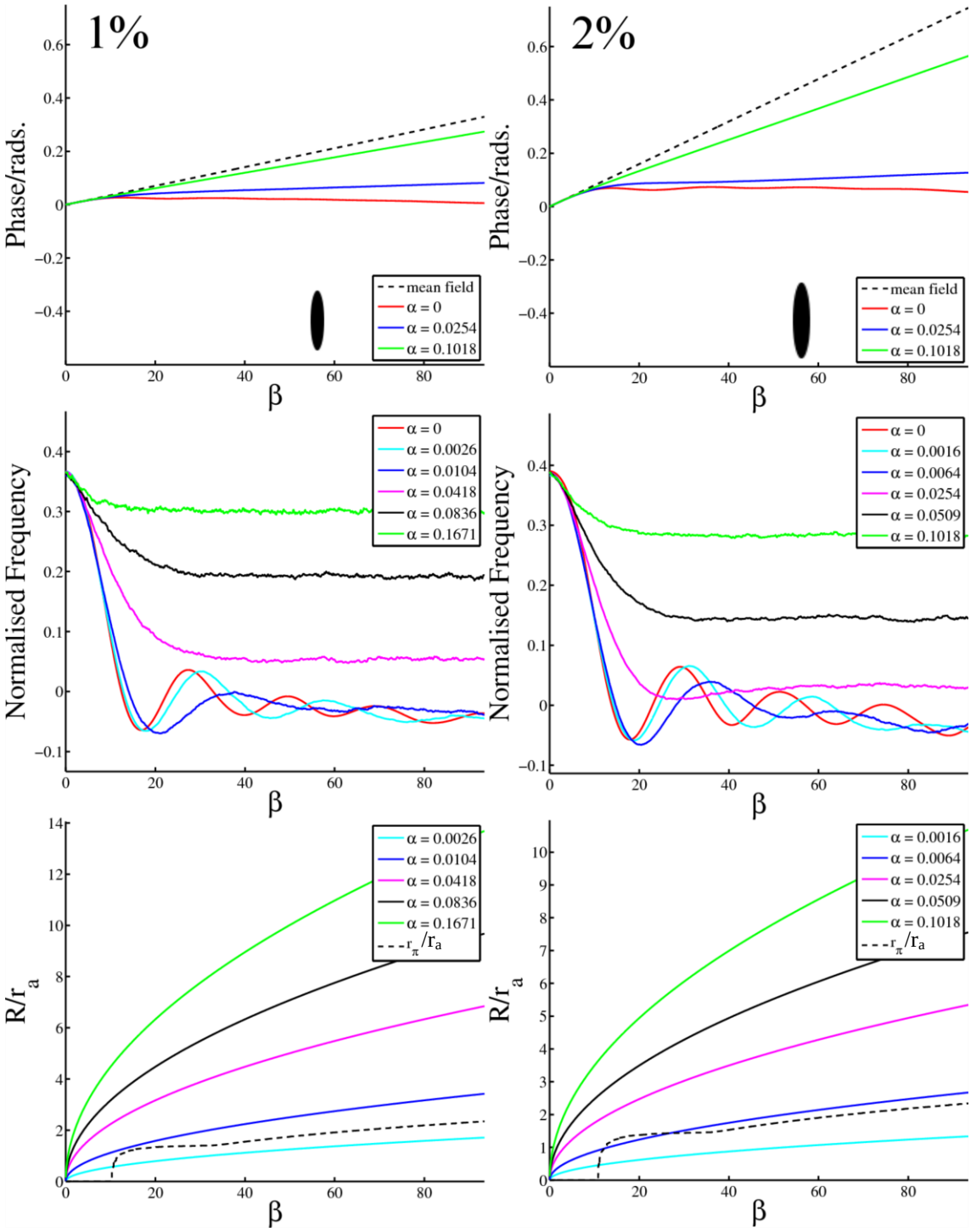

Figure 7-24 – Variation of phase, NF, r_π and R for an oblate perturber with $q = 0.25$ /$D_{ze} = 0.7036$ and varying α-values and β. Volume fractions of 1% and 2% were considered.

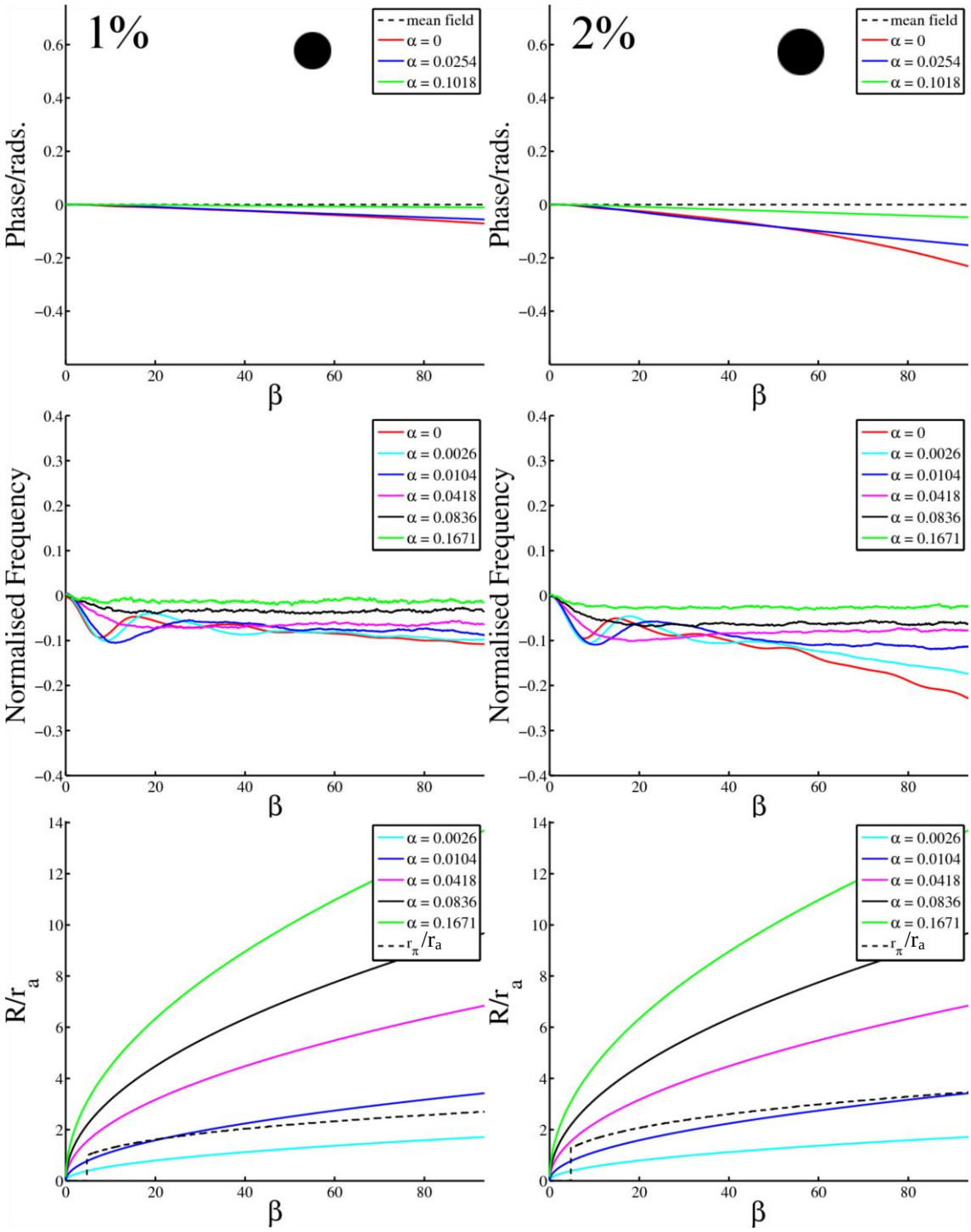

Figure 7-25 - Variation of phase, NF, r_π and R for a spherical perturber with $q = 1.00$ /$D_{ze} = 0.3333$ and varying α-values and β. Volume fractions of 1% and 2% were considered.

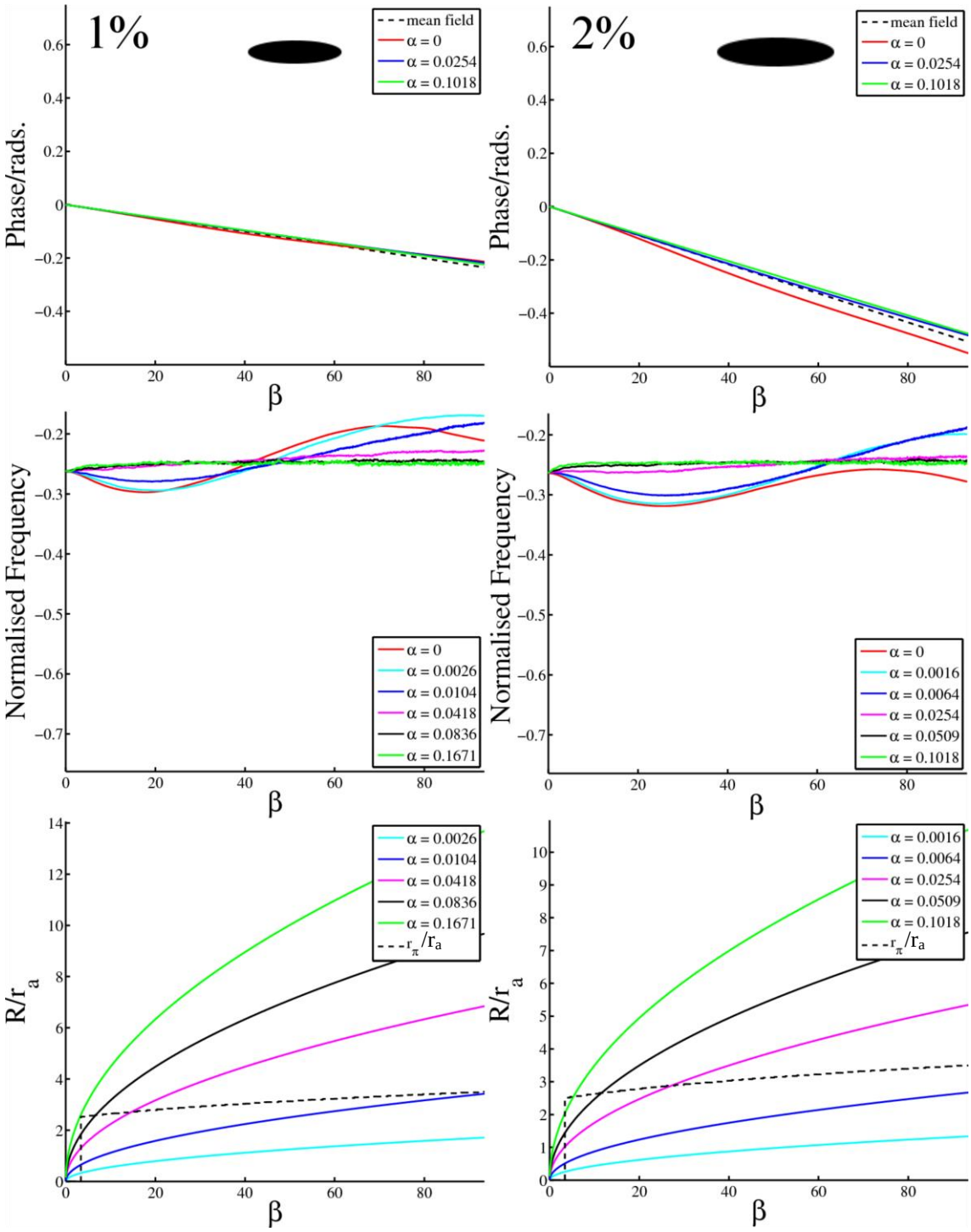

Figure 7-26 – Variation of phase, NF, r_π and R for a prolate perturber with $q = 4.00$ /$D_{ze} = 0.0754$ and varying α-values and β. Volume fractions of 1% and 2% were considered.

7.5 Discussion

The results presented in this chapter demonstrate that in a system of oriented NMR invisible spheroidal perturbers, the measured phase does not simply reflect the bulk susceptibility, governed by the volume fraction, but rather it is also dependent on the shape of the perturbers.

The shape dependence of the frequency is demonstrated in Figures 7-19 and 7-20. Considering the static regime, not only does the frequency vary linearly with $D_{ze} - 1/3$ when $t = 0$, but it also deviates from this value over time, with a magnitude which correlates approximately with D_{ze}. This observation may be explained by consideration of Figure 7-7.

For the most oblate perturbers, the field varies rapidly over a large region at the positive poles, while the negative poles only correspond to a small region of rapid dephasing (here, we refer to positive/negative 'poles' to describe the points at the surface of the perturber where the magnitude of the positive/negative field perturbation is greatest). For the most prolate perturber, the field varies even more rapidly at the positive poles, but over a far smaller volume than for the oblate perturber. In contrast, the field at the negative poles of the prolate perturber is both significantly more slowly varying and covers a large volume. When t = 0 s, no dephasing has occurred, and so the frequency reflects the total mean field perturbation over the volume. However, when t=500 ms, significant dephasing has occurred in regions close to the poles of the perturbers, meaning that the frequency contribution from these areas is not reflected in the measured average frequency.

The points highlighted above are consistent with the static regime results seen in Figure 7-19 and Figure 7-21. For the most oblate perturber, a large number of particles reside in the relatively large regions with rapidly-varying, positive field perturbations. Significant dephasing of signal from these regions would result in a large net reduction in the mean apparent frequency. As the perturbers become less oblate, the size of these regions reduces, and the negative deviation of the frequency from the mean field reduces accordingly, becoming slightly positive in the case of the 1 % volume fraction perturbers with $D_{ze} - 1/3 \leq 0.1957$.

In the case of the sphere, where the field follows a dipolar pattern, the positive poles subtend a smaller volume (~42%) of the spherical region surrounding the dipole than

the negative poles, however the phase in these regions still varies more rapidly than the slightly larger negative poles, and consequent dephasing of signal from these regions dominates and results in a negative deviation of the measured frequency at t = 500 ms. This is consistent with the previously reported expectation that at sufficiently long times in the static regime, the frequency measured from a volume containing spherical perturbers will have a negative offset [19]. This offset would correspond to a normalised frequency of -0.053 [19], which is less negative than the offsets at t = 500 ms seen in Figures 7-19 and 7-20. This may be explained by the relatively large size of the perturbers in our simulation relative to the restricted volume considered. At long times, the signal will completely dephase throughout the volume. However, this will happen first in the more rapidly varying positive regions, causing our results at long times to be negatively biased compared to a simulation over a larger volume.

Such a negative bias in our results at long times would also explain the larger negative deviation of the NF at t = 500 ms for the 2 % VF compared to the 1 % VF. While the normalisation of the frequency removes the VF dependence of the field perturbation, it does not account for the larger relative size of the sample volume surrounding the 1 % VF perturbers compared to the 2% VF perturbers.

In all cases, introducing diffusion reduces the deviation of the NF from its original value over time. This is consistent with our argument, as with increasing diffusion each particle will, on average, sample more of the space around the perturber over a given time, and the average phase accumulated by each particle will therefore converge on that expected from the mean field within the volume.

The phase and frequency evolutions with β may also be explained in terms of the mean field perturbation over the volume and the size and rate of signal loss from the regions of rapidly varying field at the positive and negative poles. The phase evolution clearly illustrates that diffusion causes convergence of the phase behaviour on that expected from the mean field, however the effect of perturber shape is better discussed in terms of the frequency evolution, which gives a clearer picture of the instantaneous rate of phase accumulation of the signal recorded from the ensemble of particles.

In their work describing NMR signal from a sample containing a system of randomly oriented spheroidal perturbers, Sukstanskii and Yablonskiy [7] describe the dephasing of the signal from spins outside of the perturbers as falling broadly into 3 regimes over time. They describe a regime at short times where dephasing is dominated by spins close to the perturbers, an intermediate time regime where dephasing is strongly dependent on the shape of the perturber, and a third regime where the remaining coherent spins are at a distance much greater than the perturber's longest dimension, and 'sense' the perturber as a point dipole. In our results, we observe frequency behaviour consistent with the first two regimes. In order to observe behaviour corresponding to the third regime, the volume fraction would have to be reduced to the point where the radius of the volume under consideration was significantly larger than the longest dimension of the perturber, and simulations carried out to times where signal from the whole region where the field is influenced by the perturber shape had dephased.

For all perturber shapes and volume fractions, when $\beta = 0$ the frequency reflects the mean field perturbation, which is non-zero for non-spherical perturbers due to the deviation of the field near to the perturber from the spherical dipolar form. This is consistent with the first regime described in [7], where dephasing in this region dominates. The NF then deviates from its initial value as the contribution from particles very near to the perturber decreases, and evolves in a strongly shape-dependent manner. The NF initially decreases, with a magnitude that is greatest for the most oblate perturber and least for the most prolate perturber. This is consistent with rapid dephasing at the positive poles, whose relative contribution to the total signal is inversely proportional to D_{ze}.

The subsequent oscillation of the NF is shape-dependent in both its amplitude and frequency of variation, in a manner consistent with the second regime described in [7]. This may be explained by the contribution to the measured frequency from particles within a region where dephasing is not so rapid that the signal contribution is lost, nor so slowly varying that there is no interference of signals from different particles. In such a region, superposition of the signal from spins precessing at different frequencies may explain the periodic oscillation observed, in a manner analogous to a beat frequency. The relatively high frequency oscillation observed in the case of the oblate perturbers may be explained by the rapid variation of the phase

in regions surrounding the positive poles, and the increased damping of this oscillation as D_{ze} decreases corresponds to the reduction in volume of these regions as the perturber becomes more spherical. The lower frequency oscillation, which becomes prominent as the perturber becomes increasingly prolate, may be explained by the increasing contribution to the frequency of particles in the increasingly large slowly varying volumes surrounding the negative poles.

A comparison of the effects of varying volume fraction on the non-normalised frequency can be seen in Figures 7-22 and 7-23, where the magnitude of the initial frequency offset and subsequent fall in frequency scale with the volume fraction. The subsequent evolution of the frequency would be expected also to scale with volume fraction, however our results show a general downward trend in the case of the 2 % VF perturbers relative to that seen in the case of the 1% VF perturbers. As discussed above, this is likely a consequence of the limited volume over which our simulation was carried out.

The effect of diffusion on both the 1% and 2% volume fractions falls broadly into two categories. When the RMS displacement, R, is less than or on order of r_π, the maximum radius at which the phase reaches a value of π in the static regime, diffusion attenuates the oscillation after the initial decrease in NF. When R becomes significantly greater than r_π, the NF reaches a steady state value. As α increases this value tends towards the frequency predicted by the mean field. This may simply be explained by each particle, on average, sampling a greater proportion of the total field over a given period of time.

The main significance of our results lies in our demonstration that in the presence of oriented, NMR invisible spheroidal perturbers, the NMR signal from a volume with a constant bulk susceptibility will have a phase which is both dependent on the shape-dependent demagnetizing factor of the perturber, the rate of diffusion of the target nuclei, and the time at which the signal is sampled.

If we consider a fixed apparent diffusion coefficient $ADC = 0.70 \times 10^{-3}\ \mathrm{mm\,s^{-1}}$, which falls within the range of diffusion coefficients found in healthy brain tissue [20], we may gain some insight into the relevance of our results in a biological system. Using Eq. 7.16 to find δ_Δ for each combination of n and N and a step time $\Delta t = 1\ \mathrm{ms}$, we find that our results may be used to represent perturbers with a

volume fraction of 1% and $r_a = 4.73 - 37.90$ μm, and a volume fraction of 2% and $r_a = 6.06 - 48.50$ μm. These are mesoscopic length scales, of the order of the size of biological inclusions such as red blood cells (6-8 μm). β is related to the time at which phase is measured, as well as the characteristic frequency shift $\delta\omega_s$, which in turn is related to the magnetic field strength B_0 and the susceptibility of the inclusion relative to its surroundings, $(\chi_i - \chi_e)$.

At 7 T, the echo times typically of interest in a gradient echo based sequence are of order $5 - 40$ ms, corresponding to $\beta \sim 1 - 8$ when $(\chi_i - \chi_e) = 0.1$ ppm. As such, the phase measured from the system we present here would reflect the behaviour observed in the first regime at short echo times when $TE \sim 5$ ms, where the frequency is representative of the mean field perturbation of a given perturber shape at a fixed volume fraction of 1 or 2 %, regardless of the absolute size of the perturber, with an increasing dependence on α as D_{ze} increases. If the A*DC* is fixed, this would correspond to a dependence on the absolute size of the perturber that increases with *TE*. If $(\chi_i - \chi_e)$ were increased to 1 ppm, however, the interesting range of β would become of order $10 - 80$. In this case, the measured phase would reflect the oscillating behaviour observed in the second regime, and the measured phase would be highly α-dependent. This would correspond to a strong dependence on the absolute size of the perturber.

While the results presented here demonstrate interesting and behaviour which deviates significantly from that expected from simple models, Yablonskiy et al, previously noted that "in many practically important cases of biological systems nuclear motion does not substantially affect dephasing of a FID signal caused by susceptibility-induced mesoscopic magnetic field inhomogeneities." [7, 19, 21], as relatively large length scale field inhomogeneities dephase the signal before diffusion causes the phase accumulated by each spin to average out. Factors such as externally generated field inhomogeneity, and others such as longitudinal relaxation were not included in our model, therefore while the signal behaviour observed in these simulations may contribute significantly to certain measurements, they only represent one contribution to real measurements from such a system.

7.6 Conclusions

In this chapter we used Monte Carlo simulation to demonstrate that the average frequency offset produced by orientated, NMR invisible inclusions can be strongly dependent on the shape of the inclusions, even in the presence of diffusion, and doesn't therefore simply relate to the bulk magnetic susceptibility. In the short time ($\beta \ll 1$) and high diffusion ($R \gg r_\pi$) regimes, the offset has a simple dependence on the demagnetizing factor of the oriented spheroidal inclusions. At longer times and lower diffusion rates, a more complex behaviour emerges with little dependence on the mean field perturbation. Considering the system in terms of a fixed, biologically realistic diffusion rate, it can be seen that the extent of the observed frequency and phase evolution that falls within a relevant range of times is strongly dependent on the susceptibility of the perturber relative to the background. These results give detailed insight into the phase and frequency evolution measured from a volume containing oriented, NMR-invisible spheroidal inclusions with non-zero magnetic susceptibility, and contribute to the body of evidence that the phase measured from such volumes is not simple and linear in time, rather it is influenced by a complex combination of factors, and as such must be interpreted with care.

7.7 References

1. Lee, J., et al., *Sensitivity of MRI resonance frequency to the orientation of brain tissue microstructure.* Proceedings of the National Academy of Sciences, 2010. **107**(11): p. 5130-5135.
2. Li, W., et al., *Magnetic susceptibility anisotropy of human brain in vivo and its molecular underpinnings*. NeuroImage, 2012. **59**(3): p. 2088-2097.
3. Wharton, S. and R. Bowtell, *Fiber orientation-dependent white matter contrast in gradient echo MRI.* Proc Natl Acad Sci U S A, 2012. **109**(45): p. 18559-64.
4. He, X. and D.A. Yablonskiy, *Biophysical mechanisms of phase contrast in gradient echo MRI.* Proceedings of the National Academy of Sciences, 2009. **106**(32): p. 13558-13563.
5. Oh, S.-H., et al., *Origin of B0 orientation dependent R2* (=1/T2*) in white matter.* NeuroImage, 2013. **73**(0): p. 71-79.
6. Chen, W.C., S. Foxley, and K.L. Miller, *Detecting microstructural properties of white matter based on compartmentalization of magnetic susceptibility.* NeuroImage, 2012. **70C**: p. 1-9.

7. Sukstanskii, A.L. and D.A. Yablonskiy, *Theory of FID NMR signal dephasing induced by mesoscopic magnetic field inhomogeneities in biological systems.* Journal of magnetic resonance, 2001. **151**(1): p. 107-117.

8. Sukstanskii, A.L. and D.A. Yablonskiy, *Gaussian approximation in the theory of MR signal formation in the presence of structure-specific magnetic field inhomogeneities. Effects of impermeable susceptibility inclusions.* Journal of magnetic resonance, 2004. **167**(1): p. 56-67.

9. Yablonskiy, D.a., et al., *Biophysical mechanisms of MRI signal frequency contrast in multiple sclerosis.* Proceedings of the National Academy of Sciences of the United States of America, 2012. **109**: p. 14212-7.

10. Sukstanskii, A.L. and D.A. Yablonskiy, *On the role of neuronal magnetic susceptibility and structure symmetry on gradient echo MR signal formation.* Magnetic Resonance in Medicine, 2014. **71**(1): p. 345-353.

11. Liu, C., *Susceptibility tensor imaging.* Magnetic Resonance in Medicine, 2010. **63**(6): p. 1471-1477.

12. Liu, C., et al., *3D fiber tractography with susceptibility tensor imaging.* NeuroImage, 2012. **59**(2): p. 1290-1298.

13. Yablonskiy, D.A., et al., *Biophysical mechanisms of MRI signal frequency contrast in multiple sclerosis.* Proceedings of the National Academy of Sciences, 2012. **109**(35): p. 14212-14217.

14. Jackson, J., *Classical Electrodynamics Third Edition*. 1998: Wiley.

15. Kiselev, V. and S. Posse, *Analytical model of susceptibility-induced MR signal dephasing: effect of diffusion in a microvascular network.* Magnetic Resonance in Medicine, 1999. **41**(3): p. 499-509.

16. Osborn, J., *Demagnetizing factors of the general ellipsoid.* Physical Review, 1945. **67**(11-12): p. 351.

17. Ulrich, R., R.W. Glaser, and A.S. Ulrich, *Susceptibility corrections in solid state NMR experiments with oriented membrane samples. Part II: Theory.* Journal of magnetic resonance, 2003. **164**(1): p. 115-127.

18. Blazejewska, A.I., et al., *Understanding the effects of oriented susceptibility inclusions on the phase and magnitude of gradient echo signals*. Proc. Intl. Soc. Mag. Reson. Med. 19, 2011.

19. Yablonskiy, D.A. and E.M. Haacke, *Theory of NMR signal behavior in magnetically inhomogeneous tissues: The static dephasing regime*. Magnetic Resonance in Medicine, 1994. **32**(6): p. 749-763.

20. Helenius, J., et al., *Diffusion-Weighted MR Imaging in Normal Human Brains in Various Age Groups.* American Journal of Neuroradiology, 2002. **23**(2): p. 194-199.

21. Yablonskiy, D.A., *Quantitation of intrinsic magnetic susceptibility-related effects in a tissue matrix. Phantom study*. Magnetic Resonance in Medicine, 1998. **39**(3): p. 417-428.

8 CONCLUSIONS

8.1 Summary

The primary focus of the work described in this thesis was to explore the underlying mechanisms of magnetic-susceptibility-induced field variations in MRI through the measurement of MRI signal phase. This was achieved through the comparison of phase imaging and quantitative susceptibility mapping in the *in vivo* investigation of multiple sclerosis, exploration of the effects of magnetic susceptibility anisotropy through macroscopic phantom experiments, and the use of Monte Carlo simulation to characterise the effect of shape and diffusion on the signal phase measured from a system of particles in a field perturbed by oriented, NMR-invisible spheroidal susceptibility inclusions.

Early interest in phase and susceptibility-weighted imaging suggested that MRI signal phase may be a local indicator of tissue magnetic susceptibility, and specifically tissue iron content [1-6]. This hypothesis is flawed due to the non-local relationship between magnetic susceptibility variation within a volume and the resulting perturbation of the applied magnetic field, from which local phase variation arises [7, 8]. In the work presented here, isotropic high-resolution, 3D gradient echo imaging of white matter lesions in multiple sclerosis was used to show the significance of this non-local effect *in vivo*, and to demonstrate how the application of quantitative susceptibility mapping reveals a magnetic susceptibility distribution consistent with both T_2^*-weighted magnitude images and previously reported findings from histology [9]. Lesions were viewed in sagittal, coronal, and axial planes, and clear examples of non-local, dipolar contrast were identified in phase images, and shown to be corrected by the application of QSM processing to the data. The identification and characterisation of peripheral rings around some white matter

lesions was compared for both phase and QSM images. The results of this comparison confirm that images based on local phase contrast must be interpreted with caution, and support the use of quantitative susceptibility mapping as a means of extracting information about local magnetic susceptibility from MRI signal phase.

This thesis then goes on to consider in greater detail the effect of sub-voxel level microstructure on the signal phase measured in MRI. The practical limitations of the resolution achievable *in vivo* using MRI make the ability to infer information about such structure a potentially powerful tool. Recent studies have shown orientation and time-dependence in the frequency and apparent susceptibility recorded from some regions of the brain [10-18], which has been attributed to the magnetic susceptibility anisotropy exhibited by myelin. This effect has been used as the basis of novel fiber tracking techniques, and as an explanation of the time and orientation dependent frequency of the MRI signal from voxels in certain regions. Mathematical representations of this effect have been based on either the assignment of an orientation-dependent isotropic susceptibility to anisotropic materials [13], or the representation of their magnetic susceptibility by a susceptibility tensor [12, 16, 19]. The work presented here explored the effect of magnetic susceptibility anisotropy using phantoms composed of pyrolytic graphite sheet (PGS), a highly diamagnetic and anisotropic material. The results of this work show novel field perturbations produced by macroscopic cylindrical and spherical shells and point-like sources of PGS, which can only be explained by the full, tensor-based description of magnetic susceptibility anisotropy. The most important implication of these results is that field perturbations due to magnetic susceptibility anisotropy cannot be accurately predicted by a simple orientation-dependent isotropic representation of susceptibility, but rather the full, tensor-based derivation must be used. The results are in agreement with previously published expressions for the field perturbation inside and outside of a cylindrical shell with anisotropic magnetic susceptibility, and further demonstrate radius-dependent uniform field offsets inside spherical shells, which are consistent with previous studies into the NMR line-position of the signal acquired from spherical lipoproteins [20].

The final experimental chapter describes how Monte Carlo simulation was used to investigate variations in the frequency and phase measured from an ensemble of

particles surrounding oriented, NMR-invisible, spheroidal perturbers with shape and volume fraction, and in the presence and absence of diffusion. The results of this work show that at very short echo times the signal frequency depends on the shape-dependent demagnetizing factor of the perturber, however as time goes on the measured frequency and phase evolve in a non-linear fashion in the static regime, and this variation is damped as the rate of diffusion increases. The key significance of these results lies in the demonstration that in such a system phase accumulation is not simply dependent on bulk susceptibility or mean magnetic field within a volume, but rather is a complex function of the shape and size of the perturbers, diffusion of the target nuclei, and the time at which the signal is sampled. Consideration of the results in the context of realistic diffusion rates in brain tissue and at practically relevant echo times showed that effects such as those shown here must be considered in the interpretation of local phase and frequency measurements in MRI.

This research was carried out at a time of increasing interest in the exploitation of MRI phase data to provide quantitative insight into the composition and microstructure of tissue *in vivo*. While the increasing body of literature shows that phase-based techniques can indeed provide powerful new insights, the results presented here demonstrate that appropriate care must be taken in the interpretation of phase-based image contrast, and in the consideration of the theoretical representation of the effects of tissue microstructure on such measurements.

8.2 Future Work

Considering the numerous recent advances in the exploitation of MRI signal phase and frequency, including quantitative susceptibility mapping [7, 8, 21-34], susceptibility tensor imaging [12, 35], and other developments in the observation and exploitation the effects of tissue microstructure [11, 14, 15, 17-19, 36-39], it is unsurprising that through the work carried out over the course of this thesis, questions have arisen which may be answered through future work.

Investigations into the pathology of multiple sclerosis have long been a prominent area of research in MRI, and since the development of quantitative phase-based imaging in the form of susceptibility-weighted imaging [1] and subsequently quantitative susceptibility mapping, the application of these techniques in MS has remained an active field [3, 6, 9, 37, 40-68], particularly due to interest in iron

deposition in the brain. Recently, MRI frequency shifts have been considered as a marker of tissue damage in multiple sclerosis [69], and such contrast has been linked to the breakdown of tissue microstructure [37]. In their work on fiber orientation-dependent contrast in white matter [16, 19], Wharton and Bowtell demonstrated that the effects of susceptibility anisotropy due to the structure of the myelin sheath caused orientation-dependent frequency offsets in the white matter that are non-linear in time, and they modelled this effect using the tensor form of susceptibility anisotropy discussed in Chapter 6 of this thesis. This orientation and time dependence of frequency offsets means that the monitoring of frequency offsets measured at a single time point does not constitute a reliable marker of tissue integrity. Future work will investigate longitudinal changes in frequency difference measurements during acute MS lesion formation. Frequency difference measurements will be combined with the results of DTI to identify fiber tracts in the white matter, to allow the utility of these measurements as a marker of white matter tissue integrity to be assessed. Additionally, high-resolution multi-echo T_2^*-weighted images will allow the calculation of quantitative R_2^* maps and quantitative susceptibility maps, allowing the comparison of changes in multiple quantitative MRI measurements during MS lesion formation.

The novel field perturbations caused by the spherical shells of PGS presented in Chapter 6 also suggest a potential avenue for further research. Previous research by Lounila et al [20] used NMR spectroscopy to demonstrate that shifts in the NMR line position of the signals recorded from inside lipoproteins were dependent on the size of the lipoprotein particle, attributing this to magnetic susceptibility anisotropy of the lipid shell. The work presented here demonstrated using theory and experiment that spherical shells of material with anisotropic magnetic susceptibility generate uniform internal magnetic field shifts with a magnitude inversely proportional to their internal radius, while generating a very weak external field perturbation. If this effect were reproducible and controllable on the microscale, it could form the basis of a novel method of generating tuneable MRI frequency contrast. Nanoscale, ordered mesoporous carbon spheres with graphitic walls have been synthesised by researchers interested in applications including catalysts, storage materials, and electrode construction [70-72]. If the walls of these shells are suitably ordered, and

porous to the extent that exchange could occur between internal and external water pools, they tuneable frequency contrast may be achievable.

While the simulations described in Chapter 7 clearly demonstrate a complex relationship between the shape and size of magnetic field perturbers, the diffusion rate of precessing particles in the surrounding magnetic field, and the measured signal frequency and phase; this work could be further developed by the more detailed consideration of how these relationships could affect real measurements made in the lab. Inclusion of T_1 and T_2 relaxation, as well as background fields from other susceptibility sources in more complex simulations would provide a more detailed insight into the possible implications of such effects. It may also be possible to validate the simulated results in the laboratory through the measurement of the real-world effects observed in the static regime using agar phantoms containing macroscopic, doped agar spheroids.

8.3 Final Conclusions

Over the last decade, advances in the exploitation of MRI signal phase have opened up several fields of quantitative MRI research, allowing *in vivo* measurement of local magnetic susceptibility through quantitative susceptibility mapping [7, 8, 22, 24, 25, 27, 30-32, 34, 73], novel fiber tracking methods exploiting magnetic susceptibility anisotropy [12, 19, 35], and greater insight into tissue microstructure through frequency difference measurement [16, 19]. The work presented here has shown that care must be taken in the interpretation of local phase measurements, in the modelling of magnetic susceptibility anisotropy, and also in any assumption made about the rate of phase accumulation in time and its link to bulk susceptibility or mean magnetic field in a volume. Consideration of the results presented and contemporary literature suggest potential avenues for future research, including the application of frequency difference measurements in the assessment of white matter integrity in multiple sclerosis, and the generation of tuneable MRI frequency contrast based on structures with anisotropic magnetic susceptibility.

8.4 References

1. Haacke, E.M., et al., *Susceptibility weighted imaging (SWI).* Magnetic Resonance in Medicine, 2004. **52**(3): p. 612-618.
2. Duyn, J.H., et al., *High-field MRI of brain cortical substructure based on signal phase.* Proceedings of the National Academy of Sciences of the United States of America, 2007. **104**: p. 11796-801.
3. Haacke, E.M., et al., Establishing a baseline phase behavior in magnetic resonance imaging to determine normal vs. abnormal iron content in the brain. Journal of Magnetic Resonance Imaging, 2007. **26**(2): p. 256-264.
4. Deistung, A., et al., *Susceptibility weighted imaging at ultra high magnetic field strengths: theoretical considerations and experimental results.* Magnetic resonance in medicine : official journal of the Society of Magnetic Resonance in Medicine / Society of Magnetic Resonance in Medicine, 2008. **60**: p. 1155-68.
5. Hopp, K., et al., Brain iron detected by SWI high pass filtered phase calibrated with synchrotron X-ray fluorescence. Journal of Magnetic Resonance Imaging, 2010. **31**(6): p. 1346-1354.
6. Grabner, G., et al., Analysis of multiple sclerosis lesions using a fusion of 3.0 T FLAIR and 7.0 T SWI phase: FLAIR SWI. Journal of magnetic resonance imaging : JMRI, 2011. **33**: p. 543-9.
7. Marques, J.P. and R. Bowtell, Application of a Fourier-based method for rapid calculation of field inhomogeneity due to spatial variation of magnetic susceptibility. Concepts in Magnetic Resonance Part B: Magnetic Resonance Engineering, 2005. **25B**: p. 65-78.
8. Wharton, S., A. Schäfer, and R. Bowtell, *Susceptibility mapping in the human brain using threshold-based k-space division.* Magnetic resonance in medicine : official journal of the Society of Magnetic Resonance in Medicine / Society of Magnetic Resonance in Medicine, 2010. **63**: p. 1292-304.
9. Bagnato, F., et al., Tracking iron in multiple sclerosis: a combined imaging and histopathological study at 7 Tesla. Brain : a journal of neurology, 2011. **134**: p. 3602-15.
10. Chu, K., et al., *Bulk magnetic susceptibility shifts in NMR studies of compartmentalized samples: use of paramagnetic reagents*. Magnetic Resonance in Medicine, 1990. **13**(2): p. 239-262.
11. Lee, J., et al., *Sensitivity of MRI resonance frequency to the orientation of brain tissue microstructure.* Proceedings of the National Academy of Sciences, 2010. **107**(11): p. 5130-5135.
12. Liu, C., *Susceptibility tensor imaging.* Magnetic Resonance in Medicine, 2010. **63**(6): p. 1471-1477.
13. Lee, J., et al., *T2*-based fiber orientation mapping.* NeuroImage, 2011. **57**(1): p. 225-234.

14. Chen, W.C., S. Foxley, and K.L. Miller, *Detecting microstructural properties of white matter based on compartmentalization of magnetic susceptibility.* NeuroImage, 2012. **70C**: p. 1-9.

15. Li, W., et al., *Magnetic susceptibility anisotropy of human brain in vivo and its molecular underpinnings.* NeuroImage, 2012. **59**(3): p. 2088-2097.

16. Wharton, S. and R. Bowtell, *Fiber orientation-dependent white matter contrast in gradient echo MRI.* Proc Natl Acad Sci U S A, 2012. **109**(45): p. 18559-64.

17. Oh, S.-H., et al., *Origin of B0 orientation dependent R2* (=1/T2*) in white matter.* NeuroImage, 2013. **73**(0): p. 71-79.

18. Wisnieff, C., et al., *Magnetic susceptibility anisotropy: Cylindrical symmetry from macroscopically ordered anisotropic molecules and accuracy of MRI measurements using few orientations*. NeuroImage, 2013. **70**(0): p. 363-376.

19. Wharton, S. and R. Bowtell, *Gradient echo based fiber orientation mapping using R2* and frequency difference measurements*. NeuroImage, 2013. **83**: p. 1011-1023.

20. Lounila, J., et al., *Effects of orientational order and particle size on the NMR line positions of lipoproteins*. Phys Rev Lett, 1994. **72**(25): p. 4049-4052.

21. Li, L. and J.S. Leigh, *Quantifying arbitrary magnetic susceptibility distributions with MR.* Magnetic Resonance in Medicine, 2004. **51**(5): p. 1077-1082.

22. Liu, T., et al., *Calculation of susceptibility through multiple orientation sampling (COSMOS): a method for conditioning the inverse problem from measured magnetic field map to susceptibility source image in MRI.* Magnetic resonance in medicine : official journal of the Society of Magnetic Resonance in Medicine / Society of Magnetic Resonance in Medicine, 2009. **61**: p. 196-204.

23. Shmueli, K., et al., *Magnetic susceptibility mapping of brain tissue in vivo using MRI phase data.* Magnetic resonance in medicine : official journal of the Society of Magnetic Resonance in Medicine / Society of Magnetic Resonance in Medicine, 2009. **62**: p. 1510-22.

24. de Rochefort, L., et al., *Quantitative susceptibility map reconstruction from MR phase data using bayesian regularization: validation and application to brain imaging.* Magnetic resonance in medicine : official journal of the Society of Magnetic Resonance in Medicine / Society of Magnetic Resonance in Medicine, 2010. **63**: p. 194-206.

25. Wharton, S. and R. Bowtell, *Whole-brain susceptibility mapping at high field: a comparison of multiple-and single-orientation methods*. NeuroImage, 2010. **53**(2): p. 515-525.

26. de Rochefort, L., et al., *Quantitative susceptibility map reconstruction from MR phase data using bayesian regularization: validation and application to brain imaging.* Magnetic Resonance in Medicine, 2010. **63**(1): p. 194-206.

27. Wharton, S., *Susceptibility Mapping in High Field MRI*. 2011. p. 190.

28. Schweser, F., et al., *Quantitative imaging of intrinsic magnetic tissue properties using MRI signal phase: an approach to in vivo brain iron metabolism?* NeuroImage, 2011. **54**: p. 2789-807.

29. Li, W., B. Wu, and C. Liu, *Quantitative susceptibility mapping of human brain reflects spatial variation in tissue composition*. NeuroImage, 2011. **55**: p. 1645-56.

30. Liu, J., et al., *Morphology enabled dipole inversion for quantitative susceptibility mapping using structural consistency between the magnitude image and the susceptibility map*. NeuroImage, 2012. **59**(3): p. 2560-2568.

31. Schweser, F., et al., *Quantitative susceptibility mapping for investigating subtle susceptibility variations in the human brain*. NeuroImage, 2012. **62**(3), 2083-2100.

32. Schweser, F., et al., *Toward online reconstruction of quantitative susceptibility maps: Superfast dipole inversion.* Magnetic Resonance in Medicine, 2013. **69**(6): p. 1581-1593.

33. Liu, C., et al., *Susceptibility-weighted imaging and quantitative susceptibility mapping in the brain.* Journal of Magnetic Resonance Imaging, 2014. DOI: 10.1002/jmri.24768

34. Haacke, E.M., et al., *Quantitative susceptibility mapping: current status and future directions.* Magnetic Resonance Imaging, 2015. **33**(1): p. 1-25.

35. Liu, C., et al., *3D fiber tractography with susceptibility tensor imaging.* NeuroImage, 2012. **59**(2): p. 1290-1298.

36. Liu, C., et al., *High-field (9.4T) MRI of brain dysmyelination by quantitative mapping of magnetic susceptibility*. NeuroImage, 2011. **56**(3): p. 930-938.

37. Yablonskiy, D.a., et al., *Biophysical mechanisms of MRI signal frequency contrast in multiple sclerosis.* Proceedings of the National Academy of Sciences of the United States of America, 2012. **109**: p. 14212-7.

38. Lee, J., et al., *The contribution of myelin to magnetic susceptibility-weighted contrasts in high-field MRI of the brain*. NeuroImage, 2012. **59**(4): p. 3967-3975.

39. van Gelderen, P., et al., *A torque balance measurement of anisotropy of the magnetic susceptibility in white matter*. Magn Reson Med, 2014. DOI: 10.1002/mrm.25524

40. Fazekas, F., et al., *MRI to monitor treatment efficacy in multiple sclerosis.* Journal of neuroimaging : official journal of the American Society of Neuroimaging, 2007. **17 Suppl 1**: p. 50S-55S.

41. Stankiewicz, J., et al., *Iron in chronic brain disorders: imaging and neurotherapeutic implications.* Neurotherapeutics : the journal of the American Society for Experimental NeuroTherapeutics, 2007. **4**: p. 371-86.

42. Bakshi, R., et al., *MRI in multiple sclerosis : current status and future prospects.* Society, 2008: p. 615-625.

43. Hammond, K.E., et al., *Development of a robust method for generating 7.0 T multichannel phase images of the brain with application to normal volunteers and patients with neurological diseases*. NeuroImage, 2008. **39**: p. 1682-92.

44. Hammond, K.E., et al., *Quantitative in vivo magnetic resonance imaging of multiple sclerosis at 7 Tesla with sensitivity to iron*. Annals of neurology, 2008. **64**: p. 707-13.

45. Eissa, A., et al., *Detecting lesions in multiple sclerosis at 4.7 tesla using phase susceptibility-weighting and T2-weighting*. Journal of magnetic resonance imaging : JMRI, 2009. **30**: p. 737-42.

46. Ge, Y., et al., *Diminished visibility of cerebral venous vasculature in multiple sclerosis by susceptibility-weighted imaging at 3.0 Tesla*. Journal of magnetic resonance imaging : JMRI, 2009. **29**: p. 1190-4.

47. Haacke, E.M., et al., *Characterizing iron deposition in multiple sclerosis lesions using susceptibility weighted imaging*. Journal of magnetic resonance imaging : JMRI, 2009. **29**: p. 537-44.

48. Mainero, C., et al., *In vivo imaging of cortical pathology in multiple sclerosis using ultra-high field MRI*. Neurology, 2009. **73**: p. 941-8.

49. Ropele, S., et al., *MRI assessment of iron deposition in multiple sclerosis.* Journal of magnetic resonance imaging : JMRI, 2011. **34**: p. 13-21.

50. Al-Radaideh, A.M., et al., *Increased iron accumulation occurs in the earliest stages of demyelinating disease: an ultra-high field susceptibility mapping study in Clinically Isolated Syndrome*. Multiple Sclerosis Journal, 2012, **19**(7), 896-903.

51. Bian, W., et al., *A serial in vivo 7T magnetic resonance phase imaging study of white matter lesions in multiple sclerosis*. *Multiple Sclerosis Journal*, 2012, ***19***(1), 69-75.

52. Hagemeier, J., et al., *Iron deposition in multiple sclerosis lesions measured by susceptibility-weighted imaging filtered phase: a case control study*. Journal of magnetic resonance imaging : JMRI, 2012. **36**: p. 73-83.

53. Zivadinov, R., et al., *Abnormal subcortical deep-gray matter susceptibility-weighted imaging filtered phase measurements in patients with multiple sclerosis: a case-control study*. NeuroImage, 2012. **59**: p. 331-9.

54. Yao, B., et al., *Chronic Multiple Sclerosis Lesions: Characterization with High-Field-Strength MR Imaging*. Radiology, 2012. **262**(1): p. 206-15.

55. Chen, W., et al., *Quantitative Susceptibility Mapping: Initial Experience for Multiple Sclerosis Lesion Characterization* (P03. 058). Neurology, 2012. **78**(Meeting Abstracts 1): p. P03. 058.

56. Present, T., *Magnetic Resonance Techniques in Multiple Sclerosis*. 2013. **68**: p. 1514-1520.

57. Langkammer, C., et al., *Quantitative Susceptibility Mapping in Multiple Sclerosis.* Radiology, 2013, **267**(2), 551-559.

58. Walsh, A.J., et al., *Multiple Sclerosis: Validation of MR Imaging for Quantification and Detection of Iron*. Radiology, 2013, **267**(2), p. 531-542.

59. Chen, W., et al., *Quantitative Susceptibility Mapping of Multiple Sclerosis Lesions at Various Ages*. Radiology, 2013. **271**(1): p. 183-192.

60. Bonnier, G., et al., *Advanced MRI unravels the nature of tissue alterations in early multiple sclerosis*. Ann Clin Transl Neurol, 2014. **1**(6): p. 423-32.

61. Wisnieff, C., et al., *Quantitative susceptibility mapping (QSM) of white matter multiple sclerosis lesions: Interpreting positive susceptibility and the presence of iron*. Magn Reson Med, 2014. DOI: 10.1002/mrm.25420

62. Hagemeier, J., et al., *Phase white matter signal abnormalities in patients with clinically isolated syndrome and other neurologic disorders*. AJNR Am J Neuroradiol, 2014. **35**(10): p. 1916-23.

63. Eskreis-Winkler, S., et al., *Multiple sclerosis lesion geometry in quantitative susceptibility mapping (QSM) and phase imaging*. Journal of Magnetic Resonance Imaging, 2014: DOI: 10.1002/jmri.24745

64. Chen, W., et al. *Quantitative susceptibility mapping of multiple sclerosis lesions at various ages.* Radiology, 2014, *271*(1), 183-192.

65. Blazejewska, A.I., et al., *Increase in the iron content of the substantia nigra and red nucleus in multiple sclerosis and clinically isolated syndrome: A 7 Tesla MRI study.* Journal of Magnetic Resonance Imaging, 2014, **41**(4), p. 1065-1070.

66. Chen, W., et al., *Quantitative susceptibility mapping of multiple sclerosis lesions at various ages*. Radiology, 2014. **271**(1): p. 183-92.

67. Rudko, D.A., et al., *Multiple Sclerosis: Improved Identification of Disease-relevant Changes in Gray and White Matter by Using Susceptibility-based MR Imaging.* Radiology, 2014. **272**(3): p. 851-864.

68. Ropele, S., et al., *Determinants of iron accumulation in deep grey matter of multiple sclerosis patients.* Multiple Sclerosis Journal, 2014. **20**(13): p. 1692-1698.

69. Wiggermann, V., et al., *Magnetic resonance frequency shifts during acute MS lesion formation. Neurology*, 2013. **81**(3): p. 211-218.

70. Xia, Y. and R. Mokaya, *Synthesis of Ordered Mesoporous Carbon and Nitrogen-Doped Carbon Materials with Graphitic Pore Walls via a Simple Chemical Vapor Deposition Method*. Advanced Materials, 2004. **16**(17): p. 1553-1558.

71. Xia, Y.D. and R. Mokaya, *Ordered Mesoporous Carbon Hollow Spheres Nanocast Using Mesoporous Silica via Chemical Vapor Deposition*. Advanced Materials, 2004. **16**(11): p. 886-891.

72. Xia, Y., Z. Yang, and R. Mokaya, *Templated nanoscale porous carbons.* Nanoscale, 2010. **2**(5): p. 639-659.

73. Wang, Y. and T. Liu, *Quantitative susceptibility mapping (QSM): decoding MRI data for a tissue magnetic biomarker*. Magnetic Resonance in Medicine, 2015. **73**(1): p. 82-101.